EURATOM-MEdC
Annual Report 2012

Summary of the 2012 research activities of the Association Euratom – MEdC Romania

The EURATOM – MEdC Association is part of the European integrated effort of research devoted to the realization of a new source of energy with unprecedented properties: clean, safe, sustainable. The year 2012 has been characterized by an acceleration of the processes leading to the construction of ITER, approaching the moment when this experimental device, the first reactor, will become available to the research. The pace being higher, the exigencies have been raised accordingly.

The EURATOM – MEdC Association can report for 2012 important achievements both in basic physics of fusion plasma and in technological research devoted to the advancement of the concept. The constant orientation to the ITER physics and technology was the dominant and unifying factor.

In 2012, the MEdC Association was composed of groups from seven institutes:

- Institute of Atomic Physics – Management Group of the Research Unit
- National Institute of Laser, Plasma and Radiation Physics (NILPRP)
- National Institute of Cryogenic and Isotope Technology (NICIT)
- National Institute of Physics and Nuclear Engineering (NIPNE)
- National Institute of Physics of Materials (NIPM)
- University of Craiova (UCv)
- University A. I. Cuza from Iassy (UAIC)

The number of persons participating to the activity of the Association in 2012 was 109, representing 33 ppy.

The year 2012 has been characterized by an active participation of the groups of research from the Romanian Association to the advancement of understanding the plasma physics of high confinement regimes. The principal focus was a better description of the plasma close to reactor regime, with the intention to converge toward the identification of a scenario for high performance ITER plasma.

As usual, the subjects have been aligned with the content of the EFDA Work Programme and are classified in terms of its structure. This has favoured the collaboration and the exchange of ideas with groups from other Associations.

The subject of transport in plasma has been well sustained in this year, in different approaches. The study of the transport due to the plasma turbulence has been extended along the line of statistical description of test particle dynamics. The role of the eddies that can induce trapping and further initiate formation of

coherent structures has been revealed and argued as a still unexplored origin of robust vortices with strong effect on transport. The perspective is to use this kind of approach to examine the formation of zonal flows, seen as coherent structure and fed by the eddies of the drift wave turbulence.

A related subject concerns the stochasticity of the fields, an intermittent phenomenon that can cause a sudden loss of confinement on large volumes. The instruments to study these events belong to the mathematics of stochastic systems and suggests exploiting the parallel with Hamiltonians for low dimensional mappings. In addition this approach has been extended with solution of fluid differential equations in view of implementing the effect of pellet fueling on the frequency of the Edge Localized Modes. This provides possible integrations of the continuum and iterative methods and this development will be pursued in future.

The stochasticity that can exist in tokamak and induce higher rates of transport has further been examined as a perturbation to Electron Temperature Gradient modes. Under the effect of noise the threshold for stability of the modes is affected and the evolution in close proximity of the linear regime can be described by Lyapunov exponents. This study will have to continue focusing on effect of random switching to unstable regimes.

There is a stable and productive preoccupation for the analytical and numerical description of the Resistive Wall Modes. In previous stages codes have been written specifically to overcome the obstacle raised by the complex geometry of the vacuum chamber. Taking into account of the holes is a prerequisite for the correct numerical description of the growth rates and the geometry of the eigenmodes. Analytical formulations have been identified that made possible a more economic numerical solution and allow to explore applications for particular tokamak configurations.

In a different approach the Resistive Wall Modes (RWM) have been studied with a main focus on the interaction of the external kink mode with the plasma. The plasma viscosity is the dominant factor that controls the rotation, with essential effect on the damping of the RWM. The trapping and the drifts of the particles are neoclassical effects that have been included in the analytical model.

The experimental measurements prepared for the linear machine Pilot – Psi (Holland) have been the object of continuous improvement and now they offer a wide spectrum of results and suggestions of interpretation. This was possible by combining the improvement of the technical means with numerical 2D mapping of the floating potential, Monte Carlo studies, with particularly careful determination of the behavior of the probes. A new method was proposed and verified, for determination of the ion branch of the probe characteristic.

In 2012 there has been a stable continuation of the contribution of our Association to the Atomic, Molecular, Nuclear and Surface Data Base. This is an important topic since the results become available to other parallel domains, like astrophysics, science of materials, etc. Electron -impact excitation rates and charge exchange rates have been provided and can now be currently used for the study of the dynamics of the density in tokamak plasma. The cross-sections have been calculated and compared with the published results and with experiments where available.

The physics of the plasma rotation has continued to attract the interest in view of the identification of the phenomenological explanation for recent experimental observations. The reversal of the toroidal rotation has become a test for the theory, either neoclassical or invoking the turbulent Reynolds stress. Our main contribution in 2012 was to confirm our original explanation for the reversal of rotation, by proving that the random rise and decay of convections will sustain the quasi-laminar flow of the H-mode at the edge of the tokamak.

The participation in the PWI Programme is structured in a wide range of subjects related mainly to fuel retention assessment, tools for removing fuel and dust from the wall surface and mixed material deposition.

- Several studies were dedicated to the deuterium retention mechanisms in order to determine the influence of surface composition, structure, and temperature as essential parameters able to allow predictions of the behaviour of multi-component first walls in JET and ITER.
    - The influence of the nanostructured tungsten coatings on the fuel retention was extensively studied. The impact of the coating characteristics (thickness, structure, etc.) and also of the substrate material (carbon-based and also Eurofer) on D retention were assessed. A new experimental device for plasma exposure and thermo-desorption analysis has been designed, built and commissioned.
    - A couple of studies are dedicated to the deuterium trapping mechanisms of ITER beryllium-related mixed materials and to the clarification of the influence of Be-containing redeposited layers on D-retention and release. The sample preparation is based on the thermionic vacuum arc method developed in our Association. Comprehensive analysis were performed in cooperation with IPP Garching, Germany, and IJS Ljubljana, Slovenia
- An intense campaign of X-ray microtomography measurements of most relevant composite materials for fusion technology has been sustained. A consistent comparison of different composite materials has been accomplished. An effective method for the evaluation of total porosity and its parameters as open porosity, pore area or size distribution has been developed. The method can provide useful information for fuel retention studies.
- With the final aim of the complex characterization of atomic intermixing processes and related structural properties of thin films and multilayers involving typical elements used in plasma facing components, detailed studies have been focused on both the issue of the buffer layers for subsequent growing of Be and W films and on the Be/W and W/Be bilayers grown on the previously studied buffers. Also thin films of ternary and quaternary systems containing C, W and Mg in chemical compounds including oxygen were developed by mean of the pulsed laser deposition (PLD) and Radio-Frequency assisted PLD techniques. Studies on the physical and chemical properties of ternary compounds containing oxygen and on the influence of the ratios between elements on film properties were carried out.

- As long-term fuel inventory in plasma-facing components is a critical issues to be resolved in order to ensure safe viable operation of a reactor the development of reliable and efficient methods of fuel removal has been explored.
    - The work on the development of plasma torch tool for removal of carbon and carbon/metal co-deposited layers from flat surfaces and from inside gaps continued with the investigation of surface modification by erosion of the graphite material due to plasma torch, formation and transport of solid phase and gas phase products in the exhaust, and their characterization.
    - The potential of the helium RF discharge as a fuel removal technique was investigated mainly in what concerns the re-adsorption of D in W. The main contribution of our Association consist in the preparation of non-deuterated and deuterated W-MS samples (with different W/D ratios or variable D profiles), deposited by magnetron sputtering (MS) technique.

The development of the optimum design configuration for translating the fusion power generation concept into a commercially viable technology depends on the selection of materials. The development of the DEMO fusion reactor is established as a priority in EU. The reactor's structure is complex, fast evolving and needs for its construction the support of different materials with certain specifications. The field of Materials has been included in the Work Plan of our Association, on the basis of an exclusive support from the National Authority in 2010. The fusion material topic is now an active component of our Association, with four projects accepted in WP12-MAT, attempting to solve critical issues:

- Complex components should be realized based on the current DEMO design, like e.g. divertor tiles or other armour components. A new method to realize complex materials and pieces starting with W (plates, foils, and pieces), W-steel FGMs and steel pieces was developed for specific shapes.
- In the current DEMO design, plasma facing components are made of W. Joining with similar W-based components or structural parts (usually made of steel) raises several technological problems. The FAST (Field Assisted Sintering Technique) was applied to join W to W and W to steel (Eurofer 97) by brazing with an intermediate powder layer. A new procedure was defined for powder brazing, using a mixture of micron and nanometre sized metal powders.
- With the stop of the production of Eurofer steels - a former candidate to be used as a structural material on which the armour material is placed -, a replacement is looked for among ODS steels. At this stage of research, laboratory scale fabrication and characterization of ODS are one of the key aspects. New laboratory scale routes based on powder metallurgy and spark plasma sintering have been investigated, with the objective to evaluate the potential of powders processing involving SPS for fabrication of ODSFS.

JET, as the machine closest to ITER in terms of size, its tritium capability and its use of the ITER first wall materials, will remain the focus of the European programme on tokamak physics. The participation of our Association at JET Enhancement and Experimental Program is structured on following main directions:

- Development of studies related to the ILW project, focusing on the following topics:
    - As it is very important for the exploitation of the new JET wall to know in advance the limits of the W coatings when they are subjected to a high number of heating pulses (thousands) relevant to JET operation, the limits of the W coatings deposited on CFC tiles for the ITER-like wall has been investigated. The influence of the Combined Magnetron Sputtering and Ion Implantation coating parameters on the thermo-mechanical properties of the coatings were studied with the aim to improve these properties to investigate the capability of this technology to increase the W coating thickness towards 100 microns.
    - The behaviour of W coatings to a cyclic thermal loading relevant for JET operation has been studied. As far as long pulse thermal loading is concerned, in order to get relevant information about the W coating limits under more realistic loading conditions (including steady-state plasma and ELM-like transients), additional tests were carried out in Magnum-PSI, DIFFER, Netherlands.
    - An advanced procedure for the calibration of the measure this emissivity and to calibrate the JET KP-M1AP IR camera was developed in 2011 in order to be used for temperature measurement of the W coating during JET operation. The influence of the substrate structure, viewing angle and W coating temperature on the emissivity in more details has been investigated using a new experimental setup.
    - A combination of X-ray non-destructive techniques, based on high resolution X-ray absorption, X-ray fluorescence mapping, and X-ray backscattering, have been developed in our Association for tungsten coating thickness analysis. They allow the measurement of the thickness of layers and, therefore, the determination of the 2-dimensional erosion pattern on a whole PFC, for example a divertor tile. The methods were applied for the post-mortem coating thickness measurements of samples from the W-coated JET outer divertor tiles 7 and 8 (exposed during the 2007-2009 campaigns). X-ray micro-radio and tomography measurements have been performed in order to assess the substrate morphology the erosion pattern.
    - High sensitivity accelerator mass spectrometry analysis (AMS) and Full Combustion flowed by scintillator Counting (FCM) allowed the determination of the tritium retention in the MkII-HD divertor protection tiles of JET. The depth profiling distributions of tritium retention revealed an enhanced accumulation of tritium on the back side of the tile in comparison to the bulk by more than 3 orders of magnitude. This result confirmed independently by two different experimental techniques: Accelerator Mass Spectrometry and Full Combustion followed by scintillation detection of tritium.

- Development of instruments, tools and techniques for JET diagnostics:
    - The participation of the MEdC Association to the Enhancement Project II at JET continued with the work on the two projects leaded by our Association: i) the upgrade of the GammaRay Cameras (GRC) by development and construction of the KN3-NA neutron attenuators system and ii) the upgrade of the JET Tangential Gamma-Ray Spectrometer KM6T by developing a Tandem Collimators System. The commissioning of the neutron attenuators system has been successfully accomplished by complex and extensive experiments. The neutron attenuation factors retrieved in the experiments are in agreement with values initially proposed, taking into account the additional technical constraints (port insulation thickness, thermal expansion, disruption displacements) which were imposed. It was clearly demonstrated that the system provides adequate n/γ filtering for deuterium experiments. The evaluation of the physical performance of the tandem collimator system has been performed also by extensive experiments during C30 JET experimental campaign, allowing the commissioning of the system.
    - In the framework of developing imaging diagnostic techniques based on video data, two methods, based on phase congruency principle and on sparse image representation and overcomplete dictionaries, respectively, has been developed for MARFE automatic identification. The methods were tested on JET experimental data and have proved to provide a good prediction rate.
- The Participation to JET campaign C30 was related to the investigation of the behaviour of W coatings during JET operation and to video image processing methods for plasma diagnostic. Our Association also supplied staff for Diagnostic Coordinator and Video System Operator positions.

Public information actions

In 2012 the Association has organized the "Workshop on basic aspects of fusion plasma physics", dedicated to more fundamental researches and aiming to promote the understanding of the fusion plasma in the context of the concentration of the community effort on the ITER construction. This Workshop has been accompanied by a special Session dedicated to the late Professor Radu Balescu, the great Romanian physicist which, besides fundamental contribution to science, has had an essential role in the development of our Euratom Association. Finally, the third associated event was our yearly reporting meeting, the Association Days. The programme of these meetings is available at the address http://www.euratom.ro. This entire event has been appreciated by all participants and has been reflected in press.

A TV studio broadcast (29 August 2012) has been devoted to the realizations of the Romanian researcher leading the beryllium group of our Association. With this occasion, aspects of the works and achievements of our EURATOM Association have been discussed.

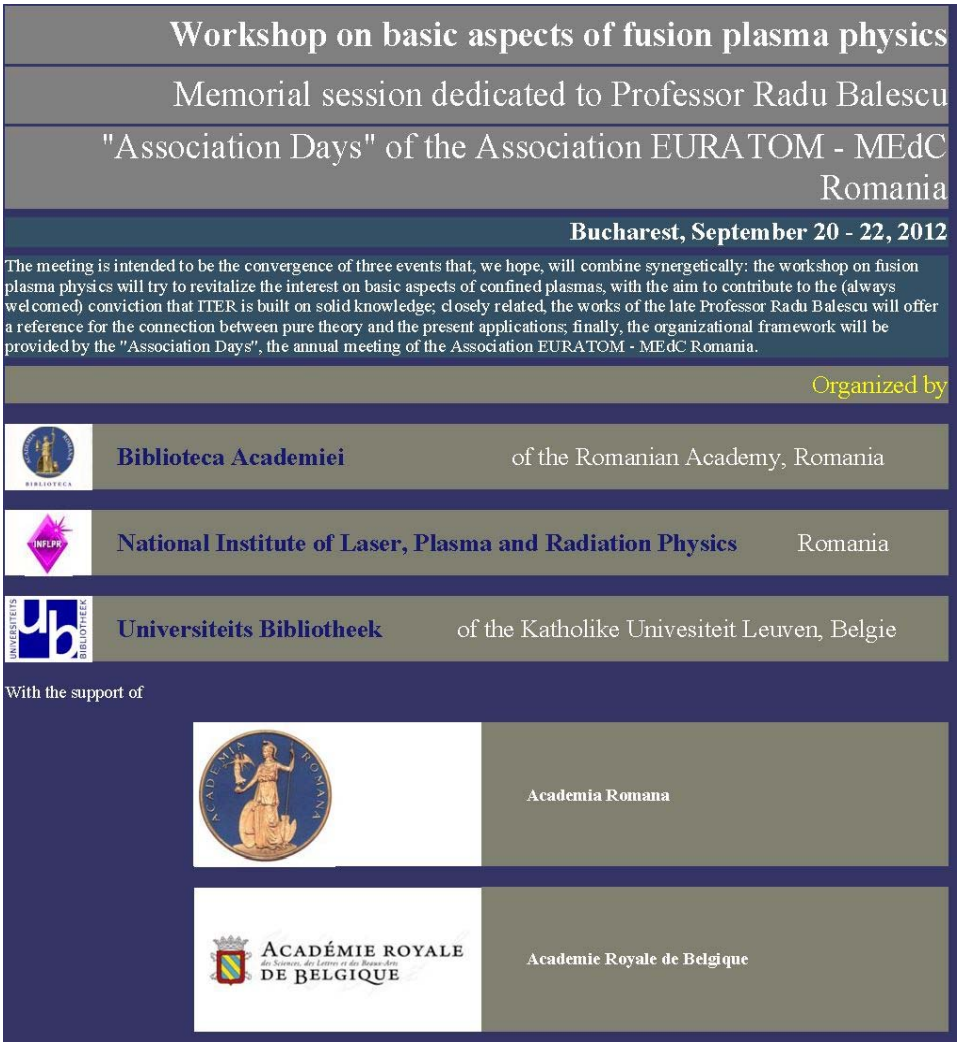

Two presentations on fusion science in general and on our Euratom Association, in particular, have been invited at the meeting “Diaspora 2012”:

- “The EURATOM collaboration: the research on the Controlled Thermonuclear Fusion”, at the “Workshop International Collaborations”.
- “How to achieve an ideal: the controlled fusion”, at the “Workshop Energy from renewable sources”

Madalina Vlad, *Head of Research Unit*

Teddy Craciunescu, *Deputy*

CONTENT

PHYSICS OF THE TOKAMAK PLASMA

PLASMA-WALL INTERACTION

PREPARATION AND COMPLEX CHARACTERIZATION OF (BE, W, C) CONTAINING FILMS FOR FUEL RETENTION

V. Kuncser, G. Filoti, P. Palade, G. Schinteie, S.G. Sandu, A. Lungu, C.P.Lungu, I. Jepu, C.Porosnicu

PRODUCING AND CHARACTERIZATION OF THIN FILMS OF TERNARY AND QUATERNARY SYSTEMS: W/C/MG/O/N

D. Colceag, A. Andrei, R. Pascu, A. Matei, N. Scarisoreanu, R. Birjega, M. Dinescu

GASEOUS INCLUSION TRAPPING MECHANISM STUDY OF ITER BERYLLIUM RELATED MIXED MATERIALS

C. Porosnicu

FUSION MATERIAL DEVELOPMENT

W-FGM-STEEL COMPONENTS BY POWDER METALLURGY ROUTES

A. Galatanu, I. Enculescu, M. Galatanu, B. Popescu, M. Valeanu, M. Walter

SPS JOINING&BRAZING W-W AND W-STEEL

M. Galatanu, B. Popescu, M. Enculescu, P. Palade, A. Galatanu

ODSFS BY SPARK PLASMA SINTERING OF PLANETARY MILLED AND MELT SPINNING PRECURSORS

P. Badica, P. Palade, M. Burdusel, C. Bartha, V. Kuncser

THE INFLUENCE OF THE CHEMICAL COMPOSITION AND RESIDUAL PROCESS CONTROL AGENT ON THE MICROSTRUCTURE AND MICROHARDNESS OF ODSFS'S

V. Mihalache, I. Mercioniu, A. Velea, G. Aldica, P. Palade

PARTICIPATION AT JET ENHANCEMENT AND EXPERIMENTAL PROGRAM

THE LIMITS OF THE W COATINGS DEPOSITED ON CFC TILES FOR THE ITER-LIKE WALL AT JET

C. Ruset, E. Grigore, I. Munteanu, M. Gherendi

ADVANCED CALIBRATION OF THE PIW IR CAMERAS

C. Ruset, D. Falie, E. Grigore, I. Munteanu, M. Gherendi, V.L. Zoita

W-COATING ELM-LIKE TESTS IN MAGNUM-PSI

C. Ruset, E. Grigore, I. Munteanu, M. Gherendi, D. Nendrean

EROSION/DEPOSITION STUDIES OF SELECTED PFC SAMPLES FROM JET BY X RAYS

I. Tiseanu, T. Craciunescu, C. Dobrea, A. Sima, M. Lungu, C. P. Lungu, I. Jepu, A. M. Lungu, P. Chiru, J. Likonen, A Hakola

A STRIKING EFFECT OF FUEL RETENTION IN PROTECTION TILES OF TOKAMAK VESSELS

C. Stan-Sion, G. Kizane, M. Enachescu, J. Likonen, N. Bekris, P. Batistoni

UPGRADE OF THE JET TANGENTIAL GAMMA-RAY SPECTOMETER (KM6T)

S. Soare, M. Curuia

UPGRADE OF GAMMA RAY-CAMERAS: NEUTRON ATTENUATORS

M. Curuia, M. Anghel, T. Craciunescu, M. Gherendi, S. Soare, Vasile Zoita

AUTOMATIC REAL-TIME DISRUPTION PREDICTION BY FAST VISIBLE CAMERA VIDEO IMAGE PROCESSING

T. Craciunescu, Andrea Murari, I. Tiseanu, Jesus Vega

PHYSICS OF THE TOKAMAK PLASMA

INVESTIGATION OF HELICAL PERTURBATIONS IN TOKAMAKS

C.V. Atanasiu[1], L.E. Zakharov[2], D. Dumitru[1]

[1]*National Institute for Lasers, Plasma and Radiation Physics, Bucharest, Romania*
[2]*Princeton University, Plasma Physics Laboratory, Princeton, USA*

[BS_1/WP12-ITM]

Abstract

During the period January-December 2011, the theoretical and modelling research activity of the "*Mathematical Modelling for Fusion Plasmas Group*" has been focalized calculations of the response of 3D thin multiple connected walls to an external kink mode in diverted axisymmetric tokamak configurations. To calculate the contribution of the plasma perturbed magnetic field in the vacuum region in toroidally symmetric tokamak discharges, we have made use of the concept of a surface current [1]. In order to simplify the description and calculation of the stability of modes and the plasma response, we limited ourselves to the reduced MHD approximation. The expression of the normal component of the magnetic field produced by the perturbation of the flux function has been calculated using a previously developed methodology [2]. In a vacuum gap separating the toroidal plasma from the wall and other current-currying current elements, the perturbed magnetic field can be expressed as a sum due to the rotating plasma contribution, to the wall contributions and to the electrical currents flowing outside the wall. Expressing the current density via a scalar stream function we have obtained a diffusion type equation describing the current density distribution in the wall, with known wall thickness, electrical wall conductivity, metric coefficients and Jacobian. A very fast mathematical algorithm has been developed. To the best of our knowledge, this solving method applied to thin walls with holes is new.

Papers

[1] C.V. Atanasiu, A.H. Boozer, L.E. Zakharov, A.A. Subbotin, and I.G. Miron, *Determination of the vacuum field resulting from the perturbation of a toroidally symmetric plasma,* Phys. Plasmas **6**, (1999) 2781-2790.

[2] C.V. Atanasiu, S. Günter, K. Lackner, and L.E. Zakharov, *Linear tearing modes calculation for diverted tokamak configurations*, Phys. Plasmas **12**, (2004) 5580-5594.

[3] C.V. Atanasiu, L.E. Zakharov, *Response of a 3D thin wall to an external perturbation of rotating plasma*, Phys. Plasmas (submitted 2013)

Conferences

[1] C.V. Atanasiu, L.E. Zakharov, *Response of a 3D thin wall to an external kink mode of a rotating plasma*, EPS39 Conference on Plasma Physics, 2-6 July, 2012, Stockholm, Sweden; P1.003.

[2] C.V. Atanasiu, L.E. Zakharov, D. Dumitru, *Calculation of the reaction of a 3D thin wall to an external kink mode of rotating plasma,* 16th Int. Conf. on Plasma Physics and Applications, 2013 June 20-25, Magurele, Bucharest Romania (oral presentation).

Detailed results

One of the major goals in thermonuclear fusion research is to produce stable high-pressure plasma, preferably at steady state, for the economic production of fusion energy. High power density implies high β but the maximum magnetic field *B* is limited by practical engineering constraints. Ideal magnetohydrodynamic (MHD) instabilities impose hard limits on the achievable β. In tokamaks, if internal instabilities are avoided by a suitable choice of the plasma current profile, the β limit comes about by the onset of External Kink Modes (EKMs). They cause a deformation of the plasma boundary, grow on the Alfvénic timescale of the order of 10^{-6}s and can terminate the plasma

discharge abruptly. In the presence of resistive wall, the plasma configuration becomes unstable, the stability limit being virtually the same as in the case without wall. However, the modes grow much more slowly, namely, on the resistive timescale of the wall, which is typically of the order of 10^{-2}s. These decelerated EKMs are denoted Resistive Wall Modes (RWMs). Stabilization of RWM is one of the key topics addressing prevention of disruptions in tokamaks. There are a vast number of papers investigating the physics of Resistive Wall Modes [1-5].The effects of 3-D electromagnetic structures on RWM stability of reversed field pinches [6] and a model-based dynamic RWM identification and feedback control in the DIII-D [7], both using existing numerical codes, have been investigated. Finally, a comprehensive review of the present status of the conceptual foundations and experimental results on the stabilization of the external kink and the resistive wall mode is given in Ref. [8].

The wall response is an important ingredient of realistic modelling of the RMW physics, which is now covered by a variety of numerical codes developed over decades of existence of the topic. New topic, related to disruptions emerged when the current sharing effect was discovered in 1996 during a large vertical disruption event on JET, which generated a *m/n*=1/1 kink mode (*m, n* are its toroidal and poloidal wave numbers), a large sideways force on the vacuum vessel, and the current exchange between plasma and the wall [9, 10]. The initially adopted explanation of the current sharing by so-called halo currents was rejected in Ref. [11] as contradicting all vertical disruption cases on JET in the sigh of the effect. Instead, a basic model for the Wall Touching Kink Mode (WTKM) was proposed as consistent with both MHD theory and JET experiments [12].

The present work was motivated by the fact that most of wall models, developed for RWM are not applicable for WTKM. Thus, DCON and VACUUM codes [13-14] are an example of the use of scalar potential representation for the vacuum field. First, it is suitable only for closed toroidal shells without holes, second, WTKM need the explicit use of electric currents in the wall to describe both Hiro and eddy currents [12]. Several other codes, like, such as the MARS-F code [15] and the KINX code [16] rely on axisymmetric walls. At the same time, 3-D wall structure is essential for the physics of WTKM. VALEN code [17], one of the first codes which model the 3-D structure of the wall, uses wire mesh representation of currents in the wall, which is singular. Being suitable for RWM, it is not applicable for WTKM, which requires reliable magnetic field and current calculations at the wall surface. The CARMA combination of MARS-F/CARIDDI codes [18] can address realistic stabilization of the slow dynamics of the feedback stabilized RWM. At the same time, the volumetric finite elements used for wall representation are inconsistent with the near surface concentrated distribution of the Hiro and eddy currents during the fast stage of disruption. In this regard, the thin wall representation seems to be more adequate. Essentially, only one wall model, used for RWM and developed by Merkel stability code STARWALL and the feedback optimization code OPTIMX [19, 20], can be used for WTKM as well. It uses a triangle representation of a conducting thin wall.

Here, we present an alternative approach, which is not as universal as triangle-based model, but can be considered as complimentary to them due to its very high speed of simulations. Due to the importance of the effect of the plasma touching the wall, the investigation of the Wall Touching Kink Modes represents the primary goal of the present work. We will present a method to calculate the response of a thin 3D multiple connected thin wall to an EKM, based on our first results [21, 22]. To calculate the contribution of the plasma perturbed magnetic field in the vacuum region in toroidally symmetric tokamak discharges, we have used the concept of a surface current [23]. The expression of the normal component of the magnetic field produced by the perturbation of the flux function

has been calculated using the methodology developed in Ref. [24]. We will consider a coordinate system (a,ϑ,ϕ) attached to the wall, while the plasma surface will be described by the coordinate system (a',ϑ',ϕ'). ϑ and ϕ represent the poloidal and toroidal angles, respectively, while $a=a_0$ and $a'=a'_0$ represent the wall surface and the plasma surface, respectively. In a vacuum gap separating the toroidal plasma from the wall and other current-currying current elements, the perturbed magnetic field can be expressed as $\mathbf{B}=\mathbf{B}^{pl}+\mathbf{B}^{w}+\mathbf{B}^{ext}$, where each term corresponds to the plasma contribution, to the wall contributions and to the electrical currents flowing outside the wall, respectively. The eddy current distribution in the thin wall is described by the known diffusion equation [21]

$$\nabla^2 I(t,\theta,\varphi) = d\sigma \frac{\partial B_n(t,\theta,\varphi)}{\partial t}$$

where $I=I(t,\vartheta,\phi)$ is the stream function of the eddy currents introduced by the relation $\mathbf{J}=\nabla I \times \mathbf{n}$ with $\mathbf{J}$ the linear eddy current density, $\mathbf{n}$ the external normal to the wall, B_n the normal to the wall component of the magnetic field, d the wall thickness and σ the electrical conductivity of the wall. If on the plasma surface ($a'=a_0'$) the perturbed magnetic field produced by the plasma (a real value) was excited by many modes, one can write the following equations in the wall frame

$$B_n^{pl}(t,\theta,\varphi) = \sum_{mN} \underline{B^{pl}}(a)\exp[\gamma^r t + i\alpha + i\omega t],$$

$$B_n^{w}(t,\theta,\varphi) = \sum_{mN} \underline{B^{w}}(a)\exp\left[\gamma^r t + i\alpha + i\omega t + i\beta_b\right] = \sum_{mN} \underline{\hat{B}^{w}}(a)\exp[\gamma^r t + i\alpha + i\omega t],$$

$$I(t,\theta,\varphi) = \sum_{mN} \underline{I}(a)\exp[\gamma^r t + i\alpha + i\omega t + i\beta_I] = \sum_{mN} \underline{\hat{I}}(a)\exp[\gamma^r t + i\alpha + i\omega t],$$

with γ^r the growth rate of the mode in the plasma reference system, $\omega=m\Omega_\vartheta - n\Omega_\phi$ the angular frequency, $\theta=d\vartheta'/dt$ and $\Omega_\varphi=d\phi'/dt$ the constant angular speeds of the plasma mode. $\beta_{I,b}=\beta_{I,b}(\vartheta,\phi)$ is the phase due to the RL circuit character of the wall (in general, $\beta_b \neq \beta_I$) and $\alpha = m\vartheta - n\phi$. m and n are the wave numbers. Let us define a curvilinear coordinate system (u,v,w)

$$\boldsymbol{r}_u \equiv \frac{\partial \boldsymbol{r}}{\partial u},\ \boldsymbol{r}_v \equiv \frac{\partial \boldsymbol{r}}{\partial v},\ \boldsymbol{r}_w \equiv \frac{\partial \boldsymbol{r}}{\partial w} \equiv d\frac{\boldsymbol{r}_u \times \boldsymbol{r}_v}{|\boldsymbol{r}_u \times \boldsymbol{r}_v|}.$$

where the two first covariant basis vectors are tangential to the wall surface $\mathbf{r}_u\ \mathbf{n}=0$, $\mathbf{r}_v\ \mathbf{n}=0$, $\mathbf{r}$ denotes the vector from an arbitrary origin to a variable point, and $\mathbf{n}$ is the external normal to the wall. The third basis vector $\mathbf{r}_w$ is normal to the wall surface and determines the w coordinate. d is the wall thickness. The metric tensor has only four components g_{uu}, g_{vv}, g_{ww}, and $g_{uv}=g_{vu}=0$, while the contra-variant basis vectors perpendicular to the plane ($\mathbf{r}_u$, $\mathbf{r}_v$) is given by $\mathbf{r}^w = \mathbf{r}_w/d^2$ and defines the normal vector to the wall $\mathbf{n}=d\mathbf{r}^w$. The current density $\mathbf{j}$ [A/m^2] and the correspondent surface current density $\mathbf{i}$ [A/m] are coplanar with the wall surface and can be expressed with the help of a stream function

$$\boldsymbol{j} = \nabla I \times \boldsymbol{r}^w = \frac{1}{dD}\frac{\partial I}{\partial v}\boldsymbol{r}_u - \frac{1}{dD}\frac{\partial I}{\partial u}\boldsymbol{r}_v, \quad \boldsymbol{i} = d\int_0^1 \boldsymbol{j}\, dw = \frac{1}{dD}\frac{\partial I}{\partial v}\boldsymbol{r}_u - \frac{1}{dD}\frac{\partial I}{\partial u}\boldsymbol{r}_v.$$

$D=\sqrt{g_{uu}-g_{uv}^2}$ is the 2D Jacobian at the wall surface. The electric and the magnetic fields are connected via the potentials Φ_E and $\mathbf{A}$ and Ohm's law at the wall surface

$$\boldsymbol{E} = -\nabla\phi_E - \frac{\partial \boldsymbol{A}}{\partial t}, \qquad \boldsymbol{B} = \boldsymbol{\nabla}\times\boldsymbol{A}, \qquad -\frac{\partial \boldsymbol{A}}{\partial t} - \nabla\phi_E = \frac{\boldsymbol{j}}{\boldsymbol{\sigma}},$$

while the differential equation determining the stream function is given by the parabolic equation

$$d\frac{\partial(\boldsymbol{r}^w\cdot\boldsymbol{B})}{\partial t}=\frac{1}{D}\left\{\frac{\partial}{\partial u}\left[\frac{1}{\sigma d}\left(\frac{g_{vv}}{D}\frac{\partial I}{\partial u}-\frac{g_{uv}}{D}\frac{\partial I}{\partial v}\right)\right]+\frac{\partial}{\partial v}\left[\frac{1}{\sigma d}\left(\frac{g_{uu}}{D}\frac{\partial I}{\partial v}-\frac{g_{uv}}{D}\frac{\partial I}{\partial u}\right)\right]\right\}.$$

In the following, we present a fast numerical algorithm we have developed. It is well known that the solution of a non-homogeneous partial differential equation is a linear combination between the general solution of the homogeneous equation and any particular solution of the non-homogeneous solution. The problem being a linear one, the stream function *I* can be considered as a linear combination of the constants C_n, representing the constant unknown values of the stream function at the n_g hole contours, and some scalar functions $F_n^{\,h}$ and $F_n^{\,nh}$

$$I=\sum_{n=1}^{n_g}C_nF_n^h+F^{nh}\rightarrow\nabla I\times\boldsymbol{n}_s=\sum_{n=1}^{n_g}C_n\nabla F_n^h\times\boldsymbol{n}_s+\nabla F_n^{nh}\times\boldsymbol{n}_s,$$

where the superscripts ^{h} indicate that part of the function corresponding to the homogeneous part of the equation, while the superscript ^{nh} corresponds to the non-homogeneous equation. The scalar function $F_n^{\,h}$ can be determined by solving a sequence of particular problems. With the notation $P_{k,n}=\oint_{\Gamma_k}\nabla F_n^{nh}\times\boldsymbol{n}_s\,d\boldsymbol{l}_{\Gamma_k}$, the following system of equations was obtained with C_n the unknown constant stream functions on the hole contours.

$$\sum_{n=1}^{n_g}C_nP_{kn}\quad=-\oint_{\Gamma_k}\nabla F_n^{nh}\times\boldsymbol{n}_s\,d\boldsymbol{l}_{\Gamma_k}-\sigma_s\int_{S_{\Gamma_k}}\frac{\partial\boldsymbol{B}}{\partial t}d\boldsymbol{S}_{\Gamma_k},k=1,2,\dots n_g$$

Such a superposition process eliminates the necessity of nested iterations and gives a significant gain in the speed of simulations, as is illustrated in Table 1. To the best of our knowledge, this solving method applied to thin walls with holes is new.

Table 1 Comparative running times between a classical solving method and the superposition one for different number of grid points along u and v coordinates.

Solving method	No. of grids points	Running time [s]
Dual iteration	101 × 101 (u × v)	103
Superposition	101 × 101 (u × v)	3
Dual iterations	151 × 151 (u × v)	690
Superposition	151 × 151 (u × v)	14

To check our results, analytical expression for practical calculations of magnetic field components of a single toroidal harmonic of the stream function have been deduced for a stream function of the form $I(l,\varphi')=\bar{I}(l)\cos n\varphi'$

$$\boldsymbol{B}_r=\frac{\mu_0}{4\pi}\cos n\varphi\oint\left(\frac{\alpha}{2rr'}\right)^{\frac{3}{2}}\frac{2}{(1+\alpha)^{1/2}}\left\{\bar{\boldsymbol{J}}_t\left[t_zr'+t_r\left(z-z'\right)\right](H_{n-1}-H_{n+1})+\bar{\boldsymbol{J}}_\varphi(z-z')(H_{n-1}-H_{n+1})\right\}r'dl,$$

$$\boldsymbol{B}_{\boldsymbol{\varphi}}=\frac{\mu_0}{4\pi}\cos n\varphi\oint\left(\frac{\alpha}{2rr'}\right)^{\frac{3}{2}}\frac{2}{(1+\alpha)^{1/2}}\left\{\bar{\boldsymbol{J}}_t\left[2t_zrH_n-t_r\left(z-z'\right)\right](H_{n-1}-H_{n+1})+\bar{\boldsymbol{J}}_\varphi(z-z')(H_{n-1}H_{n+1})\right\}r'dl,$$

$$\boldsymbol{B}_z = \frac{\mu_0}{4\pi}\cos n\varphi \oint \left(\frac{\alpha}{2rr'}\right)^{\frac{3}{2}} \frac{2}{(1+\alpha)^{1/2}} \left\{-\bar{\boldsymbol{J}}_t t_r r\,(H_{n-1} - H_{n+1}) + \bar{\boldsymbol{J}}_\varphi [2r' H_n - r(H_{n-1} - H_{n+1})]\right\} r' dl,$$

where

$$H_n = \frac{(1+\alpha)^{\frac{1}{2}}}{4} \int_0^{2\pi} \frac{\cos n\phi \, d\phi}{(1-\alpha\,\cos\phi)^{3/2}}, \qquad \alpha = \frac{2r_p r_q}{r_p^2 + r_q^2 + \left(z_p - z_q\right)^2}.$$

In these equations we have to calculate the integrals H_n for different toroidal wave numbers n. This represents the most challenging part due to the fact that recurrence relations failed for $k=[2\alpha/(1+\alpha)]^{0.5}$ <0.4 and n>4, and yield incorrect results. To overcome this, we have developed a new calculation method of the H_n integrals by using the associated Legendre functions [25-27]. Thus, by using the associated Legendre functions, the H_n integral has been computed exactly up to the ninth digit for any k and for n up to 20. Our approach has been applied to a toroidal wall with circular cross-section, with big radius R=4m and small radius a=1m with a surface current distribution of the form $I=\sin m\vartheta \cos n\phi$. Two domains have been chosen: one external to the toroidal wall located and the second the interior of the same wall The distributions $B_r(\vartheta,\phi)$ and $B_z(\vartheta,\phi)$ in both domains are presented in Figures 1 and 2.

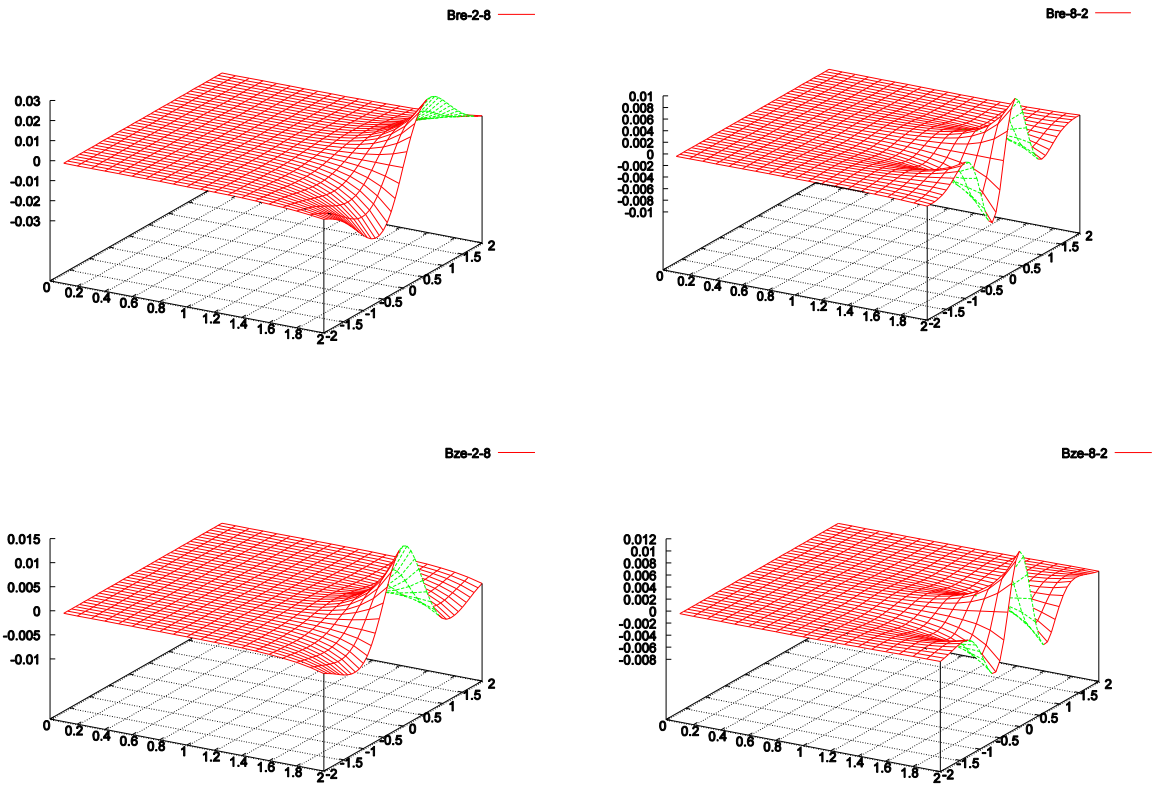

Figure 1 - Distribution of the radial and axial components of the magnetic field $B_r(r,\phi,z)$ and $B_z(r,\phi,z)$ in an external domain with respect to the wall, given by a surface current distribution of the form $I=I_0\sin(m\vartheta)\cos(n\phi)$ on an axis-symmetric closed tokamak wall. e indicates the external domain where this component has been calculated, 2 represents the poloidal wave number m, and 8 the toroidal wave number n

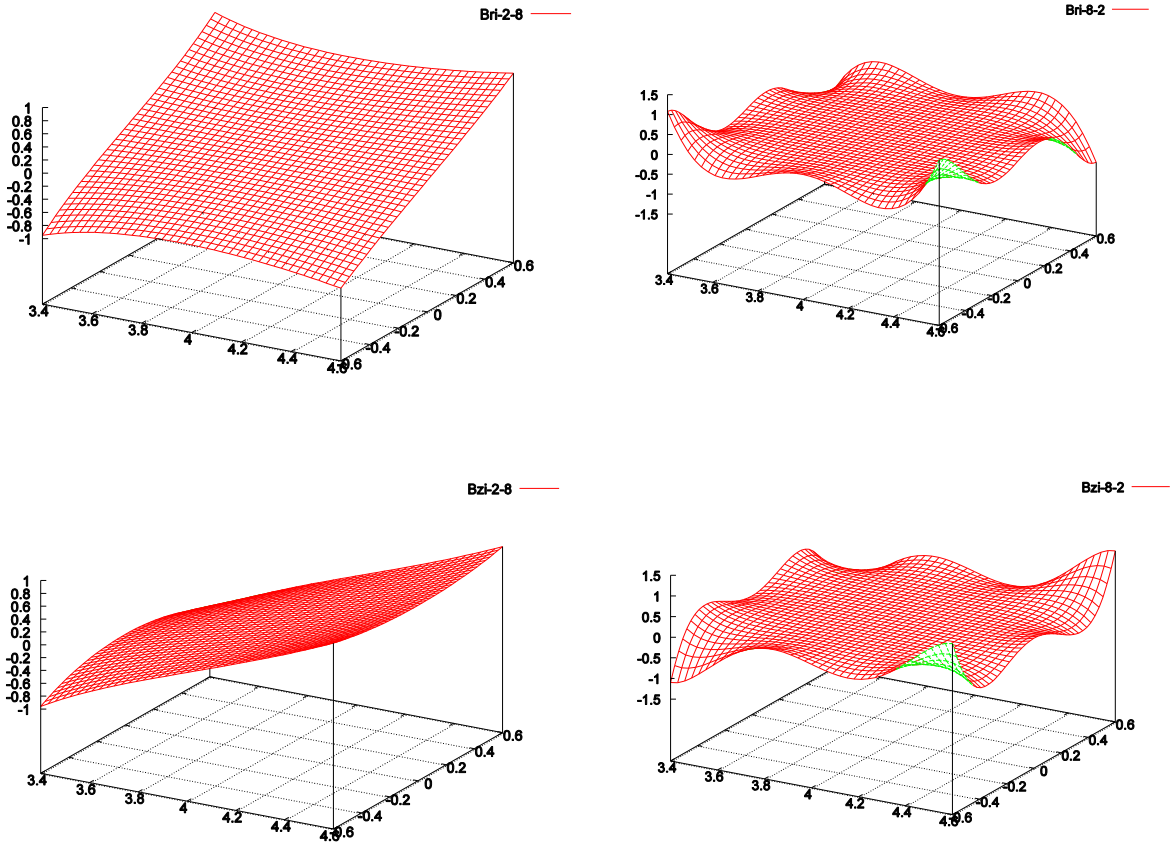

Figure 2 - Distribution of the radial and axial components of the magnetic field $B_r(r,\phi,z)$ and $B_z(r,\phi,z)$ in an internal domain with respect to the wall, given by a surface current distribution of the form $I=I_0\sin(m\vartheta)\cos(n\phi)$ on an axis-symmetric closed tokamak wall. i indicates the internal domain where this component has been calculated, 8 represents the poloidal wave number m, and 2 the toroidal wave number n

Conclusion

In the present work, a simple fast algorithm for calculation of the response of the 3-D thin conducting shell to magnetic perturbations is presented. Due to its high speed of calculations, the method is complimentary to the more universal approach, based on wall representation by conducting triangles with a uniform current density. The method is applicable for RWM studies and at the same time is consistent with the physics requirements of the Wall Touching Kink Mode and disruption simulations. The use of curvilinear coordinates, adjusted to the hole geometry was utilized efficiently with high accuracy of computations. While for a cylindrical or elliptical wall cross-section the metric coefficients could be described analytically, the Chebyshev polynomials interpolation have been tested and used for other wall geometries. A numerical superposition solving method of the stream function equation has been developed and was found to be order of magnitude faster than a straightforward, dual iteration solving method. Finally, analytical expressions have been derived for accurate, high speed calculations of toroidal harmonics of the vacuum magnetic field generated by the surface currents on axisymmetric walls. Unlike earlier used

scalar potential expression for vacuum field, the new expressions are suitable for the WTKM and Hiro currents.

Acknowledgement

Part of this work was conducted during a research stay by CVA to the Max-Planck Institute for Plasmaphysics in Garching, Germany. The hospitality of that Institute is greatly appreciated. This work was partially supported by the Contract BS-1 of the Association EURATOM-MEdC (CVA & DD), and partially by US DoE Contract No. DE-AC02-09-CH11466 (CVA and LEZ).

References

[1] Pfirsch and H. Tasso, Nucl. Fusion **11**, 259 (1971).

[2] R. Fitzpatrick, Phys. Plasmas **1**, 2931 (1994).

[3] M.S. Chance, M.S. Chu, M. Okabayashi and A.D. Turnbull Nucl. Fusion **42**, 295 (2002).

[4] M.S. Chu, M.S. Chance, A.H. Glasser and M. Okabayashi, Nucl. Fusion **43**, 441 (2003).

[5] M.S. Chu, A. Bondeson, M.S. Chance, Y.Q. Liu, A.M. Garofalo, A.H. Glasser, G.L. Jackson, R.J. La Haye, L.L. Lao, G.A. Navratil, M. Okabayashi, H. Remierdes, and J.T. Scoville, Phys. Plasmas, **11**, 2497 (2004).

[6] F. Villone, Phys. Rev. Lett. **100**, 255005 (2008).

[7] Y. In, J. S. Kim, D. H. Edgell, E. J. Strait, D. A. Humphreys et al. , Phys. Plasmas **13**, 062512 (2006).

[8] M.S. Chu and M. Okabayashi, Plasma Phys. Contrl. Fusion **52**, 123001 (2010).

[9] R. Litunovski, "The observation of phenomena during plasma disruption and the interpretation of the phenomena from the point of view of the toroidal asymmetry of forces," JET Internal Report Contract No. JQ5/11961, 1995.

[10] P. Noll, P. Andrew, M. Buzio, R. Litunovski, T. Raimondi, V. Riccardo, and M. Verrecchia, in Proceedings of the 19th Symposium on Fusion Technology, Lisbon, edited by C. Varandas and F. Serra (Elsevier, Amsterdam,1996), Vol. 1, p. 751.

[11] L. E. Zakharov, Phys. Plasmas **15**, 062507 (2008).

[12] L.E. Zakharov, S.A. Galkin, S.N. Gerasimov, Phys. Plasmas, **19**, 055703 (2012).

[13] A.H. Glasser and M.S. Chance Bull. Am. Phys. Soc. **42** 1848 (1997).

[14] M.S. Chance, Phys. Plasmas **4**, 2161(1997).

[15] Y. Q. Liu, A. Bondeson, C. M. Fransson, B. Lennartson, and C. Breitholtz, Phys. Plasmas **7**, 3681 (2000).

[16] L. Degtyarev, A. Martynov, S. Medvedev, F. Troyon, L. Villard, and R.Gruber, Comput. Phys. Commun. **103**, 10 (1997).

[17] R. Albanese and G. Ribonacci, Adv. Imaging Electron Phys. **102**, 1 (1998).

[18] J. Bialek, A. Boozer, M. E. Mauel, and A. Navratil, Phys. Plasmas **8**, 2170 (2001).

[19] P. Merkel, C. Nührenberg, and E. Strumberger, Europhys. Conf. Abstr. 28G, P-1.208, 2004.

[20] E. Strumberger, P. Merkel, M. Sempf, and S. Günter, Phys. Plasmas **15**, 056110 (2008).

[21] C.V. Atanasiu, A. Moraru and L.E. Zakharov, *Influence of a Nonuniform Resistive Wall on the RWM Stability in a Tokamak*, American Physical Society Plasma 51st Annual Meeting, Atlanta, USA, 2-6 November 2009.

[22] C.V. Atanasiu, A. Moraru and L.E. Zakharov, *MHD Modeling in Diverted Tokamak Configurations*, 7th ATEE-2011 International Symposium, May 12-14, 2011, Bucharest, Romania.

[23] C.V. Atanasiu, A.H. Boozer, L.E. Zakharov, A.A. Subbotin and I.G. Miron, Phys. Plasmas **6**, (1999).

[24] C.V. Atanasiu, S. Günter, K. Lackner, and L.E. Zakharov, Phys. Plasmas **12**, (2004).

[25] A. Erdélyi, *The Bateman Manuscript Project*, McGraw-Hill, New York (1953), Vol. 1.

[26] M. Abramovitz and I.A. Stegun, *Handbook of Mathematical Functions*, Dover Publications, Inc., New York (1994).

[27] I.S. Gradshtein and I.M. Ryzhik, *Table of Integrals, Series and Products*, Academic Press (2007).

THE ROLE OF CONVECTIVE STRUCTURES IN THE POLOIDAL AND TOROIDAL ROTATION IN TOKAMAK

Florin Spineanu, Madalina Vlad

National Institute of Laser, Plasma and Radiation Physics, Bucharest, Romania
[BS_2/WP12-IPH-A04-1-11/BS]

Abstract

The connection between the poloidal and the toroidal rotation of plasma in tokamak is important for the high confinement regimes, in particular in reactor regime. The sudden onset of closed convection structures in the poloidal section, due to the baroclinic production of vorticity, will sustain a fast increase of the poloidal velocity and a substantial effect on the toroidal rotation. However this is limited to the short time of the onset transition. In real plasma however there is random generation and suppression of convection cells and the sequence of these transient events can prove able to sustain the effect on the toroidal rotation. We formulate a simplified model which consists of a laminar sheared, regular, flow situated at the boundary of a region of drift-wave turbulence. Vortical structures, randomly generated in this turbulent region are spontaneously advected toward the flow and are absorbed there, sustaining with their vortical content, the sheared flow. We examine this dynamics in the wavenumber $\mathbf{k}$ space, using reasonable approximations. We derive a system of equations (which is a class of Devay-Stewartson system) and find that indeed, the vortices advected and absorbed into the layer can preserve its regular, poloidal, flow.

Introduction

Mixed regimes consisting of large scale flows (H-mode, Internal Transport Barriers) and turbulence are expected to be the current state in ITER. The rotation, either spontaneous or induced, will play a major role in the quality of the confinement. Cells of convection consisting of closed, large scale flows with unique sense of rotation can be spontaneously generated, triggered by streamers sustained by the baroclinic term able to generate vorticity. Similar to the Reyleigh-Benard first bifurcation (from purely conductive to convective regime), the onset is very fast and the drive exerted on the poloidal rotation leads to a fast time variation of the polarization radial electric field. This is sufficient to create a distinction between the phases (first half, second half) of bounce on a banana of trapped ions and, implicitly, leads to acceleration in the toroidal direction. This phenomenological model has been proposed recently [1] and the estimations are compatible with the observed effect of reversal of the toroidal rotation in tokamak. However if the convection cells become saturated and stationary, then the efficiency of sustaining toroidal acceleration of bananas decreases rapidly to zero. The process must be repeated if it is to sustain its effect on the toroidal rotation.

On the other hand, it is more realistic to regard the generation of convective structures as a stochastic process consisting of a random sequence of transient events, taking place on a range of spatial scales between ρ_s-scale drift vortices up to cells of convection with dimensions comparable with the minor radius a. We should study the way these transitory structures create the impulsive increase of the poloidal velocity such as, on the average, to sustain the toroidal effect on bananas. A marginal stability regime can be established, where the external sources sustain the gradient of the pressure, the convection rolls are formed transitorily and the excess of the gradients relative to a threshold is transformed into pulses of heat and momentum in the radial direction. This problem requires a treatment based on the stochastic nature of the generation and destruction of the

transversal convection cells, seen as a random transitory process. Such a treatment simply does not exist, not even for the famous Rayleigh-Benard system.

We formulate a model which is relevant for the physical problem of sustainment of poloidal rotation by stochastic rise and decay of vortices on different scales. We estimate the average density of high amplitude vortices that are generated inside a volume of plasma (in our case it is question of an area within the poloidal cross-section since the third - toroidal - axis is considered irrelevant). Then we remind the known mechanisms on motion of a vortex on a background of gradient of vorticity, in order to see how random elements of vorticity of only one sign will join the flow layer where they are absorbed. Finally, we examine this dynamics in the wavenumber space $\mathbf{k}$ and derive a model system of equations reflecting the interaction between the laminar flow and the incoming drops of vorticity. This is actually the Davey Stewartson system and indeed, the class of solutions called solitoffs show that the final state exhibits unidirectional (poloidal) alignment of the resulting flow.

Formulation of the model

We consider a layer of laminar sheared rotation where we assume that the instabilities are suppressed (this is an ideal representation of the zonal flow or of the H -mode layer). The layer is connex to a region where drift-type turbulence exists. The width of the layer is much smaller than the region of turbulence. In the drift-turbulent region there is stochastic generation of convective motions and of strong vortical structures.

Since the background has a gradient of vorticity a vortex will move in a direction which depends on the sign of its vorticity relative to the one of the background: the *clumps* (positive sign circulation vortices) are ascending the gradient of vorticity, toward the maximum of vorticity in the rotation layer and the *holes* (negative sign circulation vortices) are moving toward the minimum of vorticity, equivalently - they are repelled from the sheared layer [7]. In short, vortices of only one sign are joining the layer.

We take the layer of plasma flow in the y ($\equiv$ longitudinal, streamwise, poloidal in tokamak) direction with sheared velocity varying in the x ($\equiv$ transversal on the layer of flow, radial in tokamak) direction. It is described by a scalar function $\hat{A}(x,y,t)$ which is the complex amplitude of slow spatial variation of the envelope of the eddies of drift turbulence. From $\hat{A}(x,y,t)$ the components of the velocity are derived as $\mathbf{v}_E = -\nabla\hat{\mathbf{A}}(x,y)\times\hat{\mathbf{n}}/B$ where $\hat{\mathbf{n}}$ is the versor of the magnetic field. We also define a scalar function $\varphi(x,y,t)$ which represents the field associated to the incoming vortices that will interact and will be absorbed into the sheared, laminar, flow, transferring to it their vorticity content. The process in which a localized vortex is peeled-off and absorbed into the sheared flow may be seen as a transfer of energy in the spectrum from the small spatial scales involved in the structure of the vortex toward larger spatial scales of the sheared flow, with much weaker variations on the poloidal direction. This can be seen as a propagation in $\mathbf{k}$ space.

We must first estimate what is the number of high amplitude, robust vortices that are generated by the drift-turbulence in a unit area. This problem is treated in Ref. [22] where it is shown that the density of strong vortices is $n = 3/(\pi\lambda^2)$ where λ is the typical size of the drift eddies normalized to ρ_s .

Due to the existence of the background gradient of vorticity the vortices are self-advected. This has been clearly described for non-neutral plasma in [7] and is also known in the physics of fluids [13], the physics of the atmosphere [12] and in astrophysics (accretion disks) [14]. The prograde vortices are moving toward the maximum of vorticity and the retrograde vortices are moving toward the minimum of vorticity. The prograde vortices eventually are absorbed by the sheared layer and they contribute with their vorticity content to the momentum of the background flow. This is a source of momentum which sustains the sheared flow, in particular sustains the sheared poloidal rotation against the damping due to the magnetic pumping.

In the following, we will analyse this process as an interaction between the two fields: $\hat{A}(x,y,t)$ and the field representing the incoming vortices.

Dynamics in the $\mathbf{k}$ - space of the interaction between the laminar flow field and the field of the vortical cells

The typical equation in the hydrodynamic description is Rayleigh-Kuo or *barotropic* equation and the multiple space-time scale analysis leads to the Nonlinear Schrodinger Equation for the amplitude $W(x,y,t)$ of the *envelope* of the oscillatory waves excited in the fluid [16]. The general structure of this equation is

$$i\frac{\partial W(x,y,t)}{\partial t} = \Delta W(x,y,t) - \gamma |W|^2 W^* \tag{1.1}$$

The interesting term is the nonlinearity (the last term) which may be seen as arising from a self-interaction potential $V[W(x,y,t)]$ (see the next Section). The later potential results naturally from the multiple scale analysis and it is the effect on the envelope amplitude of the nonlinearity consisting of convection of the vorticity by its own velocity field. We must work with an amplitude $A(k_x,k_y,t)$ in the spectral $\mathbf{k}$ - space, which we see as the envelope of oscillations representing propagation of perturbation in the spectrum, this propagation being a reflection of what is the process of the incoming vortex dissolving itself and being absorbed by the flow, - in the physical space. Looking for an analytical model for A in the $\mathbf{k}$ -space we will use the structure which is suggested above.

We expect to have a diffusion in $\mathbf{k}-$ space and the same self-limiting nonlinear term

$$i\frac{\partial A(k_x,k_y,t)}{\partial t} = \left(\frac{\partial^2}{\partial k_x^2} + \frac{\partial^2}{\partial k_y^2}\right) A(k_x,k_y,t) - \gamma |A|^2 A^* + S \tag{1.2}$$

and we have added a source S that represents the interaction of the basic flow A with the vortices that are randomly generated in the drift turbulence and are joining the flow.
The addition of drops of vorticity is represented by the $\mathbf{k}$ -space scalar function ϕ

$$\phi(k_x,k_y,t) \tag{1.3}$$

Several space scales are present in the structure of the function $\phi(x,y,t)$ in real space. The reason is that we must consider that the vortices that are continuously generated in the turbulent region have two characteristics:

- the space extension of individual vortices coming into the layer has a wide range of values. The

range extends from vortices of the dimension ρ_s (the natural result of excitations sustained by the ion-polarization drift nonlinearity) up to convective events representing streamers with - closed (roll-type) geometry and spatial extension given by the inverse of $k_\theta = m/r$ for m of only few units.

- the spatial distribution of the place where these vortical structures are reaching the layer of sheared flow is random over practically all the circumference of the poloidal flow.

We will draw conclusions about the $\mathbf{k}$ -space profile of ϕ based on the contributions coming in from various scales in the real space. The simplest description neglects the random aspect of the content of ϕ and simply enumerates the possible spatial scales. For this we adopt a discrete representation of the dimensions of vortices, starting from a minimal size of the order of ρ_s up to a low- m fraction of the circumference $2\pi r$ of the poloidal rotation layer, this last scale corresponding to large convection roll-type events.

The above elementary assumption, *i.e.* the discrete number of space extension of vortices, implies that the function $\varphi\left(k_x, k_y\right)$ presents higher amplitudes around wavenumbers $\mathbf{k}$ which correspond to the inverses of the spatial scales. The simplifying assumption which takes uniform spatial distribution of the events of arrival of vortices (of any scale) to the layer implies periodicities on various spatial scales.

We consider separately the y direction (poloidal). One periodicity can be at the level of a smallest vortex, $k_y^{(1)}$. This means that a sequence of maxima of $\phi(x,y)$ appear with spatial periodicity $2\pi / k_y^{(1)}$ and this corresponds to the addition of smallest vortices into the flow layer. Further, on a longer space scale there is another periodicity, $k_y^{(2)}$. This means that the sequence on the lower scale (with much denser spatial granulations of vorticity, $2\pi / k_y^{(1)}$) is modulated on a longer space scale with a periodicity $2\pi / k_y^{(2)}$. This is because larger vortices (but not yet convection rolls) are absorbed into the flow layer. Large vortices carry smaller vortices. These considerations can be extended to other, intermediate, levels of periodicity. Finally we can have the largest (accessible) spatial scale $2\pi / k_y^{(n)}$ where a convective event occurs as a result of a stochastic event, or a streamer sustained by the baroclinic term and having the close-up property.

We note that the periodicity in the poloidal direction y cannot occur without a corresponding periodicity in the $x \equiv$ radial direction, as far as the vortices and convective events are concerned. It is reasonable to assume a linear dependence: small scale periodicities in the poloidal direction (small scale robust drift vortices) occur on a similar radial scale, *i.e.* again small periodicity in the $x \equiv$ radial direction. With larger y wavelengths, we expect to involve also larger radial wavelengths since the physical process involves more fluid motion in the closed-up convection cell.

This suggests a proportionality between the periodicities on the poloidal direction, y, and the periodicities on the radial, x , direction, in the structure of $\phi\left(k_x, k_y\right)$. This means that the Fourier components along y (*e.g.* at k_y) are proportional with the Fourier components along x (at k_x) with the same proportionality coefficient on all the spectral interval. The fact that there is (assumed) proportionality on the periodicities on y and on x , requires for analytical description a

hyperbolic operator

$$\left(\frac{\partial^2}{\partial k_x^2}-\frac{1}{a^2}\frac{\partial^2}{\partial k_y^2}\right)\phi\left(k_x,k_y\right)\approx 0 \tag{1.4}$$

where the D'Alambertian operator $\Box_{k_xk_y}\equiv\frac{\partial^2}{\partial k_x^2}-\frac{1}{a^2}\frac{\partial^2}{\partial k_y^2}$ is the signature of the correlated periodicities on the poloidal and radial directions of the field ϕ representing the incoming drift vortices - up to convection rolls, generated in the drift turbulence region, moving against the gradient of vorticity, and finally absorbed into the rotation layer. The "velocity" a is the ratio of the periods on the two k -space directions and we take it $a\approx 1$. The centers of the vortices reach points that belong to the lines $y=\pm ax$. The general form of the solution of the homogeneous equation is

$$\varphi\left(k_x,k_y\right)\sim\exp\left(ik_xx+ik_yy\right) \tag{1.5}$$

When ϕ is "free" it is double periodic and it verifies the above equation. However the destruction (*peeling-off*) of the incoming vortices and their absorption through interaction with the background flow, A, is the loss of the double periodicity. The departure relative to the $\mathbf{k}$ -space double periodicity (the "free" state of ϕ) feeds the flow field $A\left(k_x,k_y,t\right)$ such as to enhance it in spectral regions comparable to those where the vortices are localised, *i.e.* higher $\left|\mathbf{k}\right|$. Basically, if the free $A\left(k_x,k_y,t\right)$ is localised on k_y close to $k_y\sim 0$ (equivalent to an uniform poloidal flow), the source induced by ϕ is a charge which acts through a Poisson equation on the "potential" given by the amplitude AA^*. We should recall that we want to represent the physical process in which incoming vortices transfer via absorption their vortical content to the sheared flow, sustaining and/or enhancing the poloidal, y, rotation. This is mainly manifested as the evolution of an initial oscillation generated by ϕ on the k_y -spectrum with collection of the energy in a region close to $k_y\sim 0$, since this corresponds in real space to the uniformization of the flow in the poloidal direction, after an event of absorption of a vortex. Then, ignoring the less significant periodicity in k_x direction, corresponding to periodic perturbation propagating in the x (radial) direction, the interaction may be represented as

$$-\beta\frac{\partial^2}{\partial k_y^2}\left|A\right|^2\approx\left(\frac{\partial^2}{\partial k_x^2}-\frac{\partial^2}{\partial k_y^2}\right)\varphi\left(k_x,k_y\right) \tag{1.6}$$

The constant β is a measure of the permittivity of the equivalent electrostatic problem. Using the specific terminology β measures the decrease of the effectiveness of the effect of the charge (right hand side of the Eq. (6)) on the potential $\left|A\right|^2$ due to the polarization. Essentially, the amount of destruction of the incoming vortex, measured by the departure from the free state by the right hand side of the Eq. (eq6) is transferred to the background flow by first exciting elementary waves in real space, while A is only an envelope. The perturbation of the sheared flow A (via the left hand side of the Eq. (6)) results from the nonlinear interaction of these excited waves, *i.e.* by convecting the modified vorticity with the background velocity flow. This is the nonlinear term of the right-hand side of Eq.(2). Then it is reasonable to assume $\beta\approx\gamma$.

Returning to the equation for $A\left(k_x,k_y,t\right)$ we specify the interaction between the two fields A and ϕ in the simplest way

$$S = 2\varphi\left(k_x,k_y,t\right)A\left(k_x,k_y,t\right) \tag{1.7}$$

Then

$$i\frac{\partial A\left(k_x,k_y,t\right)}{\partial t} = \left(\frac{\partial^2}{\partial k_x^2}+\frac{\partial^2}{\partial k_y^2}\right)A\left(k_x,k_y,t\right) - \gamma\left|A\right|A^* + 2\varphi A \tag{1.8}$$

to which we add the equation for ϕ ,

$$\left(\frac{\partial^2}{\partial k_x^2}-\frac{\partial^2}{\partial k_y^2}\right)\varphi\left(k_x,k_y,t\right) \approx -\gamma\frac{\partial^2}{\partial k_y^2}\left|A\right|^2 \tag{1.9}$$

These two equations are known as Davey-Stewartson system and our case is DS-I [17]. It is exactly integrable and several analytical solutions are available, in terms of Riemann theta functions or Jacobi elliptic functions. Of particular importance for our physical problem are the *long wave limit* solutions, as obtained by Chow using the Hirota method. We reproduce here his result [17]

$$A = \frac{r\left(1-k\right)}{2}\left[\frac{\tanh\left(sk_x\right)-\sqrt{k}\,\mathbf{sn}\left(rk_y,k\right)}{1+\sqrt{k}\,\mathbf{sn}\left(rk_y,k\right)\tanh\left(sk_x\right)}\right]\exp\left(-i\Omega t\right) \tag{1.10}$$

$$\begin{aligned}\varphi = {} & 2r^2\left(1-\frac{E}{K}\right) \\ & -2r^2\frac{k\left(k\,\mathbf{sn}^2\left(rk_y,k\right)+\tanh^2\left(sk_x\right)\right)+\left(1+k^2\right)\sqrt{k}\,\mathbf{sn}\left(rk_y,k\right)\tanh\left(sk_x\right)}{\left(1+\sqrt{k}\,\mathbf{sn}\left(rk_y,k\right)\tanh\left(sk_x\right)\right)^2}\end{aligned} \tag{1.11}$$

These solutions are called *solitoffs* and they decay in all directions except a preferred one.

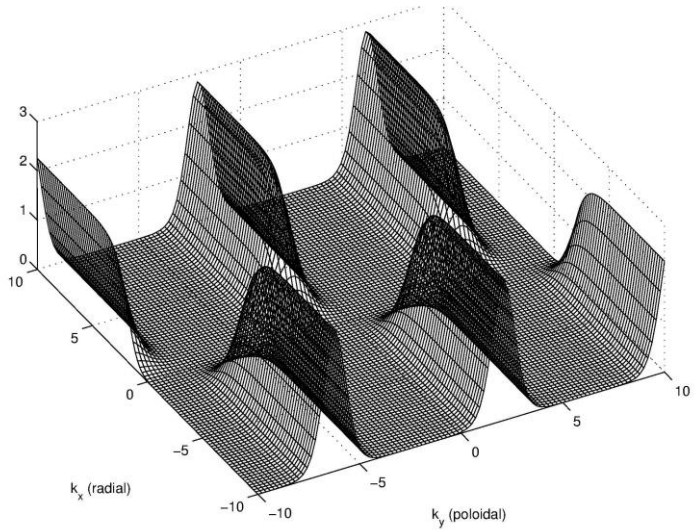

They are "semi-infinite solitary waves". For example, for $k = 0.7$ and $r = 1$ the solution shows a peak of $\left|A\right|^2$ around $k_y \approx 0$ which in physical terms means quasi-uniform flow along the poloidal direction. This is compatible with what we expect from this analytical model: the turbulence advects

drops of vorticity into the rotation layer and this does not destroy the flow but sustains it. It is actually a *discrete* Reynolds stress, or a process which is reversed version of the usual Kelvin-Helmholtz instability.

Discussion

The Figure (1) represents the amplitude of the solution given in Eq.(10). We now want to understand in more detail what the origin of the final spectral structure (*i.e.* the solution written above) was in our previous analysis, which was mostly qualitative and based on several assumptions.

We note that the solution looks compatible with our idea about the build-up and/or sustainment of a sheared laminar flow out of random convection of momentum from the deep region where turbulence is active. We first refer to the term $-\gamma |A|^2 A^*$. Essentially this term is the quantitative translation of the physical fact that the flow, after a perturbation (which later we will specify as "absorbing" an incoming vortex), will try to re-establish the uniformity of the flow by spreading the new perturbing vorticity as shear of the flow. Although this is a very approximate image we expect that this term in the action functional (*i.e.* in the integral of the Lagrangian density) to penalize departures of the flow configurations from uniformity of the flow. The departures are measured as the square of the difference between the actual magnitude of AA^* and a reference uniform configuration. Then the system moves in the function space in a potential $V\left[\phi(\mathbf{k})\right]$ with two extrema $\pm\nu$ (symmetric relative to $\phi(\mathbf{x},t)\equiv 0$. We see that in the presence of a *source* the solution for fixed, greater than zero, k_x , is not exactly at the "poloidal uniform flow" $k_y = 0$ but shifted, the spectrum is peaked in k_y at a small but finite value. This means that our description actually obtains longwave poloidal oscillations but not exactly symmetric $m \equiv 0$ poloidal flow. This shift is due to the *average* of the spatial extensions of the incoming perturbations and is dependent on the scale factor ('wavelength') r . The two parameters r and s must be seen as representative space scales along the poloidal (y) respectively radial (x) directions.

We have simply neglected the structure of the spectrum on k_x (radial). In the solution it occurs with a uniform k_x -space contributions for positive wavenumbers (the $\tanh$ function rises rapidly after a space scale s and remains constant after that for all $k_x > 1/s$). This means that the structure of the flow on the transversal direction (a cross section along the radius) contains all possible motions and modulations, without however placing emphasis on any of them. It becomes effective the assumption that the convections and vortices are coming in all sizes, and we have neglected the second derivative of the flow amplitude A to k_x in Eq.(6), compatible with the approximate independence of A on k_x .

We note that the identical reproduction of the localized maximum close to $k_y \approx 0$ at periodic intervals along k_y axis is the result of the periodicity

$$sn\left(rk_y, k\right) = sn\left(rk_y + 4K, k\right)$$

of the Jacobi elliptic function sn , where

$$k = 2s / r - 1 \text{ and}$$

$$K(k) = \int_0^{\pi/2} \frac{d\xi}{\sqrt{1 - k^2 \sin^2 \xi}}$$

For slightly elongated perturbations along the direction of the flow (poloidal)

$$s \le r$$

we have

$$k \le 1 \;\rightarrow\; K \to \infty$$

which means that the periodicity does not appear to be relevant in our case.

Conclusion

In conclusion, this simple analytical analysis supports the idea that the randomly generated vortical motions, including the convection rolls that rise and decay transiently in the plane transversal to the magnetic field, are able to sustain poloidal rotation. When the time scale is very short, as for convection rolls driven by the *baroclinic* effect, the poloidal flow arising as envelope of the rolls has fast time variation and the neoclassical polarization effect acts effectively on the toroidal rotation. This process accompanies every event consisting of configuration of a closed convection pattern. Then, even if these events are random, their statistical average is an effective source of poloidal flow.

Acknowledgement

Work supported partially by the Contracts BS-2 and BS-14 of the Association EURATOM - MEdC Romania. The views presented here do not necessarily represent those of the European Commission.

References

1. F. Spineanu and M. Vlad, Nucl. Fusion **52** (2012) 114019.
2. F. Spineanu, M. Vlad, K. Itoh, S.-I Itoh, *http://arxiv.org/pdf/physics/0311138*.
3. D.A. Schecter and D.H.E. Dubin, Phys.Fluids **13** (2001) 1704.
4. F. Spineanu, M. Vlad, Phys. Rev.E **67**, (2003) 046309.
5. F. Spineanu, M. Vlad, Phys. Rev. Lett. **94** (2005) 025001 and *http://arxiv.org/pdf/physics/0501020*.
6. B. Wang, X. Li and L. Wu, Journal of Atmospheric Sciences 54 (1997) 1462.
7. P.S. Marcus, J. Fluid Mech. **215** (1990) 393.
8. H. Lin, J.A. Barranco, P.S. Marcus, Center for Turbulence Research, Annual Research Briefs 2002, Stanford University.
9. D.A. Schecter, D.H.E. Dubin, Phys. Rev. Lett. **83** (1999) 2191.
10. F. Spineanu and M. Vlad, Phys. Rev. Lett. **89** (2002) 185001, and: *http://arxiv.org/pdf/physics/0204050*.
11. K.W. Chow, Wave Motions **35** (2002) 71.
12. R.H. Kraichnan and D.C. Montgomery, Rep.Prog.Phys.**43** (1980) 547.
13. M.V. Berry and J.H. Hannay, J. Phys.A: Math. Gen., **10** (1977) 1809.
14. F. Spineanu and M. Vlad, http://arxiv.org/pdf/1301.0892.

Figure caption

Graphical representation of the solution of the Devay Stewartson system for the parameters $k = 0.7$ and $r = 1$.

ANOMALOUS TRANSPORT IN PLASMA. ELECTRON HEAT TRANSPORT AND MULTI-SCALE PHYSICS

Gyorgy Steinbrecher[1], Nicolae Ion Pometescu[2]

[1,2]*University of Craiova, Faculty of Exact Sciences, Physics Department, 13 A. I. Cuza, Cod 200585, Craiova*

[BS_3A/WP12-IPH-A05-1-13/BS]

Abstract

Stochastic perturbation model was applied to the analysis of both numeric multi-scale turbulence simulations and fluctuation measurements. The linear stochastic stability of the ETG modes was studied in the particular framework of drift kinetic model for electrons and ions respectively drift kinetic model for electrons and adiabatic ion response. The effect of the stochastic perturbations on the electronic heat transport was computed. The main effect is that the destabilization of the low wave number modes has a dominating role in the increase of the electronic heat transport. By analytic methods, in the framework of a soluble model, the dynamics of electrons under the effect of random potential was studied. At this stage, the two resulting equations for the two point correlation functions were studied in the local approximation. New numerical method and a C program for solving the generalized eigenvalue problems related to the computation of the Liapunov exponents were elaborated. The choice of the framework of this model allows the study of the destabilization of ETG modes without using large computational resources, at the expense of additional input: the spectral properties of the temperature and density fluctuations. Class of steady state reference distribution functions was studied. The entropy production in plasma was analysed for a non-ohmic multicomponent plasma heated at the ion cyclotron resonance for particular case of low concentration of ^{3}He ions colliding with a thermal background plasma, composed by Deuterium and electrons.

Papers

[1] G. Steinbrecher, X. Garbet, *Linear stochastic stability analysis of nonlinear systems. Parametric destabilization of wave propagation*, arXiv:1212.1365v1[math-ph], (2012).

[2] G. Sonnino, A. Cardinali, M. Tlidi, Ph. Peeters, G. Steinbrecher, A. Milovanov, *General Approach for Deriving Reference Distribution Functions for Systems out of Equilibrium by Statistical Thermodynamics*, arXiv: 1203.4181v4, (2012).

[3] G. Sonnino, G. Steinbrecher, A. Cardinali, A. Sonnino, M. Tlidi, *Family of Probability Distribution Function Derived from Maximal Entropy Principle with Scale Invariant Restrictions*, Phys. Rev**. E 87**, 014104 (2012).

[4] G. Steinbrecher, X. Garbet, B. Weyssow, *Mean sojourn time fraction in frozen, homogenous isotropic and self-similar electrostatic turbulence*, Ann. University of Craiova, (*Physics AUC*), vol.**22**, (2012) p 1-14.

[5] N. I. Pometescu, *Entropy production in plasma with RF heating*, Ann. University of Craiova, (*Physics AUC*), vol.**22**, (2012) p 15-23.

Conferences

[1] G. Steinbrecher, X. Garbet, B. Weyssow, *Mean sojourn time of charged particles in frozen electrostatic turbulence*, Memorial Session dedicated to Radu Balescu, 20-22 September 2012, Bucharest, Romania

Reports

[1] G. Steinbrecher, N. I. Pometescu, *ETG instabilities driven by parametric perturbations and electron heat transport*, Workshop on fusion plasma physics of the Association EURATOM-MEdC, 20-22 September 2012, Bucharest, Romania

Detailed results

- *Stochastic perturbation model applied to the analysis of both numeric multi-scale turbulence simulations and fluctuation measurements.*

The results are derived in the framework of the shearless slab geometry of the magnetic field. The starting point is the system of nonlinear drift kinetic-Poisson equations for ions and electrons used in drift-kinetic model, respectively drift kinetic model for electrons and adiabatic response for ions. In order to study the stochastic stability, under parametric perturbations of the deterministic solutions, we perform the linear approximation [1, 2, 3] starting from a background solution with zero electrostatic potential and Maxwell distribution in the velocity space, with time- and position-dependent temperature. The final result of this stochastic linearization program is a system of linear stochastic partial differential equations, for the linearized perturbation components of the distribution functions: $\delta f_{electron}(t, R_{GC}, v_{\|}, \mu)$, $\delta f_{ion}(t, R_{GC}, v_{\|}, \mu)$, where $R_{GC} = (x, y, z)$.

The linear stochastic system of integro-differential equations was transformed in a system of linear deterministic equations for the equal time correlation functions

$\left\langle \delta f_{electron}(t, R_{GC}', v_{\|}', \mu') \delta f_{electron}(t, R_{GC}'', v_{\|}'', \mu'') \right\rangle$, $\left\langle \delta f_{electron}(t, R_{GC}', v_{\|}', \mu') \delta f_{ion}(t, R_{GC}'', v_{\|}'', \mu'') \right\rangle$,
$\left\langle \delta f_{ion}(t, R_{GC}', v_{\|}', \mu') \delta f_{ion}(t, R_{GC}'', v_{\|}'', \mu'') \right\rangle$

Assuming that the spatial correlation functions of the fluctuations of the background field are invariants under spatial and temporal translations, the Liapunov exponent is related to the spectrum of an integro-differential operator. The corresponding eigenvalue problem was studied by local Fourier decomposition. The first analytic result is: The real part of the maximal eigenvalue increases with the intensity of the background noise.

The exact value of the Liapunov exponents can be found by numerical methods. For small values of the intensity of the noise, perturbation methods can be used. The perturbative method used in ref. [3] was generalized. Denoting by σ the intensity of the fluctuations, the following dependence was found: $\mathrm{Re}(\lambda(\sigma)) = \mathrm{Re}(\lambda(0)) + K\sigma^2 + O(\sigma^4)$

The results were obtained in the framework of drift kinetic models for electrons and ions, respectively drift kinetic for electrons and adiabatic response of the ions. The shearless slab model was used, with constant magnetic field. The background temperature and density profile has only radial dependence. The background temperature and density functions were perturbed by random time and space dependent fluctuations. It is known from previous works that parametric noise can destabilize the stable stationary states. This work is a part in a larger program intended to clarify the effects of the stochastic perturbations on the stability of the plasma in tokamak. The stochastic stability in this framework we describe by the large time behaviour of the n-point equal time correlation functions. The parametric perturbations at this stage are modelled by temporal white noise with general space correlations.

The first step of the stochastic linear stability was the linearization, was performed according to the new methodology exposed in the work [1].

The fluctuations of the density generated an effective fluctuating potential that appears in the resulting equations as a multiplicative noise. The resulting fluctuations of the electrostatic potential was modelled by a random Gaussian field, with white noise behavior in temporal direction and

correlation function derived from the experimental or simulated correlation functions of the temperature or density fluctuations. The resulting linear stochastic differential equations were studied according to the general rules exposed in the works [1-3]. Deterministic linear evolution equations were derived for the *n*-point correlation functions in two cases: the propagation of the Langmuir waves with stochastic background density, and in the case of the integro-differential equations that arise from the linearization of the kinetic equations coupled with Poisson equations.

In the case of stochastic wave equation, variational and perturbative methods were elaborated for the study of the stability of the evolution of the two-point correlation function. For the integro-differential equations, we elaborated a perturbative method applicable in the limit of small noise intensity that allows the computation of the large time behaviour of the n-point cross correlation functions of the distribution function and electric potential. In order to have a good starting point for the linearization, special attention to the choice of the reference distribution function, used for the linearization, was given [4, 5].

A typical effect that appears in a dynamical system exposed to random perturbation, the smooth transition between stable and unstable states, was studied in the perturbative regime. The leading Liapunov exponents of the destabilized modes were computed. An interesting effect is related to the existence of a threshold for the stochastic perturbation intensity, such that below this threshold the mode remains stable. This threshold increases both with the toroidal and poloidal wave numbers. Consequently the large wavelength modes are destabilized first, both in the perturbative study of the ETG destabilization and in fluid models [1].

The association of this effect to the streamers observed in nonlinear simulations is under subsequent study. The impact of the temperature fluctuations on the electron heat transport was described in the perturbative regime by the sensitivity of the unperturbed eigenvalues to the random noise, computed in the first order of perturbation theory [6]. Partial results are exposed in the subsequent figures. The Liapunov exponents are normalized to the electron density characteristic length and electron thermal velocity. The wave numbers are normalized to the electron Larmor radius.

The effect of the stochastic perturbations on the electronic heat transport was computed. The main effect is that the destabilization of the low wave number modes has a dominating role in the increase of the electronic heat transport.

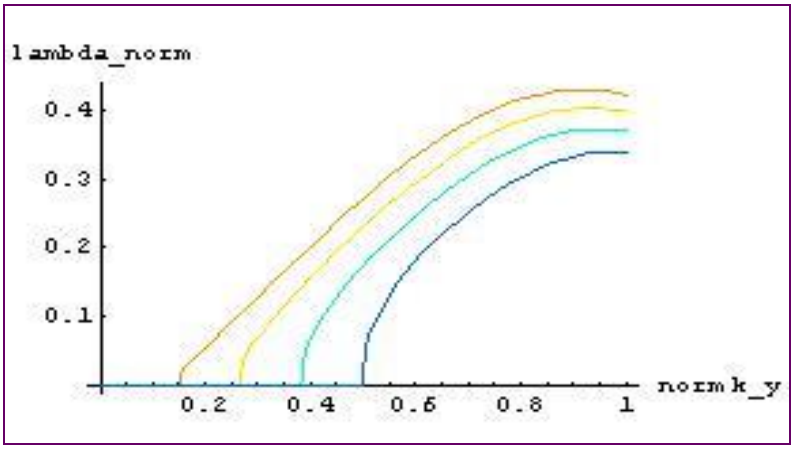

Figure 1 - The unperturbed normalized Liapunov exponent. Electron / ion temperature fraction takes the values from: 0.5 (red), 1.0, 1.5, 2 (blue). The normalized toroidal wave number is 0.3.

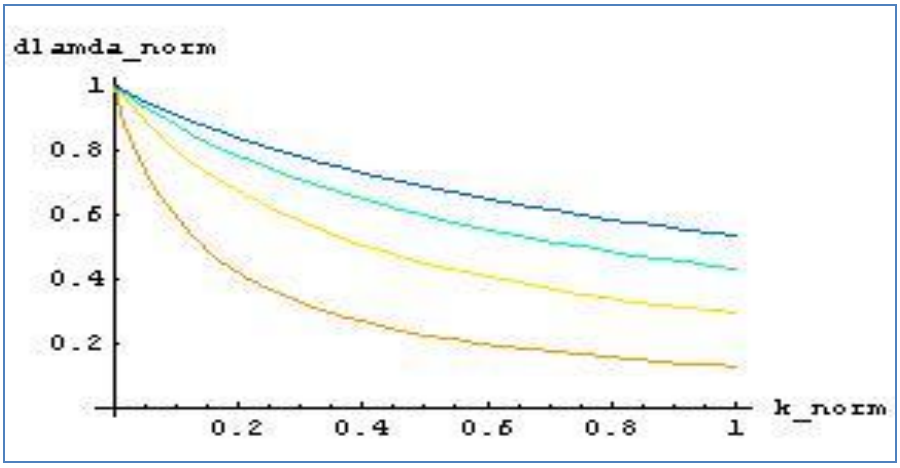

Figure 2 - The dependence of the normalized perturbed part of the Liapunov exponent on the normalized wave number. Also the very low k modes are destabilized, despite the fact that they appear stable in Figure 1. The normalization is with respect to k=0 mode.

By analytic methods, in the framework of a soluble model, the dynamics of electrons under the effect of random potential was studied [7, 8]. The result is: in the framework of the model, the trajectories of the electrons are either unbounded, or have a very small area. The correlation of this result with ETG effects is under study.

- *Elaboration of numerical methods and subroutine for evaluation of the leading Liapunov exponents*.

At this stage, the two resulting equations for the two point correlation functions were studied in the local approximation. A new numerical method and a C program for solving the generalized eigenvalue problems related to the computation of the Liapunov exponents were elaborated. The choice of the framework of this model allows the study of the destabilization of ETG modes, without using large computational resources, at the expense of additional input: the spectral properties of the temperature and density fluctuations.

- *Entropy production in plasma with RF heating*

The framework of our calculation is that of gyrokinetic theory and ion-cyclotron frequency waves with resonant wave-particle interactions and electromagnetic plasma response. We consider a non-ohmic multi-component plasma heated at the ion cyclotron resonance for species *i*, in particular the case of a low concentration of ^{3}He ions colliding with a thermal background plasma, composed of Deuterium and electrons.

The usual kinetic form of the entropy per unit volume is used to evaluate the entropy production. The distribution function is split into two contributions: one corresponding to the time averaged part (secular behavior) and the second one corresponding to the rapidly varying part of the distribution (due to rf waves). We consider these two distribution functions as deformed Maxwellian and evaluate the entropy production revealing the contributions from the Maxwellian part, and respectively from the deformation factor of the Maxwellian. Different terms that contribute to the entropy production are given in the general form and their significance is identified [9].

The ^{3}He minority is supposedly about 2%-3% of the density of the background plasma, and heated by ion cyclotron resonant heating (ICRH). For the ^{3}He minority, the analysis is limited to the

simplified, quasi-linear Fokker-Planck equation, where only the contribution due to the perpendicular component of the electric field is taken into account, which is concordant to the direction of rotation of the minority. The work will continue by evaluating the entropy production, using the specific form of the distribution function.

Conclusion

The linear stochastic stability study of the ETG modes, in the particular framework of drift kinetic model for electrons and ions, respectively drift kinetic model for electrons and adiabatic ion response, was completed. The linear stochastic stability study of the ETG modes will be continued. The destabilization effect of the temperature and density fluctuations will be studied in the framework of stochastic linearized coupled full Poisson-Vlasov equations for ions and electrons without gyro averaging. For optimization of the delta-f codes for first principle study of ETG modes, new class of reference distribution function will be studied and new numerical methods will be elaborated.

Acknowledgement

The reported work includes contributions from the following people outside the EUATOM-MEdC Association: X. Garbet, (IRFM, EURATOM-CEA, IRFM, Cadarache, France), G. Sonnino, B. Weyssow, (Association EURATOM-Etat Belge, Department of Statistical Physics and Plasma, ULB, Bruxelles, Belgium).

References

[1] Steinbrecher G., Garbet X. , arXiv:1212.1365v1[math-ph], (2012).

[2] Steinbrecher G., Weyssow B., Physical Review Letters **92**, 125003 (2004).

[3] Steinbrecher G, Garbet X, Weyssow B, arXiv: 1007.0952v1 [math. PR], (2010).

[4] Sonnino G, Cardinali A, Tlidi M, Peeters Ph, Steinbrecher G, Milovanov A, arXiv:1203.4181v4 , (2012).

[5] Sonnino G, Steinbrecher G, Cardinali A, Sonnino A, Tlidi M, Phys. Rev. **E 87,** 014104 (2012).

[6] Steinbrecher G, Pometescu N, Workshop on fusion plasma physics of the Association EURATOM-MEdC, 20-22 September 2012, Bucharest, Romania.

[7] Steinbrecher G, Garbet X, Weyssow B, Memorial Session dedicated to Radu Balescu, 20-22 September 2012, Bucharest, Romania.

[8] Steinbrecher G, Garbet X, Weyssow B, Ann. University of Craiova, (Physics AUC), vol.**22**, (2012) p 1-14.

[9] Pometescu N, Ann. University of Craiova, (Physics AUC), vol.**22**, (2012) p 15-23.

ANOMALOUS TRANSPORT IN PLASMA. STOCHASTIC PROCESSES AND TRANSPORT IN TURBULENT PLASMA

I. Petrisor[1], M. Negrea[1], Dana Constantinescu[2]

[1]*Department of Physics, Faculty of Exact Sciences, University of Craiova, Romania*
[2]*Department of Applied Mathematics, University of Craiova, Romania*

[BS_3B/WP12-IPH-A05-1-11/BS]

Abstract

The low dimensional model proposed in a previous paper was extended to describe the pellet injection and its influence on ELM cycle. From the numerical simulations we concluded that important experimental observations (pellets are able to increase ELM frequency but a reduction is not possible and the increase of the ELM frequency is accompanied by reduction of the ELM amplitude, but the total power outflow remains the same) are confirmed by the theoretical model. It results that the proposed low dimensional model provides useful tools for understanding the basic physics and allows estimating relative quantities, even if it does not qualify for a complete description of the plasma phenomena such as ELM or sawtooth. A Hamiltonian model of a magnetic field configuration was studied for small amplitudes of the perturbations, comparable with those encountered in experiments and a chaotic behavior was pointed out. It was shown that a robust transport barrier can be obtained in a prescribed zone by locally modifying the safety factor. The influence of the reversed magnetic shear on the diffusion coefficients in turbulent plasmas coefficients in the following cases: *streamer*, *zonal flow* and *blob*, that are relevant for ITER were studied. We have calculated the mean squared displacements, the higher order moments that are used for the calculation of the skewness and kurtosis and the probability density functions (PDFs) of the electrostatic potential, electric field, magnetic field and of the components of the particle velocity, i.e. the radial, poloidal and the toroidal one. The influence of the level of electrostatic turbulence given by the electrostatic Kubo number K and the influence of the magnetic shear given by the shear Kubo number K_s on the above mentioned quantities was observed. We adapted a parallel version of TURBO_for_particle code on some available parallel computers. First results display that the transport of charged particles in magnetized plasma is strongly influenced by the level of electromagnetic field fluctuations. Coherent structures developed by complex electromagnetic fields may be characterized by a trapping effect of particle trajectories. On the contrary, small-scale structures may increase the anomalous transport of charged particles. The competition between these two effects makes the theoretical analysis of charged particle transport very difficult while its numerical simulation is extremely time consuming. The work is in progress, the computational time obtained on some parallel machines is spread on 12 months or more.

Papers

[1] D. Constantinescu, O. Dumbrajs, V. Igochine, K. Lackner, R. Meyer-Spasche, H. Zohm and ASDEX Upgrade team, Phys. Plasmas 18, (2011) 062307. doi:10.1063/1.3600209
[2] Andrejs Reinfelds, Olgerts Dumbrajs, Harijs Kalis, Jānis Cepītis, Dana Constantinescu, Mathematical Modelling and Analysis, Volume 17 Number 2 (2012) http://dx.doi.org/10.3846/13926292.2012.662659
[3] D. Constantinescu, M-C Firpo, International Journal of Bifurcation and Chaos, Vol 23, No 2 (2013), 1350034 doi:10.1142/S021812741350034X
[4] D. Constantinescu, M-C Firpo, Nucl. Fusion 52 (2012) 054006, doi:10.1088/0029-5515/52/5/054006.
[5] I. Petrisor, M. Negrea, C.C. Lalescu, B. Knaepen, On the diffusion of ions in an electrostatic stochastic field and an unperturbed space dependent sheared magnetic field (to be submitted).
[6] I. Petrisor, M. Negrea, Physics AUC, vol.22, 2012, pp. 68-76.

Conferences

[1] V. Igochine, D. Constantinescu, O. Dumbrajs, K. Lackner, R. Meyer-Spasche, H. Zohm and the ASDEX-Team, 39-th European Physical Society Conference on Plasma Physics and the 16-th International Congress on Plasma Physics, Stockholm, 2-6 July 2012.
[2] M-C Firpo, D. Constantinescu, presented to The 54st Annual Meeting of The American Physical Society Division of Plasma Physics, 29 Oct.-2 Nov. 2012, Providence, USA.
[3] Petrisor I., Negrea M., Lalescu C.C., Carati D., Proceedings of the 2012 International Conference on High Performance Computing and Simulation, HPCS (2012), art. no. 6266983 , pp. 623-627.

Detailed results

1. Test particle transport in a turbulent magnetohydrodynamics

The wider purpose of this work is the understanding of particle transport in turbulent (fully ionized) plasma. Plasmas are generally composed of several species of charged particles, but in this approach the plasma is modeled with the incompressible MHD equations. This means that only a main species is considered; the particles themselves are treated as passive. This is a common approximation for impurities in fusion plasmas. The interaction of charged particles (electrons and different species of ions) with frozen electromagnetic fields derived from nonlinear magneto-hydrodynamic simulation was investigated. Various regimes of frozen (prescribed) turbulence could be generated with TURBO code like an input for the movement of charged particles in such prescribed turbulence. We investigated the effect of a given turbulence in the transport of different charged particles. Few cases of superdiffusion and subdiffusion, next to normal diffusion, depending on the different turbulence regimes have been investigated, to evaluate the full transport coefficients and anomalous diffusion exponents as functions of the Reynolds number and particle species. The approximation of a large charged impurity, for which collisions can be approximated by a drag term, is:

$$\dot{\mathbf{r}} = \mathbf{v}$$

$$\dot{\mathbf{v}} = \alpha[\mathbf{e}(\mathbf{r}) + \mathbf{v} \times \mathbf{b}(\mathbf{r})] + \chi\,|\mathbf{v} - \mathbf{u}|$$

where α corresponds to the charge to mass ratio in the Lorentz force and χ is the inverse of a friction timescale. This model is a natural extension of the usual model for particles with mass moving in turbulent Navier-Stokes fluids. For this particular study, a turbulent regime of $Re = Re_m = 100$ was chosen, in order to be built upon in future work. For the particles, two values of β (1 and 10) are investigated, and four pairs (γ, St): $(1/2,1)$,$(1/2,1/10)$, $(1/4,1)$ and $(1/4,1/10)$.

The fluid equations are solved with a pseudo-spectral solver, in a periodic box of dimensions $6\pi L \times 2\pi L \times 2\pi L$, using a uniform, rectangular grid with $784 \times 128 \times 128$ nodes. The velocity distribution functions for VFL and CP are shown in Figure 1.

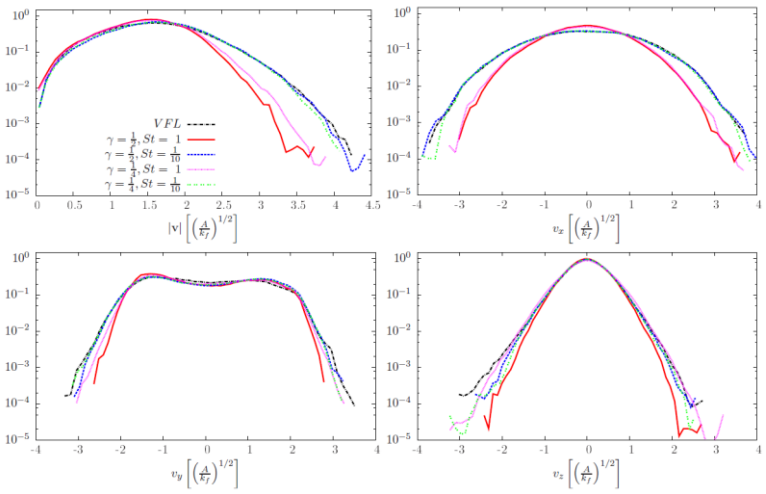

Figure 1 - Velocity PDF for velocity field lines (VFL) and charged particle (CP)

It seems that, for these values of the parameters, the drag term controls CP behaviour (because CP results are very close to VFL results). It is noted that the distribution function for *vy* is apparently the

sum of two Gaussian distributions. This further confirms the presence of two "streams" along the *y* axis. Superdiffusive transport for VFL is explained by these two maxima — particles may be caught in one vertical stream or the other, and they can experience long flights.

For the needed numerical simulations, we used the computer facilities of ULB, Belgium, in collaboration with the research group from ULB, Belgium. The study is in progress [5].

2. Development of non-linear MHD models of ELM cycle, including the effect of magnetic or pellet perturbations

Larger scale plasma instabilities not leading to an immediate termination of a discharge often result in periodic nonlinear perturbations of the plasma. Examples of such behaviour are Edge Localized Modes (ELMs), sawtooth crashes and other events. A minimal possible physical model is formulated for description of these systems with drive and relaxation processes which have strongly different time scales. This low-dimensional model contains only three parameters: power input h, relaxation of the instability δ and influence of the instability on the heat diffusion coefficient η.

The model is based on two equations. The first equation being responsible for the relaxation dynamics and can be derived either from linearization of the energy principle or from linear MHD force balance equation $\left(\rho_{m0}\left(d^2\vec{\xi}/dt^2\right)=-\hat{K}_{MHD}\cdot\vec{\xi}\right)$ and has the following form [1]:

$$\underbrace{\frac{d^2}{dt_n^2}\xi_n=\left(p_n'-1\right)\cdot\xi_n}_{oscillator}-\underbrace{\delta\cdot\frac{d}{dt_n}\xi_n}_{relaxation/damping} \tag{1}$$

The second equation represents the energy balance either for edge (ELM case) or for the core (sawtooth case) and derived as well in [1]:

$$\frac{d}{dt_n}p_n'=\eta\cdot\left(\underbrace{h}_{\substack{input\\power}}-\underbrace{p_n'}_{\substack{regular\\loss\\term}}-\underbrace{\beta\cdot\xi_n^2\cdot p_n'}_{\substack{loss\\due\_to\\perturb.}}\right) \tag{2}$$

where ξ_n is the normalized displacement due to instability, $p_n'=dp_n/dr$ is the normalized radial critical gradient, t_n is the normalized time.

The model can be extended to describe the pellet injection and its influence on ELM cycle. In this case, an additional perturbation is introduced in the first equation (1). It produces short periodic bursts which simulate pellet injection. The overall power balance is not affected by the pellet which keeps the equation (2) unchanged.

$$\frac{d^2}{dt_n^2}\xi_n=\left(\left[p_n'+pellet(t)\right]-1\right)\cdot\xi_n-\delta\cdot\frac{d}{dt_n}\xi_n \tag{3}$$

$$\frac{d}{dt_n}p_n'=\eta\cdot\left(h-p_n'-\beta\cdot\xi_n^2\cdot p_n'\right) \tag{4}$$

It is possible to model typical experimental situation using equations (3) and (4). The result is shown in Figure 2. Initial phase (0s-1s) has no pellets and natural ELM frequency $\left(f_{natural}\right)$ sets up after a short transition phase (1s-1.4s). In the next phase (1.4s-3s), the ELM frequency locks to the pellet

frequency $\left(f_{pellets} \approx 5 \cdot f_{natural} \right)$. This behaviour of the system reproduces experimental situations where the ELM frequency was increased by pellet injection. There are two important experimental findings regarding pellet ELM frequency and size, which could be checked for our model:

I. Pellets are able to increase the ELM frequency if $f_{pellets} > f_{natural}$. (Reduction of the ELM frequency is not possible.)

II. Increase of the ELM frequency is accompanied by reduction of the ELM amplitude, but the total power outflow remains the same. (This is true both for natural ELMs and pellet triggered ELMs).

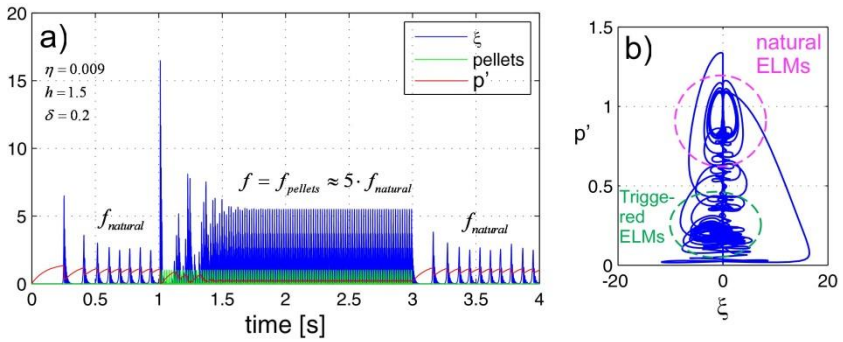

Figure 2 - Experimental situation is modelled by solving the system of equations (3, 4)

Pellets are introduced into the system between 1s and 3s (Figure 2a). After a short transition phase (1s-1.4s), the ELM frequency is locked to the pellet frequency. The phase space evolution is shown on Figure 2b.

The Figure 3a shows that reduction of the ELM frequency could not be achieved if $f_{pellets} \le f_{natural}$. ELM frequency is about natural ELM frequency in this phase. The exact ELM behaviour depends on the initial conditions (natural ELM frequency, pellet frequency, start of the pellet time). Increase of the pellet frequency leads to a locking of the ELM frequency to the pellet frequency. Thus, the first experimental observation is reproduced.

In our model, the power per pellet is characterized by changes in the pressure gradient $\left(\delta p' = p'_{beforeELM} - p'_{afterELM} \right)$. This change is much smaller in pellet phase compare to natural ELM case (see Figure 2a). Scan of the pellet frequency shows that increase of the pellet frequency leads to reduction of $\delta p'$ (Figure 3c). At the same time, the total power, $\delta p' \cdot f_{ELM}$, remains constant (see Figure 3b). This verifies the second observation for the pellet case. It is also interesting that no upper frequency limit for pellet triggering was found. The maximal applied frequency ($f_{pellet} \approx 6 f_{natural}$) leads to oscillated behaviour of the pressure gradient.

One could change the natural ELM frequency without pellets by changing the plasma stability and/or relaxation of the MHD perturbations (in our case parameter δ). A scan similar to Figure 3 was performed for natural ELMs. The result is similar to the ELM case and agrees with experimental observations that the total power per ELM, $\delta p' \cdot f_{ELM}$, remains the same. The main results are presented in [6]. We also studied the single mode gyrotron equations from a numerical point of view. For the study of the stationary and non-stationary problems in large time interval with complex oscillating initial conditions we used the implicit finite difference schemes and the method of lines. Two versions of gyrotron equation were investigated through different numerical methods. The main physical result is the possibility to determine the maximal value of the wave amplitude and the electron efficiency coefficient.

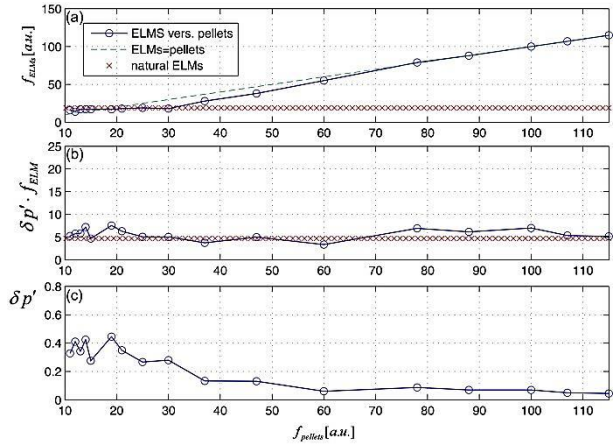

Figure 3 - (a) ELM frequency dependence on the pellet frequency, (b) average total energy release per ELM, (c) Energy per ELM

3. The investigation of the effects of a non-axisymmetric magnetic field on the transport properties (formation of the transport barriers) and the characterization of edge turbulence

The benefit and drawbacks of low magnetic shears on the confinement in magnetic fusion toroidal devices were studied using a Hamiltonian description of the magnetic field lines (which is allowed because the magnetic field is divergence-free). The existence of transport barriers in 3/2 degrees of freedom degenerate Hamiltonian systems was studied using the associated stroboscopic maps. It was analytically proved that, for small enough amplitudes of the perturbations, a transport barrier (formed by infinitely many invariant rotational circles which form a degenerate annulus) is formed in the low shear zone of the unperturbed Hamiltonian [4]. These results were applied to Hamiltonian models which describe some magnetic configurations in tokamak plasmas. The Hamiltonian of the model (i.e. the poloidal magnetic flux)

$$H(\theta,\psi,\zeta)=H_0(\psi)+H_{pert}(\theta,\psi,\zeta)=\int d\psi / q(\psi)+K\frac{2\psi}{1+\psi}\sum_{n=-M}^{M}\cos(4\theta-n\zeta) \qquad (5)$$

depends on the safety factor $q=q(\psi)$ and on the perturbation amplitude K. In the previous formula (θ,ψ,ζ) are the toroidal coordinates. It was shown that, by conveniently modifying the safety factor $q=q(\psi)$, one can obtain transport barriers in a prescribed position [3]. Similar results were reported in [3, 4]. The dual impact of low magnetic shear was also studied. It was observed that it induces a drastic enhancement of magnetic confinement if it is situated way from the main MHD modes. However, when low-shear occurs for values of the winding of the magnetic field lines close to low-order rationals, the amplitude thresholds of the resonant modes that break internal transport barriers by allowing a radial stochastic transport of the magnetic field lines may be much lower than the ones obtained for strong shear profiles [4]. In order to incorporate our theoretical results into a realistic model a mapping procedure for the magnetic field lines which includes the MHD modes was used. The safety factor, corresponding to ASDEX-Upgrade experiments, is

$$q=q(\psi)=1/(0.8-0.5\psi) \qquad (6)$$

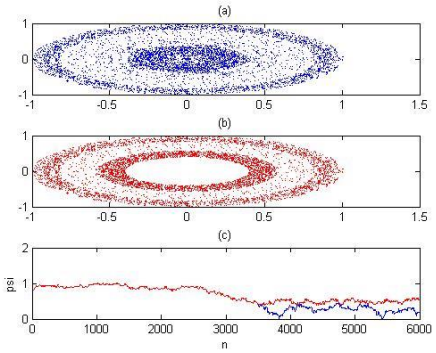

Figure 4 - The orbit of $(\theta_0,\psi_0)=(2.621,0.829)$ *in the initial magnetic configuration (a) and of the controlled one (b). Variation of the toroidal flux* ψ *along the orbits (c).*

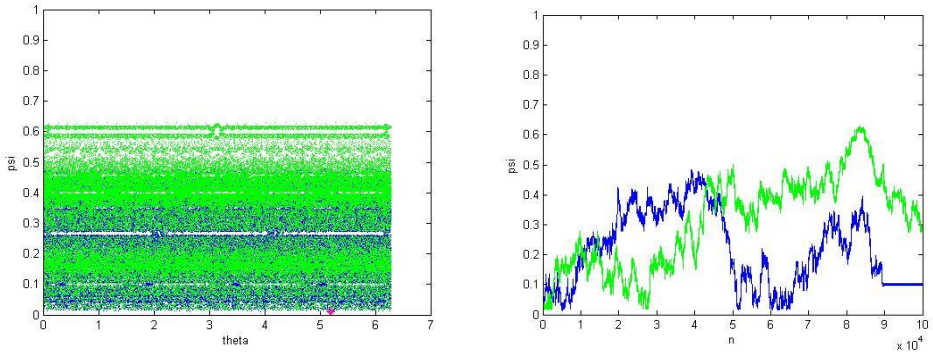

(a) *(b)*

Figure 5 - (a) Two orbits of close starting points in the initial magnetic configuration. (b) The variation of ψ *along the orbits drawn in (a)*

The internal magnetic perturbation containing several helical (m,n) modes which are resonant at the magnetic surfaces ψ_{mn} (i.e. $q(\psi_{mn})=m/n$) was considered. The perturbation of the Hamiltonian can be modeled as

$$H_{pert}(\theta,\psi,\zeta)=\sum_{m,n}\varepsilon_{mn}H_{mn}(\psi)\cdot\cos(m\theta-n\zeta) \qquad (7)$$

Where ε_{mn} is the amplitude of (m,n) MHD mode. The function $H_{mn}(\psi)$ can be modelled in the following form (Δ is a parameter that characterizes the sharpness of the pick of the modes located at the resonant surface $\psi=\psi_{mn}$):

$$H_{mn}(\psi)=\frac{n}{m}\left[\cosh\left(\frac{1}{\Delta}\ln\left(\frac{\psi}{\psi_{mn}}\right)\right)\right]^{-m\cdot\Delta/2}$$

In the simulations we considered all (m,n) modes such that $q(0)<m/n<q(1)$. The amplitude of all modes was $\varepsilon=10^{-5}$.

Figure 4a presents a single chaotic orbit starting from $(\theta_0,\psi_0)=(2.621,0.829)$ in the described magnetic configuration (5), (6), (7). The orbit of the same initial point in controlled magnetic configuration is presented in Figure 4b. A transport barrier was built around the surface $\psi=0.3$ by modifying the safety factor around $\psi=0.3$. The magnetic field line cannot cross the transport

barrier. In Figure 4c the variation of ψ along the orbit can be observed: the first 3500 iterations the initial and the controlled orbit are identical (blue and red points are superposed and only red points, corresponding to the controlled orbit are visible); after this, the controlled orbit is confined above $\psi = 0.3$, but it cannot cross the barrier. The control of the safety factor was accomplished using the method presented in [4].

Figure 5 shows that the system exhibits "sensitive dependence on initial condition", the essential condition for chaotic behaviour. Indeed, the long orbits (10^5 iterations) of the close starting points $(\theta_0, \psi_0) = (5.2025, 0.0103)$ and $(\theta_1, \psi_1) = (5.1880 \quad 0.01192)$ (blue, respectively green in Figure 5a) have different asymptotical behaviour (Figure 5b).

The realistic model we studied shows that the low shear is an important condition of obtaining robust transport barriers, but the reversed shear is not mandatory. The results are comparable with the experimental ones, because the stochasticity parameter is very small, $\varepsilon = 10^{-5}$.

4. The diffusion coefficients for different specific models [e.g. streamer, zonal flow and blob, which are relevant to ITER conditions]

We have considered in slab sheared geometry an electrostatic turbulence represented by an electrostatic stochastic potential Φ(**X**, Z, t), where **X** = (X,Y) are the Cartesian coordinates in the plane perpendicular to the main magnetic field. The z component of the magnetic field, i.e. $\mathbf{B}_z$ depends on the radial coordinates X and has the form $\mathbf{B}_z = B_o(1 + X/R)^{-1}\mathbf{e}_z$. The dimensionless system of equations obtained in the second approximation of the guiding center in the case of the reversed magnetic shear field as $\mathbf{B} = B_o[\mathbf{e}_z - s^2(X)\mathbf{e}_y]$

$$dx/d\tau = - K\partial\varphi/\partial y$$

$$dy/d\tau = K\partial\varphi/\partial x - K_s\alpha_S x^2$$

$$dz/d\tau = K_{zs}\alpha_S x\partial\varphi/\partial x + K_z$$

was analyzed and the influence of the reversed magnetic shear on the diffusion coefficients in turbulent plasmas was studied. In this context we work on the influence of this magnetic field on the diffusion coefficients in the following cases: streamer, zonal flow and blob, which are relevant for ITER. In particular, we have determined by numerical simulations [5,6] the diffusion coefficients for different parameters of the plasmas. The used equations are specific to LCFS (last-closed flux surface) and SOL (scrape-off-layer) and the aforementioned magnetic field was implemented in.

5. Test particles simulations, using existing codes that give the electromagnetic fields, for investigate transport mechanisms leading to inward convection of particles and/or impurities in edge turbulence simulations

Our aim is to relate the particle diffusion coefficient properties to the characteristics of the electromagnetic fields. The guiding centre equation gives us a dimensionless system which contains several Kubo numbers. Varying these Kubo numbers we obtain different regimes for the particle transport, i.e. also for an impurity introduced in plasma. We have considered in slab sheared geometry an electrostatic turbulence represented by an electrostatic stochastic potential Φ(**X**, Z, t), where **X** = (X,Y) are the Cartesian coordinates in the plane perpendicular to the main magnetic field. The z component of the magnetic field, i.e. $\mathbf{B}_z$ depends on the radial coordinates X and has the form $\mathbf{B}_z = B_o(1 + X/R)^{-1}\mathbf{e}_z$. The dimensionless system of equations obtained in the second approximation of the guiding center and with a linear magnetic shear component (a normal one) $X/L_S\ \mathbf{e}_y$ is

$$dx/d\tau = -K\ (1 + \alpha_R x)\ \partial\varphi/\partial y$$

$$dy/d\tau = K\,(1 + \alpha_R x)\,\partial\varphi/\partial x + K_s x$$

$$dz/d\tau = K_{zs} x\,\partial\varphi/\partial x + K_z b^{-1}(\alpha_R x)$$

The dimensional diffusion coefficients scale as: $D_{ij}(T) = (\lambda_\perp^2/\tau_c)(K^2/(K_{ionz}+1))F_{ij}(T, K, K_{ionz}, K_{ions})$ $i, j = x,y$ and the tensor F_{ij} is calculated using the Lagrangian correlations corresponding to the fluctuating velocities of the ions. The DCT (decorrelation trajectory method) formalism was developed for these two models. In the numerical we have used the TURBO code, which is designed to solve numerically the equations for an incompressible fluid in a three dimensional geometry with periodic boundary conditions in the three directions. Our numerical code for tracking particle trajectories was developed in a modular fashion as an extension of TURBO solver [5,6]. We have calculated the mean squared displacements and also higher order moments that are used for the calculation of the skewness and kurtosis. Moreover we have calculated probability density functions (PDFs) of the electrostatic potential, electric field, magnetic field and of the components of the particle velocity, i.e. the radial, poloidal and the toroidal one. The influence of the level of electrostatic turbulence given by the electrostatic Kubo number K and the influence of the magnetic shear given by the shear Kubo number Ks on the above mentioned quantities was observed.

6. The investigation of particle transport regimes using some parallel codes under EGI (European Grid Infrastructure)

Currently, there are numerous opportunities to conduct numerical simulations involving parallel computations. There is a national program that coordinates all HPC (High Performance Computing) activities. Through this program, we obtained access to VO-fusion - a structure of EGI (European Grid Infrastucture) that shares the computing resources of many virtual organizations, including VO-fusion - an organization that includes some activities related to EURATOM program. Another possibility to perform numerical simulations (HPC): we applied and got a computational credit in the IFERC-CSC program (International Fusion Energy Research Centre - Computational Simulation Centre) under HELIOS parallel computer. This is an application in partnership with the EURATOM group from ULB (Free University of Brussels); we employ parallel codes (derived from TURBO3D) to evaluate the transport of charged particles in various configurations of electromagnetic fields. We note the application (the acronym S3TP2) began in November 2012 and will be held for at least 12 months.

Conclusion

The low dimensional model proposed in [1] was extended to describe the pellet injection and its influence on ELM cycle. From the numerical simulations we concluded that important experimental observations (pellets are able to increase ELM frequency but a reduction is not possible and the increase of the ELM frequency is accompanied by reduction of the ELM amplitude, but the total power outflow remains the same) are confirmed by the theoretical model. It results that the proposed low dimensional model provides useful tools for understanding the basic physics and allows estimating relative quantities, even if it does not qualify for a complete description of the plasma phenomena such as ELM or sawtooth.

A Hamiltonian model of a magnetic field configuration influenced by many MHD perturbations was studied. For small amplitudes of the perturbations, comparable with those encountered in experiments, a chaotic behavior was pointed out. It was shown that a robust transport barrier can be obtained in a prescribed zone by locally modifying the safety factor. The main importance of the results is that they point out the essential role of the safety factor in building magnetic transport barriers. The influence of the reversed magnetic shear on the diffusion coefficients in turbulent

plasmas coefficients in the following cases: *streamer*, *zonal flow* and *blob* that are relevant for ITER was studied. We have calculated the mean squared displacements and also higher order moments that are used for the calculation of the skewness and kurtosis. Moreover we have calculated probability density functions (PDFs) of the electrostatic potential, electric field, magnetic field and of the components of the particle velocity, i.e. the radial, poloidal and the toroidal one. The influence of the level of electrostatic turbulence given by the electrostatic Kubo number K and the influence of the magnetic shear given by the shear Kubo number K_s on the above mentioned quantities was observed.

Acknowledgement

The reported work includes contributions from the following people outside the EURATOM-MEdC Association: H. Isliker, A. Vogiannou, L. Vlahos (EURATOM - Hellenic Republic Association, University of Thessaloniki, Greece), D. Carati and B. Knaepen (EURATOM – Belgium State Association, ULB, Belgium), Marie-Christine Firpo (Laboratoire de Physique et Technologie des Plasmas (CNRS UMR 7648), Ecole Polytechnique, 91128 Palaiseau Cedex, France), O. Dumbrajs (Association Euratom-UL, University of Latvia), V. Igochine, K. Lackner, R. Meyer-Spasche, H, Zohm (Max-Planck Institut für Plasmaphysik, Association Euratom-IPP, Germany).

MAGNETIZED PLASMA COLUMN DIAGNOSIS USING ELECTRICAL PROBES

C. Agheorghiesei, V. Anita, S. Costea, C. Costin, G. Popa, L. Sirghi

Alexandru Ioan Cuza University, Faculty of Physics, Iaşi, Romania

[BS_6/WP12-DIA]

Abstract

Experimental measurements and numerical simulations were performed in order to understand the particularities of electrical probe characteristics obtained in magnetized plasmas, when the probe is parallel to the magnetic field lines. Experiments were conducted both in a facility designed and built in our laboratory and in Pilot-PSI facility at Dutch Institute for Fundamental Energy Research (DIFFER), Nieuwegein, The Netherlands. The facility in Iasi allows obtaining a linear plasma column in the presence of a magnetic field up to 0.42 T. The aim was to explain the presence of a negative slope region in the electron saturation branch of the probe characteristic. It was found that an important role in the amplification of the electron saturation current is played by the presence of the probe holder (insulating material) via its negative floating potential. To illustrate the role of this potential on the probe characteristic, the insulating material was replaced by a conductive guard ring biased at different potentials with respect to plasma potential. A Monte Carlo code was used to calculate the fraction of the charged particles coming from the magnetized plasma column that is collected by the cylindrical probe when it is biased with respect to plasma potential. The calculations were made for several magnetic field strengths, for collisional and non-collisional plasma, with and without probe holder. Ion saturation currents collected by the probe were calculated for argon and hydrogen plasma. Correlation measurements of the ion saturation currents were done in Pilot-PSI, both in the plasma volume and at the target surface. It was shown that a floating target collects from the plasma column electron current in the centre and ion current at outer radii. Even if the sum of the two currents (electron and ion) is zero for a floating target, the results prove the existence of radial currents flowing inside the floating target.

Detailed results

This study was dedicated to ***magnetized plasma diagnosis***, namely the investigation of some specific characteristics of probe measurements in a magnetized plasma column. The investigations were focused on both measurements and simulations of probe current-voltage characteristics. The results are relevant for the interpretation of the probe measurements performed in the last years in fusion related devices such as Pilot-PSI and COMPASS tokamak.

Probe measurements in a linear magnetized plasma device (Iasi)

The experiments on probe characteristics were performed on a linear device specially designed and realized to produce magnetized plasma in our laboratory (Iasi). Plasma source consists of a DC discharge with hot cathode. The discharge chamber is a cylindrical glass (pyrex) tube with inner diameter of 44 mm and length of 420 mm. Plasma confinement is achieved using a system of four magnetic coils.

For the diagnostic of the non-isothermal magnetized plasma produced in this device there were used plane and cylindrical probes with variable length. Plane probes were aligned with their active surface perpendicular to the magnetic field lines and cylindrical probes were primarily aligned with their symmetry axis parallel to the magnetic field lines. The experiments were aimed mainly to characterize the behaviour of electrical probes in magnetized plasmas and to understand the obtained current-voltage (I-V) characteristics.

Probe's volt-ampere characteristics were recorded using the following control parameters: the probe length (from 0 – equivalent to a plane probe, up to a length of 7 mm) the diameter of the tungsten probe (0.2, 0.5 and 1.6 mm), the magnetic field strength (up to a maximum of 0.42 T) and the working gas pressure (0.01 ÷ 0.1 Pa). The discharge current intensity was maintained constant at 1 A. For magnetic field strength below a certain threshold (in this case approximate 0.06 T) which depends on gas pressure, length of the probe and its orientation to the magnetic field, the probe characteristics have a classical shape [1]. These characteristics have both electron and ion saturation currents increasing simultaneously with the absolute value of the bias potential applied on the probe. The ratio of these saturation currents depends on magnetic field strength and is much smaller than the ratio obtained for unmagnetized plasma [2].

When both the magnetic field strength and the cylindrical probe's length are increasing, electron saturation current may decrease, with increasing of positive polarization of the probe. This corresponds to a negative slope on the volt-ampere characteristic. A typical example for the probe characteristics obtained in argon plasma for a pressure of 0.13 Pa is shown in Figure 1.

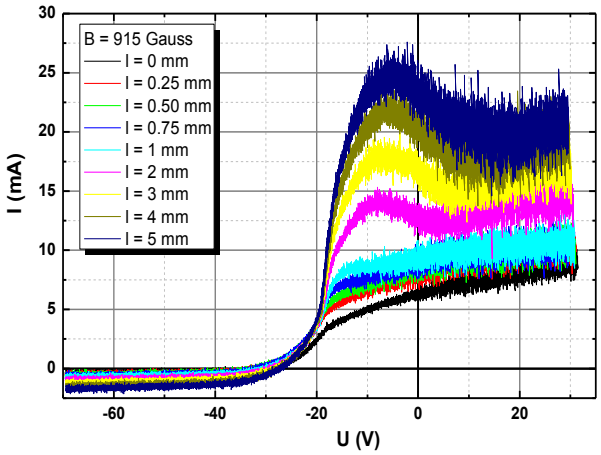

Figure 1 - Probe I-V characteristics obtained in argon magnetized plasma column (B = 0.0915 T) at a pressure of 0.13 Pa, using a cylindrical tungsten probe with a diameter of 0.5 mm and different lengths

This type of probe characteristics were obtained and reported for the first time in the scientific literature in 1964 [3]. A review of relevant literature showed us that there were no other reported results and the only model that attempts an explanation of these results is the one proposed in this work. The I-V characteristics shown in Figure 1 have some obvious features: *i)* a negative slope in the region of the electron saturation current; *ii)* change of the slope in the branch of electron current probe, when the probe potential is around plasma potential, which is well marked for certain lengths of the probe; the change of the slope of the I-V characteristics is related first to a significant increase of the electron current intensity followed by the negative slope; *iii)* significant increase of the electron current fluctuation (as amplitude) when the negative slope region appears on the probe characteristic.

To explain both increasing of the electron current of the probe followed by the presence of the region with negative slope, we proposed a new approach that is based on the kinetics of electrons near the probe. The former result can be a result either of additional inelastic collisions of electrons around the probe or by some other mechanism of local increasing the electron flux for positive bias of the probe with respect to plasma potential. The previous results obtained in our lab [4] show that inelastic collisions are not significant and could not be a reason for doubling the electron current

intensity of the probe. Consequently, another mechanism has to be involved and this is the electron reflection by the floating potential of the dielectric surrounding the cylindrical probe. Due to the presence of a strong magnetic field, the electrons are strongly magnetized and electron Larmor radius is smaller than the thickness of the dielectric insulator of the probe. Consequently, a rather large amount of electrons flowing along the magnetic field lines and parallel to the cylindrical probe surface are reflected by the end of the insulator and returned into the electronic space charge developed around the positive biased probe. These reflected electrons can explain significant (up to double) increasing of the electron current intensity. In order to study this mechanism a stainless steel guard ring was mounted in front of the ceramic tube of the cylindrical probe. This guard ring was differently biased in order to study its influence on the probe characteristic, first on the region of the electron current increasing and then with negative slope too. For the measurements presented in Figure 2, the guard ring potential varied from the floating potential (-38 V) up to -14 V. As illustrated, when the potential applied on the guard ring becomes more positive, the measured electron saturation current decreases. This happens because when the potential of the ring become positive compared with the plasma potential the electrons are collected by the metal ring. When the ring is not installed the potential of the ceramic shaft is equal to the floating potential (negative) and most of the electrons which come to the probe are reflected back along the magnetic field lines. This fact determines the increase of the electron density around the probe and consequently the increase of the electron current collected by the probe [6].

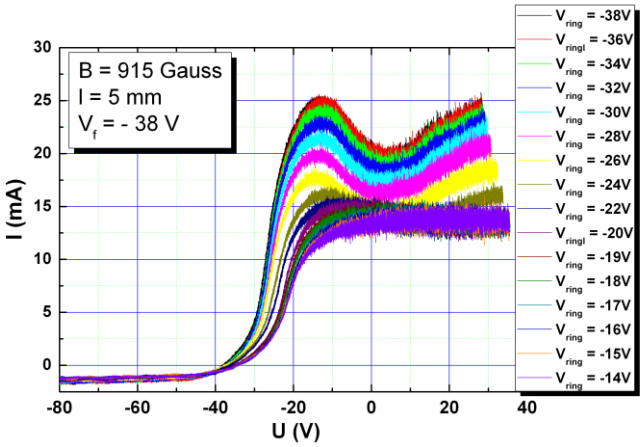

Figure 2 - Probe I-V characteristics obtained in the same conditions as Figure 1 (probe length l = 5mm). The ceramic shaft was replaced by a guard ring biased at different voltages

Moreover, both incoming electrons and reflected ones may also explain the later noticed effect as negative slope of the probe characteristics. Essentially, explanation is based on the idea that for positive potentials of the probe biased with respect to plasma potential, around the probe on radial direction an electronic space charge is formed. An electric field appears in this electronic space charge, produced by the difference between positive bias potential of the probe and the potential of undisturbed plasma. The direction of the electric field is from the probe towards the plasma and it is almost perpendicular to the magnetic field lines. The action of these two mutually perpendicular fields E and B will determine an electric drift motion [5] of particles inside the space charge.

The decrease of probe current in the region that corresponds to electron saturation current above a certain positive bias of the probe is caused by the increase of the space charge impedance load when a significant fraction of the both incoming and reflected electrons is involved in the movement

of electric drift. This motion influences the flow of particles towards the probe once the probe potential exceeds a certain positive value with respect to the plasma potential.

Particle flux simulations by Monte Carlo code

The Monte-Carlo (MC) code was improved in order to acquire further insight and understand the probe measurements made both in Pilot-PSI and in the linear magnetized plasma column produced in our laboratory. The new features of the code consist of having the probe biased with respect to the plasma potential, taking into account electron-neutral collisions and the presence of the probe holder (insulator). The code was used to calculate the fraction of the particles introduced in the simulation domain that is collected by a cylindrical probe and the charged particle fluxes collected by the probe. The cylindrical probe, with 5 mm length and 0.5 mm in diameter, is placed on the symmetry axis, parallel to the magnetic field lines. The probe holder is an insulator of 0.5 mm thick. The simulation was made for hydrogen and argon at 6.67 Pa. Electrons and ions are introduced in the simulation domain with maxwellian distribution function, for electron and ion temperature of 4 eV and 0.1 eV, respectively.

The current density in the plasma source is uniform along the radial direction. Plasma is confined by a uniform axial magnetic field and its strength varies from 0.06 to 0.4 T. Electron's trajectories are affected by elastic, excitation and ionization collisions. The probe was biased in the range of -35 to +35 V. The floating potential of the insulator (probe holder) was calculated to be -10 V with respect to the plasma potential. In the case of electrons, the presence of the probe holder and the collisions with the neutral atoms leads to a raise in the number of electrons collected by the probe. A fraction of electrons, due to collisions, can change direction and return to the plasma source. This is most obvious for the electrons leaving the plasma source at radii smaller than the radius of the cylindrical probe (Figure 3b and 3d). Due to their heavier masses, the ions have large Larmor radius and, therefore, they are, in this simulation, almost not affected by the presence of the probe holder, but they are affected by the presence of the sheath around the probe. The plasma source region from where the charged particles are collected is larger (in radius) for higher mass ions (see Figs. 4 and 5).

Current measurements at the target of Pilot-PSI

The multi-probe system (with 61 probes) was combined with a new electrical circuit (Figure 6) in order to measure the spatio-temporal distribution of the ion saturation current at the target surface. An example of radial distribution of the ion saturation current is given in Figure 7 for argon and hydrogen discharge, for several discharge current intensity. The cross-correlation analysis of the ion saturation currents, applied for different operating conditions (gas, discharge current or magnetic field strength) showed no spatio-temporal correlation between the signals measured by different probes, no matter if the probes were fixed in the target or the probe was placed in the plasma column. The result is different from the one obtained when the cross-correlation analysis was applied to electron current, when a rotation of the correlation maximum could be observed at the target surface.

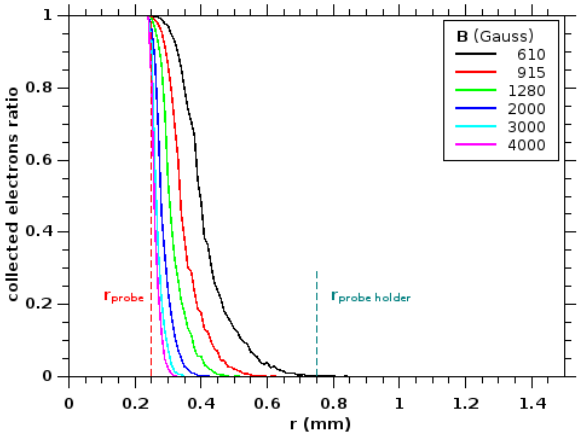

a) probe holder NO / collisions NO

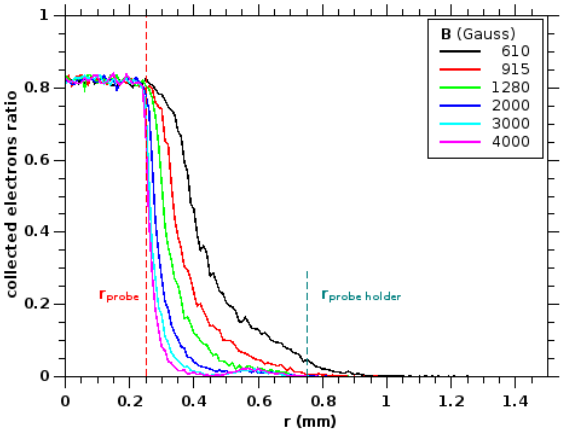

b) probe holder NO / collisions YES

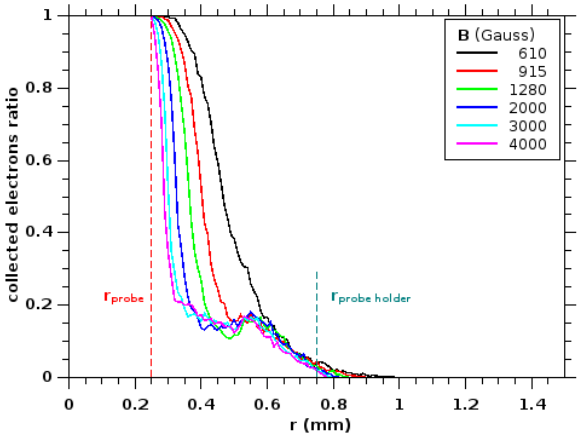

c) probe holder YES / collisions NO

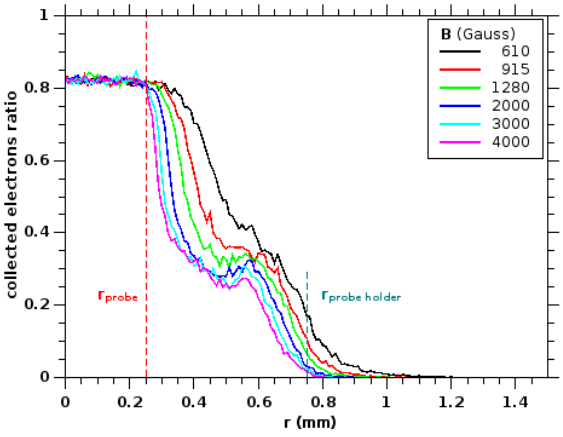

d) probe holder YES / collisions YES

Figure 3 - The fraction of electrons from the plasma source that is collected by the probe

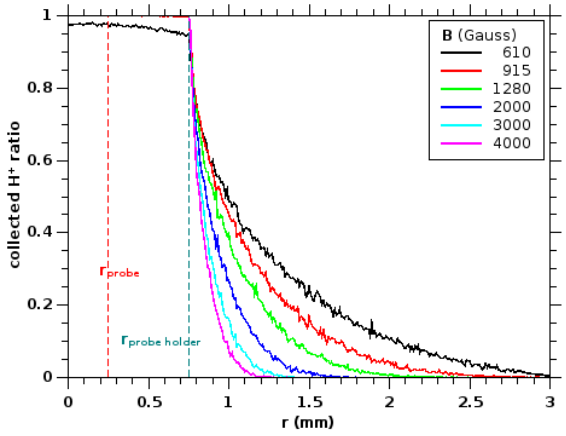

Figure 4 - The fraction of H^+ ions from the plasma source that is collected by the probe

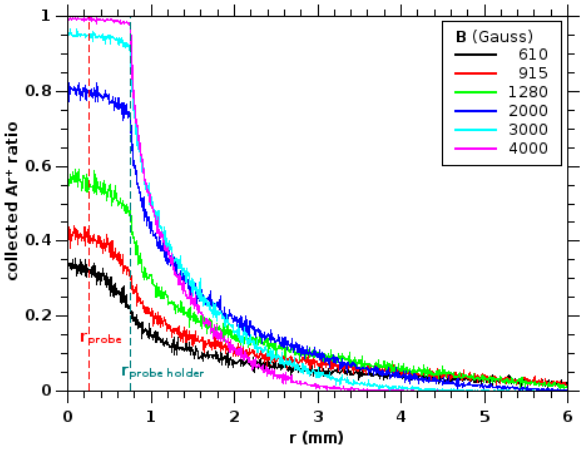

Figure 5 - The fraction of Ar^+ ions from the plasma source that is collected by the probe

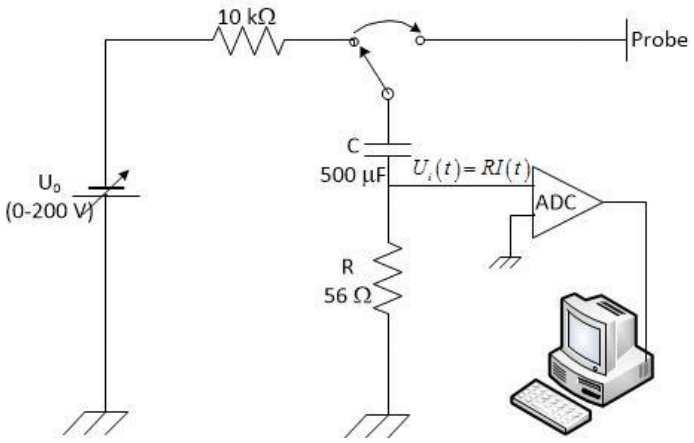

Figure 6 - Electrical circuit designed to measure the ion saturation current (example for a single probe)

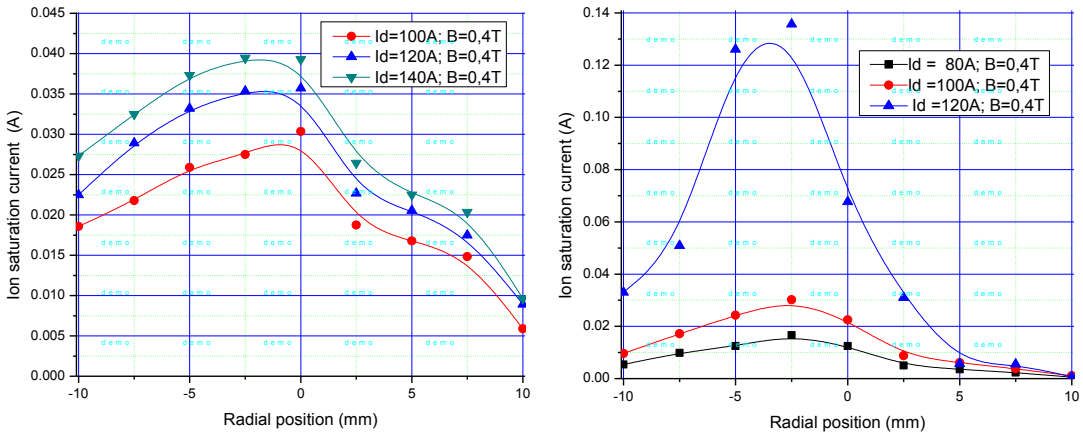

(a) *(b)*

Figure 7 - Radial distribution of the ion saturation current in (a) argon and (b) hydrogen discharge, having the discharge current intensity I_d as parameter (B = 0.4 T)

Measurements at floating target revealed interesting results. The floating potential was measured at the target surface on a diameter of the multi-probe system, in the same time with the floating potential of the carbon plate that protects the probes, considering its floating potential as corresponding to a compact target. An example of such measurement is given in Figure 8 for a discharge operated in Ar+H_2 (1:1), at 80 A and 0.4 T. It can be observed that the central probes (red plots) have the floating potential more negative than the carbon plate while the floating potential of the other probes is more positive than the one of the carbon plate. The new measuring circuit allowed us to bias all the probes at the floating potential of the carbon plate (-13 V) and to measure the currents collected by the probes (Figure 9). All the probes having the floating potential more negative than the carbon plate (red plots) collect electron current (negative) while the others collect ion current (positive). As the total current to the floating target is zero, it means that the electrons arriving to the central part of the target flow through the target to recombine with the ions arriving at outer radii. This result proves the existence of a current that flows inside of a compact floating target that interacts with non-homogeneous plasma. As the tiles of the wall and of the divertor of tokamak devices face very non-homogeneous plasma, they will also have inner currents even if the tiles have the same potential.

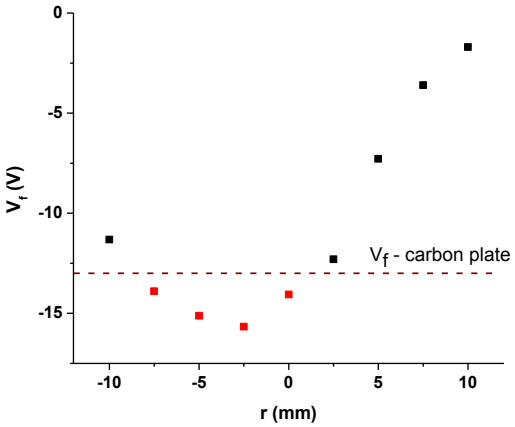

Figure 8 - Radial distribution of the floating potential measured on a diameter of the multi-probe system (scatter plots) and the floating potential of the carbon plate (dash line at -13 V) (Ar + H_2, 0.4 T, 80 A)

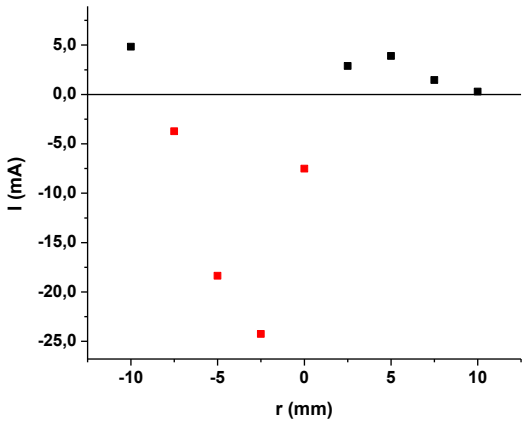

Figure 9 - Radial distribution of the current measured on a diameter of the multi-probe system when the probes were biased at the floating potential of the carbon plate (-13 V) (Ar + H_2, 0.4 T, 80 A)

Reconstruction of the ion branch of a probe characteristic only from current measurements

The ion part of a probe characteristic was obtained by two methods. Both procedures used the registration of the ion current intensity $I(t)$ collected from the plasma, measured as the potential drop $U_i(t)$ across a resistor R = 56 Ω (Figure 6). This current discharges the capacitor C = 500 µF that was initially charged by the power supply at a voltage U_0, more negative than the floating potential of the probe.

In the first method, the potential of the probe $U_p(t)$ was registered simultaneously with the ion current, using a second channel of the data acquisition system. A voltage divider of 1/100 was used for the registration of $U_p(t)$. The time dependence of the signals $U_i(t) = RI(t)$ and $U_p(t)/100$ measured with respect to the ground are showed in Figure 10, exactly as they were registered by the data acquisition system. Using these data, the ion branch of the current voltage characteristic was reconstructed and plotted in Figure 11 (black curve), according to the classical convention for the representation of the probe's characteristic (the ion current is negative).

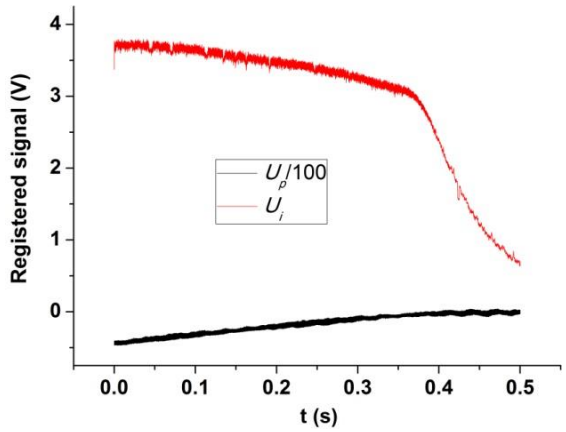

Figure 10 - Time dependence of the registered signals $U_i(t)=RI(t)$ and $U_p(t)/100$, for the central probe (Ar, 1.2 T, 80 A)

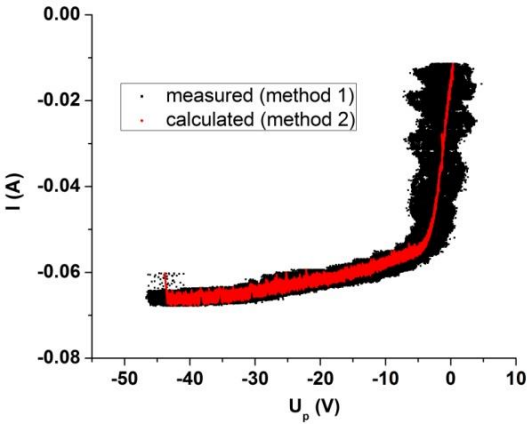

Figure 11 - Comparison of the ion branch of the probe's current-voltage characteristic reconstructed with the two methods

The second method does not need the measured probe voltage but it computes it using the time evolution of the current intensity $I(t)$. Based on the electrical circuit from Figure 6, the probe voltage $U_p(t)$ can be calculated as:

$$U_P(t) = U_0 + \frac{1}{C}\int_o^t I(t')dt' + RI(t),$$

where U_0 = - 50 V is the initial voltage of the charged capacitor C. The ion branch of the probe's current-voltage characteristic obtained with this method is also plotted in Figure 11 (red curve). A very good agreement was found between the two methods, validating thus the new method that requires only a single acquisition channel to obtain the ion branch of the probe characteristic. It has a big advantage when working with a large number of probes.

The ion branch of the probe characteristic can be subsequently used to determine the local electron temperature with good space resolution in the region of the target using the multi-probe system. Knowing the electron temperature and using Bohm's expression for the ion saturation current, the local plasma density can be also estimated. In this way the spatial distribution of the main plasma parameters, as electron temperature, density and ion fluxes, can be registered in the cross section of the plasma column of Pilot-PSI machine.

Conclusion

The last measurements performed in Pilot-PSI completed the picture of plasma parameters at the target surface. Thus, 2D maps of the floating potential, ion saturation current, electron current at the grounded target are now available for different operating conditions. A method that requires only a single acquisition channel to obtain the ion branch of the probe characteristic was presented and validated. Experimental measurements and numerical simulations were performed to investigate the particularities of probe's I-V characteristic in magnetized plasmas.

Acknowledgement

The reported work includes experiments on Pilot-PSI device at Dutch Institute for Fundamental Energy Research (DIFFER), Nieuwegein, The Netherlands, Association EURATOM-FOM.

References

[1] V. I. Demidov, S. V. Ratynskaia, and K. Rypdal, Rev. Sci. Instrum. 73 (2002) 3409

[2] V. I. Demidov, S. V. Ratynskaia, R. J. Armstrong, K. Rypdal, Phys. Plasmas 6 (1999) 350

[3] T. Dote, H. Amemiya, T. Ichimiya, Jpn. J. Appl. Phys. 3 (1964) 789

[4] M. L. Solomon, I. Mihaila, C. Costin and G. Popa, "On the particular behavior of current-voltage characteristic of electrical probes in magnetized plasma", 9th International Workshop on Electric Probes in Magnetized Plasmas, 21–23 September 2011, Iaşi, Romania

[5] P. C. Stangeby, Plasma Diagnostics, vol. 2, Surface Analysis and Interactions, ed. O. Auciello and D. L. Flamm, Boston: Academic Press (1989) pp. 157-209

[6] I. Mihaila, M. L. Solomon, S. Costea, C. Costin, G. Popa, „Electrical probes in magnetized plasma", 5th Internation Workshop on Plasma Physics, 25-30 June 2012, Kiten, Bulgaria

THE INFLUENCE OF THE KINETIC EFFECTS ON THE RESISTIVE WALL MODES STABILIZATION

Iulian Gabriel Miron

National Institute of Laser, Plasma and Radiation Physics, EURATOM-MEdC, Romania

[BS_13/WP12-IPH-A02-2-1-06/BS]

Abstract

A model that describes the effect of the resonance between the resistive wall mode (RWM) frequency and the magnetic precession drift or bounce frequency of the thermal trapped particles on the RWM stabilization is developed. The above mentioned resonance is considered as an important dissipation channel for the RWM instability. The proposed model does not follow the kinetic MHD energy principle, but starts from the perturbed MHD equations with the kinetically derived pressure tensor term. The bounce and precession motions of the thermal trapped particles are considered. The trapped particles influence the RWM through their resonant and non-resonant contributions. The multimode approach of the proposed theoretical model allows us to compare the latter contributions.

Recent theoretical damping models and experimental results suggest that the RWM resonance with the thermal ions at their bouncing (or passing) frequencies does not significantly affect the RWM behavior. On the other hand, at lower frequencies, such as the precession drift frequencies of the trapped particles, the RWM resonance is higher. Therefore the RWM behavior seems to be significantly affected by the latter kinetic effects. The proposed theoretical model measures the above dissipative effects.

The perturbed pressure tensor is analytically derived. A semianalytic RWM dispersion relation that includes explicitly derived kinetic terms is obtained. The RWM and the particle bounce/precession drift frequency resonance phenomenon is investigated in order to calculate the RWM damping efficiency. The influence of the plasma rotation and the effect of the passive and active feedback systems action are investigated within the frame of the above kinetic scenario (at bounce/precession drift frequency resonance).

Detailed results

Introduction

The stabilization of the resistive wall modes (RWM) by plasma rotation, by means of various damping phenomena, has been widely studied, both theoretically and experimentally. In recent years, it has been found that the resonance of the RWM frequency with the toroidal precession frequency of the trapped energetic particle banana orbits stabilizes the RWM at slow toroidal plasma rotation. The damping mechanism greatly reduces the RWM growth rate. The particle drift motion frequency (diamagnetic or precessional) is comparable with the RWM frequency. The diamagnetic drift can be neglected if the plasma rotation frequency is higher than the diamagnetic frequency. The particle bounce resonance condition requires fast plasma rotation. For a slow plasma rotation, the bounce/circulating particles frequency does not resonate with the RWM real frequency. Being almost locked to the wall, the RWM frequency is much smaller compared to the particle bounce motion frequency. Therefore, for a RWM, the resonance with the trapped particles bounce-averaged precession frequency provides RWM stabilization only. The latter physical mechanism is proposed as an important dissipation channel in order to stabilize the RWM at low plasma rotation. The zero bounce harmonic number contribution to the resonance is considered, in a slow plasma rotation regime. The proposed model includes a three-dimensional description of the magnetic perturbations (due to the nonaxisymmetric feedback system) for a two-dimensional, axisymmetric equilibrium magnetic field geometry (toroidicity, Shafranov shift, ellipticity and triangularity parameters are considered). General natural (flux) coordinates will be used. The

following milestones have been achieved: i) Derivation of the kinetic terms, and ii) Derivation of the RWM dispersion relation.

This work has also been accomplished under the EFDA Task Agreement WP12-IPH-A02-2-1-06.

Derivation of the kinetic terms

To derive the parallel and perpendicular components of the perturbed pressure tensor terms

$$p_{\parallel} = \sum_{\alpha=e,i} \int d\mathbf{v}\, M_{\alpha} v_{\alpha\parallel}^2 f_{\alpha}^1 , \qquad p_{\perp} = (1/2) \sum_{\alpha=e,i} \int d\mathbf{v}\, M_{\alpha} v_{\alpha\perp}^2 f_{\alpha}^1 \tag{1}$$

the perturbed particle distribution function, f_{α}^1, has to be found. The perturbed pressure tensor is $\mathbf{p} = p\mathbf{I} + p_{\parallel}\,\mathbf{nn} + p_{\perp}(\mathbf{I} - \mathbf{nn})$, where p is the scalar perturbed pressure, $\mathbf{I}$ is the unit tensor and $\mathbf{n} = \mathbf{B}/B$ is the equilibrium magnetic field unit vector. The integration is performed over the particle velocity space. M_{α} is the particle mass and $v_{\alpha\parallel}$, and $v_{\alpha\perp}$ are the particle parallel and perpendicular velocities. The $\nabla\mathbf{p}$ term is included into the perturbed MHD momentum equation that has finally to be solved in order to derive the RWM growth rate.

According to [1], the perturbed particle distribution function is $f^1 = p_{\varphi}\partial f^0/\partial P_{\varphi} - \mu\,(b_{\parallel}/B)\partial f^0/\partial\mu + h^1$, where h^1 satisfies the dynamic equation $dh^1/dt = (\partial f^0/\partial E)\partial L^1/\partial t - (\partial f^0/\partial P_{\varphi})\partial L^1/\partial\varphi$, L^1 being the particle perturbed Lagrangian. We use the (r,θ,φ) natural (flux) coordinates that keep the magnetic field lines straight on a constant flux surface. The particle quantities, p_{φ}, P_{φ}, μ, E, and f^0 are the perturbed and the equilibrium canonical momentum, the magnetic moment, the particle energy and the equilibrium (Maxwellian) particle distribution function, respectively. $\mathbf{b}$ is the perturbed magnetic field and is parameterized as $\mathbf{b} = \nabla\times\{[(1/B)\nabla\phi\times\mathbf{B}]\times\mathbf{B}\}$, where $-\partial\phi/\partial t$ is the perturbed scalar electric potential. Our calculus leads to the following expression of the perturbed particle distribution function

$$\begin{aligned} f^1 = &-\frac{if^0}{KTR_0^2q^2B_{z0}} \sum_{m,n,l} \Big\{ Mv_{\parallel}^2 [r(m-nq)(1+O(\varepsilon))\phi'_{mn} + ((2-s)(m-nq) - ms + O(\varepsilon))\phi_{mn}] \\ &- \mu B(2-s)(m-nq+O(\varepsilon))\phi_{mn}\Big\}\exp[i(m\theta - n\varphi) + \gamma t] \\ &+ \frac{if^0}{KTrR_0q^2B_{z0}} \sum_{m,n,l} \frac{\gamma + inv_{\parallel}/R^2}{\gamma + i(m\Omega_{\theta} - n\Omega_{\varphi} + l\omega_b - n\omega_D)} \Bigg\{ Mv_{\parallel}^2 \Bigg[iR\left(\sin\theta - \frac{r}{2R_0}\sin 2\theta + \frac{a\varepsilon}{r}\frac{\partial\Delta_R}{\partial\theta}\right)\phi'_{mn} \\ &- m\left(\cos\theta + \frac{r}{2R_0}(3-\cos 2\theta) + a\varepsilon\frac{\partial\Delta_R}{\partial r} + O(\varepsilon^2)\right)\phi_{mn}\Bigg] + \mu Bq^2\Bigg[R_0\left(m + \frac{ir}{R_0}\left(1-\frac{1}{q^2}\right)\sin\theta + O(\varepsilon^2)\right)\phi_{mn} \\ &+ m\left(\cos\theta + \frac{r}{2R_0}\left(3(1+\cos 2\theta) + \frac{2n}{mq}(2-s)\right)\right)\phi_{mn}\Bigg]\Bigg\}\exp[i(m\theta - n\varphi) + \gamma t] \end{aligned} \tag{2}$$

K is the Boltzmann constant, T the temperature, R_0 the tokamak major axis, B_{z0} the equilibrium toroidal magnetic field in the major axis and $\varepsilon = a/R_0$, where a is the plasma boundary "radial" flux coordinate (minor radius). q is the safety factor and $s = rq'/q$. The calculus is performed within the large aspect ratio approximation. $'\equiv\partial/\partial r$. m, n and l are the harmonic numbers in the helicoidal (poloidal and toroidal) and bounce orbit expansion, respectively. γ is the RWM growth rate, Ω_{θ},

Ω_φ are the plasma poloidal and toroidal angular rotation frequencies, and ω_b and ω_D are the trapped particles bounce and bounce-averaged toroidal precession frequencies. As it has been considered, the diamagnetic drift is neglected for a higher plasma rotation frequency compared with the diamagnetic frequency of the thermal particles.

In (R,Z,φ) cylindrical coordinates, $R=R_0[1-(r/R_0)\cos\theta-(r^2/R_0^2)(1-\cos 2\theta)-\varepsilon^2\Delta_R]+O(\varepsilon^2)$ describes the plasma shaping, where

$$\Delta_R=-\sum_{j=1}^{3}\frac{(-1)^{\delta_{j1}}}{2j}\left\{[(j+1)\Lambda_j+(j-1)r\Lambda'_j]\cos(j-1)\theta+[(j-1)\Lambda_j-r\Lambda'_j]\cos(j+1)\theta\right\} \tag{3}$$

$\Lambda_j\equiv\Delta\delta_{j1}+E\delta_{j2}+T\delta_{j3}$ ($j=1,2,3$ and δ Kronecker delta), where Δ, E and T are the Shafranov shift, ellipticity and triangularity parameters.

We start from the particle guiding center equations in order to find the bounce and the bounce-averaged toroidal precession frequencies of the energetic particles. With the assumptions that the finite orbit width of the energetic particles is neglected and $\mathbf{v}_d\sim O(\varepsilon^{3/2})\mathbf{v}_\parallel$ [1], the obtained bounce frequency of the trapped particles is $\omega_b=(\pi/2qR_0K(k^2))\sqrt{\mu B_{z0}r/MR_0}$. $K(\kappa^2)$ is the complete elliptic integral of the first kind and $\kappa=\sin\theta_b/2$ is the normalized pitch angle parameter, θ_b being the maximum bounce orbit angle. $\mathbf{v}_d=(1/eB)\mathbf{n}\times[\mu\nabla B+Mv_\parallel^2(\mathbf{n}\cdot\nabla)\mathbf{n}]$ is the particle drift velocity, having the electric charge e. For trapped particles, using coordinates that keep the magnetic field lines straight on a constant flux surface, the bounce-averaged toroidal precession frequency is calculated as [2]

$$\omega_D=-\frac{q\omega_b}{\pi}\int_{-\theta_b}^{\theta_b}\frac{v_d^\theta}{|v_\parallel n^\theta+v_d^\theta|}d\theta \tag{4}$$

The θ upper index refers to the θ contravariant component. We have obtained the following compact expression for the bounce-averaged toroidal precession frequency in $O(\varepsilon^2)$ approximation

$$\begin{aligned}\omega_D=&\frac{2q\mu}{erR_0K(\kappa^2)}\left\{\left[1-\kappa^2-\frac{r}{R_0}(1+2\kappa^2-2\kappa^4)\right]I_0(\kappa^2)+\left[1+\frac{2r}{R_0}(3-2\kappa^2)\right]I_2(\kappa^2)+\frac{2r}{3R_0}I_4(\kappa^2)\right.\\&-a\varepsilon\sum_{j=1}^{3}\frac{(-1)^{j+\delta_{j1}}}{2j}\left[(j-1)(2j\Lambda'_j+(j-1)r\Lambda''_j)\sum_{i=0}^{j-1}\sum_{n=1}^{j-1}\frac{(j+n-2)!}{(j-n-1)!}\right.\\&\left.\left.+(j+1)((j-2)\Lambda'_j-r\Lambda''_j)\sum_{i=0}^{j+1}\sum_{n=1}^{j+1}\frac{(j+n)!}{(j-n+1)!}\right](-1)^n\frac{2^{1-\delta_{i0}}}{(2i-1)!!}I_{2i}(\kappa^2)\kappa^{2(n-i)}+O(\varepsilon^2)\right\}\end{aligned} \tag{5}$$

$I_{2i}(\kappa^2)$ $(i=0,..,4)$ are explicitly derived expressions. All we have to do is to insert the derived expressions of the bounce and bounce-averaged precession frequencies into the perturbed distribution function formula. The following exact relation has been obtained (usually $\Omega_\varphi>>\Omega_\theta$)

$$\int d\mathbf{v}\,Mv_\parallel^2 f^1=\sum_{m,n}\left\{\frac{15\sqrt{\pi}}{8}(KT)^{7/2}\left[\alpha_1^{mn}\int_{\Lambda_{\min}}^{\Lambda_{\max}}\left(1-\frac{\Lambda B}{B_{z0}}\right)^{3/2}d\Lambda+\alpha_2^{mn}\int_{\Lambda_{\min}}^{\Lambda_{\max}}\frac{\Lambda B}{B_{z0}}\left(1-\frac{\Lambda B}{B_{z0}}\right)^{1/2}d\Lambda\right]\right. \tag{6}$$

$$+\gamma_1^{mn} KT \int_{\Lambda_{\min}}^{\Lambda_{\max}} \frac{1-\Lambda B/B_{z0}}{(\gamma_2^{mn}\Lambda B/B_{z0})^3}\left[\beta_1^{mn}\left(1-\frac{\Lambda B}{B_{z0}}\right)+\beta_2^{mn}\frac{\Lambda B}{B_{z0}}\right]\left[\bar{\gamma}^2-\bar{\gamma}\,KT\gamma_2^{mn}\frac{\Lambda B}{B_{z0}}+2(KT)^2\left(\gamma_2^{mn}\frac{\Lambda B}{B_{z0}}\right)^2\right]d\Lambda$$

$$-\gamma_1^{mn}\bar{\gamma}^3\int_{\Lambda_{\min}}^{\Lambda_{\max}}\frac{1-\Lambda B/B_{z0}}{(\gamma_2^{mn}\Lambda B/B_{z0})^4}\left[\beta_1^{mn}\left(1-\frac{\Lambda B}{B_{z0}}\right)+\beta_2^{mn}\frac{\Lambda B}{B_{z0}}\right]\lim_{E\to 0}\Gamma\left[0,\frac{1}{KT}\left(\frac{\bar{\gamma}\,B_{z0}}{\gamma_2^{mn}\Lambda B}+E\right)\right]\exp\left(\frac{\bar{\gamma}\,B_{z0}}{KT\gamma_2^{mn}\Lambda B}\right)d\Lambda$$

$$+\gamma\sqrt{KT}\int_{\Lambda_{\min}}^{\Lambda_{\max}}\frac{\sqrt{1-\Lambda B/B_{z0}}}{4(\gamma_2^{mn}\Lambda B/B_{z0})^3}\left[\beta_1^{mn}\left(1-\frac{\Lambda B}{B_{z0}}\right)+\beta_2^{mn}\frac{\Lambda B}{B_{z0}}\right]\left[4\bar{\gamma}^2-2\bar{\gamma}KT\gamma_2^{mn}\frac{\Lambda B}{B_{z0}}+3(KT)^2\left(\gamma_2^{mn}\frac{\Lambda B}{B_{z0}}\right)^2\right]d\Lambda$$

$$-\gamma\bar{\gamma}^{5/2}\pi\int_{\Lambda_{\min}}^{\Lambda_{\max}}\frac{\sqrt{1-\Lambda B/B_{z0}}}{(\gamma_2^{mn}\Lambda B/B_{z0})^{7/2}}\left[\beta_1^{mn}\left(1-\frac{\Lambda B}{B_{z0}}\right)+\beta_2^{mn}\frac{\Lambda B}{B_{z0}}\right]\times\left[1-\mathrm{erf}\left(\sqrt{\frac{\bar{\gamma}\,B_{z0}}{KT\gamma_2^{mn}\Lambda B}}\right)\right]\exp\left(\frac{\bar{\gamma}\,B_{z0}}{KT\gamma_2^{mn}\Lambda B}\right)d\Lambda\Bigg\}$$

$$\times\exp[i(m\theta-n\phi)+\gamma t]$$

where $\bar{\gamma}\equiv\gamma-in\Omega_\varphi$. α_1^{mn}, α_2^{mn}, β_1^{mn}, β_2^{mn}, γ_1^{mn} and γ_2^{mn} are known expressions of ω_b and ω_D. The first term on the right hand side drops out in the $O(\varepsilon^2)$ approximation. The term involving the erf function (difficult to handle) are negligible compared to neighboring terms due to higher values of $|KT\gamma_2^{mn}\Lambda B/B_{z0}|\geq 10^5$, where $\gamma_2^{mn}=-(in/B)\omega_D/\mu$. E is the particle total energy. $\Lambda_{\min}=1/(1+\varepsilon)$ and $\Lambda_{\max}=1/(1-\varepsilon)$. We limit to the $l=0$ bounce case, for a slow plasma toroidal rotation in order to describe the RWM/particle precession drift resonance mechanism. A straightforward calculus leads to the following expression of the perturbed parallel pressure tensor

$$p_\parallel=\sum_{\alpha=e,i}\sum_{m,n}\sum_{s=0}^{1}\sum_{t=0}^{2}\gamma^s(\gamma-in\Omega_\varphi)^t\left[\bar{I}_{st}^{mn}\phi'_{mn}+I_{st}^{mn}\phi_{mn}\right]\exp[i(m\theta-n\phi)+\gamma t] \tag{7}$$

and $\bar{I}_{st}^{mn}$ are exactly derived coefficients, nonlinear in the RWM growth rate, γ. A similar expression is obtained for the perpendicular perturbed pressure tensor

$$p_\perp=\frac{1}{2}\sum_{\alpha=e,i}\int d\mathbf{v}\,M_\alpha v_{\alpha\parallel}^2\frac{\Lambda B/B_{z0}}{1-\Lambda B/B_{z0}}f_\alpha^1 \tag{8}$$

The above expressions for the perturbed pressure tensor components are nonlinear in γ. Inserted into the perturbed plasma moment equation, we finally obtain an exact RWM dispersion relation.

Derivation of the RWM dispersion relation

We start from the perturbed kinetic momentum equation

$$\rho(\gamma-in\Omega_\varphi)\mathbf{v}=-\nabla\cdot\mathbf{p}-\nabla\cdot\Pi+\mathbf{j}\times\mathbf{B}+\mathbf{J}\times\mathbf{b} \tag{9}$$

$\rho(r)$ is the plasma mass density, $\mathbf{\Pi}=-3\eta\,(\mathbf{nn}-\mathbf{I}/3):\nabla\mathbf{v}(\mathbf{nn}-\ddot{\mathbf{I}}/3)$ the perturbed MHD parallel stress tensor, where $\mathbf{v}$ is the fluid velocity parameterized as $\mathbf{v}=(\gamma/B)\nabla\phi\times\mathbf{B}$ [3] and η is the ion viscosity coefficient. $\mathbf{j},\mathbf{J}$ are the perturbed and the equilibrium current densities.

We have already obtained the following system of equations at plasma boundary, $r=a$

$$\sum_{j=0}^{4}\gamma^j\sum_{l=j}^{4}\binom{l}{j}\sum_{h=m-3}^{m+3}(-in\Omega_\varphi)^{l-j}\left(P_{h,n,h-m}^{l}\,\phi_{hn}+\tilde{P}_{h,n,h-m}^{l}\,\phi'_{hn}\right)=0 \tag{10}$$

$P^{l}_{h,n,h-m}$, $\widetilde{P}^{l}_{h,n,h-m}$ are derived coefficients depending on the plasma boundary parameters taken into account: ρ, parallel ion viscosity η, speed of sound c_s, plasma safety factor q, plasma shear s, Δ, E, T and its "radial" flux derivative Δ', E', T'. A similar system of equations has been obtained from the Laplace equation in vacuum and from the surrounding feedback system circuit equations, at $r = a$

$$\sum_{j=0}^{2} \gamma^{j} \sum_{h,k} \left(F^{j,h,k}_{m,n} \, \phi_{hk} + \widetilde{F}^{j,h,k}_{m,n} \, \phi'_{hk} \right) = 0 \tag{11}$$

A thin toroidally inhomogeneous resistive wall and an active system consisting of a number of rectangular, radially thin coils and detectors centred at the same local coordinates have been considered [4]. $F^{j,h,k}_{m,n}$ and $\widetilde{F}^{j,h,k}_{m,n}$ are analytically derived coefficients as functions of all the feedback parameters. The coefficients $P^{l}_{h,n,h-m}$, $\widetilde{P}^{l}_{h,n,h-m}$, $F^{j,h,k}_{m,n}$, $\widetilde{F}^{j,h,k}_{m,n}$ of the above system of equations do not depend on the RWM growth rate γ, when the scalar perturbed pressure is considered only . Therefore the zero determinant condition is equivalent to a simple polynomial equation (in γ) to be solved. If the $p_{\parallel}, p_{\perp}$ terms are considered and the kinetic effects are taken into account, the above coefficients depend on γ. The zero determinant condition provides a complicated nonlinear equation to be solved.

As long as the toroidal plasma rotation Ω_{φ} is not very low, the remaining powerful nonlinear term (incomplete gamma function) from the particle species perturbed kinetic pressure (6) are negligible compared to the rest of the polynomial terms in γ. At very slow plasma rotation, the incomplete gamma function term significantly increases when the RWM frequency and the particle toroidal precession frequency resonate. The kinetic effects prevail and the dissipative process stabilizes the RWM. When the RWM resonance approaches the particle precession resonance, we can approximate $\Gamma[0, x] \approx \bar{\gamma} + \log(x) - x + x^2/4 + \vartheta(x^3) \approx \log(x), x \to 0$, where $\bar{\gamma}$ is the Euler gamma constant. Using equations (10) and (11), after inserting the perturbed kinetic pressure terms contributions, we have analytically derived the following RWM dispersion relation

$$\sum_{k=0}^{6L} \gamma^{k} \sum_{\substack{l_1,..l_{2L}=1 \\ distinct}}^{2L} \operatorname{sgn}(l_1,..,l_{2L}) \sum_{\substack{\alpha_1,..\alpha_{2L}=0 \\ \alpha_1+...+\alpha_{2L}=k}}^{4} \prod_{s=1}^{2L} \Gamma^{l_s}_{s\alpha_s} = 0 \tag{12}$$

If the kinetic contributions are considered, the above $\Gamma^{l_s}_{s\alpha_s}$ coefficients depend on γ and the above equation is no more a pure γ-polynomial equation. sgn is the sign of the permutation and L depends on the number of the poloidal and toroidal modes taken into account [4].

The plasma parameters are the HBT-EP type tokamak parameters: $a = 0.15m$, $R_0 = 0.92m$, $q_0 = 1.3$, $q_a = 2.95$, $B_{z0} = 0.35T$, $\rho_a = 6 \cdot 10^{-9}\, kg/m^3$. $\tau_A = (R_0 / B_{z0})\sqrt{\mu_0 \rho_a} \approx 2 \cdot 10^{-7}\, s$ is the Alfven time at plasma boundary. If no kinetic effect is considered, the (3,1) RWM expected behavior is shown in Figure 1.

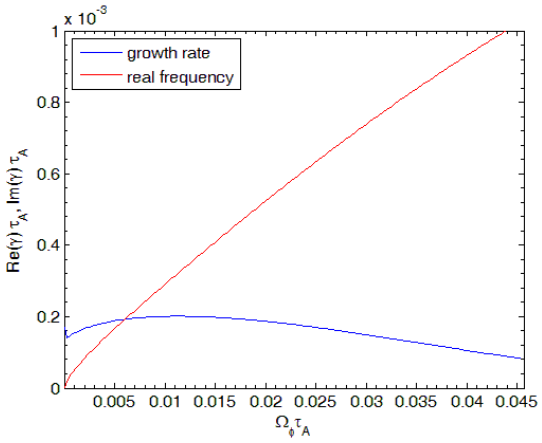

Figure 1

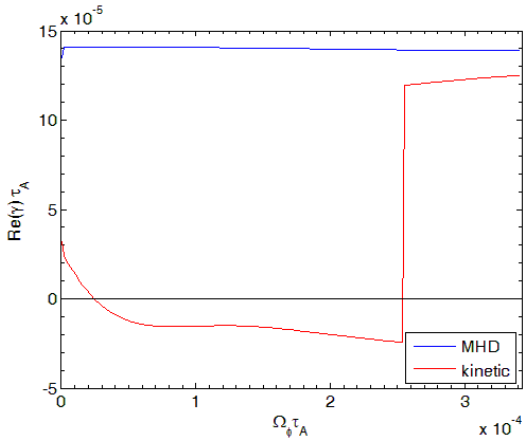

Figure 2

With the increase of the plasma rotation, the RWM real growth rate starts to decrease due to the dissipative effect of the perturbed parallel MHD stress tensor. The real frequency of the mode increases, but is significantly lower compared to the plasma rotation frequency. The fluid versus the kinetic RWM behavior is plotted in Figure 2. It can be seen that the resonance between the RWM real frequency and the trapped particles bounce-averaged precession frequency stabilizes the mode at very slow plasma rotation. As the plasma rotation becomes higher, the above kinetic effects damp, the RWM becomes unstable and the kinetic tends to resemble the fluid behavior. The RWM growth rate is plotted versus the slow toroidal plasma angular velocity for different values of the feedback system parameters, in f0igures below. To make an analytic approach possible, all figures below are drawn in the vicinity of the RWM/particle precession resonance approximation, not valid at higher levels of plasma rotation.

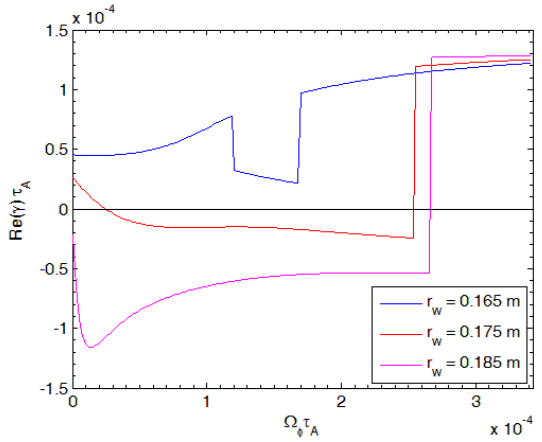

Figure 3

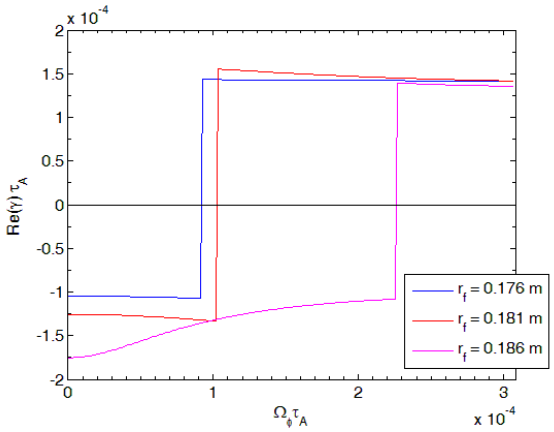

Figure 4

The RWM growth rate is shown is Figure 3 for different radial flux coordinates of the resistive wall. A higher r_w means a stronger RWM stabilization and a wider stability window. The same situation is observed in Figure 4, at different radial flux coordinates of the active feedback coils, r_f .

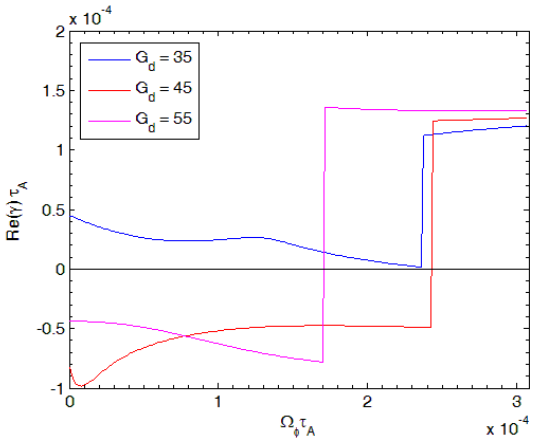

Figure 5

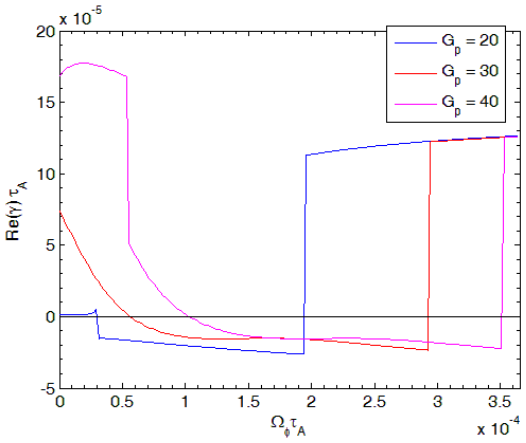

Figure 6

The influence of the feedback amplification gains are showed in Figures 5 and 6. The increase of the derivative gain G_d makes the RWM more stable, but no monotonic behavior is observed concerning the width of the stability window. It seems that an optimum finite derivative gain is to be found. On the other hand, the proportional gain does not influence the stability amplitude of the RWM, but the width of the stability window. A higher G_p means a wider RWM stability window (Figure 6). The plasma shaping parameters influence on the RWM real growth rate can be seen in the next figures. The positive plasma boundary ellipticity corresponds to a higher mode stabilization whereas the zero ellipticity corresponds to a wider stability window (Figure 7). Figure 8 shows that a higher triangularity indicates a slightly stronger RWM stabilization. The stability window is practically unchanged.

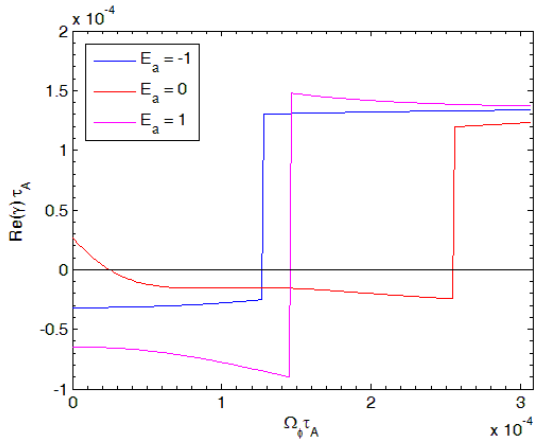

Figure 7

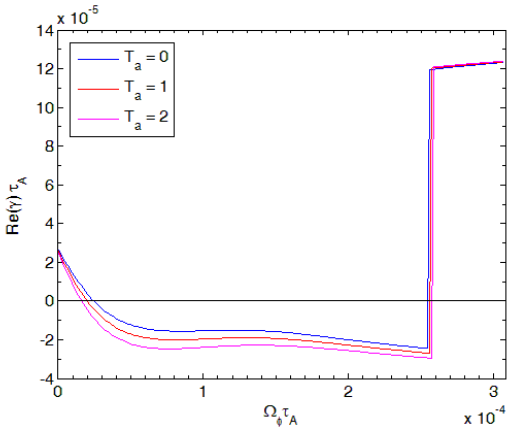

Figure 8

To summarize, it can be stated that a more distant resistive wall or feedback coils increases the kinetic effects and the width of the perturbation stability window. A higher proportional amplification factor also increases the stability window width. Whereas a higher ellipticity provides a higher RWM stability amplitude, a more regular plasma boundary shape extends the RWM stability window. At least according to the present model, it seems that the plasma boundary triangularity has little influence on the RWM stability in the RWM/trapped particle precession frequencies resonance regime.

Conclusion

A semianalytic model describing the kinetic phenomena involving the RWM and the trapped particles bounce-averaged precession frequencies resonance has been derived. A new RWM dispersion relation including the kinetic effects at very slow plasma rotation has been obtained. It has been proved the stabilization of the RWM at very slow plasma rotation when the RWM real frequency resonates with the toroidal precession particle drift frequency. The influence of the feedback system and plasma shaping parameters on the RWM stabilization has been evaluated. This model could be a handy tool to find better RWM stability conditions when the kinetic effects are considered. No huge numerical codes are needed.

References

[1] F. Porcelli, R. Stankiewicz and W. Kerner, Phys. Plasmas 1 (1994) 470.

[2] Y.I. Kolesnichenko, R.B. White and Y.V. Yakovenko, Phys. Plasmas 10 (2003) 1449.

[3] R. Fitzpatrick and J. Bialek, Phys. Plasmas 13 (2006) 072512.

[4] I.G. Miron, Plasma Phys. Control. Fusion 50 (2008) 095003.

NONLINEAR EFFECTS OF THE E×B DRIFT ON TRANSPORT AND STRUCTURE GENERATION IN TURBULENT PLASMAS

M. Vlad, F. Spineanu

National Institute of Laser Plasma and Radiation Physics

[BS_14/WP12-IPH-A05-1-11/BS]

Abstract

The objectives for 2012 of the studies dedicated to the complex topic of transport and structure generation in turbulent plasma are:

1. *Test particle approach applied to the analysis of the characteristics of multi-scale turbulence and transport*
2. *Effects of trapping on the evolution of drift type turbulence beyond quasilinear stage*

The first objective represents our contribution to EFDA Programme ITER Physics WP12-IPH under the contract WP12-IPH-A05-1-11/BS.

1) Test particle approach applied to the analysis of the characteristics of multi-scale turbulence and transport

Electron energy transport was studied in the frame of test particle approach with the aim of determining the regimes of transport. The model was developed by introducing a realistic description of the turbulence, with spectrum and Eulerian correlation similar with the results of the numerical simulations. This special shape of the Eulerian correlation of the drift type turbulence has strong effects on the electron diffusion regimes, which are different of those obtained for a simple decaying correlation. We have shown that a rich class of anomalous regimes appears when particle trapping is statistically significant. The condition concerns the combined action of the decorrelation mechanisms, which has to be weak enough. We have shown that regimes with high electron energy transport (of the order of the experimental one) appear in two-scale turbulence (ITG and ETG type) and we have determined the conditions for these regimes. These results were presented in papers presented at two important conferences (a), (b). Transport in magnetic turbulence was studied in (c).

2) Effects of trapping on the evolution of drift type turbulence beyond quasilinear stage

Recent results obtained in other contracts have shown the existence of a strong connection between ion stochastic trapping and the evolution of drift turbulence in the strongly nonlinear regime. This conclusion was drawn from the study of test modes on idealized turbulent plasma (with constant confining magnetic field). A first development of these results was presented in (d). We have extended this study to a system that is relevant for tokamak plasmas, the trapped electron modes (TEM). We have shown that ion trapping generates zonal flow modes and the nonlinear attenuation of the TEM turbulence.

a) M. Vlad, *Multi-scale turbulence and electron heat transport*, EPS Conference on Plasma Physics / International Congres on Plasma Physics 2012, Stockholm, P2-025.

b) M. Vlad, F. Spineanu, *Test particle study of multi-scale turbulent transport*, 17th Joint EU-US Transport Task Force Meeting in combination with the 4th EFDA Transport Topical Group Meeting, 3-6 September 2012, Padova, Italy.

c) M. Vlad, F. Spineanu, *Charged particle transport in 3-dimensional stochastic magnetic fields*, EPS Conference on Plasma Physics / International Congress on Plasma Physics 2012, Stockholm, O4.407.

d) M. Vlad, F. Spineanu, *Nonlinear evolution of drift turbulence: inverse cascade, zonal flows, intermittency*, O4-416, 38th EPS Conference on Plasma Physics, Strasbourg, 27 June -1st July 2011

Detailed results

1. Test particle approach applied to the analysis of the characteristics of multi-scale turbulence and transport

A theoretical study of electron heat transport based on test particle approach is developed. Test particle approach means essentially to consider a given turbulence (described by a known spectrum or Eulerian correlation). The heat transport coefficient is evaluated using the "test particle expression", as time integral of the Lagrangian velocity correlation (LVC) or as derivative of electron mean square displacement. The LVC has to be determined for given Eulerian correlation (EC) of the fluctuating potential. The LVC determines the time dependent diffusion coefficient and it is also a measure of the statistical memory of the stochastic motion. A close agreement between the diffusion coefficient obtained from the flux of temperature fluctuations and the test particle diffusion coefficient exists if there is space-time scale separation between temperature fluctuations and average. Numerical simulations confirm this property [1, 2].

The transport coefficients for a realistic model of the EC, which includes the existence of large scale potential fluctuations, is obtained. This approach is in some sense independent and complementary to the self-consistent simulations. It can determine the regimes of transport as functions of turbulence statistical parameters, not as function of the gradients.

The diffusion coefficients are determined using a semi-analytical method, the decorrelation trajectory method [2, 3]. The latter is based on a set of smooth trajectories determined by the Eulerian correlation of the turbulence.

1.1 Turbulence model

Low frequency turbulence (ITG, TEP, ETG) is characterized by similar shape of the spectrum. It has two (symmetrical) maxima in the poloidal wave number $k_\theta = \pm k_0$ and zero amplitude around $k_\theta=0$. The main difference consists in the typical wave numbers: $k_\theta\rho_i<1$ for ITG, $k_\theta\rho_i\sim1$ for TEP and $k_\theta\rho_e\sim1$ for ETG. The Eulerian correlation (EC) corresponding to these spectrum has zero integral in the poloidal direction with negative domains and sometimes oscillatory behaviour determined by the dominant wave number. Also, the potential drifts with the diamagnetic velocity V_* (of electron or of ions, depending on the type of turbulence). A simple model of the EC with these properties that also includes anisotropy is

$$E(x,y,z,t)=A\exp\left(-\frac{x^2}{2\lambda_x^{\,2}}-\frac{|z|}{\lambda_z}-\frac{t}{\tau_1}\right)\frac{\partial}{\partial y}\left[\exp\left(-\frac{(y-V_*t)^2}{2\lambda_y^{\,2}}\right)\frac{\sin\left[k_0(y-V_*t)\right]}{k_0}\right] \qquad (1)$$

where A is the amplitude of potential fluctuations, k_0 is of the order of $1/\lambda_y$, $\tau_{1\,is}$ the correlation time and λ_i are the correlation lengths. We have considered a multi-scale spectrum of the stochastic potential, modelled by the superposition of two functions (1), one with small correlation lengths λ_{xl}, λ_{yl} and the other with much larger correlation lengths λ_{xL}, λ_{yL}. The subscripts L for the large scale and l for the small scale were introduced in the parameters. We have previously shown that the transport does not strongly depend on the details of the EC and thus this simplified model is adequate for determining the transport regimes. The model is rather complex and contains 12 parameters that describe the turbulence plus the diamagnetic velocity V_* and the parallel velocity v_z. The potential motion with the diamagnetic velocity, electron parallel motion and the time variation

of the potential represents decorrelation (detrapping) mechanisms which hinder electron motion on the contour lines of the potential.

The diffusion regimes are analyzed and the conditions when they appear are identified. A rich class of anomalous diffusion regimes appears when trajectory trapping is effective, i.e. when the combined action of the decorrelation mechanisms is weak enough. Trapping influences not only the values of the diffusion coefficients but also their scaling laws. We have shown that it is possible to obtain transport coefficients that are completely different of the sum of the transport coefficients produced separately by the large scale turbulence and respectively small scale turbulence even when the spectrum is composed by two well separated parts. We have investigated three physically relevant domains. First domain corresponds to electron heat transport in small scale turbulence. This is an important step, which permitted to evaluate the importance of electron trapping or eddying in the ETG type turbulence. We have shown that this effect can appear and that in these conditions the transport is strongly modified. The second study evaluates the influence of the large scale stochastic potential on electron heat transport. We have shown that the transport coefficient can strongly increase due to the combined action of the small and large scale turbulence. The third study evaluates the effects of small scale turbulence on ion transport.

1.2. Electron transport in ETG type turbulence

The results obtained for the special EC (1) are different from those for a decaying EC in the quasilinear case when there is no trapping. The differences appear in the poloidal transport coefficient, which has reversed dependence on the characteristic decorrelation time τ_d compared with a normal (decaying) EC. The diffusivity decreases with the increase of τ_d and the transport becomes sub diffusive in the limit of infinite τ_d (no decorrelation). On the contrary, in the nonlinear regime characterized by the existence of trajectory trapping, the poloidal transport is super diffusive if there is no decorrelation and for weak decorrelation (large τ_d) the diffusion coefficients are large and have linear dependence on τ_d. The cause of this behavior is the rotation of the turbulence with the diamagnetic velocity. The poloidal transport means actually the transport along the average velocity of the potential. This component of transport does not affect electron heat loss, but it provides (as shown below) the mechanism of interaction with the large scale potential fluctuations.

The radial transport is strongly reduced due to potential rotation and also due to trapping, which contribute to the limitation of electron radial excursions. Turbulence rotation with V_* is equivalent with an average potential xV_*, which modifies the contour lines of the potential and reduces their radial extension and trapping keeps electron on the contour lines.

1.3. Effects of the large scale turbulence on the electron transport

Essentially, the large scale determines local average velocities V_L, which are randomly oriented in different regions. Their influence on electron heat transport depends on the ratio of the average velocity V_L and the amplitude of the electric drift produced by the small scale stochastic potential V_l.

When $V_L > V_l$ there is no small scale electron trapping and V_L determines a decorrelation mechanism. The local transport coefficients depend on the value of V_L and also on its orientation. The average on the large scale of the local transport coefficients (essentially the average over the orientation of the large scale velocity) leads to a global radial diffusion coefficient, which is in most cases a decreasing function of V_L.

When $V_L < V_l$ and the other decorrelation mechanisms are very weak, electron trajectory small scale trapping is effective. In this case, V_L determines a strong modification of the diffusion, which becomes non-isotropic with the diffusion coefficient along the V_L much larger than in the perpendicular direction. This increased diffusion is produced by the splitting of the probability of electron displacements in two parts, one remaining at the initial radial position and the other moving radially with an average velocity V_r. The stationary part accounts for trapped trajectories and the moving one for the free electrons, which have V_r larger than the radial component of $\mathbf{V}_L$ such as to maintain the Eulerian flux.

The above results are obtain for $V_*=0$. In the presence of poloidal rotation velocity, the transport becomes much more complicated due to the contribution of V_* to the decorrelation from both small and large scale potential. Large variations of the diffusion coefficient appear for small changes of the parameters, which are not easy to understand. The anisotropy of the turbulence also influences the electron heat diffusion. Due to the complexity of the model and to the large number of parameters clear transport regimes appear only in particular conditions.

1.4. Effects of the small scale turbulence on ion transport

Essentially, the contribution of the small scale can be represented as a collisional process with the diffusion coefficient D_l determined by the decorrelation process induced by the large scale velocity. Due to the gyro average of the small scale, D_l is much smaller than ion diffusion produced by the large scale potential. However, in the nonlinear condition when ion large scale trapping is important, D_l determines a strong increase of the ion effective diffusion with a value that is much larger than D_l.

1.5. Conclusions

The main conclusion of this work is that the electron heat transport in multi-scale turbulence can be much larger that in small scale turbulence. The physical process responsible for increased transport is electron trajectory trapping combined with the existence of a large scale velocity. Our results show that the transport processes in two-scale turbulence are complex and that strong nonlinear effects appear in the presence of trapping. They suggest that simple well defined scaling in the global parameters of the plasma and extrapolations cannot be obtained. These results represent the first theoretical (semi-analytical) evaluation of the electron transport in multiple scale turbulence. Our test particle approach brings a complementary contribution to the understanding of the complex processes of electron transport, which is mainly obtained from large scale numerical simulations.

2. Effects of trapping on the evolution of drift type turbulence beyond quasilinear stage

We study linear modes on turbulent plasma with the statistical characteristics of the potential considered known. Trapped electron modes (TEP) in hot magnetized plasmas are considered. Analytical expressions are derived, which approximate the growth rates and the frequencies of the test modes as functions of the characteristics of the background turbulence. They provide an image of turbulence evolution.

We show that there is a sequence of processes, which appear at different stages of evolution as transitory effects and that the turbulence has an oscillatory (intermittent) evolution. A different perspective on important aspects of the physics of drift type turbulence in the strongly non-linear regime is deduced. The main role in these processes is shown to be played by ion trapping.
The electron response is approximately the same in quiescent plasmas because actually they do not

"see" the turbulence due to the fast decorrelation produced by the motion along the magnetic field.

The ion response is influenced by finite Larmor radius effects. Their response to potential perturbation depends on the background turbulence.
The approximate operator for derivation along ion trajectories is

$$O^i \equiv \partial_t - \frac{\nabla\phi\times\mathbf{b}}{B}\cdot\nabla$$

and the equation for the distribution function is

$$O^i f^i + f^i \nabla\cdot\mathbf{u}_p = 0$$

The distribution

$$f_0^i = n_0(x)F_M^i\left(1+\frac{e\phi(\mathbf{x}-\mathbf{V}_{*e}t)}{T_e}\right)$$

represents the approximate equilibrium because $O^i f_0^i = 0$ and the term $\nabla\cdot\mathbf{u}_p << 1$ is of the order $(\omega/\Omega_i)(k_\perp^2\phi/B) = (\omega/\Omega_i)Vk_\perp$. The divergence has the dimension of t^{-1} and it introduces a characteristic time, which is of the order $\tau_p = (\Omega_i/\omega)(Vk_\perp)^{-1} = (\Omega_i/\omega)\tau_{fl}$ thus very large, much larger than the time of flight. It means that for time much smaller than this the remaining term is negligible and the ion distribution function can be approximated by the above equation.

Perturbing the potential with $\delta\phi$, the operator is perturbed by $\delta O^i = -\nabla\delta\phi\times\mathbf{e}_z/B\cdot\nabla$ and a change of the distribution function appears $f^i = f_0^i + h$. The linearized equation in this perturbation is

$$(O^i+\delta O^i)(f_0^i+h)+(f_0^i+h)\nabla\cdot(\mathbf{u}_p+\delta\mathbf{u}_p)=0$$
$$O^i h+\delta O^i f_0^i + h\nabla\cdot\mathbf{u}_p + f_0^i\nabla\cdot\delta\mathbf{u}_p = 0$$

Since the background potential remains small compared with the kinetic energy $e\phi/T_e << 1$, the equilibrium distribution function in the second and fourth term can be approximated by $n_0(x)F_M^i$

$$O^i h + h\nabla\cdot\mathbf{u}_p = -in_0(x)F_M^i\frac{e\delta\phi}{T_e}\left(k_y V_{*e} - \omega\rho_s^2 k_\perp^2\right)$$

This equation shows that the right side term is the same as for quiescent plasmas. The effects of the background potential appear in the trajectories (in the operator of derivation along trajectories) and in the second term which accounts for the divergence of the polarization drift produced by the turbulence. The formal solution is

$$h(\mathbf{x},v,t) = -n_0(x)F_M^i\frac{e\delta\phi}{T_e}\left(k_y V_{*e} - \omega\rho_s^2 k_\perp^2\right)\Pi^i$$

where the propagator is

$$\Pi^i = i\int_{-\infty}^{t} d\tau\exp\left[i\mathbf{k}\cdot(\mathbf{x}(\tau)-\mathbf{x})-i\omega(\tau-t)\right]\exp\left[-\int_\tau^t\nabla\cdot\mathbf{u}_p(\mathbf{x}(\tau'))d\tau'\right]$$

and the integrals are along ion trajectories obtained from

$$\frac{d\mathbf{x}}{d\tau} = -\frac{\nabla\phi(\mathbf{x}-\mathbf{V}_{*e}t)\times\mathbf{e}_z}{B}, \qquad \mathbf{x}(t;\mathbf{x}) = \mathbf{x}$$

The ion response (the propagator) is averaged over the stochastic trajectories

$$\overline{\Pi}^i = i\int_{-\infty}^{t} d\tau\, M(\tau,t)\exp\left[-i\omega(\tau-t)\right]$$

where M is the average over the stochastic trajectories in the background potential

$$M(\tau,t) \equiv \left\langle \exp\left[i\mathbf{k}\cdot\left(\mathbf{x}(\tau)-\mathbf{x}\right) + \frac{m_i}{eB^2}\int_{\tau}^{t} d\tau' \partial_{\tau'}\Delta\phi\left(\mathbf{x}(\tau')\right)\right]\right\rangle$$

The ion density is

$$\delta n^i(\mathbf{x},v,t) = -n_0(x)\frac{e\delta\phi}{T_e}\left(k_y V_{*e} - \omega\rho_s^2 k_\perp^2\right)\overline{\Pi}^i$$

The distribution of displacements strongly depends on the ordering of the characteristic tines of the stochastic process. The motion of the potential with the diamagnetic velocity defines the diamagnetic time $\tau_{*e} = \lambda_y / V_{*e}$. The change of the shape of the potential has as characteristic time the correlation time $\tau_c = \gamma^{-1}$. The time of flight (or eddy time) is the decorrelation time by the $\mathbf{E}\times\mathbf{B}$ motion, defined by $\tau_{fl} = \tau_{flx} = V_x/\lambda_x = \beta/B\lambda_x\lambda_y = \tau_{fly}$, and it has the same value for the two directions even for non-isotropic turbulence.

The term determined by the compressibility can be written as

$$C = \rho_s^2 \frac{1}{B}\frac{\partial_x n_0}{n_0}\int_{\tau}^{t} d\tau' \partial_y \Delta\phi\left(\mathbf{x}(\tau')\right).$$

where we have used

$$V_{*e} = -\frac{T_e\partial_x n_0}{|e|Bn_0} = \frac{T_e}{\Omega_i m_i L_n} = \frac{c_s^2}{\Omega_i L_n} = \Omega_i\rho_s^2\frac{1}{L_n} = c_s\frac{\rho_s}{L_n}$$

The average that has to be determined is

$$M = \left\langle \exp\left[i\mathbf{k}\cdot\left(\mathbf{x}(\tau)-\mathbf{x}\right) + a\int_{\tau}^{t} d\tau' \partial_y \Delta\phi\left(\mathbf{x}(\tau')\right)\right]\right\rangle$$

where, after normalizing the potential with its amplitude β and the distances with λ_x, λ_y, the constant is

$$a = \rho_s^2\frac{\partial_x n_0}{n_0}\frac{1}{B}\frac{\beta}{\lambda_\perp^2\lambda_y}$$

$$C \cong -\frac{\rho_s^2}{\lambda_\perp^2}\frac{\lambda_x}{L_n}\frac{1}{\tau_{flx}}$$

$\tau_{flx}^{-1} = V_x/\lambda_x = \left(\beta/B\lambda_y\right)/\lambda_x$ is the inverse of the flight time in the x direction. τ_{flx} is chosen to normalize the time (in the integral) and the dimensionless parameter of the compressibility factor is

$$a = \frac{\rho_s^2}{\lambda_\perp^2}\frac{\lambda_x}{L_n} << 1.$$

The properties of the compressibility term are:

- Its average is zero.
- The correlation with the displacements could be non-zero. It is non-zero in the initial point $\mathbf{x}$ because an average of the type $\left\langle v_i \partial_y \Delta\phi \right\rangle$ contains four derivatives of the potential EC. Actually, only the average $\left\langle v_x \partial_y \Delta\phi \right\rangle \neq 0$ because it contains even number of derivatives for both directions (the other component has one derivative three times and the other one time).
- We note that there is no problem due to the high order of derivation that appears in the compressibility term. It does not mean that this term is important only for large k. This is because the derivatives apply on the EC of the background potential, not on the mode potential.

The propagator was evaluated using the decorrelation trajectory method and the nested subensemble approach [3, 4]. More details about these methods and on their applications for the study of test particle statistics and of passive fields stochastic advection can be found in [5-8]. We have started from the Eulerian correlation of the potential that results from the growth rates of the TEM

$$E(x,y,z,t) = A\exp\left(-\frac{x^2}{2\lambda_x{}^2} - \frac{|z|}{\lambda_z} - \frac{t}{\tau_1}\right)\frac{\partial}{\partial y}\left[\exp\left(-\frac{(y-V_* t)^2}{2\lambda_y{}^2}\right)\frac{\sin\left[k_0(y-V_* t)\right]}{k_0}\right].$$

Its shape is actually similar to all the types of drift turbulence, and only the parameters are different for ITG, TEM or drift turbulence. We note this shape of the EC leads to diffusion coefficients that are different from those obtained in [5] for the case of a stochastic potential with decaying EC. In particular, the poloidal diffusion coefficient in the quasilinear regime is much smaller than that in Ref. [5]. This ensures the development of the turbulence to the nonlinear regime characterized by ion stochastic trapping on eddying motion.

Preliminary results show that:

- the diffusive damping of Dupree type [9], which appears in the initial stage of turbulence evolution, is rather weak and allows the development of the TEM turbulence in the nonlinear regime characterized by ion trapping or eddying;
- the ion flows produced by ion trapping in the moving potential determine two parallel effects: nonlinear damping of TEM and generation of zonal flow modes;
- there is time correlation between the maximum growth rate of zonal flow modes and the damping of the drift modes, as observed in experiments and in the numerical simulations.

These preliminary results will be developed in 2013. The conclusion at the present stage of the study is that the nonlinear process that determines the evolution of TEP turbulence is similar with the process appearing in the case of drift turbulence [10-11]. The main role is played by ion stochastic trapping or eddying, which combined with the motion of the potential with the diamagnetic velocity generates ion flows. The onset of turbulence is strongly dependent on the toroidal geometry, but the nonlinear saturation appears to be essentially a local process in drift type turbulence.

References

[1] Bassu R., Jessen T., Naulin V., Rasmusses J. J., Phys. Plasmas 10 (2003) 2696.
[2] [Hauff T., Jenko F., Phys. Plasmas 14 (2007) 092301.
[3] Vlad M., Spineanu F., Misguich J.H., Balescu R., Phys. Rev. E 58 (1998) 7359.
[4] Vlad M. and Spineanu F., Phys. Rev. E 70 (2004) 056304.
[5] M. Vlad, et al., Plasma Physics and Controlled Fusion **46,** 1051 (2004).
[6] M. Vlad, F. Spineanu, S. Benkadda, Physical Reviews Letters 96 (2006) 085001.
[7] M. Vlad, F. Spineanu, S. Benkadda, Physics of Plasmas **15** (2008) 032306.
[8] M. Vlad, F. Spineanu, S. Benkadda, Plasma Physics Controlled Fusion **50** (2008) 065007.
[9] T. H. Dupree, Phys. Fluids 15 (1972) 334.
[10] M. Vlad, F. Spineanu, "Nonlinear evolution of drift turbulence: inverse cascade, zonal flows, intermittency", Romanian Journal of Physics **56** Supplement (2011) 23-29.
[11] M. Vlad, "Trajectory trapping and the evolution of drift turbulence beyond the quasilinear stage", electronic paper arXiv: 1209.2083 [physics.plasm-ph] (29pp) (2012).

ATOMIC DATA FOR PLASMA SPECTROSCOPY: RADIATIVE AND COLLISIONAL DATA FOR LIGHT ELEMENT ATOMS AND THEIR IONS

V. Stancalie, V. F. Pais, A. Stancalie, A. Mihailescu

INFLPR, Lasers Department

[BS_4B/WP12-ITM-AMNS-ACT1; BS_4B/WP12-ITM-AMNS-ACT2]

Abstract

The aim of this project is to contribute with accurate atomic data to the AMNS data bases. The present theoretical work reports results from fairly extensive non-relativistic and relativistic calculations for the electron collision with neutral carbon and progress in the development of documentation for *AMNS* codes (WP11**-ITM-AMNS-ACT1 and WP11-ITM-AMNS-ACT2)**.

We have attempted to obtain an accurate description of electron correlations both in the initial and final states. The *R*-matrix method is used to calculate collision strengths and cross sections for low energy inelastic scattering of electrons by this atomic system. In summary, we have investigated the importance of including configuration interaction wave functions both in the target-state expansion and in the (N+1)-electron quadratically integrable function expansion. The electron correlation effects were explored by carrying out separate calculations with and without the configurations: $2s2p^3$, $2s2p2nl$ (n=3,4), $2p^4$ in the target state expansion, and $2s^22p^3$, $2s2p^4$, $2s2p3nl$ (n =3,4) in the (N+1)-electron wave function.

The results for fine-structure energy levels, the term splitting, and the wave-functions composition are calculated with the extended average level (EAL) multi-configurational Dirac-Fock (MCDF) method in the general-purpose relativistic atomic structure package (GRASP), while for collision calculation we have used the *D*irac-*A*tomic *R*-matrix code.

Partial dataset is archived in the Atomic, Molecular, Nuclear and Surface (AMNS) database (http://www.efda-itm.eu).

Papers

[1] V. Stancalie, V.F. Pais, A. Mihailescu , *"Fine-structure splitting calculation in the Ar III ion: comparison of perturbative (Breit-Pauli) and non-perturbative (MCDF-EAL) predictions",* Eur. Phys. J.D: 66-Art ID 84(2012)1-15

Conferences

[1] A. Stancalie, A. Matea, A. Mihailescu, V. F. Pais, V. Stancalie, *"Atomic collisions in plasma transport modeling of the laser-produced Cu plasma in air and in vacuum"*, 39th EPS Conference on Plasma Physics, 2-6 July 2012, Stockholm, Sweden.

[2] V.F. Pais and ITM-TF contributors, *"New single sign-on mechanism for EFDA Integrated Tokamak Modelling Task Force portal",* 39th EPS Conference on Plasma Physics, 2-6 July 2012, Stockholm, Sweden.

[3] V. F. Pais, A. Stancalie, A. Mihailescu, V. Stancalie, *"Accessing physics data using web services"*, International Conference on optics, Micro-to-Nano-Photonics III, ROMOPTO, September 3-6, 2012, Bucharest, Romania.

[4] A. Stancalie, S. Ciobanu, V.F. Pais, A. Mihailescu, V. Stancalie, *"Escape factors approximation in radiation-transfer codes",* International Conference on optics, Micro-to-Nano-Photonics III, ROMOPTO, September 3-6, 2012, Bucharest, Romania.

Reports

[1] V. Stancalie, The low-energy inelastic scattering of electron by atomic systems, Annual report of the Coordinated Research Project on “Light Element Atom, Molecule and Radical Behaviour in the Divertor Plasma Regions” from 23 to 25 May 2011 at the IAEA Headquarters in Vienna.

Introduction

The aim of this project is to contribute with accurate atomic data to the AMNS data bases which are foreseen to be used for the next generation of plasma experiments taking place at ITER and JET. This document presents results obtained during 2012, from semi-relativistic and relativistic calculations of atomic data for carbon atoms and further reports on the progress in the development of documentation for *AMNS* codes. These objectives were accordingly to the **WP11-ITM-AMNS-ACT1 and WP11-ITM-AMNS-ACT2** tasks.

For fusion related interests, carbon is an appealing element due to the fact that it serves as a diagnostic tool for physical conditions, such as density and temperature. The main populating and depopulating mechanisms of the excited energy levels of ions in divertor and edge plasmas with densities < 10^{23} – 10^{24} are electron collisional excitation of the ion's ground state and radiative decay, respectively, with the majority of electron population being in the ground state of the ionization stage. Electron collisional ionization is predominantly expected to take place from one ground state to that of the next higher ionization stage. As neutral, singly ionized C^+ or in molecular compounds, carbon serves as a diagnostic tool for density and temperature in fusion plasma device. Data for electron-impact excitation of C^{2+} have been used at the EFDA-JET fusion experiment to model impurity inflow into the edge plasma from the surface with which the plasma interacts. Charge-exchange process of carbon ions with hydrogen atoms also provides a useful plasma diagnostics. A detailed knowledge of carbon transport properties, and consequently of accurate cross-section data, are required. However, the difficulties in obtaining sufficient quantities of atomic carbon in a well-defined initial state have resulted in the complete absence of experimental cross-section measurements. This absence of experimental data made theoretical investigations a computational grand challenge.

This requires an accurate knowledge of its transport properties, hence accurate knowledge of its atomic cross-section data. The available information on electron-impact excitation of carbon in the literature is rather limited, thus a reliable assessment of the data accuracy being impossible.

To begin with, the electron-impact excitation cross sections have been evaluated in different ways. Methods of calculation have increased in complexity. In neutral carbon the calculation is made more difficult by the fact that low-energy electron scattering is dominated by a resonance due to the $1s^2 2s^2 2p^3\ {}^3P^0$ state of the negative ion, C^-. The theoretical prediction of the location of this resonance, and of the $1s^2 2s^2 2p^3\ {}^4S^0$ and ${}^2D^0$ bound states of C^-, depends on a balance between short-range correlation and long range polarization effects.

The ground-state configuration of carbon in the independent-particle model is $(1s)^2(2s)^2(2p)^2$, which leads to the ground-state terms ${}^3P$, ${}^1D$, ${}^1S$. In order to get reliable data, the wave functions of the N-electron target state and of the negative ionic states that have N+1electrons should be calculated with the same degree of accuracy. In the calculation of low-energy electron scattering by neutral carbon atoms must take into account long-range polarization effects and short –range correlation between the incident electron and the electron attachment effects that lead to scattering resonances. The early theoretical methods applied to low-electron energy scattering from atomic carbon could be summarized as follows: *a*) The polarized-orbital method [1, 2] uses single configuration which treats target-atom dipole polarizability and the resulting long-range polarization potential accurately, but involves approximations to the short-range interaction that are difficult to evaluate. The polarized-orbital method cannot describe resonances; *b*) The close-coupling method

[3,4] which is capable, in principle, of representing the full structure of the electronic continuum wave functions through a series of expansion in the stationary sates of the target atom. Elaborate calculation including some target correlation effects and a limited pseudostate representation of target polarizability has also been reported [5,6]; *c*) The matrix variational method including configuration interaction approximation (CI) that takes into account the effect of near-degenerate configuration interaction [7-9]. The major innovation in this method is that LS eigenfunctions are used through the calculations, but does not describe resonances.

All these calculations were limited in elastic scattering from ground states and transitions amongst the *n* =2 states at low collision energies. In the last two decades the most cited works have been reported by Dunseath *et al*. [10], Zatsarinny *et al*. [11] and Liu, Wang and Zhou [12]. Their predictions show significant discrepancies for cross sections with those reported by Dunseath et al. There are differences up to a factor of 2 in the absolute scale, while the energy dependence of the excitation functions is similar. The work has reported cross sections for important transitions from the ground state $2p^2\ ^3P$, and the metastable $2p^2\ ^1D$ and ^1S states. The largest differences were found for transitions of the form $1s^22s^22p^2 – 1s^22s2p^3$, which are dominant in the calculation by Zatsarinny *et al* [11]. For spin forbidden transitions, there is good agreement for the relatively strong transition $1s^22s^22p^2(^1D) – 1s^22s2p^3(^3D)$ whereas large differences are found for the transitions from the $1s^22s^22p^2(^1S)$ state.

We conclude this introductory survey by mentioning that in these works a) all cross sections agree well in shape, b) large discrepancies in magnitude exist among all these calculations: Dunseath's results is 32% higher than the calculation of *B* –spline R-matrix method, and the results of CCO method are 18% lower than the calculation of *B* –spline R-matrix method. Suno and Kato [13] review the available data for all ionization stages of carbon.

Detailed calculation and results

In the present work we report results from a new set of calculation. We propose here to investigate the role of including configuration interaction (CI) wave functions both in the target state expansion and in the (N+1)-electron quadratically integrable function expansion. Target –atom states were computed using the Hartree-Fock ground configuration $2s^22p^2$ plus the near-degenerate configurations $2s2p^3$ and $2p^4$. In addition, for consistency with the virtual excitation pattern used for scattering wave functions, all virtual excitations of $2s^22p^2$ of the form 2p-np and 2p-nf were included. Results for the levels energy and radiative transition probability for important transitions have been obtained. The process we seek to study is:

$$e + C(1s^2 2s^2 2p^2) \rightarrow C^-(1s^2 2s^2 2p^3, 1s^2 2s2p^4) \rightarrow C(1s^2 2s^2 2p^2, 1s^2 2s2p^3, 1s^2 2p^4) + e \qquad (1)$$

The electron correlation effects are explored by carrying out separate calculations with and without the configurations: $2s2p^3$, $2s2p^2nl$ (*n* =3,4), $2p^4$ in the target state expansion, and $2s^22p^3$, $2s2p^4$, $2s2p^3nl$ (*n* =3,4) in the (N+1)-electron wave function. For this set of calculation the RMATXI with FARM code [14, 15] in the external region is used. The (N+1)-electron configurations data have been obtained by adding one electron to the N-electron configurations in all possible way. This wave function was augmented by including all configurations arising from virtual excitation of a 2p orbital.

We reproduce from [10] in Figure 1 the complexity of atomic states included into the calculation for neutral carbon.

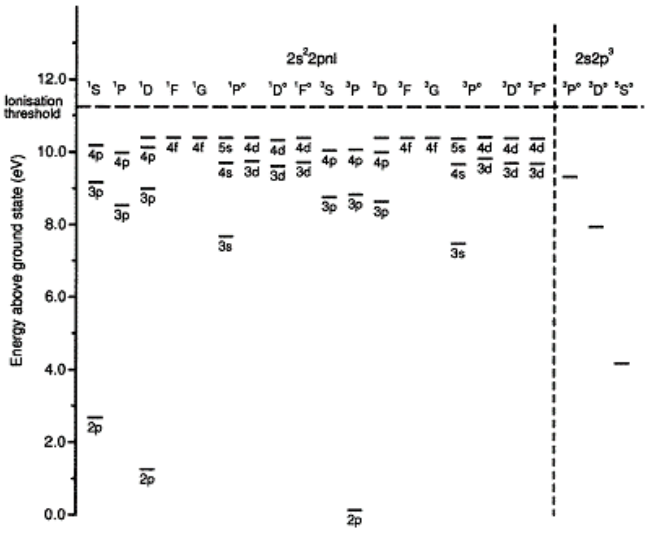

Figure 1

Exploratory calculations indicated that further 2s virtual excitations could be neglected. Our results are in satisfactory agreement with the calculation of Dunseath *et al* [10] for transition involving the $2s2p^3$ states, whereas for the $2s^22p3l$ states are closer to those reported by Zatsarinny *et al* [11].

Table 1 presents our calculated values and comparison with the earlier theoretical works. The calculated values are compared with the available experimental data in Atomic Structure Database of the National Institute for Standards and Technology wherever available (NIST) [16]. The agreement between the calculated and the experimental data is reasonably good, the energy difference average percentage of the low-lying levels usually agreeing to within 2 % of each other.

Table 1 - Excitation energies (in eV) for the spectroscopic target states. The results are compared with experimental energy splittings and those obtained by other theoretical works.

	State	Term	Present	Ref.[10]	Ref.[11]	NIST [16]
1	$2s^22p^2$	^3P	0.00	0.00	0.00	0.00
2	$2s^22p^2$	^1D	1.557	1.545	1.353	1.260
3	$2s^22p^2$	^1S	2.602	2.545	2.833	2.680
4	$2s2p^3$	$^5S^0$	3.092	3.133	4.069	4.179
5	$2s^22p3s$	$^3P^0$	7.401	8.488	7.488	7.481
6	$2s^22p3s$	$^1P^0$	7.740	8.936	7.727	7.680
7	$2s2p^3$	$^3D^0$	8.340	8.412	8.082	7.942
8	$2s^22p3p$	^1P	8.451	9.456	8.528	8.534
9	$2s^22p3p$	^3D	8.600	9.589	8.647	8.642
10	$2s^22p3p$	^3S	8.772	9.785	8.737	8.767
11	$2s^22p3p$	^3P	9.309	10.390	8.822	8.845
12	$2s^22p3p$	^1D	9.443	10.757	9.012	8.998
13	$2s^22p3p$	^1S	10.424	11.370	9.256	9.168
14	$2s2p^3$	$^3P^0$	9.517	9.981	9.504	9.326
15	$2s^22p3d$	$^1D^0$	9.772	10.719	9.647	9.627
16	$2s^22p4s$	$^3P^0$	10.142	10.810	9.708	9.683
17	$2s^22p4s$	$^1P^0$	9.549	10.834	9.708	9.709
18	$2s^22p3d$	$^3F^0$	9.517	10.809	9.729	9.695
19	$2s^22p3d$	$^3D^0$	9.607	10.888	9.731	9.705
20	$2s^22p3d$	$^1F^0$	9.607	10.947	9.759	9.732
21	$2s^22p3d$	$^1P^0$	9.653	10.970	9.782	9.758
22	$2s^22p3d$	$^3P^0$	13.407	11.018	9.983	9.830
23	$2s2p^3$	$^1D^0$	14.470	14.645	12.984	12.132
24	$2s2p^3$	$^3S^0$	13.407	15.366	13.273	13.114
25	$2s2p^3$	$^1P^0$	15.927	16.182	14.949	14.860
26	$2p^4$	^3P	19.361	21.149	19.986	
27	$2p^4$	^1D	19.621	22.677	20.877	
28	$2p^4$	^1S	20.479	26.227	24.389	

Our results are in satisfactory agreement with the calculation of Dunseath *et al* [10] for transition involving the $2s2p^3$ states, whereas for the $2s^22p3l$ states are closer to those reported by Zatsarinny *et al* [11]. The oscillator strengths are very important to obtain reliable absolute values for cross sections and rates. Table 2 presents our calculated values and comparison with the earlier works.

Table 2 - Oscillator strengths in C

Lower level	Upper level	Present	Ref.[10]	Ref.[11]	NIST[16]
$2s^22p^2\ ^3P$	$2s^22p3s\ ^3P^0$	0.124	0.154	0.133	0.140
	$2s2p^3\ ^3D^0$	0.098	0.152	0.107	0.072
	$2s2p^3\ ^3P^0$	0.028	0.117	0.055	0.063
	$2s^22p4s\ ^3P^0$	0.023	0.010	0.009	0.021
	$2s^22p3d\ ^3D^0$	0.112	0.132	0.107	0.094
	$2s^22p3d\ ^3P^0$	0.340	0.069	0.098	0.040
	$2s2p^3\ ^3S^0$	0.171	0.269	0.134	0.152
$2s^22p^2\ ^1D$	$2s^22p3s\ ^1P^0$	0.128	0.103	0.118	0.118
	$2s^22p3d\ ^1D^0$	0.009	0.007	0.013	0.013
	$2s^22p4s\ ^1P^0$	0.004	0.010	0.004	0.011
	$2s^22p3d\ ^1F^0$	0.061	0.099	0.118	0.085
	$2s^22p3d\ ^1P^0$	0.018	0.014	0.011	0.009
	$2s2p^3\ ^1D^0$	0.344	0.529	0.396	
	$2s2p^3\ ^1P^0$	0.351	0.333	0.257	
$2s^22p^2\ ^1S$	$2s^22p3s\ ^1P^0$	0.021	0.076	0.098	0.094
	$2s^22p4s\ ^1P^0$	0.007	0.001	0.004	0.005
	$2s^22p3d\ ^1P^0$	0.050	0.142	0.196	0.125
	$2s2p^3\ ^1P^0$	0.122	0.633	0.458	

In Figure 2 we compare and contrast the collision strengths as output from two different *LS* calculations where the terms arising from the $1s^22s^22pnl$ manifolds, and those arising from $1s^22s^22pnl$ and $2s2p^3$ and $2p^4$ manifolds are, respectively, included into the *R*-matrix expansion.

In calculating electron excitation rates for light atom elements it is usually possible to neglect the energy splitting of the fine structure levels as the splitting corresponds to temperatures much less than the electron temperature in the plasma. For carbon atom the $^3P_0 - {}^3P_2$ energy splitting, for example, is 62.5 K, which is comparable to electron temperature found in cool regions of the fusion devices. Under these circumstances it is important to include fine-structure calculation in the present study. We have performed full relativistic calculation. The flexible atomic code (FAC) [17] is adopted for calculating data although GRASP (general-purpose relativistic atomic structure package [18] has also been used for making comparisons. Starting with previously obtained data on this system (an R-matrix calculation in *LS* coupling) we initiated a detailed study of fine structure splitting using perturbative (Breit-Pauli) [19, 20] and non perturbative (Full relativistic) Dirac calculations [21, 22].

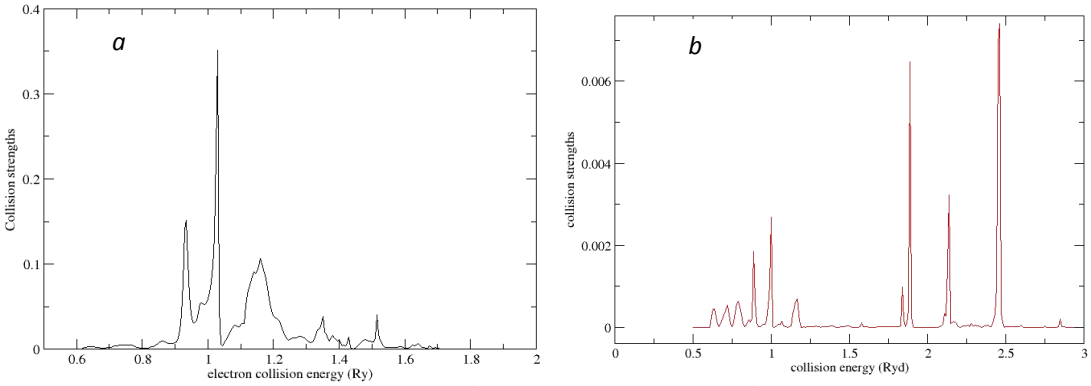

Figure 2 - Collision strengths for the first ^3P -^1D transition for the $^4P^0$ symmetry; a) the only configurations arising from $1s^2 2s^2 2pnl$ manifolds are included into the R-matrix expansion; b) all configurations arising from the $1s^2 2s^2 2pnl$ and $2s2p^3$ and $2p^4$ manifolds are included into the R-matrix expansion

The results for fine-structure energy levels, the term splitting, and the wave-functions composition are calculated with the extended average level (EAL) multi-configurational Dirac-Fock (MCDF) method in the general-purpose relativistic atomic structure package (GRASP), while for collision calculation we have used the *D*irac-*A*tomic *R*-matrix code. The calculated values are compared with the available experimental data in Atomic Structure Database of the National Institute for Standards and Technology wherever available. The following three model-calculation have been developed:

Calculation A. The energies have been computed for all levels of the $1s^2 2s^2 2p^2$ configuration state function. A total of 170 angular coefficients have been calculated. The levels energy (including zero-order (Coulomb) contribution, first-order (Breit) contribution, and quantum electrodynamics (QED) contribution), radiative transition probabilities and oscillator strengths for the lowest 5 fine structure levels have been obtained with the GRASP code.

Calculation B. Energies have been computed for all levels of $1s^2 2s^2 2p^2$, $1s^2 2s^2 2p3s$, $1s^2 2s^2 2p3p$, $1s^2 2s^2 2p3d$, $1s^2 2s2p^3$ configuration state functions. This type of calculation gives a set of 9 bound orbitals which is optimized over all the levels included. The resulting 9 relativistic orbitals produced 41 $J\pi$ levels with total $0< J < 4$, odd and even parity, all of which are to be used in close-coupling expansion.

Calculation C. Energies have been computed for all levels of $1s^2 2s^2 2p^2$, $1s^2 2s2p^3$, $1s^2 2p^4$ non-relativistic configuration state functions. The resulting 4 relativistic orbitals produced 20 $J\pi$ levels with total $0< J < 3$, odd and even parity, all of which are to be used in close-coupling expansion.
Calculation D. Energy levels, radiative transition probabilities and oscillator strengths have been obtained for all levels of $1s^2 2s^2 2p^2$, $1s^2 2s^2 2p3s$, $1s^2 2s^2 2p3p$, $1s^2 2s^2 2p3d$, $1s^2 2s2p^3$ and $1s^2 2p^4$ non-relativistic configurations. The number of relativistic configuration state functions is of 36 with a total angular momentum $0 < J < 4$.

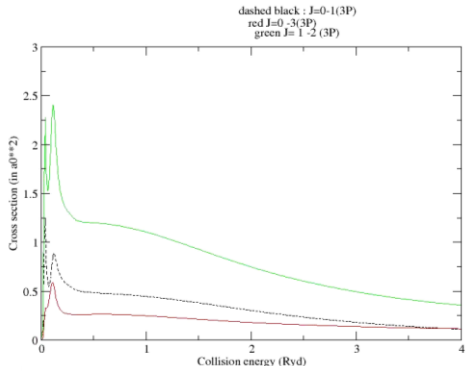

Figure3 - Plot of cross sections (in a_0^2) versus collision energy (in Ryd) for electron impact excitation of transitions between the fine structure levels belonging to ^3P ground configuration (dashed black J = 0 - 1(^3P), red J = 0 – 3(^3P), green J= 1- 2(^3P). Calculation is performed in the target model Calculation A.

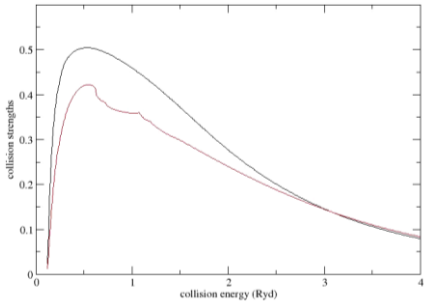

Figure 4 - Collision strengths for $^3P_0$ - $^1D_2$ with (red) and without (black) $2p^4$

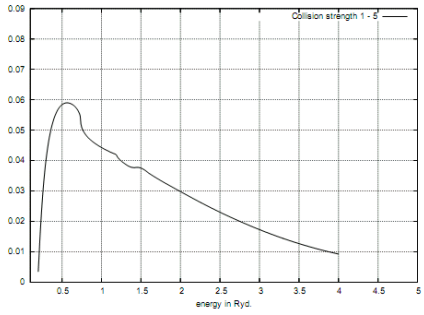

Figure 5 - Collision strengths for $^3P_0$- ^1S transition

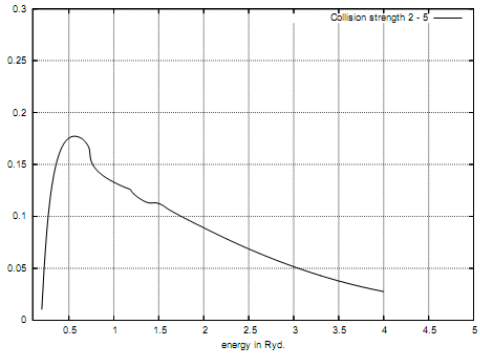

Figure 6 - Collision strengths for ^1D - ^1S transition

Conclusions

In summary, we have investigated the importance of including configuration interaction wave functions both in the target-state expansion and in the (N+1)-electron quadratically integrable function. Electron correlation effects were explored by carrying out separate calculations with and without the configurations: $2s2p^3$, $2s2p2nl$ (n=3, 4), $2p^4$ in the target state expansion, and $2s^22p^3$, $2s2p^4$, $2s2p3nl$ (n =3,4) in the (N+1)-electron wave function. The three $1s^22s2p^3$ states lie just above the first ionization threshold and they were included due to their strong coupling with the $1s^22s^22p^2$ states. Finally, the expansion also contains the three doubly excited $1s^22p^4$ with still higher excitation energies. However, relatively poor agreement between the theoretical and experimental excitation energies, which generally differ by 1eV for the n = 3 and higher states, raises the question of the accuracy of the reported data. Furthermore, some resonance structure have been observed in our calculated cross section at lower energies and a detailed study requires more accurate target wave functions that those used until now.

Fine-structure calculation has been started out. We used the extended average level (EAL) multiconfigurational Dirac-Fock (MCDF) method including quantum electrodynamics effects (QED) in the general-purpose relativistic atomic structure package (GRASP), while for determining the collision strengths the Dirac Atomic R-matrix Code (DARC) was used. We have calculated cross sections between 0.0001 and 0.62 Ryd. This work is in progress.

Partial dataset is archived in the Atomic, Molecular, Nuclear and Surface (AMNS) database.

References:

[1] A. Temkin, Phys. Rev. **107**, 1004(1957).
[2] R.J. Henry, Phys. Rev. **172**, 99(1968).
[3] P.G. Burke and K. Smith, Rev. Mod. Phys. **34**, 458(1962)
[4] P.G. Burke and M. J. Seaton, Methods Comput. Phys. **10**, 1(1971)
[5] H.E. seraph, J. Phys. B. **6**, L243(1973).
[6] S.P. Rountree, E.R. Smith and R.J.W. Henry, J. Phys. B. **7**, L167(1974).
[7] L.D. Thomas, R. S. Oberoi and R.K.Nesbet, Phys. Rev. A **10**, 1605(1974);
[8] L.D. Thomas and R. K. Nesbet, Phys. Rev. A **11**, 170(1975).
[9] L.D. Thomas and R. K. Nesbet , Phys. Rev. A **12**, 2369(1975).
[10] K. M. Dunseath et. al., J. Phys.B : At. Mol. Opt. Phys **30**, (1997), 277
[11] O. Zatsarinny, K. Bartschat et. al. Phys Rev A **71,** (2005), 042702.
[12] J. Liu, Y. Wang and Y Zhou, J. Phys. B: At. Mol. Opt. Phys. **39**, 86(2006)
[13] H. Suno and T. Kato, At. Data & Nucl. Data Tables **92**, 407(2006).
[14] P. G. Burke, "*R-Matrix theory of atomic collision, Springer Series on Atomic, Optical and Plasma Physics"* **61**, Springer Heidelberg Dordrecht London New-York (2011).
[15] V.M. Burke and C. J. Nobles, Comput. Phys. Commun. **85**, 471(1995).
[16] http://www.nist.gov
[17] M.F. Gu, Can. J. Phys. **86**, 675 (2008)
[18] P.H. Norrington and I. P. Grant, J. Phys.B : At. Mol. Opt. Phys **20**, 4869 (1987).
[19] N.S. Scott and P.G. Burke, J. Phys. B **13**, (1980), 4299.
[20] N.S. Scott and K.T. Taylor, Comput. Phys. Commun. **25**, (1982), 347.
[21] J.J. Chang, J. Phys.B : At. Mol. Opt. Phys **8**, (1975), 2327.
[22] I. P. Grant, J. Phys.B : At. Mol. Opt. Phys **41**, (2008), 055002.

MAINTAIN AND EXTEND THE ITM PORTAL

V. Stancalie, V. F. Pais, A. Mihailescu, A. Stancalie

INFLPR, Lasers Department

[BS_4A/WP12-ITM-ISIP-ACT2-01/MEdC/PS]

Abstract

The ITM-TF has a main objective to provide the European fusion community with a validated suite of simulation tools for ITER exploitation. It is envisaged that the ITM will offer the basis for a complete simulation environment for fusion plasmas. These tools must allow modelling on current devices and come in support of theory and modelling in general.

The ITM Portal acts as an interface between users and the various tools available on the ITM Gateway. The previous stage of the project involved the replacement of the existing single sign on mechanism with a new one developed to better suit the ITM needs. During the first part of 2012, the present project implemented and adjusted the existent single sign on solution in order to accommodate new applications and to offer faster response times. The new system had to include the possibility of using multiple authentication sources. This is related to the fact that previously only users with an ITM Gateway account were able to access any ITM resources. However, in recent years some special accounts were needed for limited access to tools such as subversion. Since these users do not possess a machine account, there must be a separate authentication and authorization system available, integrated with web based applications.

During the second part of 2012, our work was focused on developing the „ITM Catalogue" tool. The catalogue is a centralized database, fed at the end of a simulation workflow, to archive major parameters of a simulation. The catalogue is available to users for searching through available data. Apart from work related to the ITM Catalogue, in the second part of this year, work has been carried out to update and maintain the existing ITM web applications, including GFORGE and TWIKI. Furthermore, work has started on implementing a software release system for the ITM software. This is a new application, integrated in the ITM Portal, capable of offering software packages to be downloaded by external users, not necessarily members of ITM.

Papers

[1] V. Stancalie, V. F. Pais, A. Mihailescu, *"Fine-structure splitting calculation in the Ar III ion: comparison of perturbative (Breit-Pauli) and non-perturbative (MCDF-EAL) predictions",* THE EUROPEAN PHYSICAL JOURNAL D - ATOMIC, MOLECULAR, OPTICAL AND PLASMA PHYSICS 66-3(2012)84

Conferences

[1] A. Stancalie, A. Matea, A. Mihailescu, V. F. Pais, V. Stancalie, *"Atomic collisions in plasma transport modeling of the laser-produced Cu plasma in air and in vacuum"*,39th EPS Conference on Plasma Physics, 2-6 July 2012, Stockholm, Sweden.

[2] V. F. Pais and ITM-TF contributors, *"New single sign-on mechanism for EFDA Integrated Tokamak Modelling Task Force portal",* 39th EPS Conference on Plasma Physics, 2-6 July 2012, Stockholm, Sweden.

[3] V. F. Pais, A. Stancalie, A. Mihailescu, V. Stancalie, *"Accessing physics data using web services"*, International Conference on optics, Micro-to-Nano-Photonics III, ROMOPTO, September 3-6, 2012, Bucharest, Romania.

[4] A. Stancalie, S. Ciobanu, V.F. Pais, A. Mihailescu, V. Stancalie, *"Escape factors approximation in radiation-transfer codes",* International Conference on optics, Micro-to-Nano-Photonics III, ROMOPTO, September 3-6, 2012, Bucharest, Romania.

Detailed results

The longer term goal of the ITM-TF is to provide the European fusion community with a validated suite of simulation tools for ITER exploitation and to provide the basis for a complete simulation environment for fusion plasmas generally available for use. These tools must allow modelling on current devices and come in support of theory and modelling in general. IMPs have dual responsibilities in that they should continue to develop and manifest the physics foundations for Integrated Modelling in standalone packages, targeting the code platform environment while they are also supporting the integration efforts towards scenario modelling tools.

The ITM Portal acts as an interface between users and the various tools available on the ITM Gateway. This means that the portal has to be very responding to user requests. This translates into a very small time for processing the request and generating a response. During the previous stage of the project, the existing single sign on mechanism was replaced with a new one developed to better suit the ITM needs. The overall architecture of the portal is in accordance with the user requirements and thus it was kept. This architecture is illustrated in Figure 1 below.

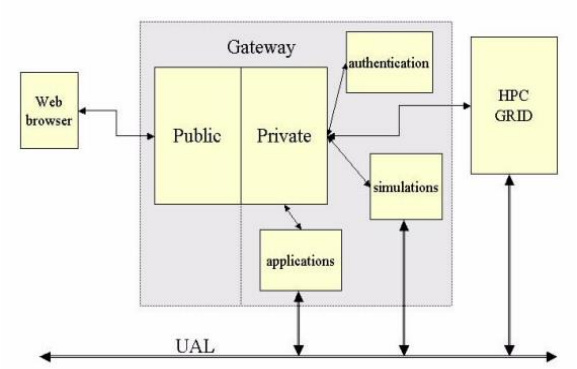

Figure 1 - ITM Portal architecture

During the first part of 2012, the single sign on solution had to be adjusted to accommodate new applications and to offer faster response times. The new system had to include the possibility of using multiple authentication sources. This is related to the fact that previously only users with an ITM Gateway account were able to access any ITM resources. However, in recent years some special accounts were needed for limited access to tools such as subversion. Since these users do not possess a machine account, there must be a separate authentication and authorization system available, integrated with web based applications.

As the systems needed to be as simple as possible, without any additional requirements on the operating system, it was decided to implement it purely in PHP. The internal structure is similar to that of any single sign-on mechanism: one identity provider and several service providers.

The identity provider (IdP) is in charge of authenticating the client and retrieving its access rights. Due to the requirement of having multiple user databases, a priority list was used to make sure machine accounts are given priority over external user accounts. The IdP is the only component actually accessing the user databases. Any other components are in direct communication with the IdP whenever authentication or authorization is required.

The service provider (SP) is installed locally on each server providing access to web applications. It is a PHP script with a configuration file, also in PHP format, that must be placed either in the root

directory of the web application or in the root directory of the web folder. This way there is no file required outside of the web directory and no modification to be made to the server's configuration. Furthermore, there is no dependency on a certain PHP version, since only the most basic features are being used, thus making it compatible with older versions. When a user tries to access a certain resource, access is intercepted by the SP script and the configuration file is checked. If the resource being accessed is deemed to be restricted, the user is redirected to the IdP for authentication. After a successful logon, the user is sent back to the SP and access rights are received from the IdP using a back-channel. This means that sensitive data never gets to the user's browser, since a direct communication channel is used between SP and IdP. The SP now sets a session cookie and caches the data received from the IdP in a special directory on the server. Once the user tries to access another protected resource on the same SP, it already knows who the user is and if it has the right to access it or not. For applications aware of single sign on technologies, the SP sets the REMOTE_USER environment variable. This is a standard way of letting the applications know who is accessing them. This way, it was possible to migrate existing applications to the new system with no modifications, since the same variable was being used with Shibboleth. Even more, the SP sets another variable to the groups the user belongs to, thus making this information available to applications, and allowing to easily develop more tight integrations without actually using any of the single sign on provided functionality.

Using the fact that all the ITM applications are in the same administrative domain, only on different servers, and are quite limited in number, it was possible to implement a central logout mechanism. This can be called from any application by redirecting the user to a logout page on the IdP. This in turn will redirect the user to all the service providers each one being allowed to completely cleanup all the session data. Of course, this implementation would not have been possible in a federated environment with a large number of service providers. However, given the size of the ITM environment it works very well and completely removes any potential security related problems introduced by session cookies remaining in the user browser. The logout feature completely destroys the session data on the user computer. This is particularly useful in secure environments. Furthermore, by integrating multiple authentication sources, the system is well suited to be used in environments with a mix of internal and external users. Even more, being written completely in PHP with no external dependencies, the system is independent of the operating system used or its update level, as long as it provides support for PHP and Apache web server. The current architecture of the ITM portal looks accordingly to Figure 2.

The Wiki component was installed during the first part of 2012 and it is based on TWiki. It had to be adapted in order to be integrated with the single sign-on component and to be presented as a page inside the portal. This made it become more user friendly and appears as part of the ITM Portal.

Furthermore, during the same period, the integration of the Profile Maker component was initiated. This is a special kind of application, requiring direct access to the user's files inside the ITM Gateway cluster. Therefore, special consideration was given to how the authentication and authorization systems specific to web pages are integrated with those specific to the cluster. Even more, since the user's profile must be loaded and available for the application, a special connection had to exist to the servers. An approach leading to establishing secure connections from the Portal to the cluster front-end nodes was taken into consideration. This causes the application to run as if started by the user on an interactive session. Of course, this imposes several security related challenges.

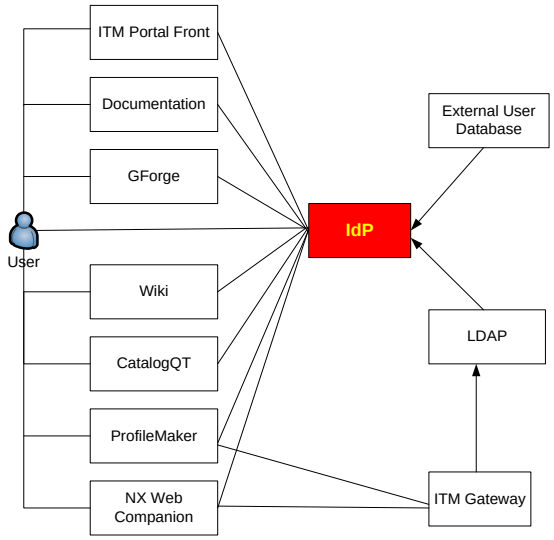

Figure 2 - Current architecture of the ITM portal

A proof of concept implementation was launched and integrated in the Portal, available for a restricted number of users, including the developers of the Profile Maker tool.

Several issues were detected, related to memory and processor usage on the front-end nodes when the application is started in this way. Nevertheless, it shows that it is possible to simulate an interactive session from the portal and run inside the user context. Therefore a refinement of the implemented proof of concept was required.

During the second part of 2012, our work was focused on developing the „ITM Catalogue" tool. The catalogue is a centralized database, fed at the end of a simulation workflow, to archive major parameters of a simulation. The catalogue is accessible by the End user, either for data access or administration of the system. Modification or creation of a catalogue entry can be done either by the GUI access (user interface) or a simulation, but in the both cases using the High Level API (warranty a coherent data management).

The architecture for the catalogue system consists of:

- Catalogue population
  - scheduler & update process
  - field derivation
    - standard transformations
    - user transformations via plugin
- High-level API
- Catalogue Service Tools
- User interface

The database feeding regroups the High Level API and the Catalogue update process, as shown in Figure 3.

A user API based on a Web Services architecture warranties an universal access whatever the source (Kepler or other platforms, codes using different languages, user interface). Logs and parameters tables can be hosted on Catalogue DB. A simulation (workflow, Fortran program, data import

script…) does not directly update the catalogue, but instead notifies the catalogue system about the physics data it created or changed. The catalogue system does then asynchronously create or update the corresponding entries. The list of variables/fields to be added in the Catalog is not directly specified in the simulation, but depends on the type of the simulation workflow. To each simulation model corresponds a list of fields to be generated; this correspondence is described in the Catalog DB.

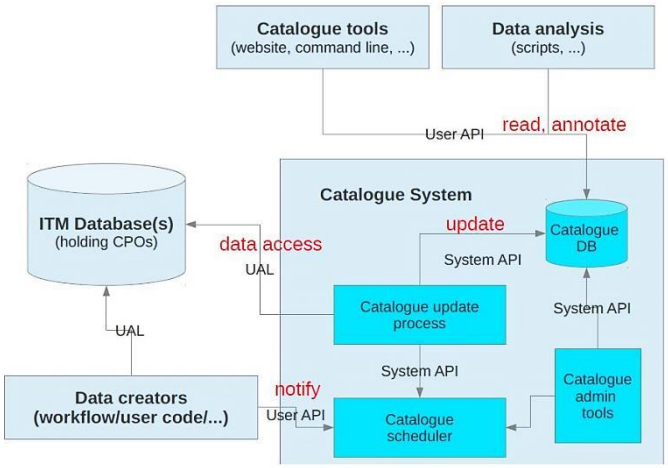

Figure 3 - ITM Database feeding

The design of the ITM Catalogue Database was an iterative process, involving all the people contributing to the task. The result was the following database structure in Figure 4.

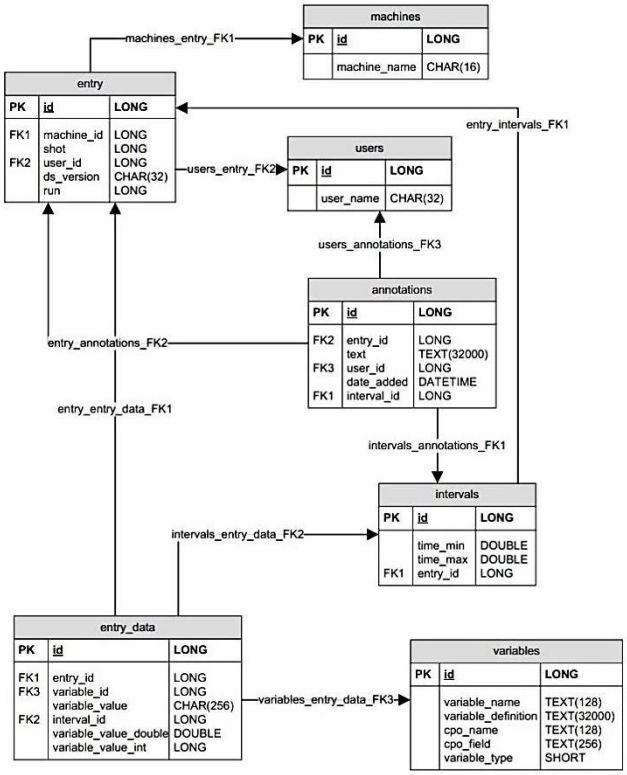

Figure 4 - Database structure

This structure covers the various aspects of storing simulation results inside the database. It can accommodate discrete values, mean values on intervals, integer/double/string variables. Furthermore, data is structured and various queries are possible, based on machine, shot number, run number, user id and variable values. Even more, comments can be added to entries or data, in the form of user provided annotations. This information can clarify aspects related to the context of running the corresponding simulation or any additional data that can be of use to the user accessing the simulation result.

Complementing the database design is a web service based interface, allowing access to data. It is intended for this web service interface to be the only access point to the underlying database. Thus, access control mechanisms could be implemented at this level. Also, it becomes possible to change the database structure in the future, if needed, without interfering with the existing applications.

The following web service methods have been implemented, offering the required catalogue functionality as depicted in Table 1.

Table 1 - Web service methods used for the interface that complements the data base

1. getUsers

Input:

None

Output:

List of all users that provided data in the catalogue

2. getMachines

Input:

None

Output:

List of all the machines for which there is data available in the catalogue

3. search

Input:

- entry_id – if this information is present, the other inputs are ignored
- user – user that produced the data
- machine – associated machine
- shot – associated shot number
- run – associated run number
- page – page number to return
- page_size – size of a page
- value_filter – expression used for searching only specified values
- detail_level - Can be any combination of the following (using a binary OR operation): 1=data;2=entry annotations

Some or all of these parameters may be empty

Output:

List of catalogue entries corresponding to the specified search criteria, containing:

- entry_id
- machine
- shot
- run
- user
- ds_version
- annotations_number

- annotations_id
- annotations_text
- annotations_users

4. getEntryDetails

Input:

- entry_id
- detail_level: Can be any combination of the following (using a binary OR operation):1=data (cpo_name/field; variable_name/def/val/type);2=intervals;4=interval annotations

Output:

List of associated entry data:

- cpo_name
- cpo_field
- variable_name
- variable_definition
- variable_value
- variable_type
- time
- time_min
- time_max
- variable_average
- annotations_number
- annotations_id
- annotations_text
- annotations_users

Some of these values may be empty, depending on data available in the database

This information is complemented by the entry_id and associated metadata obtained using the search method above.

5. addVariable

Input:

- variable_name
- variable_definition
- cpo_name
- cpo_field
- variable_type = 0-STRING Variable, 1-INTEGER variable, 2-FLOATING POINT variable

Output:

- variable_id

This method should be called prior to adding EntryData. It would either return the id of an existing variable or add a new entry for it. Matching will be performed on all fields.

6. addEntry

Input:

- machine
- username
- shot
- run
- ds_version

Output:

Entry ID (if an entry already exists for the specified data, that ID will be returned; otherwise a new entry will be created)

7. addEntryData

Input:

- entry_id
- variable_id
- variable_value
- time_min
- time_max

Output:

A boolean status will be returned indicating success or failure of inserting the new data. A failure can be caused by the database (insufficient space or database corruption) or by invalid variable_value according to its datatype (as indicated by variable_type).

8. addAnnotationToEntry

Input:

- entry_id
- text
- username

Output:

- annotation_id

9. addAnnotationToInterval

Input:

- entry_id
- time_min
- time_max
- text
- username

Output:

- annotation_id

The database with the web service implementation offers a skeleton implementation of the ITM Catalogue tool. Further development is needed in order to integrate it in applications and to add additional functionality.

The intended further developments include:

- enhanced security mechanisms
- batch processing, allowing a single web service API call for multiple database entries
- administrative calls, that could allow applications to delete/modify database entries; of course, this could be implemented only after proper security mechanisms are in place
- better user interfaces, allowing queries to be performed easily through the ITM Portal.

Apart from work related to the ITM Catalogue, in the second part of this year, work has been carried out to update and maintain the existing ITM web applications, including GFORGE and TWIKI. Furthermore, work has started on implementing a software release system for the ITM software. This is a new application, integrated in the ITM Portal, capable of offering software packages to be downloaded by external users, not necessarily members of ITM. In this context, it gathers some information about the interested party and constructs one-time download links. As a result, the user can access the ITM released software.

Plasma-Wall Interaction

DEVELOPMENT OF NANO-STRUCTURED W COATINGS AND THE IMPACT OF STRUCTURE ON FUEL RETENTION; EXPERIMENTS ON ARGON OUTGASSING FROM W-COATED ILW TILES

C. Ruset, E. Grigore, I. Munteanu, M. Gherendi

National Institute for Laser, Plasma and Radiation Physics, Bucharest, Romania, Euratom-MEdC Association

[BS_12A/WP12-IPH-A03-1-07; BS_12D/JET]

Abstract

Tungsten coatings of 3 μm, 5 μm, 10 μm, 20 μm and 37 μm were deposited on various substrates (12×15×1mm) made of fine grain graphite, CFC Dunlop DMS 780 and Eurofer using Combined Magnetron Sputtering and Ion Implantation (CMSII) technology. The coatings were exposed to deuterium ECR plasma and then they have been analyzed by Nuclear Reaction Analysis and Thermo Desorption Spectroscopy.

It was found that the deuterium retention in 10 μm W coatings was in the range of $2\text{-}5\cdot10^{21}$ D/m^2 for a fluence of $2.2\cdot10^{25}$ D/m^2. This means about one order of magnitude higher than that of bulk W or that of a 3 μm W coating deposited by conventional magnetron sputtering. This might be in connection with the nano-crystalline structure of the W coatings deposited by CMSII. The influence of the plasma exposure temperature and of the coating thickness on the D retention was investigated as well. The D concentration in the W coating is in the range of 0.2-0.5 at.% and increases at the W-Mo and Mo-Eurofer interfaces.

A new experimental device for plasma exposure and thermo-desorption analysis was designed, built and commissioned. A hollow cathode discharge is used for plasma heating. The maximum temperature was 900°C, but it can be increased up to 1200°C.

No Ar was found in the W coatings deposited by CMSII.

Conferences:

- O.V. Ogorodnikova, C. Ruset, K. Sugiyama, Yu. Gasparyan, V. Efimov, M. Balden, G. Matern, F. Koch, Plasma-induced deuterium retention in tungsten coatings produced by combined magnetron sputtering and ion implantation technique, 20th International Conference on Plasma Surface Interactions 2012, Aachen, Germany, 21. – 25 May 2012

Reports:

- C. Ruset, O.V. Ogorodnicova, Development of nanostructured W coatings and the impact of structure on fuel retention, Technical report, Nov. 2012.

Detailed results

1. Background

Nanostructured tungsten coatings are already extensively used as plasma-facing material for fusion devices. Almost 3,000 CFC and fine grain graphite (FGG) tiles have been W coated by Combined Magnetron Sputtering and Ion Implantation (CMSII) technology for ITER-like wall at JET and for ASDEX Upgrade. During the last five years the research in the field of W coatings for fusion applications was mainly focused on the thermo-mechanical properties of the coatings, particularly on their resistance to high heat fluxes ($T_{max} \leq 2{,}000$ °C).). The information concerning the deuterium retention for this type of coatings is quite limited. This subject is particular important taking into account the D-T experimental campaign which is foreseen at JET in 2015.

2. Objectives of the project

The aim of this project was studying the fuel retention in W coatings with different structures in comparison with bulk W. The main goals were:

- Investigation of the influence of the coating characteristics (thickness, structure, etc.) on the D retention.
- Determination of the impact of the substrate material (carbon-based and also Eurofer) on D retention in the coating.

3. Results and discussions

3.1. Deposition and characterization of W coatings

Tungsten coatings of 3 μm, 5 μm, 10 μm, 20 μm and 37 μm were deposited on various substrates (12×15×1mm) made of fine grain graphite, CFC Dunlop DMS 780 and Eurofer using CMSII technology.

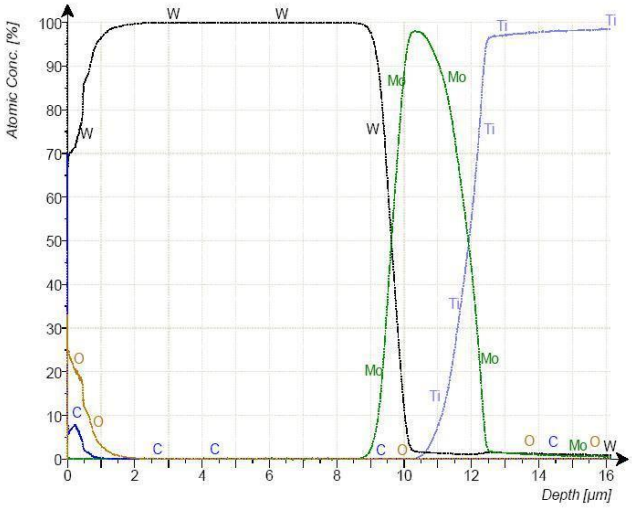

Figure 1 - GDOS depth profiles of W, Mo, C, O and Ti for a witness sample coated with 10 μm W

Usually, a Mo interlayer of 2-3 μm was introduced between W coating and substrate to compensate the mismatch in thermal expansion coefficients of W and substrate and to improve the adhesion. In order to check the influence of Mo interlayer on the D retention, some coatings were deposited without Mo. A typical GDOES (Glow Discharge Optical Emission Spectroscopy) depth profile of coating constituents is shown in Figure 1.

This was recorded on a Ti witness sample introduced in the coating run and coated together with the samples used for D retention investigation. The coating is compact, with a columnar structure as can be seen in Figure 2 where a SEM cross section through the coating is shown. A SEM image of the surface shows grains with the size in the micron range (Figure 3), but a TEM analysis of the coating indicates a nano-structure with crystallites of about 10 nm (Figure 4). The XRD analysis of the W coatings deposited by CMSII has shown a preferred orientation on (211) plane, which is different of the preferred orientation on plane (110) specific for W coatings deposited by conventional magnetron sputtering (Figure 5).

3.2. Exposure of the samples to ECR deuterium plasma

W coated samples were exposed to deuterium plasma produced by an ECR discharge. The deuterium atoms and ions (D^+, D_2^+, D_3^+) reached the W coating with an energy of about 20 eV [1].

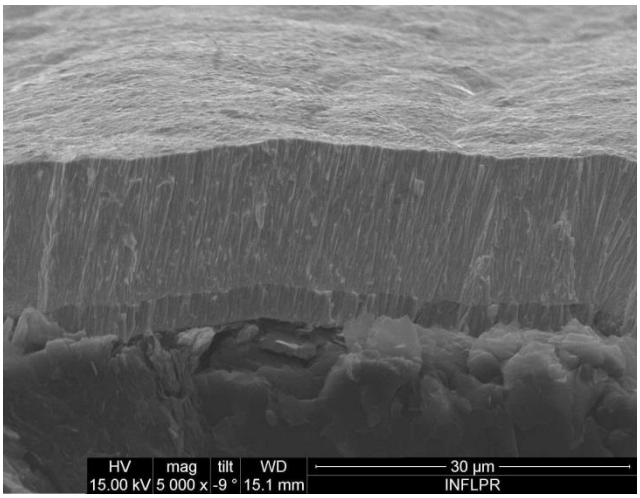

Figure 2 - SEM image of a cross section through a W coating deposited on CFC substrate

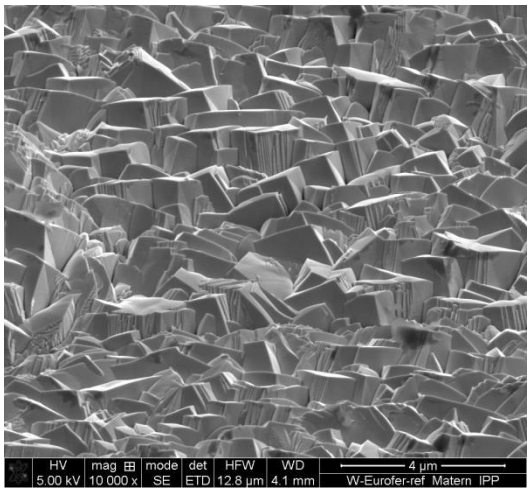

Figure 3 - Surface SEM image of the W coating deposited on Eurofer

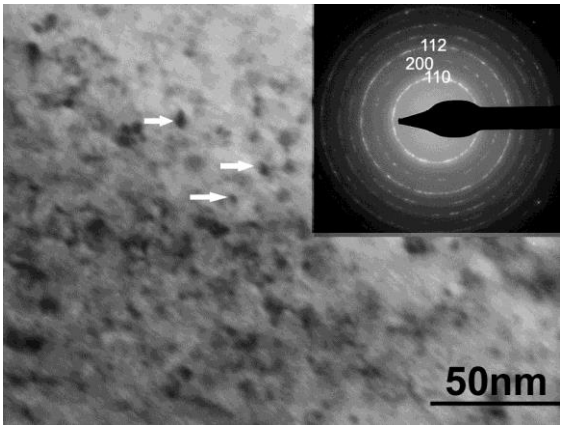

Figure 4 - TEM analysis of the W coating produced by CMSII

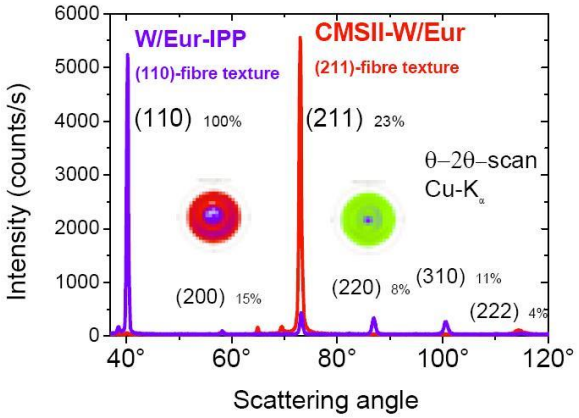

Figure 5 - XRD patterns of W coatings produces by CMSII (red) and magnetron sputtering (blue)

The ion flux was 10^{20} D/m^2·s and the maximum fluence was $2.2 \cdot 10^{25}$ D/m^2. The temperature of the W coatings during plasma exposure was in the range of 50-500 °C

3.3. Analysis of the D retention; results and discussion

The depth profile of D within the W coatings was measured by Nuclear Reaction Analysis (NRA) up to 6 µm while thermal desorption spectroscopy (TDS) was used to measure the total D retention.

Since 2009 the outer diverter of ASDEX Upgrade works with fine grain graphite tiles coated by CMSII technology with 10 µm W and Mo interlayer. The D retention in those coatings was measured after 2009 campaign estimated the incident fluences and the data were compared with the values found in this project at the laboratory scale. The results are shown in Figure 6 and they indicate a good agreement. The ratio between the retained deuterium and incident fluence decreases from $3.5 \cdot 10^{-4}$ for a fluence of $2 \cdot 10^{24}$ D/m^2 down to $0.5 \cdot 10^{-4}$ for a fluence of about 10^{26} D/m^2.

Another aspect which was investigated was the influence of the plasma exposure temperature on the D retention for different types of coatings with different thicknesses (3 µm and 10 µm) and

different substrates (C, CFC, Eurofer). The results are shown in Figure 7 for the temperatures in the range of 300-650 K. PVD means magnetron sputtering performed at IPP Garching.

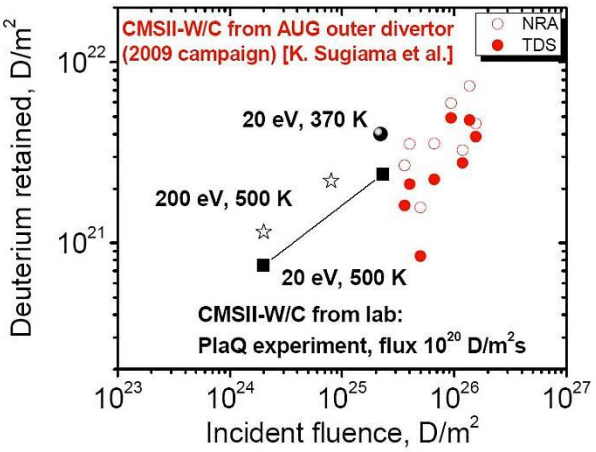

Figure 6 - D retention in CMSII W coatings measured in AUG outer divertor and in laboratory using ECR plasma

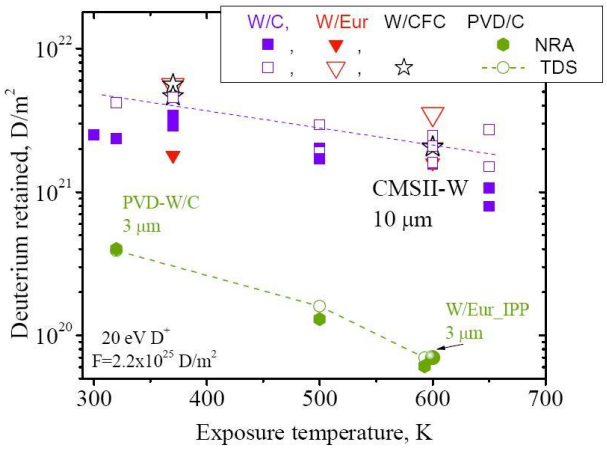

Figure 7 D - retention in W coatings deposited by CMSII (10 μm) and by conventional magnetron sputtering (3 μm)

For W coatings deposited by CMSII there is a significant spread between the values measured by NRA and those measured by TDS. Even so, it is clear that the W coatings deposited by CMSII have a D retention by at least one order of magnitude higher than those deposited by conventional magnetron sputtering. On the other hand the CMSII coatings have a thickness of 10 μm while the PVD coating have only 3 μm. The coating thickness is an important factor for D retention and its influence was investigated as well. The results are shown in Figure 8. The D retention seems to increase almost linear with the coating thickness, but for 3 μm the D retention in CMSII coating is significant higher that that of PVD coating. The Mo interlayer does not influence significantly the D retention. A comparison between the D retention in CMSII coatings and that measured under the same conditions in bulk W and bulk Eurofer is shown in Figure 9. The D retention in nano-structured CMSII coatings is higher by about one order of magnitude than in polycrystalline bulk W and much higher than in bulk Eurofer. This seems to be consistent with the measurements of permeability, diffusivity and solubility of hydrogen in W coatings produced by CMSII technology [2].

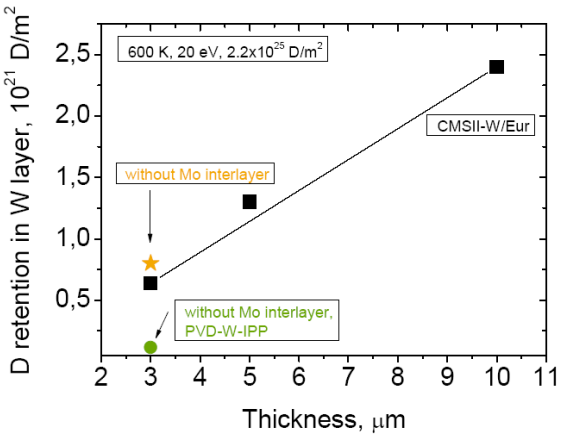

Figure 8 - The influence of W coating thickness on D retention

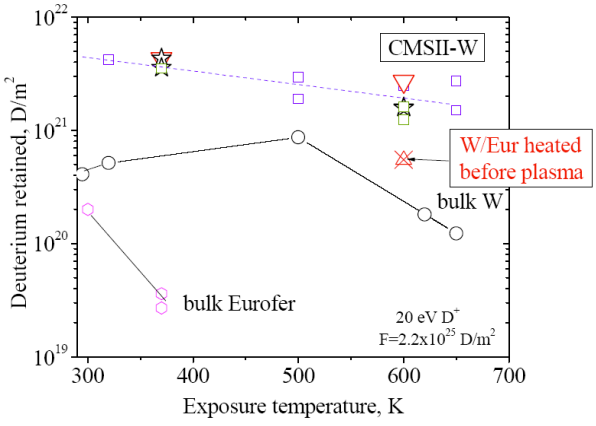

Figure 9 - Influence of plasma exposure temperature on D retention for CMSII W coatings, bulk W and bulk Eurofer

Using the NRA technique the depth profile of D across the W coatings was determined. For thin coatings (3 μm W+ Mo) a higher concentration was found at the W-Mo and Mo-Eurofer interfaces (Figure 10). Even without Mo interlayer the D concentration was higher at the W-Eurofer interface (Figure 11).

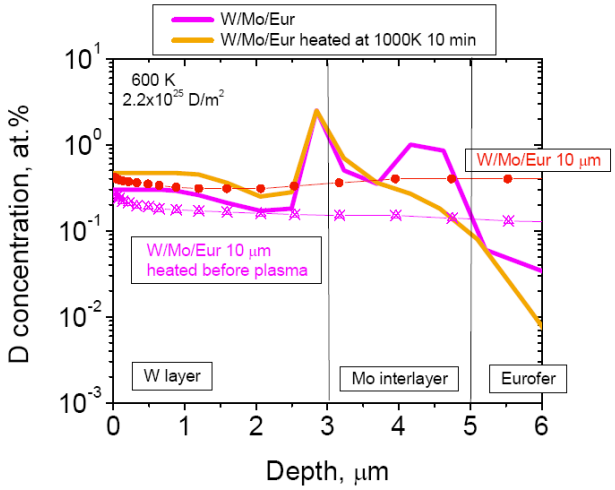

Figure 10 - D concentration profiles for W coatings of 3 μm and 10 μm with Mo interlayer

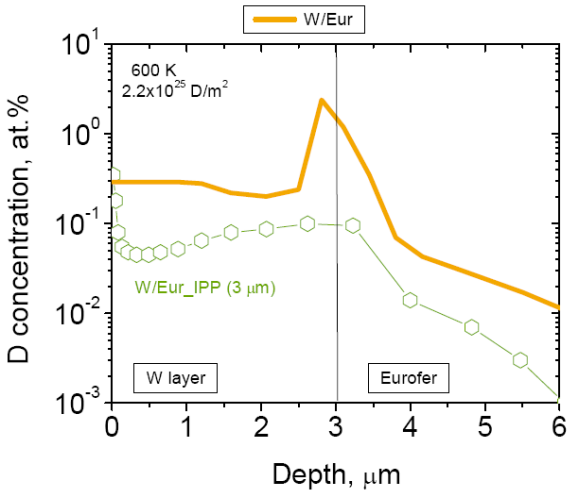

Figure 11 - D concentration profiles for W coatings of 3 μm without Mo interlayer

Due to the very low diffusivity, an accumulation of deuterium occurs at the interfaces where there is a change in material structure.

3.4. A new experimental device for plasma exposure and analysis of gas retention

The experiments carried out with the ECR plasma demonstrated that the D retention of W coatings deposited by CMSII technology on various substrates is in the range of $(6\text{-}0.8)\cdot10^{21}$ D/m^2 and decreases slowly with increasing the plasma exposure temperature from room temperature to about 400°C. Normally the W coatings deposited on CFC or fine grain graphite for the first wall in fusion devices work at significant higher temperatures reaching 1200°C or even more.

In order to measure the fuel retention of the W coatings under more realistic conditions a new experimental device was designed and manufactured. The testing chamber (Φ300x420 mm) with water cooled walls and internal heating capability is connected to H_2 and Ar lines and a gas analyzer (Figure 12). The rapid evacuation is achieved by a 360 l/s turbo-molecular pump. The gas analyzer is HAL200 type and it is supplied by Hiden Analytical, UK. A hollow cathode glow discharge is initiated between two electrodes as it is shown in Figure 13. The electrodes are W coated CFC (60x60x5 mm). The temperature is monitored with a thermocouple The device is hanged in the testing chamber and it can be observed through a side window. A temperature of 900 °C can be achieved with a power of only 660 W. The discharge is energized in DC between the hollow cathode device and the chamber wall.

This system allows plasma exposure and analysis of desorbed gases without exposing the samples to atmosphere. Plasma exposure is carried out in H2 and analysis is performed in Ar. The working pressure is ~ 0.5 torr. The partial pressures of H2, H3, N2, O2, Ar, CH4 and H2O are continuously monitored.

3.5. Hydrogen retention in W coating and CFC substrate

The plasma exposure was performed in hydrogen atmosphere at 450°C, at 0.5 torr for 3 hours. After exposure the samples were cooled down to room temperature in hydrogen atmosphere. The hydrogen retention was measured in the same configuration without exposure the samples to atmosphere, but just changing the hydrogen gas with argon. The vessel was purged with Ar two times and then the hollow cathode discharge was initiated between the two W coated CFC electrodes in Ar atmosphere. The time traces of the temperature and of the partial pressures for H_2, H_3, N_2, O_2, Ar, CH_4 are shown in Figure 14. The temperature was increased from 20°C up to 900°C in about 1 hour, it was kept constant for 3 hours and then it was decreased under control in about 2 hours. The H_2 partial pressure increases with increasing the temperature up to 900°C and then decreases gradually during the outgassing of the CFC samples. There is a small shoulder when the temperature decreases meaning that not all the hydrogen was released from samples. When the temperature of the CFC sample reached the room temperature the partial pressure of hydrogen was very close the initial one. Without changing the experimental conditions, a hydrogen calibrated needle valve was gradually opened and the hydrogen partial pressure was recorded. In this way the correlation between the hydrogen partial pressure during this experiment and the hydrogen flow rate was established. By integrated the flow rate profile for the time of experiment the amount of desorbed hydrogen was calculated. A value of $1.4 \cdot 10^{23}$ m^{-2} was found for an exposure time of 3 hours at 450°C. This amount was released from both W coating and CFC material. Using samples with the same W coated area and different volumes, the amounts of H_2 retained in the W coatings and CFC substrate can be calculated.

3.6. Determination of the Ar retention in the W coatings.

During the plasma exposure in hydrogen the partial pressure of Ar released from the W coating and the substrate was continuously monitored. The value was approx. constant at a value of $7.3 \cdot 10^{-9}$ torr. This is a confirmation of the measurement carried out at IPP Garching on the W coatings deposited by CMSII technology using the EDX technique. The Ar concentration was found to be below 1 at.%.

Figure 12 - Laboratory equipment for plasma exposure and TDS analysis of the W coatings deposited on CFC using a hollow cathode glow discharge

Figure 13 - Hollow cathode glow discharge with W coated CFC plates

4. Conclusions

- The deuterium retention for 10 μm W coatings was in the range of 2-5·10^{21} D/m^2 for a fluence of 2.2·10^{25} D/m^2. In comparison, the D retention for bulk W was of 1.5-8·10^{20} D/m^2 for the same fluence. A 3 μm W coating deposited by conventional magnetron sputtering exhibited deuterium retention of 0.7-4·10^{20} D/m^2 under the same experimental conditions.
- The deuterium retention decreases with increasing the plasma exposure temperature.
- In the range of 3 to 10 μm deuterium retention increases almost linearly with the coating thickness.
- The D concentration in the W coating is in the range of 0.2-0.5 at.% and increases at the W-Mo and Mo-Eurofer interfaces. The substrate material does not appear to have a significant influence on this concentration.
- A good agreement was found between the deuterium retention in 10 μm W coating measured at the laboratory scale and that measured on W coated ASDEX Upgrade divertor tiles after an experimental campaign in 2009.
- A new experimental device for plasma exposure and thermo-desorption analysis was designed, built and commissioned. A hollow cathode discharge is used for plasma heating. The maximum temperature was 900°C, but it can be increased up to 1200°C.
- No Ar was found in the W coatings deposited by CMSII. This is a confirmation of the value found at IPP Garching (below 1 at.%).

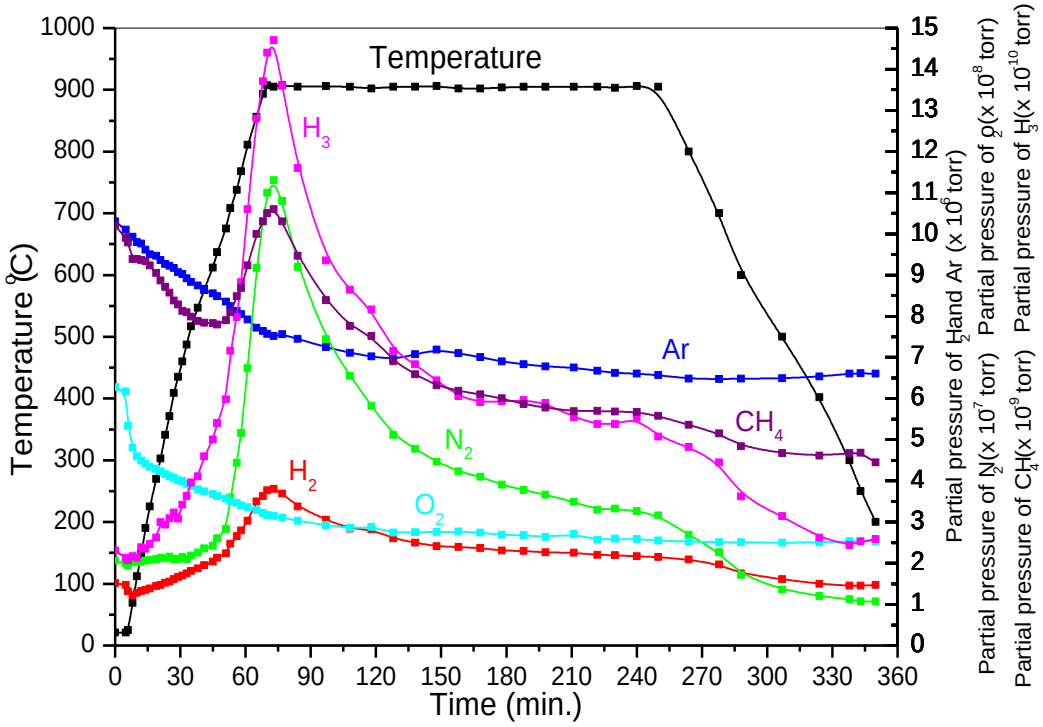

Figure 14 - Partial pressures of the gases desorbed from the W coating and CFC material during the heating process in hollow cathode configuration

Acknowledgement

The reported work includes contributions from the following people outside the EUATOM-MEdC Association: Olga Ogorodnikova and Hans Maier (Max-Plank Institut für Plasma Physik, Euratom Association, Garching, Germany),

References

[1] O.V. Ogorodnikova, C. Ruset, K. Sugiyama, Yu. Gasparyan, V. Efimov, M. Balden, G. Matern, F. Koch, Plasma-induced deuterium retention in tungsten coatings produced by combined magnetron sputtering and ion implantation technique, 20th International Conference on Plasma Surface Interactions 2012, Aachen, Germany, 21. – 25 May 2012

[2] Bojan Zajec, Vincenc Nemanic, Cristian Ruset, Hydrogen diffusive transport parameters in W coating for fusion applications, Journal of Nuclear Materials, 412 (2011), 116–122

STUDY OF DEUTERIUM TRAPPING MECHANISMS OF ITER BERYLLIUM-RELATED MIXED MATERIALS

C. P. Lungu, C. Porosnicu, I. Jepu, A. M. Lungu, P. Chiru, A. Marcu, C. Luculescu

National Institute for Laser, Plasma and Radiation Physics, Association EURATOM

[BS_18B/WP12-IPH-A01-3-01/BS; BS_18B/WP12-IPH-A01-3-01/PS]

Abstract

Using the thermionic vacuum arc method pure beryllium, Be-W having three different relative concentrations and with deuterium inclusions samples were prepared on stainless steel, graphite and silicon substrates at room temperature. All structures have been characterized with respect to morphological/structural and diffusional aspects, via SEM, EDS and XPS.

RBS measurements were performed to investigate the films compositions, the position of the oxygen, and to see if there is a mixture of the three elements. Deuterium implantation experiment will be performed in the High Current Ion Source. The amount of D retention will be determined by nuclear reaction analysis, using 3He (d, p) α reaction. The fitting of the experimental data form RBS and NRA measurements will be done using SIMNRA code, developed at IPP Garching.

The total amount of deuterium retained and released as a function of deposition parameters and deuterium gas pressure was determined by NRA measurements.

Papers

[1] K. Sugiyama, C. Porosnicu, W. Jacob, J. Roth, Th. Dürbeck, I. Jepu, C.P. Lungu, Study of deuterium retention in / release from ITER-relevant Be-containing mixed material layers implanted at elevated temperatures, Journal of Nuclear Materials. Available online 17 January 2013

Conferences

[1] C. P. Lungu, J. Likonen, A. Hakola, C. Porosnicu, I. Jepu, A. M. Lungu, P. Chiru, Gh. Oncioiu, A. Victor, P. Osiceanu and JET-EFDA contributors, *Characterization of Mixed Materials in Support of the ITER Like Wall*, Proceedings of 20th International Conference on Plasma Surface Interactions, Aachen, Germany 21-25 mai 2012,

[2] K. Sugiyama, C. Porosnicu, W. Jacob, J. Roth, Th. Dürbeck, I. Jepu, C.P. Lungu, *Study of deuterium retention in / release from ITER-relevant Be-containing mixed material layers implanted at elevated temperatures*, Proceedings of 20th International Conference on Plasma Surface Interactions, 21-25 mai 2012, Aachen, Germany.

Reports

[1] C. P. Lungu, A. Hakola, Clarification of the influence of Be-containing redeposited layers on D-retention and release" EFDA ITER Physics A01-3 - final report, Tartu, Estonia, in 28-30 November 2012

Detailed results

Introduction

The application of several materials at the first wall of ITER leads under operation to the formation of compounds. The retention mechanisms for deuterium and the influence of surface composition, structure, and temperature are essential fundamental properties which enable predictions of the behavior of multi-component first walls in e.g. JET and ITER. The MEdC Association by the research group of the National Institute for Laser, Plasma and Radiation Physics, has a broad experience in

preparing and characterization of mixed films using the original thermionic vacuum arc (TVA) method.

Sample preparation

In order to obtain depositions containing D containing Be and Be-W composite, a setup as in the Figure 1 was developed. One anode was a crucible with beryllium while the other was a tungsten rod. The distance between the anodes was 12 cm and the sample holder-anodes distances were around 28 cm. The two anodes and the substrates were positioned so that the same particle flux to be present at the same for each sample in a deposition batch, as it is shown in Figure 1. During the deposition, deuterium is introduced using a special inlet that has many small holes in order to achieve a uniform D flux.

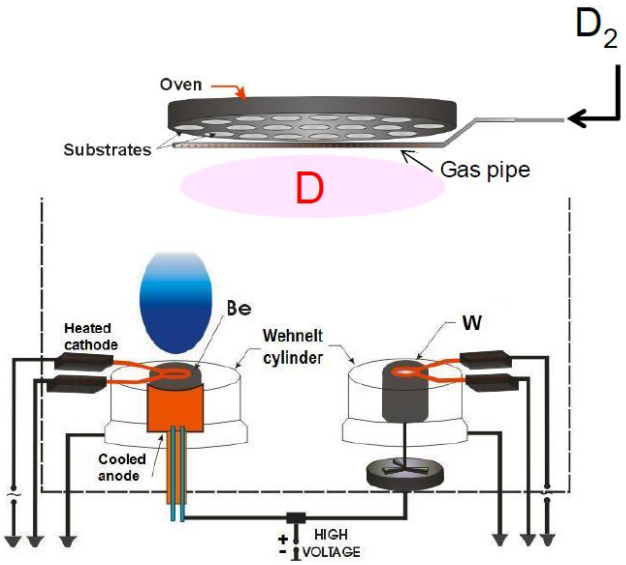

Figure 1 - Schematic representation of the deposition setup for composite D containing depositions

The electron beams produced by circular heated filaments evaporate both the beryllium and the tungsten used as anodes, by applying high voltages (1-5kV) between cathodes and respectively anodes. Bright plasmas in pure tungsten and beryllium vapors are ignited simultaneously. In order to accelerate the ions to the substrates, fact that improves the layer's adherence and compactness proven in previous studies, a negative polarization voltage was applied on the substrates.

For each batch, stainless steel, carbon and silicon substrates were used. The stainless steel and carbon substrates were mirror polished fine grain graphite. The stainless steel substrates were mirror polished round shape, having a diameter of 25 mm. The other substrates were 12 by 14 mm rectangular shape. The films were deposited at room temperature.

Eight types of samples were prepared: beryllium, with and without deuterium, Be-W having three different relative concentrations, with and without deuterium. For each type of samples, 500 and 1-1.5 µm were achieved.

The deposition parameters and the characterization of the samples using scanning electron microscopy are presented further:

The sample batch 20120607. Be-D co-deposition (Table 1)

Table 1 - Typical deposition parameters used for Be-D preparation

U_a (kV)	1.12	1.1	1.08	1	0.95	0.93
I_a (A)	0.65	0.70	0.78	0.82	0.9	0.93
I_f (A)	41.5	41.8	41.9	42	42.2	42.5
Rate (nm/s)	1	1	1	1	1	1
Thickness (nm)	1	40	76.8	131	410.1	500
Time (sec)	1	40	80	140	420	550
P_{+D2}(torr)	2×10^{-5}	2×10^{-5}	2×10^{-5}	2.2×10^{-5}	2×10^{-5}	2×10^{-5}
Temp.(ºC)	30	30	30	39	73	84

OBS : $P_{+D2} = 2 \times 10^{-5}$ torr; Rate ≈1 nm/s

When preparing Be-W mixed films, a set of processing parameters were used, as shown in Table 2:

Table 2 - Typical mixed film containing Be and W deposition parameters.

Deposition parameters	Be			W		
Time (min)	0	17	100	0	17	100
U_a(kV)	0.8	1	0.97	1.4	1.5	1.8
I_a(mA)	400	423	434	1.4	1.5	1.5
I_f(A)	53	52.4	52.3	38	40	42
Deposition rate (nm/s)	0.1	0.2	0.05	0.2	0.04	0.03

Structural and morphological studies of the layers

Various analyses were performed on the samples to check the concentration of the three materials and of the morphology as well.

Surface analysis performed by X-Ray Photoelectron Spectroscopy (XPS) was carried out on a Quantera SXM equipment, with a base pressure in the analysis chamber of 10^{-9} Torr. The X-ray source was Al K_α radiation (1486.6eV, monochromatized) and the overall energy resolution is estimated at 0.75 eV by the full width at half maximum (FWHM) of the $Au4f_{7/2}$ line. In order to take into account the charging effect on the measured Binding Energies (BEs) the spectra were calibrated by using the C1s line (BE = 284.8 eV, C-C /(CH)n bonding) of the adsorbed hydrocarbon on the sample surface. We have to emphasize that the errors in our quantitative data (relative concentrations) are found in the range of ± 10%, while the accuracy for BEs assignments is ± 0.2eV.

XPS analysis was used to determine the chemical states of the elements present on the surface and, after quantitative analysis, to find the element and the chemical state relative concentrations, as well. After Survey of XPS spectra, the high resolution photoelectron spectra of the most prominent XPS transitions (C1s, O1s, Be1s, W4f) are shown in Figure 2.

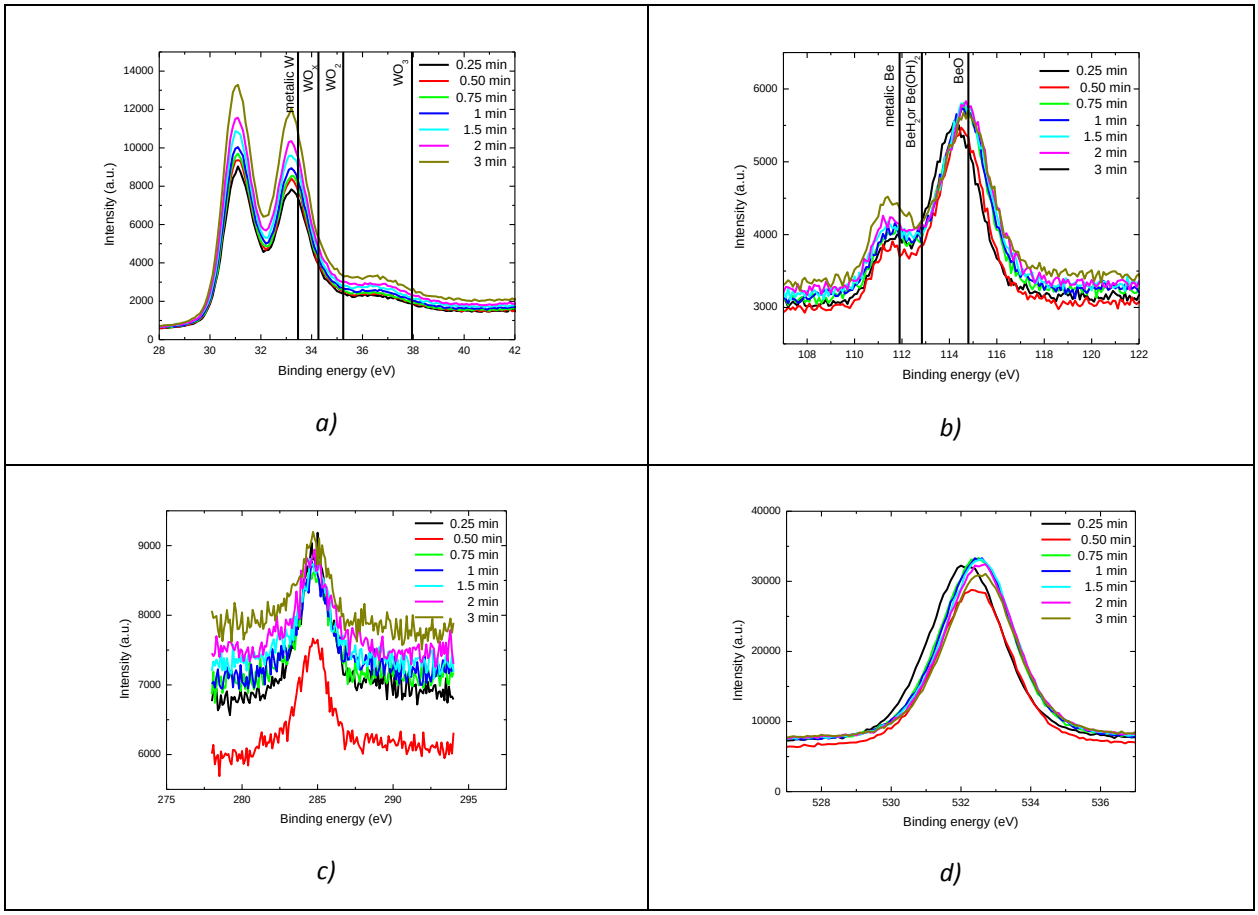

Figure 2 - High resolution photoelectron spectra of the most prominent XPS transitions: C1s: (a), O1s (b), Be1s (c), W4f (f)

The fact that C1 signal is not totally attenuated indicates that the surface contaminated layer. From the XPS spectra, after Ar cleaning (1keV) the incorporated C was found as carbides.

SEM measurements

The SEM pictures reveal smooth surfaces (Figure 3), and the EDS analyses show the relative Be/C/O/W concentrations.

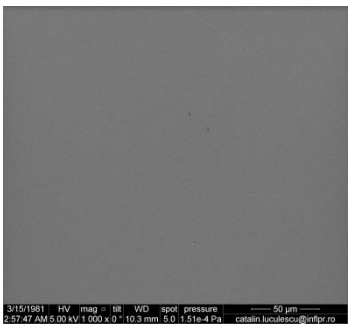

Elem	*Wt %*	*At %*	
Be	2.35	17.03	
C	2.62	14.22	
O	6.62	26.98	
Si	5.31	12.32	
W	83.09	29.45	
Total		100.00	100.00

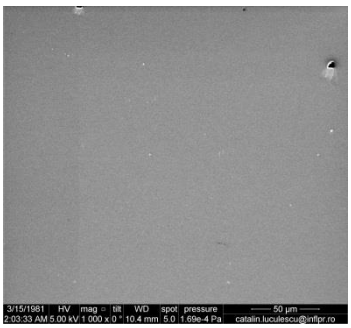

Elem	*Wt %*	*At %*
Be	6.55	23.84
C	2.92	7.97
O	25.68	52.68
Si	3.97	4.64
W	60.89	10.87
Total	100.00	100.00

Figure 3 - SEM images and EDS results concerning Be-W composite co-deposited under deuterium atmosphere

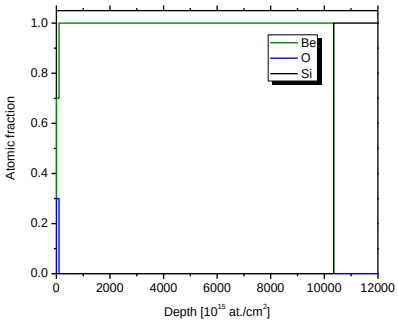

a) 500 nm Be thin film on silicon substrate

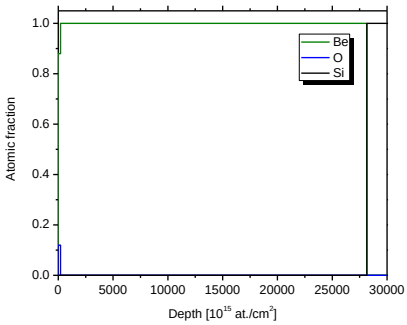

b) 1500 nm Be thin film on silicon substrate

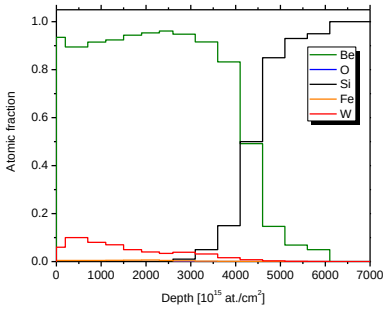

c) 500 nm W-Be (80:20Wt%) thin film on silicon substrate

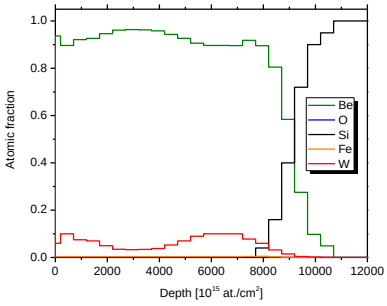

d) 1500 nm W-Be (80:20Wt%) thin film on silicon substrate

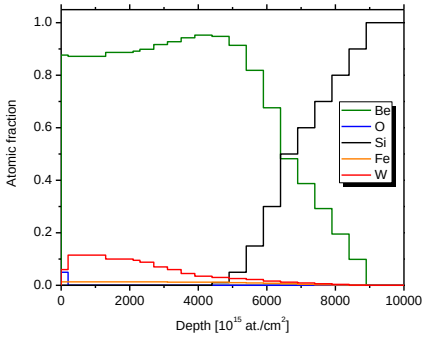

e) 500 nm W-Be (90:10Wt%) thin film on silicon substrate

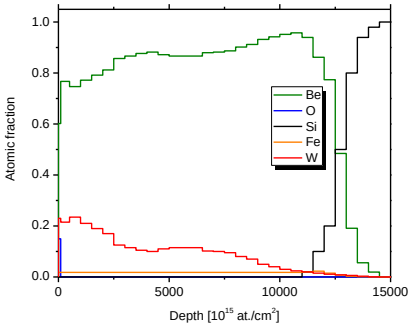

f) 1500 nm W-Be (90:10Wt%) thin film on silicon substrate

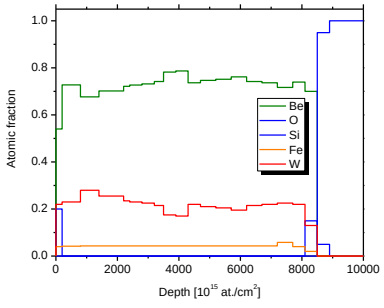

g) 500 nm W-Be (95:5Wt%) thin film on silicon substrate

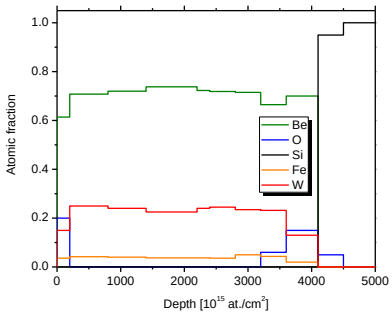

h) 1500 nm W-Be (95:5Wt%) thin film on silicon substrate

Figure 4 - Mixed films analyses using RBS

The samples were analyzed by RBS and the ones without deuterium were subject to deuterium implantation and will be subject to retention and release studies as function of morphological changes. These studies were performed at IPP Garching.

RBS measurements were performed to investigate the films compositions, the position of the oxygen and to see if there is a mixture of the three elements. For this it had been used a ^{4}He energy beam of 2.6 MeV. The beams energy value was chosen taking into account the interaction cross section of ^{4}He and Be to avoid the non-Rutherford interaction that may cause errors in the data interpretation (Figure 4 above).

Conclusion

The main aspect underlined by RBS measurements is that mixture of the materials occurs during the deposition.

The amount of D retention will be determined by nuclear reaction analysis with using 3He (d, p) α reaction. The fitting of the experimental data form RBS and NRA measurements was ad will be performed using SIMNRA code, developed at IPP Garching.

Acknowledgement

The reported work includes contributions from the following people outside the EUATOM-MEdC Association: K. Sugiyama, C. Porosnicu, W. Jacob, J. Roth, Th. Dürbeck (*Max-Planck-Institut für Plasmaphysik, EURATOM Association, D-85748 Garching, Germany*

CLARIFICATION OF THE INFLUENCE OF BE-CONTAINING REDEPOSITED LAYERS ON D-RETENTION AND RELEASE

C. P. Lungu, C. Porosnicu, I. Jepu, A. M. Lungu, P. Chiru, C. Luculescu, A. Marcu

National Institute for Laser, Plasma and Radiation Physics, Association EURATOM MEdC
[BS_18C/WP12-IPH-A01-3-13/PS]

Abstract

Films (100 nm – 5 µm) doped with deuterium were realized, using the thermionic vacuum arc (TVA) method. A new deposition system was implemented with a large deposition chamber (800 l). This device allows the preparations of films with a low content of residual gases, as for example Oxygen. In the meantime, the feeding gas system was improved, to realize pure co-depositions with pure D_2.

The realized films were first characterized by scanning electron microscopy (SEM), in order to study the surface morphology, as well as the cross-sectional aspect.

Secondary Ion Mass Spectrometry (SIMS) and Laser Induced Breakdown (LIBS) were performed in cooperation with the EURATOM Association TEKES, Finland, in order to determine the depth profile of the film composition.

Rutherford Backscattering Spectroscopy (RBS), Nuclear Reaction Analyses (NRA) and permeation measurements were performed in cooperation with IPP Garching, Germany, and IJS Ljubljana, Slovenia, concluding on the morphology and composition influence on the Hydrogen permeation, respectively that the nanostructured films have a permeation reduction factor (PRF) with a factor of magnitude higher than that of the columnar structured coatings.

Papers

[1] Bojan Zajec, Vincenc Nemanič, Marko Žumer, Cristian P. Lungu, Corneliu Porosnicu, *Hydrogen permeability through beryllium films and the impact of surface oxides,* Journal of Nuclear Materials (JNM-D-12-00743)

Conferences

[1] C. P. Lungu, J. Likonen, A. Hakola, C. Porosnicu, I. Jepu, A. M. Lungu, P. Chiru, Gh. Oncioiu, A. Victor, P. Osiceanu and JET-EFDA Contributors, Characterization of Mixed Materials in Support of the ITER Like Wall, 20th International Conference on Plasma Surface Interactions 2012, May 21st – 25th, 2012, at Aachen, Germany.

[2] C. P. Lungu, C. Porosnicu, I. Jepu, A. M. Lungu, P. Chiru, P. Osiceanu, A. Marin, G. Burcea, V. Bailescu, Influence of Thermal Treatment on the Beryllium Containing Mixed Films, Symposium on Fusion Technology, 24-28 September 2012, Liege, Belgium

Reports

[1] C. P. Lungu, A. Hakola, Clarification of the influence of Be-containing redeposited layers on D-retention and release" EFDA ITER Physics A01-3 - final report, Tartu, Estonia, in 28-30 November 2012

Detailed results

Introduction

For this task, the Romanian MEdC Association produced a set of deuterium-doped Be, Be-W, Be-C, and Be-C-W samples with different thickness, using the Thermionic Vacuum Arc (TVA) method. The samples were analyzed for their deuterium content and composition, using NRA at IPP Garching, and SIMS and LIBS in the Be-handling facilities of Tekes-VTT. The results obtained with the three

methods were compared and the dependence of the D-retention on the composition and thickness of the surface layers was determined. Measurements of the deuterium permeation of the Be containing layers were performed using the facilities of the ISJ Ljubljana, Slovenia.

Preparation of D_2 containing films

Deuterium containing films were deposited simultaneously with Be, C or W and D_2 as buffer gas into the reaction chamber. In order to feed the Deuterium gas in the close vicinity of the growing films, a stainless steel pipeline was manufactured. The schematic draw of the deposition setup is presented in Figure 1.

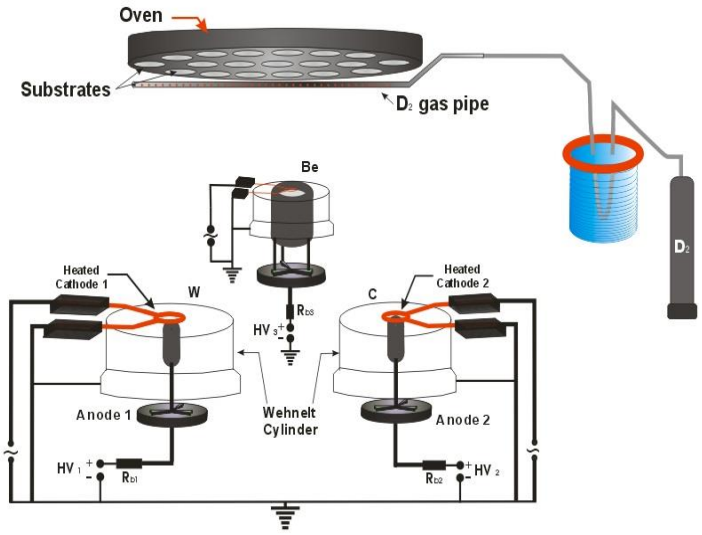

Figure 1 - The TVA setup used for D_2 co-deposition

SEM measurements

Using a scanning electron microscope (SEM, Quanta INSPECT) apparatus the surface of the samples was characterized morphologically (Figures 2-4). The cross-sectional analysis of the samples shows dense, compact layers without columnar structures (Figure 5).

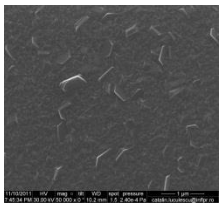

Figure 2 - SEM image of the Be-C film surface

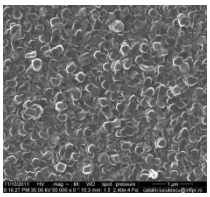

Figure 3 - SEM image of the Be-W film surface

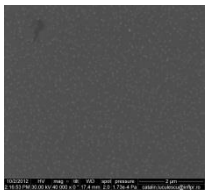

Figure 4 - SEM image of the W surface

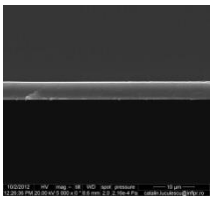

Figure 5 - Cross-sectional view of the W film

LIBS measurements

In order to perform Laser Induced Breakdown Spectroscopy (LIBS) analyses at VTT Finland, a Continuum Minilite II 1064 nm laser was used. (50 mJ per pulse, at the sample surface 27 mJ)

The spectra were collected using the following Spectrometers: 1. Avaspec-2048, resolution ≈ 1 nm, and 2. Shamrock 750 Andor, 600 l/mm, resolution ≈ 0.1 nm, + ICCD; bandpass Dl ≈ 40 nm. The spectrometer Shamrock + ICCD (Intensified Charge Coupled Device) allows the recording of time-

resolved spectra. Recording spectra during the laser irradiation, strong lines in the 300-500 nm region, belonging to Be, were collected. Due to Stark broadening, lines are very broad. The analytical lines identified for measurements were: Be I 332nm; Be II 313nm (overlapping); Be I 457nm; Be II 467 nm.

The list of the prepared samples for LIPBS measurements is presented in Table 1. In Figures 6 and 7, typical emission spectra during laser irradiation are shown. The resulted depth profiles after the measurements are presented in Figure 8.

Table 1 - The list of analyzed samples by LIBS measurements

Coating	Thickness (nm)		Concentrations (At. %)		
	Nominal	Measured	Be	W	Fe + Cr + Ni
Pure Be	1500	2340	100	0	0
Pure Be	500	860	100	0	0
Be + D	1600	1800	100	0	0
Be + D	500	570	100	0	0
Be 5% + W 95%	1100	880	70	25	5
Be 5% + W 95%	500	430	70	25	5
Be 5% + W 95% + D	1000	2070	70	25	5
Be 5% + W 95% + D	500	1000	70	25	5
Be 10% + W 90%	1200	1270	80—90	10—15	0—5
Be 10% + W 90%	500	630	80—90	10—15	0—5
Be 10% + W 90% + D	750	660	80—90	10—15	0—5
Be 10% + W 90% + D	750	680	80—90	10—15	0—5

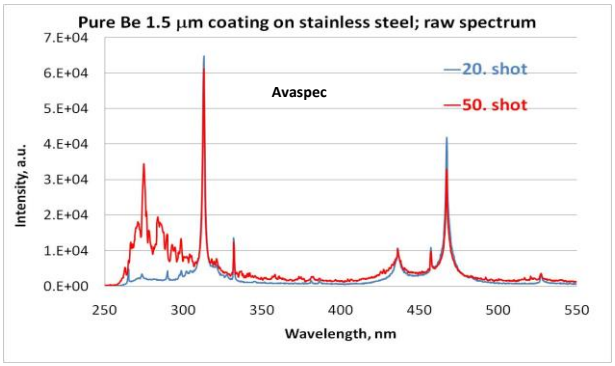

Figure 6 - Typical emission spectra of the plasma plume recoded using the Avaspec spectrometer

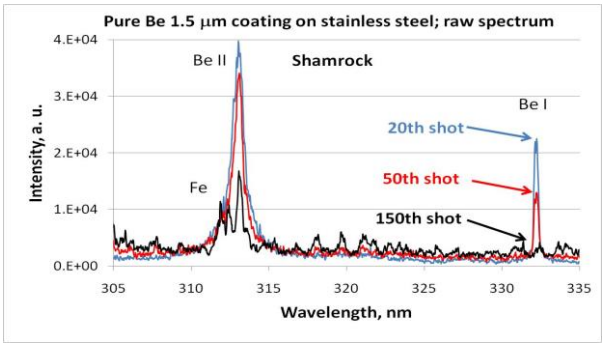

Figure 7 - Typical emission spectra of the plasma plume recoded using the Shamrock spectrometer

The LIBS measurements highlighted the following: 1. Be has strong analytical lines suitable for LIBS diagnostics; 2. At the low values of fluency applied now, the overlapping of Be lines by W and stainless steel lines is minute; 3. Deuterium was not detectable; and 4. For further testing (i) samples with lower Be content and (ii) more powerful laser are needed.

Secondary Ion Mass Spectrometry (SIMS) measurements

The measurements can be seen in the following figure (Figure 8):

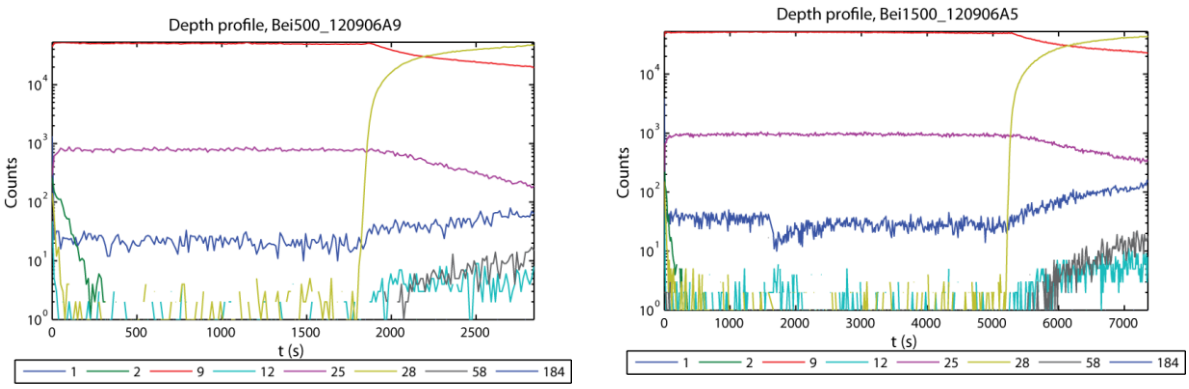

Figure 8 - SIMS depth profiles of the D_2 gas co-deposited samples: 500 nm (left) and 1500 nm (right). Deuterium peak can be clearly seen at the surface. In each case: H = 1, D = 2, Be = 9, C = 12, BeO = 25.

SIMS analyses were performed at VTT Institute in Helsinki, Finland, using the following measurement parameters: (i) VG IX70S double focusing magnetic sector SIMS; (ii) Xe^+ (5keV) primary ions, ion current 125nA and 500 nA; (iii) Sputtered area 300 × 220 μm2; (iv) Sputter rates: 0.56nm/s (Be/W). The Deuterium peak can be clearly seen at the surface of the 500 and 1500 nm pure beryllium doped with D_2, and in the whole mixed Be10W90 film.

Deuterium retention study

Deuterium implantation experiment was performed using the High Current Ion Source of IPP Garching. The energy of D ion beam was 600 eV D_3^+ (200 eV/D), and the incident direction was normal to the target surface. The implantation was carried out at room temperature with the flux of ~ 3 x 10^{19} D/m^2s. After certain continuum implantation (2.09 x 10^{21} D/m^2), the amount of D retention was determined by nuclear reaction analysis (NRA).

Thermal desorption spectroscopy (TDS) experiment was performed for the implanted samples using the TESS facility at IPP Garching. The experiment consists in heating the sample with 15K/min ramp, up to 1000K followed by a 20 minutes hold. Then the sample was allowed to cool by itself. During the entire heating process, the amount of deuterium released from the film (as D_2 and HD molecules) was measured.

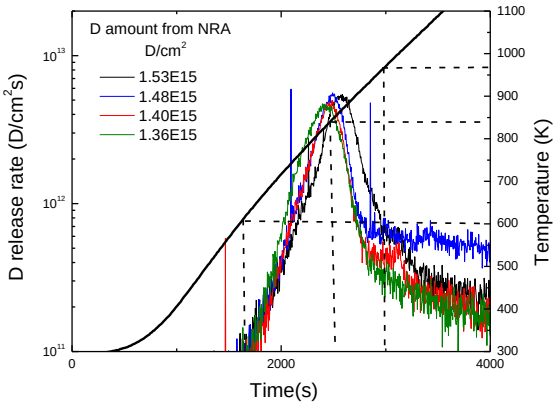

Figure 9 - Thermal desorption of D_2 implanted with different fluences (1.36E15 – 1.53E15) on the Be-W doped with D thin layers. D content ~0.1at%; O content ~20at%; Be – 62at%; W – 18at%

TDS profiles for the Be-W samples showed clear dependence of deuterium release on the D_2 flux implantation (Figure 9). For implantation at room temperature and for high Be concentrations, a pronounced D_2 desorption peak between 875 and 900 K was observed, corresponding to deuterium desorption from beryllium related trapping sites.

Permeation measurements

Using the system realized at the Josef Stefan Institute (JSI) Ljubljana, Slovenia, the prepared samples were tested at 400°C to verify integrity of the film and its capability for hydrogen isotopes migration.

Coated membranes were sealed in the permeation cell by two Au 0.6 mm thick gaskets in the shape of an O-ring. The resulting hydrogen exposed area was 8.4 cm^2. The Be coated side was oriented to the upstream chamber except in one repeated experiment. The UHV in each of the three volumes was maintained by its own turbo molecular pump. The applied gauges were: two capacitance manometers (MKS, 1 mbar F.S., and 0.05 mbar F.S.) mounted in the accumulation chamber with volume V = 0.41 L. The attachments were the following: the calibrated volume and the hydrogen container for calibrating the quadrupole mass spectrometer (MS), which is built in the analytical chamber. Applied hydrogen was purified to a level of less than 2×10^{-8} L/L using in-line gas purifier (Air Liquide). The permeation rate as low as $q \approx 7\times10^{-10}$ mol H_2 /m^2 s could be measured at 400 °C.

Results of the permeation measurements at 1 bar hydrogen upstream pressure through six Be-coated samples soon after almost a “steady flux” has been established are presented in Table 2. Two uncoated Eurofer samples were also measured within this experiment, as a reference giving the flux $j_{uncoat} = 1.12\times10^{-5}$ mol H_2 m^{-2} s^{-1}.

Table 2 - The recorded steady-state permeation rate at 400 °C and 1 bar hydrogen pressure.

Sample No.	j / mol H_2 m^{-2} s^{-1}	PRF	remark
EUROFER	1.12×10^{-5}	1	
1	2.68×10^{-7}	42	
2	4.23×10^{-7}	26	
3	9.45×10^{-8}	118	
4	7.82×10^{-7}	14	N_2 prior the H_2 intr.
5	2.43×10^{-7}	46	Ag interlayer
6	8.30×10^{-8}	135	Ag interlayer

Dynamics of the transient permeation rate, as well as final steady-state value, strongly varied among samples. Permeation rate exhibited a rapid jump within the first minute at three samples, followed by a slow increase in *j(t)* as can be seen in Figure 10.

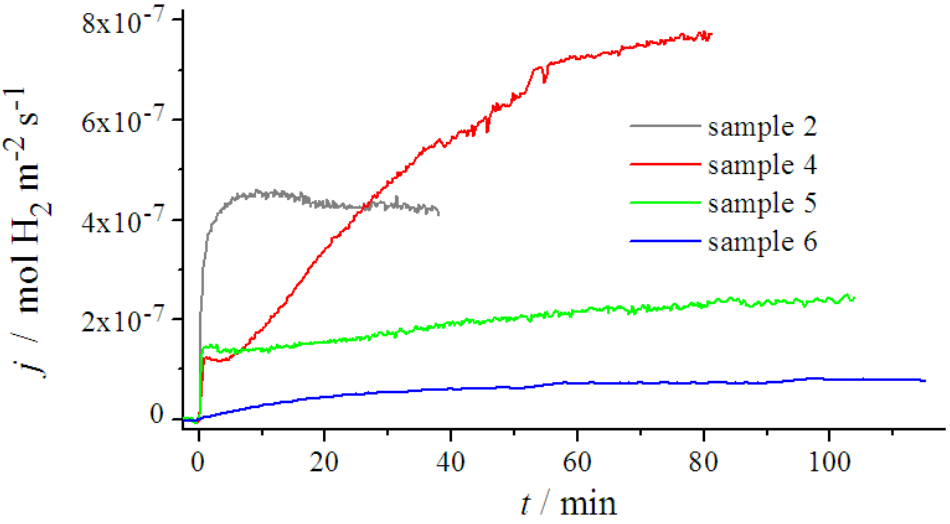

Figure 10 - A selection of permeation rate transients through four different samples. Hydrogen at 1 bar was rapidly introduced at t = 0.

The diffusion limited permeation was confirmed by measuring the steady-state permeation rate at different hydrogen driving pressures p_{HI} that revealed $j \propto \sqrt{p_{HI}}$ relation for all samples.

The permeation fluxes through all investigated Be coated membranes evidently show that the Be films have a substantially lower permeability than the substrate, the PRF values corresponding to steady-state flux being between 14 and 135. An estimation of P_{Be} can be made the following eq.:

$$PRF = 1 + \frac{d_s P_s}{d_s P_f},$$

where indices *s* and *f* denote substrate and film layer. The substrate thickness is usually much higher than the film (d_s/d_f >>1) which means that low permeability of the film P_f plays the main role in achieving high *PRF* values.

The values for the Be permeability from Table 2 give the following values: P_{Be}(400°C) = 2.3×10^{-15} mol H_2/m s Pa$^{0.5}$ for *PRF* = 135 and P_{Be}(400°C) =2.3×10^{-14} mol H_2/m s Pa$^{0.5}$ for *PRF* = 14.

If the observed steady-state permeation rates are assumed to be entirely due to the pinhole permeation (i.e. the film material is impermeable, but defective), one cannot determine pinholes size and density as they are coupled.

Figure 11 shows the diagram of fraction of exposed substrate surface θ versus pinhole radius r_o for the highest and lowest observed *PRF* value. Smaller pinholes are evidently more effective, since lower θ is required to keep PRF_o constant. Small and sparsely populated pinholes are particularly problematic to locate manually by any method of visual or electron microscopy, due to their low $r_o/\langle l \rangle$ ratio, where $\langle l \rangle = n^{-½} = r_o\,(\pi/\theta)^{½}$ is an average distance between the neighbouring pinholes. The right-hand *y* scale displays this ratio and only for PRF_o=14 and r_o larger than few μm this ratio is above 1% which can be rather arbitrarily taken as the lower limit when the pinholes are still relatively easy to spot. The pinholes, if responsible for the observed permeation rate, are thus very difficult to find in our case due to much lower $r_o/\langle l \rangle$ ratio.

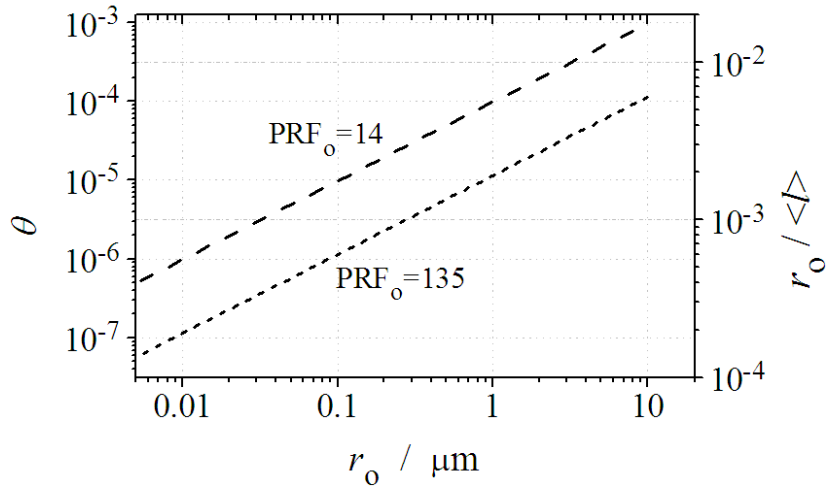

Figure 11 - The relations between the exposed fraction of substrate θ, pinhole radius vs. distance to neighboring pinholes ratio, and pinhole radius r_o for the highest and lowest PRF observed in this study

Conclusions

A correlation was performed between the elemental concentrations obtained by RBS, LIBS and SIMS measurements in order to perform an accord between the SIMS and LIBS emission signals and the relative atomic concentrations.

Hydrogen permeation flux through Be and W coated Eurofer membranes was measured at 1 bar upstream pressure and 400 °C. The initial PRF of Be film was between 14 and 135, measured on six samples, while the PRF of W films were between 50 and 80. Different contributions of pinhole permeation mechanism were found to be predominantly responsible for the scatter of obtained steady-state permeation rates and PRF. It was found that for unintentionally oxidized samples the extracted regular permeation rate is almost identical from sample to sample and accounts $\approx 1.2\times10^{-7}$ H_2 /m^2. For non-oxidized sample this value is several times higher, $\approx 6.5\times10^{-7}$ mol H_2 /m^2 s. From the latter follows $P_{Be}(1.9\cdot10^{-14}$, while P_{BeO} ~ 1×10^{-17} mol H_2/m s Pa$^{0.5}$ can be estimated assuming 35nm thick BeO layer.

Acknowledgement

The reported work includes contributions from the following people outside the EUATOM-MEdC Association: K. Sugiyama, W. Jacob, J. Roth, Th. Dürbeck (IPP Garching, *Max-Planck-Institut für Plasmaphysik, EURATOM Association, D-85748 Garching, German), J.*. Likonen, A. Hakola, (VTT Helsinki, TEKES Association), Bojan Zajec, Vincenc Nemanič, Marko Žumer (IJS Ljubljana, Slovenian EURATOM Association)

X-RAY TOMOGRAPHY FOR MICRO-STRUCTURAL CHARACTERIZATION OF FUSION TECHNOLOGY RELEVANT COMPOSITE MATERIALS

I. Tiseanu, T. Craciunescu, C. Dobrea, A. Sima

EURATOM-MEdC Association, Institute for Laser, Plasma and Radiation Physics (INFLPR) Atomistilor Str. 409, Bucharest-Magurele, ROMANIA, e-mail: tiseanu@infim.ro

[BS_20A/WP12-IPH-A03-1-03/PS]

Abstract

The evaluation of total porosity and its parameters as open porosity, pore area or size distribution are important factors in evaluation and selection of carbon-based materials - carbon-fiber composites (CFC) and graphite - for the projects in fusion energy production. The techniques used to measure the porosity of materials have very much evolved in diversity and performance, from gas adsorption/permeation or liquid extrusion to direct pore imaging. Until recently only imaging technologies providing sufficient resolution to reveal directly pores in size ranges that correlate with the mechanical, thermal or other physical properties relevant for the uses of CFCs as construction materials have been used. This approach has the merit of being flexible (a given image can be processed repetitively with e.g. newer algorithms better adapted for the various porosity characteristics). On the disadvantage side, one image characterizes only a thin slice of investigated material and thus may not be representative for the whole sample that can present important inhomogeneities or anisotropy. In the particular case of CFCs, which have an important structural anisotropy, it is necessary to image and process a big number of slices (sections) with many spatial orientations. With the advent and fast evolution of micron-resolution X-ray tomography in the last few years, the possibilities of high-resolution digital image processing were complemented with the advantage of the image data acquisition in the whole volume of the sample, during a single exposition to X-rays. Here we have sustained an intense campaign of X-ray microtomography measurements of most relevant composite materials for fusion technology measured in the same conditions. To our knowledge, this is the first time when such consistent comparison of different composite materials is proposed. In our method the porosity factor is determined as the ratio between the area of the difference between the measured histogram and the symmetrized histogram with the help of a generalized Gaussian fit. We show that our procedure for the quantitative evaluation of the sample porosity factor yields realistic results for the three types of CFC analyzed.

Conferences

[1] I. Tiseanu, T. Craciunescu, F. Cotorobai, K. Mergia, C. Dobrea, A. Sima,
X-ray tomography for micro-structural characterization of fusion technology relevant composite materials, Conference on Industrial Tomography, 19-21 Sept. 2012, Wels, Austria , published in NDT.net Issue 2012-12, http://www.ndt.net/search/docs.php3?date=2012-12&issue=1&showForm=off&rppoffset=20

[2] A. Sima, I. Tiseanu, Tomographic reconstruction implemented on uniprocessor, quad-processor and Nvidia graphic processor systems, Conference on Industrial Tomography, 19-21 Sept. 2012, Wels, Austria

[3] McCarthy, D., O'Keeffe, S., Lewis, E., Sporea, D., Sporea, A., Tiseanu, I., Woulfe, P., Cronin, J. Proceedings of IEEE Sensors 2012, Article number6411245, Sensors, 2012 IEEE, Digital Object Identifier: 10.1109/ICSENS.2012.6411600

1. Introduction

The carbon-carbon fiber reinforced (CFC) materials offer attractive properties for plasma facing components (PFC) in future fusion power plants and for the thermal protection system of space vehicles.

The carbon reinforced carbon fiber (CFC) monoblocks of ITER diverter vertical target must sustain high heat fluxes of 10 MW/m^2 during 400 s (normal operation) and up to 20MW/m^2 during 10 s (off-normal event). CFCs have a unique combination of high conductivity, low Z and resistance to damage

induced by the high heat loads. Given the demanding environmental requirements of ITER diverter, specially developed CFCs are needed as plasma facing components (PFC) materials.

The problem of fuel (tritium) retention in a carbon material is a major concern due to its radioactivity and inventory constraints within the ITER installation.

The spatial distribution of porosity and density of these materials has to be determined for assessing their performance at high temperatures and/or intense irradiation fields. The major role of porosity in both fabrication and operating of PFCs is induced by the (i) the quality of actively cooled components which depends on the metal impregnation inside the macro-pores of the composite and (ii) the co-deposition mechanism inside CFC porosity which is responsible for the most of the fuel retention. It is expected that an accurate 3D porosity description of the CFC materials provides an essential input for the quantization of the fuel retention in the material bulk.

3D X-ray computed micro-tomography (μXCT) is a convenient TECHNIQUE used to monitor the morphology on extended volumes. The method can reveal the occurrence, distribution and shape of the regions with a different density at macro local scale. μXCT is the only tool available for the simultaneous determination of porosity factor and for the 3D visualization of the pore network on a rather macroscopic sample (up to 5x5x5 mm^3).

2. Materials and methods

The non-invasive inspection was pursued on samples with or without refractory/marker metal coating, non-irradiated or post-mortem samples. The main challenge is posed by the required micron range of the spatial resolution for rather macroscopic samples.
Most experiments were carried out at our newly upgraded X-ray tomography facility [1] (Figure 1).

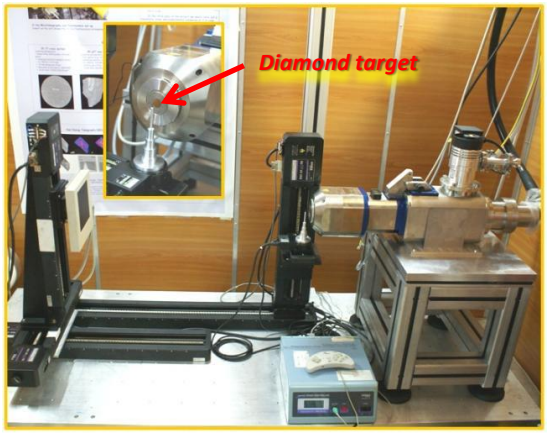

Figure 1 – View of the NILPRP Nano-CT facility.

Table 1 - X-Ray micro-tomographic system parameters

Micro-focus X-Ray source	Max. high voltage: 225 kVp Feature recognition: <1 μm Min object-focus distance: 0.3 mm X-Ray cone: 170° X-ray target power: <10÷30 W
X-Ray detection:	
- Detector elements/effective area	-768x576 / 169x169 mm2 7" XII 1024x1024/ 50x50 mm2 CMOS FP 1944x1536/ 145x115 mm2 a-Si FP panel sensor 1024x1024 flat panel sensor
Digital Output	10 to 16 bits
Sample micrometric manipulator	
-X stage	-travel up to 800 mm, loading capacity up to 30 kg
-Z stage	-travel 300 mm, loading capacity up to 6 kg
-θ stage	-accuracy 0.03°, loading capacity up to 10 kg
Magnification factor	< 2000
Spatial resolution	≥ 500 nm (JIMA mask)
Scanning time	< 15min. (1000 views)
3D reconstruction time	< 15 min (2048x2048x1024 voxels)
Scan method	Cone Beam CT; short scan CT (180° + fan angle) and Oblique cone-beam CT

The system is equipped with a last generation Nano-focus X-Ray source for non-destructive inspection. The source is operational in both micro- and nanofocus mode, at a tube voltage up to 225 kV and a maximum power of 10÷20 W. X-Ray images can be acquired by using three different high resolution detector types: Image Intensifier (XII) for rapid non-destructive examinations, flat panel (FP) detectors and a linear detector for the high density sample analysis. Positioning and turning around of the sample are insured by a set of seven high precision motorized micrometric manipulators.

Automation, control and data acquisition were obtained by means of in-house software package. The tomographic reconstruction for the cone-beam scanning is based on an optimized implementation of the modified cone beam filtered back-projection algorithm. Using a parallelization technique on multiprocessors workstations, experimental data consisting of large radiographic images (1944×1536 pixels) are processed for building the 3D reconstructions of typically 2048×2048×1024 voxels. The most important characteristics of the X-Ray tomographic system are presented in Table 1.

We have sustained an intense campaign of CT measurements of most relevant composite materials for fusion technology. For each type of material we cut three samples which have been measured in the same conditions. To our knowledge, this is the first time when such consistent comparison of different composite materials is proposed.

Optimization of the X-ray tomography setup in order to obtain appropriate spatial resolution for the analysis of the composites structure has been carried out. Materials scientist is interested in achieving a feature recognition value in the range of couple of microns. It is already a standard in our laboratory to use the JIMA mask as space resolution benchmark. The feature recognition of the X-ray source – detector system was continuously checked. Figure 2 shows a typical radiography of the JIMA mask in the micro-focus mode. One can see that the system can regularly achieve a detail recognition value under 3 µm. A set of 1440 radiographies at equidistant angles have been used for the high resolution fully 3D tomography. The voxel size was kept at 3.5 µm for the inspection of samples of 4x4 mm2 cross-sections.

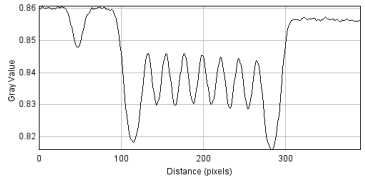

3 µm pattern line profile

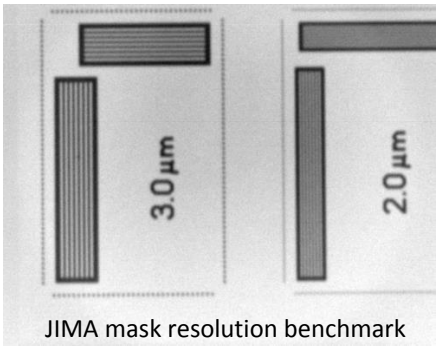

JIMA mask resolution benchmark

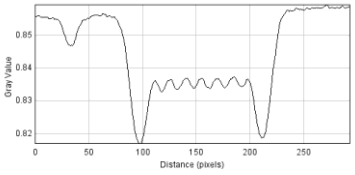

2 µm pattern line profile

Figure 2 – Microradiography of the JIMA mask in the micro-focus operation mode.

In the current work we apply cone beam micro-tomography to the comparative characterization of CFC materials relevant for fusion technology: NB31 and NB41 (SEP/Snecma) and DMS780 (Dunlop). For reference, homogenous fine-grain graphite (FGG) EK98 samples were also scanned. Table 2 gathers the materials and the relevant fusion facilities.

Table 2 - Carbon based composite materials of fusion technology relevance [2]

Material	Manufacturer	Fusion facility	Density [g/cm3]	Open porosity
CFC NB41	SEP/Snecma	ITER	>1.94	<7%
CFC NB31	SEP/Snecma	Former ITER	1.87-1.93	7%-9%
CFC DMS780	Dunlop	JET	1.75 – 1.87	12% - 15%
FGG EK986	Ringsdorff	TEXTOR	1.85	≈ 10%
CFC N11	SEP/Snecma	Tore Supra	1.71 – 1.78	≈ 12%

2.1. Qualitative comparison of CFC morphologies

Figures 3 a, b illustrate the morphology of JET type DMS780 CFC, a 2-D CFC formed by planes of PAN (polyacrylonitrile) fiber bundles perpendicularly oriented with interlayers (felt) of PAN fibers somehow randomly oriented. The size of the sample cross-section is ≈ 4 mm. The minimum detectable feature is a single fiber of 6-7 µm. The PAN fibers from the felt have a cladding of graphite of around 20 µm radius.

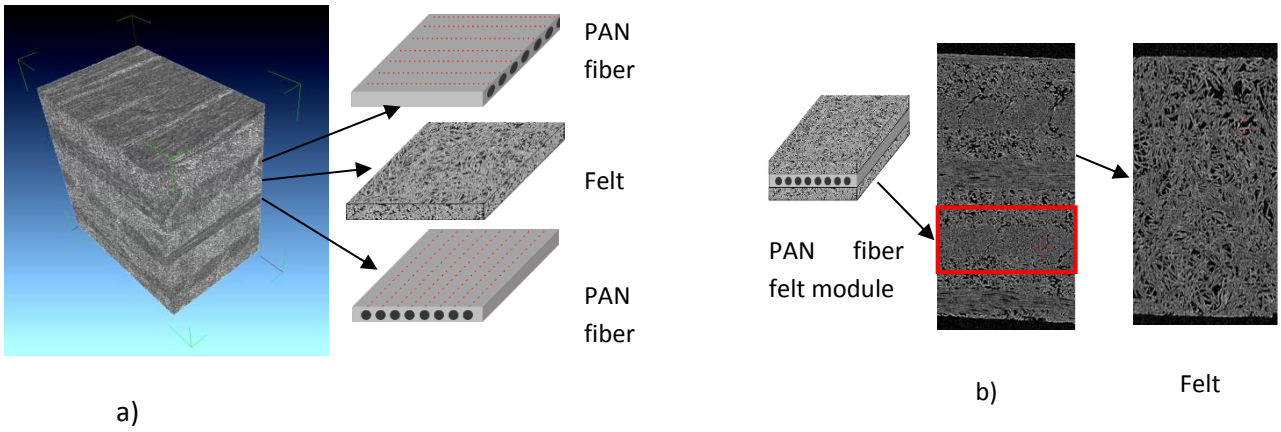

Figure 3 - a) 3D tomography reconstruction with the main components; b) the elementary module composed of one PAN and two felt layers.

Figures 4 show the architecture of the NB41, a state-of-the-art three-dimensional type of CFC.

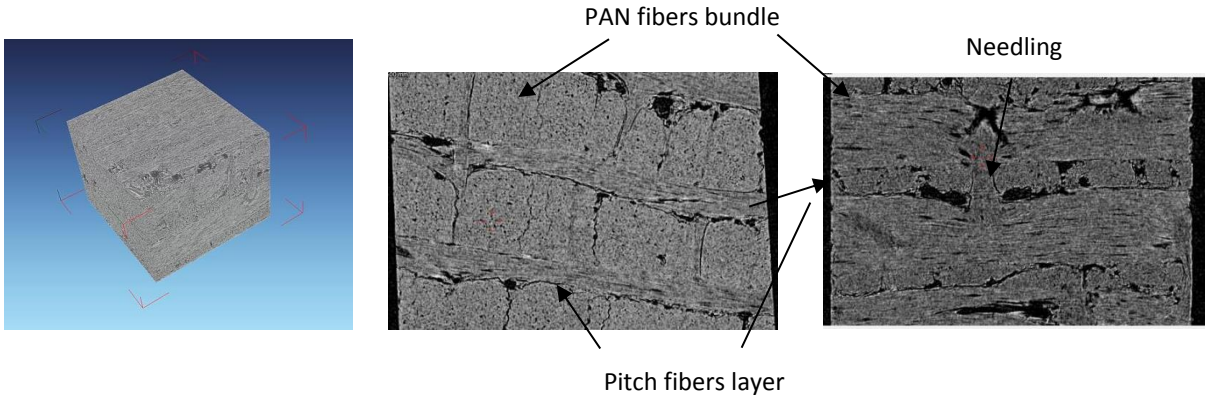

Figure 4 - 3D tomography reconstruction with the main components

The manufacturer considers that the two materials NB31 and NB41 are very similar 3D CFC types. However, one can see in Figure 5 some morphology differences related especially to the somehow more ordered nature of the newly developed NB41. Thus NB41 has in general thinner pitch fiber

layers with a clearer grid structure. Also the proportion of pitch fibers oriented in Z direction (horizontal in the picture) is larger.

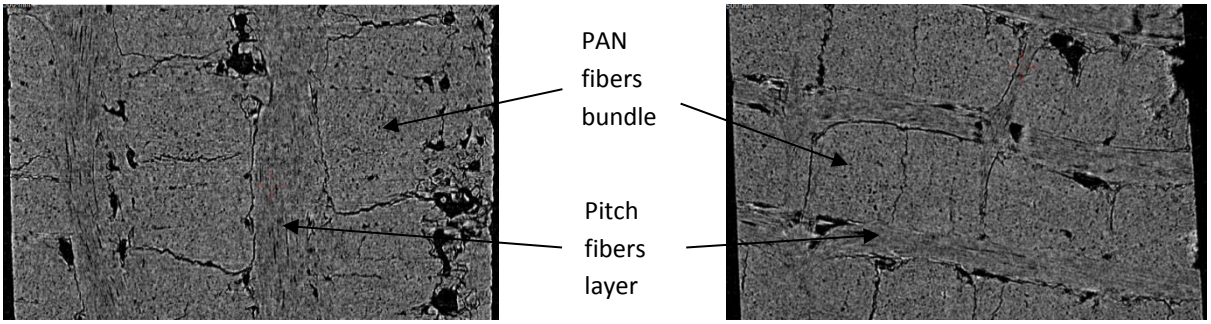

Figure 5 - Morphology differences between two types of 3D structured CFCs: NB31 and NB41. Note the somehow more ordered nature of the newly developed NB41.

2.2. Determination of porosity factors

The evaluation of total porosity and its parameters as open porosity, pore area or size distribution are important factors in evaluation and selection of carbon-based materials - carbon-fiber composites (CFC) and graphite - for the projects in fusion energy production. Since the first fusion experiments, nearly fifty years ago, the techniques used to measure the porosity of materials have very much evolved in diversity and performance, from gas adsorption/permeation or liquid extrusion to direct pore imaging. The porosity measurements for carbon materials used in projects currently running or nearing commissioning were regularly done by processing 2D gray-level images of plane sections cut from CFC samples on various directions relative to their fiber structure [3-5]. The images were obtained by optical or electron transmission microscopy or by micro-radiography. Until recently these methods were the only imaging technologies providing sufficient resolution to reveal directly pores in size ranges that correlate with the mechanical, thermal or other physical properties relevant for the uses of CFCs as construction materials. Simultaneously, the X-ray tomography of enhanced resolution of the order of 10 µm started to be employed in the investigation of relatively large porosity [6-7].

This approach has the merit of being flexible (a given image can be processed repetitively with e.g. newer algorithms better adapted for the various porosity characteristics). On the disadvantage side, one image characterizes only a thin slice of investigated material and thus may not be representative for the whole sample that can present important inhomogeneities or anisotropy.

In the particular case of CFCs, which have an important structural anisotropy, it is necessary to image and process a big number of slices (sections) with many spatial orientations, to fully characterize the sample. This is obviously expensive in terms of working effort and time required to make a complete porosity characterization for a given sample.

With the advent and fast evolution of micron-resolution X-ray tomography in the last few years, the possibilities of high-resolution digital image processing were complemented with the advantage of the image data acquisition in the whole volume of the sample, during a single exposition to X-rays [1, 8]. Of course, the presence of specific artifacts in X-ray tomographs may require some validation by classical methods as mercury [9] or gas porosimetry [5, 10], that reveal mainly the open porosity.

The tomography analysis is able to provide useful quantitative information about the porosity network of the composite samples and can be used to identify the relevant mechanism for fuel

retention into the material bulk like: fuel localization in the bulk or in the trapping sites (porosity) along fibers, or co-deposition into CFC open pores.

Figure 6 shows the attenuation coefficients histograms of the whole set of measurements. The measurements were carried out in the same conditions (X-ray energy and intensity, filters, magnification etc). The focus spot of the X-ray tube was benchmarked with the JIMA mask before each measurement. The densities of the materials are very well reproduced by the tomographic measurements. The histograms of NB31 and NB41 are very similar, as they are considered by the manufacturer to be almost identical materials. The 2D Dunlop manufactured DMS780 material has a lower density and clearly higher porosity.

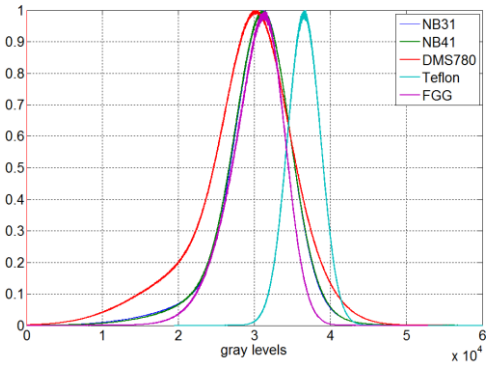

Figure 6 - Histograms of the attenuation coefficients for fusion technology relevant composite materials and a homogenous non-porous material.

A procedure for a quantitative evaluation of the sample porosity factor has been recently introduced and tested in [1]. The post-processing of the reconstructed voxel volume comprises several steps: (1) finding the optimal choice for the threshold level for voxel values (attenuation); (2) following validation, the reconstructed volume is segmented and the porous structure is extracted as an independent object which can be represented also as a 3D structure; (3) determination of the absolute value of the porosity factor. Voids volume, size and projected area distribution can also be determined.

With this method we obtained porosity factors for all fusion technology relevant CFC materials, in good agreement with the manufacturer specifications. The porosity factor uncertainty was evaluated based on the scattering of the estimated values for different samples of the same material and/or for different region of interest within the reconstructed volume. The uncertainty so determined is around half of a percent.

It must be stressed that, due to partial volume effect (the voxels located on pore edges have intermediary values between the attenuation of the sample material and that of voids), the information about porosity is easy to extract only for pore sizes sensibly larger than the resolution of tomography. This problem is treated in literature for different tomographic techniques, pore topologies and size distributions [11-12], and one can expect further improvement in this field.

The porosity factor was also evaluated by means of a second method. To demonstrate that the asymmetry of the attenuation coefficients histogram is related to the porosity of the material we present a simple experiment – tomography of two materials, with and without pores. Figure 7 shows a CT cross-section comparing a non-porous material (Teflon) with fine grain graphite EK 986, scanned side-by-side.

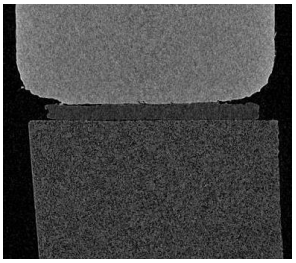

Figure 7 - µXCT of a non-porous material (Teflon) and of FGG EK986 (bottom) which has rather small pores

The histograms of the non-porous sample (Teflon) and of FGG EK986 are presented in Figure 8 a, b. As expected, the Teflon associated histogram is symmetric with a perfect fitting Gaussian. The histogram for FGG is clearly asymmetric as shown in Figure 8b.

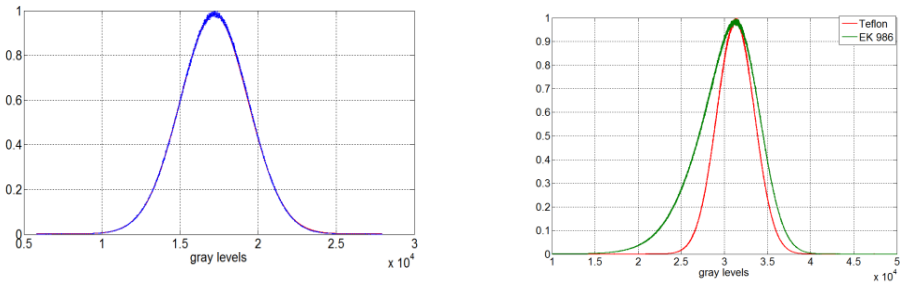

a) *b)*

Figure 8 - a) Symmetric histogram (blue) of a non-porous material (Teflon) and the Gaussian fit (red), b) histograms for Teflon (red) and EK 986, asymmetric (green)

The method for porosity evaluation would make use of this difference in the density profiles as follows:

- in a 3D visualization program (for example Volume Graphics , http://www.volumegraphics.com) a rectangular 3D selection is made;
- the histogram of the selected volume is generated;
- the histogram is further processed by fitting the right half (higher grey values) with a generalized Gaussian function;
- finally, the porosity factor is determined as the ratio between the area of the difference between the measured histogram and the Gaussian fitted one and the area of the Gaussian.

The last step is illustrated in Figure 9 a, b. The porosity factor associated with this figure is 6.4% for NB41 CFC and 12.5% for the more porous 2D CFC DMS780.

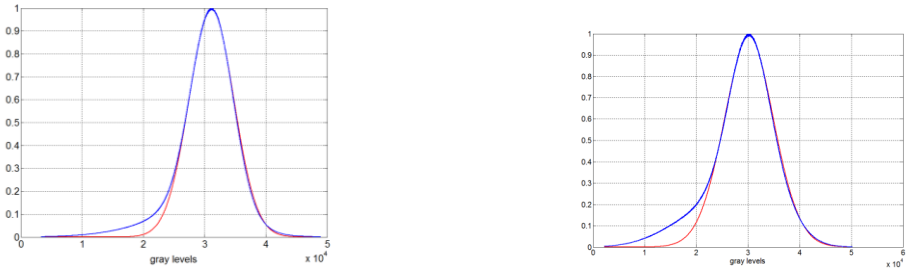

a) *b)*

Figure 9 -The porosity factor is determined as the ratio between the area of the difference between the measured histogram (blue) and the Gaussian fitted one (red) and the area of the Gaussian. a) NB41, b) DMS780.

The porosity factors are in good agreement with the manufacturer specifications. One can note that the method accounts very well for the excessive porosity of the 2D-structured DMS780 CFC material. It is also clear that in the case of EK 986 one underestimate the porosity due to the limited special resolution of the μXCT method.

Table 3: Porosity factors evaluated from tomography reconstructions

Material	NB31	DMS780	N11	NB41	EK 986
Porosity factor (%)	6.8	12.5	10.5÷12	6.4	4.25

Using the porosity factor procedure one can determine the overall porosity factor of a composite material (for example the DMS780 CFC) as a combination of the relatively low porosity of the PAN fiber layers (6÷8 %) and the more felt regions (≥20%).

3. Conclusions

Micro-tomography analysis was used for the 3D modeling of the fusion technology relevant CFC materials. For each type of material we cut three samples which have been measured in the same conditions. To our knowledge this is first time that such consistent comparison of different composite materials has been done.

High resolution morphology (voxel size ≈3.5 μm) of rather macroscopic CFC samples (4×4×4 mm^3) was obtained.

We show that our procedure for the quantitative evaluation of the sample porosity factor yields realistic results for the three types of CFC analyzed.

The results obtained by 3D micro-tomography analysis of statistically relevant volumes of CFC can be considered as a good basis for the characterization of the initial porosity of the new CFC ITER reference material NB41.

References

[1] Tiseanu I. et al. Fusion Engineering and Design, Vol. 86, Issue 9-11, October 2011, Pages 1646-1651

[2] Peacock A. T. et al. Phys. Scr. T128 (2007) 23–28

[3] Contescu C.I., Burchell T.D. report ORNL/TM-2009/192

[4] Kane J. et al. Journal of Nuclear Materials 415 (2011) 189–197

[5] Pawelko R.J. et al. INEEL/EXT-01-00481

[6] Babout L. et al. Carbon 43 (2005) 765–774

[7] Babout L. et al. Scripta Materialia 54 (2006) 829–834

[8] Kerckhofs G. et al. Review of Scientific Instruments 79(1) (2008) 013711

[9] Zhengcao Li et al. Advances in Materials Science and Engineering (2012) 640462

[10] Spitsyn A.V. et al. Journal of Nuclear Materials 390–391 (2009) 701–704

[11] Hwang S. N., Wehrli F. W. Magnetic Resonance in Medicine 47 (2002) 948–957

[12] Cooper D. et al. Calcif Tissue Int 80 (2007) 211-219

STUDY OF CONVERSION/REDEPOSITION OF REMOVED LAYERS DURING PLASMA TORCH CLEANING

C. Stancu[1], T. Acsente[1], E.R. Ionita[1], D. Allegre[2], F. Tabares[2], C. Grisolia[3], G. Dinescu[1]

[1]*Euratom-MEdC, National Institute for Laser, Plasma and Radiation Physics, PO Box Mg-36, Magurele, Bucharest, 077125, Romania*

[2]*Euratom-Ciemat, Av Complutense 22, 28040 Madrid, Spain*

[3]*Euratom-CEA, Institut de Recherche sur la Fusion par Confinement Magnétique DSM/IRFM, 13108 Saint-Pau-Lez-Durance, France*

[BS_19A/WP12-IPH-A03-2-02/PS]

Abstract

The experiments presented in this paper focused on the investigation of surface modification by erosion of the graphite material due to plasma torch, formation and transport of solid phase and gas phase products in the exhaust, and their characterization. The plasma torch jet was directed at an incident angle with respect with target surfaces, from where, after interaction with the surface was reflected and spread away. Collectors have been used to collect downstream solid phases. Various techniques (optical microscopy, electronic microscopy, energy dispersive X-ray analysis, etc.) were used for characterization of materials (target surface, and redeposited material) and for diagnostic of plasma jet and effluent gas (optical emission spectroscopy, mass spectrometry) after the jet-target interaction.

For assessment of redeposition we have worked with the nitrogen plasma torch in open atmosphere. We have observed re-deposition both on collectors positioned across the reflected jet and that positioned parallel, above and under the jet. The collected material can be classified in three categories: particulates of irregular forms, spherical particles, and film zones.

For assessment of formation of gas phase products the plasma jet and targets were mounted in a quartz enclosure, therefore the experiments proceeded in nitrogen atmosphere. For these experiments, graphite and stainless steel samples were used as targets. The optical emission spectra were very different in two cases, indicating that, comparing to the stainless steel target, a strong reaction of nitrogen plasma occurred with graphite, leading to gaseous CN radicals as main reaction product. We have found also that the CN radical emission increases strongly with the target temperature. In addition, by mass spectrometry we observed that the amounts of CO_2 and C_2N_2 molecules in the effluent gas are higher when the graphite target is exposed to the plasma jet, therefore these molecules are among the other gaseous species formed during the cleaning process.

Introduction

Previously, we have shown that plasma torch is an effective tool for removal of carbon and carbon/metal co-deposited layers from flat surfaces and from inside gaps. For example, in the case of carbon layers, consisting of graphite or hydrogenated carbon, the removal rates reached values as high as 10^{-2} g/min, by choosing appropriate gas mixtures (nitrogen, or nitrogen/oxygen) and surface temperature. The chemistry associated to the removal process, based on atomic nitrogen/oxygen erosion of the solid should lead to gaseous products, which are pumped out. Nevertheless, such hypothesis was never checked, and the possible redeposition of material, or dust formation, cannot be completely excluded. The project focuses on these aspects of the process of cleaning with a plasma torch, attempting to identify the products which result from the cleaning process.

2. Description of the work; results

2.1 Experimental setup-us

2.1.1 Experimental configuration for study of material erosion by a nitrogen plasma torch and assessment of redeposition

The main components of the experimental system were the atmospheric jet plasma source [1, 2], a graphite target and silicon substrate samples acting as collectors. The plasma source was supplied by RF power (13.56 MHz) and the value of power was 350 W. The discharge has been achieved in nitrogen gas with a mass flow rate of 3000 sccm.

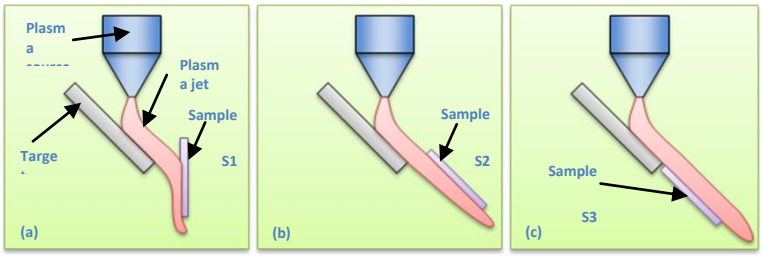

Figure 1 - Experimental arrangement of samples in relation to the position of the plasma jet and target, (a) for sample S1, (b) for sample S2 and (c) for sample S3

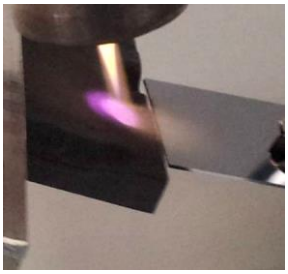

Figure 2 - The photo image during experiment

The target was a graphite plate with dimensions 30 × 30 mm by 5 mm thickness with a density of 1.75 g/cm^3. This low density, compared with that of other carbon material forms which normally presents values in the range 2.0-2.2 g/cm^3, suggests that the target material is a very porous form of carbon. In fact, this value is comparable with that of low density CFC materials.

To collect the co-deposited material we have used three silicon wafer substrate plates called sample S1, S2 and S3. The experimental arrangement of samples in relation to the position of the plasma jet and target it is presented schematic in the Figure 1 and a photo image during experiment is presented in Figure 2. The plasma jet falls at oblique incidence (45 deg) on the target and, from the incident point, flows along the target surface. The time of material collection for each sample was 3 hours. The distance from nozzle, where the plasma jet goes out from the plasma source, to target was 10 mm. The distance travelled by the plasma jet along the target surface (from the incident point to its edge) was around 5 mm.

In case of sample S1, geometry showed in Figure 1(a), the distance from edge of the target to the collector was 5 mm. In the cases presented in Figure 1 (b) respectively Figure 1 (c), the substrates (collecting samples S2 and S3) were placed parallel to target and very close to the edge of the target. The experiments were performed in open atmosphere.

2.1.2 Experimental configuration for study of conversion of eroded material in gas phase products

The experiments were performed in controlled nitrogen atmosphere by placing of graphite or stainless steel targets and the plasma source body in a quartz enclosure. In the chosen geometry the target surface was positioned at 25 degree with respect to the jet axis (Figure 3).

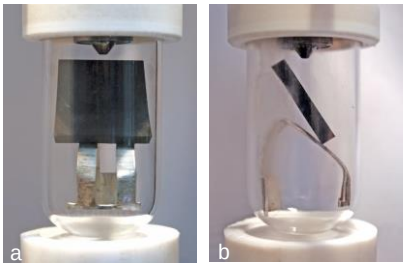

Figure 3 - Images of a graphite target positioned at 25 degree with respect to the jet axis a) front view and b) lateral view

The plasma jet was obtained in nitrogen at the following parameters: RF power = 300 W, nitrogen flows = 3000 sccm. Stainless steel and graphite samples were used as targets during the investigation of plasma jet cleaning experiments (Figure 3).The distance from nozzle to target was fixed to 10 mm.

Optical emission spectroscopy and mass spectrometry were the techniques used for diagnostic of plasma jet and effluent gas after the jet-target interaction.

2.2 Results and discussions

2.2.1 Investigation of target erosion

The photo of the target after plasma jet exposure during the entire experiment is presented in Figure 4. A series of craters is observed along its margins due to the erosion. The craters come from the fact that from time to time the target was displaced to expose a new fresh region to the jet, thus maintaining as much as possible the geometry of exposure. For the actual experimental conditions the erosion rate was about $1.6x10^{-5}$ g/sec (~10^{-3} g/min, or 0.06 g/h).

Figure 4 - Photo of the target after the target was exposed in the plasma jet

According to Figure 5 the SEM images in Figure 8 present the morphology of the carbon target in various zones, as follows: b) on the mechanically machined flat surface before the plasma action, a) from a clean fractured zone, untouched by plasma, c) from the bottom of the crater eroded by plasma; d) from the edge of the crater. It is observed that the raw material consists of compacted leaf like and particles from carbon, giving to the surface a quite rough character. The important thing, observable from Figure 6 is that in the bottom of crater the material morphology is unchanged as compared to the fractured zone; thus we conclude that plasma erode without melting or transforming the material.

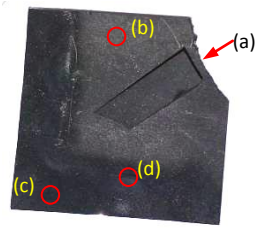

Figure 5 - Photo of target showing analysed zones

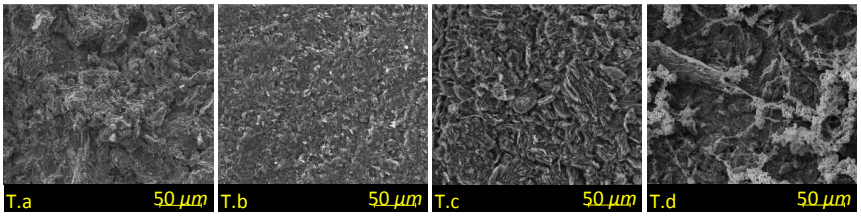

Figure 6 - SEM images of target with magnification 1000x., (T.a)-cracked zone untouched by plasma jet, (T.b)-plane zone untouched by plasma jet (T.d)-in centre of erosion crater and (T.d)- edge of erosion crater

2.2.2 Assessment of re-deposition and study of the deposits nature

The microscopic optical images of samples after exposure in the plasma jet are presented in Figure 7 (S1, S2 and S3). Also, in Figure 7 is presented the photo of an untreated substrate, sample S0. On these images the zones selected for SEM and EDX analyses are marked with red squares.

The comparison of images from Figure 7 shows, compared to sample S0, some particulates and spots appearing on the samples S1, S2, S3. Thus, we can conclude on the existence of some degree of re-deposition.

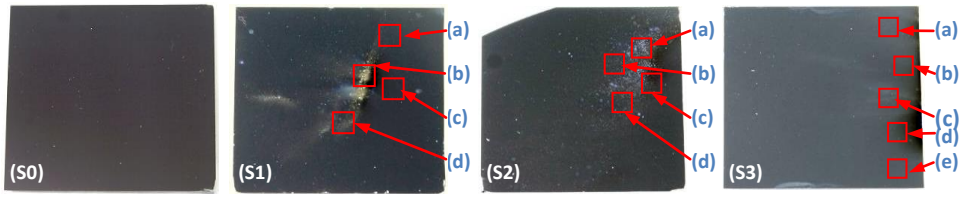

Figure 7 - The photos of the samples and the location where were investigated by SEM and EDX. Sample S0 is untreated

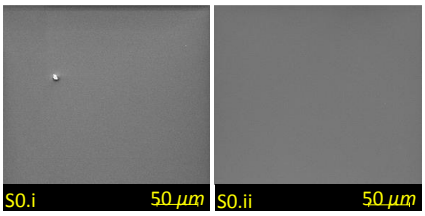

Figure 8 - SEM images of control sample acquired in two different zones with magnification 1000×

Investigation of the morphology of redeposited material

More details on the morphology the re-deposited material on the used collectors are as presented below by SEM images, recorded with different magnifications, from the zones marked with (a), (b), (c), (d) in Figure 7.

The control sample

The control sample (silicon wafer) has a clean smooth surface on which very few particles, probably from contamination by dust from atmosphere (Figure 8) are observed.

Sample S1

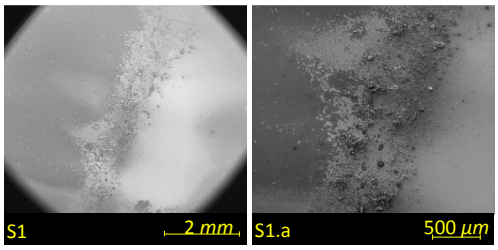

Figure 9 - SEM images of sample S1 in zone S1.a. (magnification 40× and 100×)

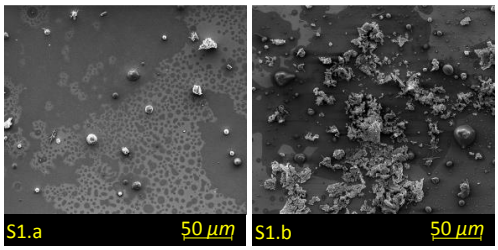

Figure 10 - SEM Images of samples S1 in zones (a) and (b) (magnification 1000×)

The redeposition of sample S1, at low magnifications (40× and 100×), is visible in Figure 9. The cloud of deposited material distributed along a line corresponds to the region of contact of plasma spread by the target surface with the collector. A detailed analysis of this region shows that the collected material is presented mainly in two forms, thin film regions, and respectively particles. The morphology of both forms of the material collected are shown in Figures 10 and 12, which show SEM images of the S1 sample in analysis areas (a), (b), (c) and (d), with magnification of 1000×. The particles have sizes in the range 0.5 to 20 µm. Two types of particles morphology can be observed (see Figure 11): i) round particles which seems to be locally synthesised on surface (probable from gaseous precursors formed via plasma species reacting with the carbon target), and ii) rough

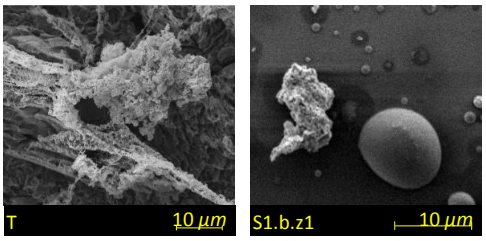

Figure 11 - SEM Images from the target crater edge (left), and zone (b) of samples S1 (right)

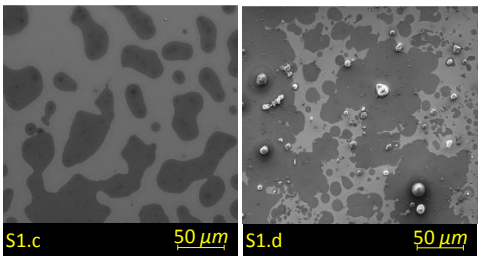

Figure 12 - SEM Images with magnification 1000× of samples S1 in zone (c) and (d)

particles, which seems to be detached from target, and transported on substrate; also these particles may have a local origin, looking like the foam observed on the crater margins, as compared in Figure 11.

Very interesting, the coating of collectors with spots of films is observed, as exemplified in Figure 12.

Sample S2

SEM analysis of sample S2 shows a collection of spherical or irregularly shaped particles.

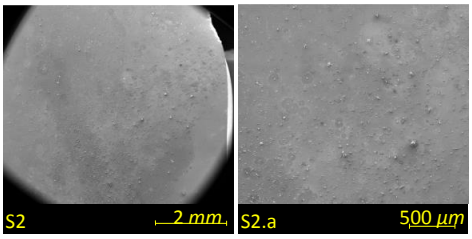

Figure 13 - SEM images of sample S2 with magnification 40× and 100× in zone S2.a.

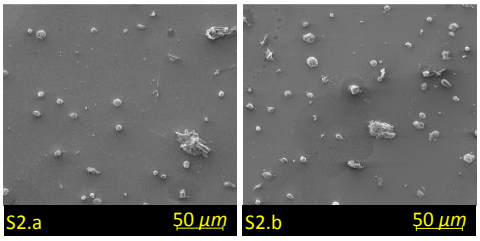

Figure 14 - SEM Images with magnification 1000× of samples S2 in zone (a) and (b).

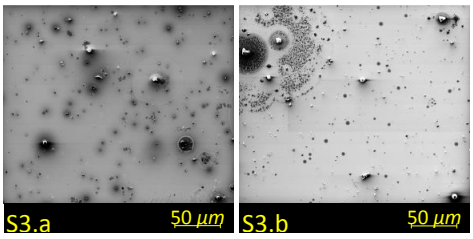

Figure 15 - SEM Images with magnification 1000× of samples S3 in zone (a) and (b)

Sample S3

The material collected on sample S3 consists mostly of spherical particles; some particles are accompanied by a halo; we should notice that the smaller particles are frequently organized around bigger particles.

Data on chemical composition of redeposited material

Details on the composition of the re-deposited material are supplied by EDX analyses. A typical EDX spectrum is presented in Figure 16. We have recorded EDX spectra in all zones marked with red squares in Figure 7. Beside Si (whose signal comes from the substrate: X-rays are excited and collected from a drop volume of around 10 microns in diameter) only C, O and N elements were observed, around in all cases. Their concentrations varied from point to point. Due to the variable amount of redeposited materials in the different areas the comparison of EDX results coming from the different zones is difficult. Therefore, we have chosen to average the composition results, obtained from all zones and to compare with the control sample. The results are presented in Table 1. It proves the increase of carbon on surface due to redeposition, but also the increased presence of oxygen and nitrogen. Therefore, we can hypothesise that beside carbon redeposition, substrate oxidation and nitridation, a carbon oxynitride can be formed.

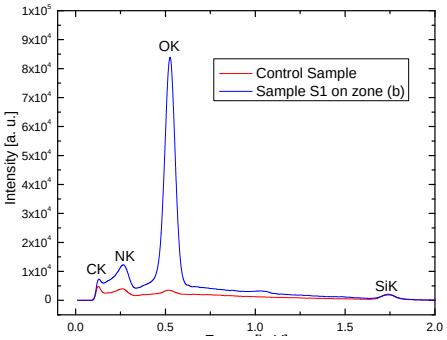

Figure 16 - Typical EDX spectra acquired on treated sample S1(b) and on control sample

Table 1. - Atomic percentage of identified elements on control sample and also mean of atomic percentage on samples S1, S2 and S3 from all investigated zones showed in Figure 9

Element	CK	NK	OK	SiK
Control Sample	3.39%	0.94%	1.56%	94.11%
Samples S1-S2	5.84%	2.38%	27.10%	64.68%

2.2.3 Assessment of conversion of removed material to gaseous species

Imagistic study of plasma jet-target system during the cleaning process

At the contact of the jet with the target a reflection and spreading of plasma is noticed. In Figure 17 are presented frontal and lateral images of the samples during cleaning process: a) and b) stainless steel target; c) and d) graphite target.

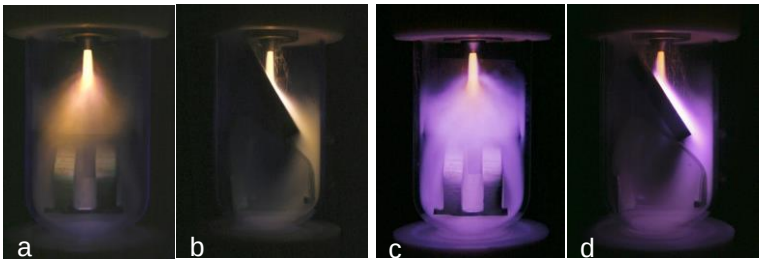

Figure 17 - Images of the samples during cleaning process a) frontal view stainless steel target; b) lateral view stainless steel target; c) frontal view graphite target and d) lateral view graphite target

From the images we observe that, compared to stainless steel, the intensity of plasma jet is higher when graphite is used as target. Also the colour is very different, indicating that the gaseous species present in plasma after the interaction with the two substrates are different.

Spectral study of the plasma jet-target system during the cleaning process

The optical emission spectroscopy (OES) experiments were realized in stationary, flowing conditions. The light for diagnostic of the plasma jet was collected from below and lateral zones of the samples, corresponding to the after plasma-target interaction region (schematic view presented in Figure 3, and picture views in Figure 17).

In Figure 18 two emission spectra collected from plasma reflected by target are presented. One spectrum is collected with stainless steel target (blue line) and second is collected with graphite target (red line). The most important emitting species can be identified through their spectral systems of molecular bands, as follows: γNO ($A^2\Sigma^+$-$X^2\Pi$), NH ($A^3\Pi$-$X^3\Sigma$, $\Delta v=0$), SPS N_2 ($X^3\Pi$-$B^3\Pi$, $\Delta v=0$), FPS N_2 ($B^3\Pi$– $A^3\Sigma$), violet CN ($B^2\Sigma^+$-$X^2\Pi$, $\Delta v=0$, +/-1). The spectra are very different as intensity, therefore are represented on different scales, left scale is for graphite spectra and right scale is for stainless steel. The comparison of spectra obtained with graphite and with stainless steel) indicates important changes as follows:

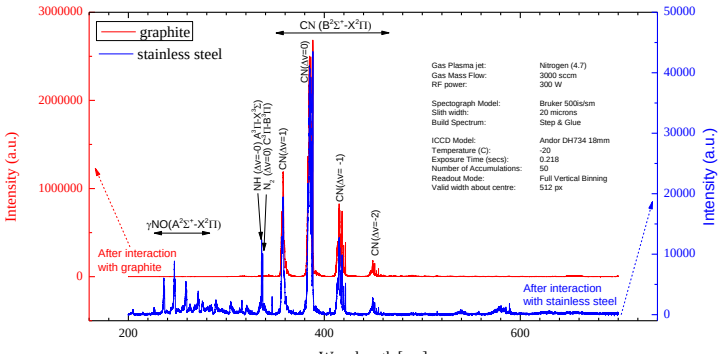

Figure 18 - Spectral emission of nitrogen plasma jet, collected after its interaction with the graphite target (red) and stainless steel target (blue)

- CN radical emission increases very much, all sequences $\Delta v=+1, 0, -1$ of the violet spectral system CN ($B^2\Sigma^+$-$X^2\Pi$) being very strong;
- emissions of SPS N_2 decreases, and those of the FPS N_2 practically disappear;
- γNO bands are disappearing.

With respect to the behaviours of CN and N_2 species, a quantitative description of these behaviours is possible by comparing the integrated intensities over the spectral ranges where these emissions appear. First spectral range (337.04 nm to 337.20 nm) is representative for the emission of N_2 species, while the second spectral range (384.1 nm to 388.5 nm) is representative for the emission of the formed CN species. According to the data, the emission of nitrogen diminishes when the stainless steel target is replaced by a carbon target, by the ratio $A(N_2, C)/ A(N_2,SS) = 0.68$, while the emission of CN increases drastically, by the ratio $A(CN, C)/ A(CN,SS) = 605$. These data come in the support of the following mechanism: the nitrogen species from plasma are used to create CN radicals, by combination with carbon species etched from the target. In addition, the disappearance of γNO bands emission suggests that nitrogen can be supplied also via the breakage of the NO radical, being possible for the released oxygen to accelerate the carbon removal, leading to gaseous CO2 and CO radicals.

Mass spectrometry diagnostic of effluent gas during the cleaning process

In order to identify species which cannot be observed by OES, the diagnostic of effluent gas during the cleaning process was realized by mass spectrometry. The difficulty of such experiments is high: species may recombine, and only long life species will survive on the way from the plasma-target interaction region to the mass spectrometer. The experiments were realized in flowing conditions, with the graphite target placed in the plasma jet. The effluent gas leaving the quartz enclosure was conducted by a long pipe (length 4m, inner diameter 4 mm) in a vacuum chamber connected to the mass spectrometer. In this experiment we recorded the following atomic and molecular species: Ar, C_2N_2, CO_2 and CN. Ar species were recorded as reference, Ar coming from the nonreactive gas impurities. Figure 19 presents the behaviours of these species densities (in counts/sec) during the cleaning process, when the nitrogen plasma was set to "on "and "off "conditions, for 2-4 minutes each step.

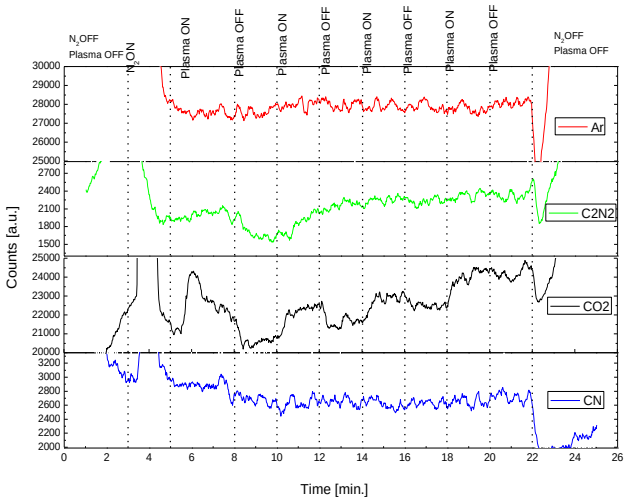

Figure 19 - Evolution of the atomic and molecular species during the nitrogen plasma cleaning process

Figure 19 shows that the counts for CO_2 and C_2N_2 increase when plasma is on, and decrease when plasma is off. However, a delay is observed, which is due the transport time of formed species through the long pipe. After a number of cycles this variation disappears, which is due to the low pumping rate of the vacuumed chamber, in which these species accumulate. The CN variation is hardly observed, indicating that CN radicals, that are so strong in emission, recombines forming other species, most probable C_2N_2.

3. Conclusions

When we worked with the nitrogen plasma torch in open atmosphere we observed re-deposition both on collectors positioned across the reflected jet and that positioned parallel, above and under the jet. The collected material can be classified in three categories: particulates of irregular forms, spherical particles, and film zones. The particles of irregular forms are probably broken parts from the target, transported to collector by the plasma flow, or foam like material synthesised on the collector. The spherical particles seems to be synthesised locally, as indicated by collecting regions formed around them; the film-like material centred on and surrounding the spherical particles, suggests a condensation process, supported by gaseous precursors formed via plasma species reaction with the carbon target. The chemical composition of the redeposited layers indicates presence of carbon, and possible formation of a carbon oxynitride compound. For assessment of formation of gas phase products the plasma jet and targets were mounted in a quartz enclosure, therefore the experiments proceeded in nitrogen atmosphere. For these experiments, graphite and stainless steel samples were used as targets. Special interaction geometry was designed, which allows the recording of spectra downstream the interaction region of plasma with the target. Thus, a comparison of spectra obtained after the interaction with graphite material, and of the spectra recorded after the interaction with stainless steel was possible. The spectra were very different in two cases, indicating that, comparing to the stainless steel target, a strong reaction of nitrogen plasma occurred with graphite, leading to gaseous CN radicals as main reaction product. The results confirm our previous hypothesis that carbon erosion by plasma is based on a chemical process in which carbon atoms reacts with nitrogen excited species leading to CN radicals [1,2]. We have found also that the CN radical emission increases strongly with the target temperature. This is in agreement with our results [3] which demonstrated that the erosion rate is higher at higher values of the substrate temperature. In addition, we have used mass spectrometry for diagnostic of effluent gas during the cleaning process, trying to identify the species which cannot be identified by OES. From these measurements we observed that the amounts of CO_2 and C_2N_2 molecules in the effluent gas are higher when the graphite target is exposed to the plasma jet, therefore these molecules are among the other gaseous species formed during the cleaning process. It is clear that the removal of carbon layer will lead also to the removal of the fuel incorporated in it.

With respect to the amount of material which is redeposited it appear to be only a small part of the eroded material, but it is difficult to give a figure. As seen above when the experiments were performed in open atmosphere solid phases have been collected on the side substrates, proving condensation of species and transport of particles broken from target. Nevertheless, in similar experiments performed in controlled nitrogen atmosphere such solid phases were not observed. This is an aspect which deserves more detailed investigation, as it can lead to dust free cleaning.

Acknowledgement

The reported results were obtained in the frame of Euratom Task WP12-IPH-A03-2-02 MEdC.

References

[1] G. Dinescu, E. R. Ionita, I. Luciu, C. Grisolia, *"Flexible small size radiofrequency plasma torch for Tokamak wall cleaning"*, Fusion Engineering and Design, 82 (15-24), 2311-2317, (2007).

[2] G. Dinescu, E. R. Ionita, "*Radio frequency expanding plasmas at low, intermediate, and atmospheric pressure and their applications"*, Pure and Applied Chemistry, 80 (9), 1919-1930, (2008)

[3] G. Dinescu, Scientific Report of the task WP11-PWI-02-04 (2011)

DEUTERIUM RE-ADSORPTION/RE-SATURATION OF W SURFACES SUBJECTED TO HELIUM RF-DISCHARGE AS A FUEL REMOVAL TECHNIQUE

T. Acsente[1], C. Stancu[1], E.R. Ionita[1], C. Grisolia[2], G. Dinescu[1],

[1]Euratom-MEdC, National Institute for Laser, Plasma and Radiation Physics, PO Box Mg-36, Magurele, Bucharest, 077125, Romania

[3]Euratom-CEA, Institut de Recherche sur la Fusion par Confinement Magnétique DSM/IRFM, 13108 Saint-Pau-Lez-Durance, France

[BS_19B/WP12-IPH-A03-2-03/PS]

Abstract

An experimental setup was configured. It allows preparation of deuterated W samples (W_D) by magnetron sputtering (MS) of a W target in Ar+D_2 gaseous mixture (with biased, grounded or heated substrate). A parametric study of deposition process was performed. Two parameters of the deposition process were considered: the D_2 content in Ar/D_2 sputtering gas mixture and the substrate temperature. All deposited samples present columnar growth and their surface morphology (SEM) is slightly dependent on deposition conditions. This result proves that our deposition setup and established working conditions allow deposition of layers in different conditions while preserving similar morphological features. The presence of deuterium in W deposited layers was proved by qualitative SNMS (Secondary Neutral Mass Spectrometry) measurements and ERDA (Elastic Recoil Data Analysis) technique. A higher content of deuterium was detected in the samples deposited in gas mixtures containing more D_2.

Other samples of W bulk material (delivered by CEA partner) and W thin films (deposited by MS in pure Ar on silicon) were deuterated by exposure to D2 plasma. AFM investigations of bulk samples did not show changes in the samples topography due to plasma treatment. AMS investigation proved incorporation of deuterium in pure W thin films; exposure of MS-W thin films to D2 plasma leads to loss of their adherence. The W bulk samples (after treatment in D2 plasma) and a sample with variable deuterium profile (three layers “sandwich”) were delivered to project partners.

Papers

A.R. Petre, T. Acsente, M. Enachescu, G. Dinescu, C. Stan-Sion, M.S. Dogaru, I. Dorobantu, L. Neagu "*AMS measurements of deuterium captured in tungsten layers deposited by magnetron sputtering*", accepted, Romanian Reports in Physics, 2013

1. Introduction

The project (joint EURATOM project between CEA /Université de Provence (CEA) – France - Jozef Stefan Institute (JSI) – Slovenia – and National Institute for Laser, Plasma and Radiation Physics from Romanian Association (NILPRP- MEdC)) combines both experimental and theoretical methods, with the aim to assess the impact of helium RF discharge as a fuel removal technique on the re-adsorption of D in W. The main contribution of the Romanian team was to prepare nondeuterated and deuterated W-MS samples (with different W/D ratios or variable D profiles), deposited by magnetron sputtering (MS) technique and delivers them to CEA/JSI.

2. Configuration of an experimental setup for deposition of W-MS type samples

The experimental setup configured for deposition of W deuterated samples is presented in Figure 1. It is based on a small vacuum chamber, presenting 5 ports (denoted A and B in Figure 1). The top A port is used for attaching to the chamber of a magnetron sputtering gun (1) (for deposition of tungsten) or of a plasma source capacitively coupled (for gentle deuteration of W substrates). The

substrate holder is positioned inside the vacuum chamber using an electrical feedthrough (2) mounted on a lateral B port, allowing to perform both mentioned plasma processes in biased (DC, RF) or grounded substrate configurations.

Figure 1 - Experimental setup configured for obtaining W deuterated samples

The opposite B port (3) is used for connecting the chamber to a vacuum pump. One of the lateral A ports (in the back part of Figure 1) is used for sustaining an ISO25 cross, on which are mounted: a pressure gauge (4), the admission point (5) of processing gasses (Ar, D_2 or mixture of Ar/D_2) and a lever (6) for a shutter. An optical window (7) is mounted on the remaining port A; this port is also used for mounting a 1 ½" electrical oven inside the vacuum chamber.

The deposition chamber allows the following type of processes to be performed:

A Deposition of W layers by magnetron sputtering with biased, grounded or heated substrate;

B Deuteration of bulk W samples using two procedures: ***Bi)*** exposing the biased W substrate to a deuterium ion flux produced by a RF plasma source or ***Bii)*** applying an RF bias on the substrate holder. The later deuteration procedure is supposed to be more energetically compared with the first one.

3 Realization of deuterated tungsten layers

3.1. Deposition of deuterated W layers by magnetron sputtering

Process parameters, deposition of preliminary samples. Three types of W samples were deposited on Si substrates using the following working gases: Ar (sample denoted W_{AR}), $Ar+D_2$ (samples denoted W_D) and $Ar+H_2$ (samples denoted W_H). W_{AR} samples were deposited using the following working parameters: 47W applied RF power, 20sccm mass flow rate of Ar, pressure of 9E-3 mbar, distance between target and substrate 7 cm. The deposition of W_D and W_H samples by MS was performing considered two approaches: ***a)*** keeping the pressure of Ar/D_2 or Ar/H_2 constant, i.e. at the same value as for deposition of W_{AR} sample (9E-3 mbar); and ***b)*** keeping the partial pressure of Ar constant (the same as in W_{AR} process) and adding supplementary D_2 or H_2. Using the approach ***a)***, the deposited W_D and W_H layers were highly stressed, delaminating from the silicon substrate even during deposition. Mechanically stable layers (having thickness of minimum 500nm) were obtained using the ***b)*** type approach. Preliminary samples were deposited using the following deposition parameters: deposition pressure 1.4 E-2 mbar, mixture gas containing 40% D_2 or H_2 (20 sccm Ar mixed with 10 sccm D_2 or H_2).

Deposition of W_D by MS at different values of process parameters. Two sets of W_D type samples were deposited on Si substrates, corresponding to modification of the following deposition parameters: content of D_2 in the Ar/D_2 mixture and the substrate temperature. The following values of D_2 content in the Ar/D_2 mixture were used: 8.5%, 15.7%, 38% and 42%. The following substrate temperatures were used (while the content of D_2 in the Ar/D_2 mixture was kept constant i.e. 15.7%):

100^{O}C, 150^{O}C, 200^{O}C and 300^{O}C. Deposition duration was 1 hour for each sample. All deposited samples were stable on the Si substrate.

Deposition of W samples with variable content of Deuterium. In addition, a "sandwich" of three tungsten layers deposited on silicon substrate: the in-between layer (660nm thick) is W_D type and is deposited in mixture of Ar and D_2 whiles the outer layers (500nm thickness) is of W_{Ar} type and is deposited in pure Ar.

3.2 Deuteration of bulk W layers by exposure to D_2 plasma

Deuteration of bulk W samples. Two samples of bulk W provided by project partners (CEA) were subjected to deuterium plasma for assessing the effect of this procedure over the samples. The samples (denoted ECH1 and ECH3) present identical dimensions (10×10×4mm); the difference between them is their surface roughness and thermal pre-treatment. Both samples were positioned on the same holder and were exposed simultaneously to the deuterium plasma produced by biasing the substrate holder with RF electrical power (method ***Bii*** presented above). The deuteration process parameters are: 10 sccm D_2 mass flow rate; 40W RF applied power (13.56 MHZ); 5 hours duration of treatment; 7.5E-2 mbar pressure during first hour and 7.4E-2 mbar to the end of process. During deuteration process, the samples temperature increased up to 320^{O}C (by plasma heating); after plasma stopping, the samples were cooled down for 30 minutes in constant flow of D_2 (10 sccm) at a pressure of 4E-1 mbar. The optical emission of the processing D_2 plasma was monitored using an OMA HR 400 optical multichannel analyzer (0.2 nm resolution). The following D_2 specific emission features were identified: D_α (656.1nm) and D_β (486.0 nm) atomic emission lines and the Fulcher α bands ($d^3\Pi_u \rightarrow a^3\Sigma_g^+$, 546-710nm) [1], [2].

Deuteration of W_{Ar} layers deposited by magnetron sputtering. W_{Ar} type samples (deposited by MS on Si substrate using Ar as sputtering gas), were exposed to D_2 plasma for 1 hour, using the same working parameters as for deuteration of bulk W samples presented previously.

4. Properties of deuterated samples

The tungsten samples deposited by MS were investigated by Scanning Electron Microscopy (SEM) in surface mode (for surface morphology evaluation) and in cross section mode (for evaluation of deposition rate). The surfaces of bulk W samples were investigated (prior and after exposure to deuterium plasma), by Atomic Force Microscopy (AFM). The content of deuterium in the W_D and W_H preliminary deposited layers was evaluated by qualitative SNMS (Secondary Neutral Mass Spectrometry) measurements. SNMS is well known for low accuracy in detecting low mass elements, in this respect efforts were made for accessing other investigation techniques, like ERDA (Elastic Recoil Data Analysis) and AMS (Accelerated Mass Spectrometry); these facilities are located at the "Horia Hulubei" National Institute of Physics and Nuclear Engineering – IFIN HH – Bucharest.

Figure 2 shows results of SEM investigations over MS deposited W_D type samples: they present columnar growth (Figure 2.a) while their surface morphology is slightly dependent on deposition conditions (Figures 2.b and c). The layers appear pretty smooth and there were no observed specific features (like pores or blisters, as reported in literature [3], [4])

Figure 3 presents the influence of considered MS process parameters on W_D layers growth rate; it can be observed that the deposition rate decreases slightly when the deuterium content or substrate temperature increases.

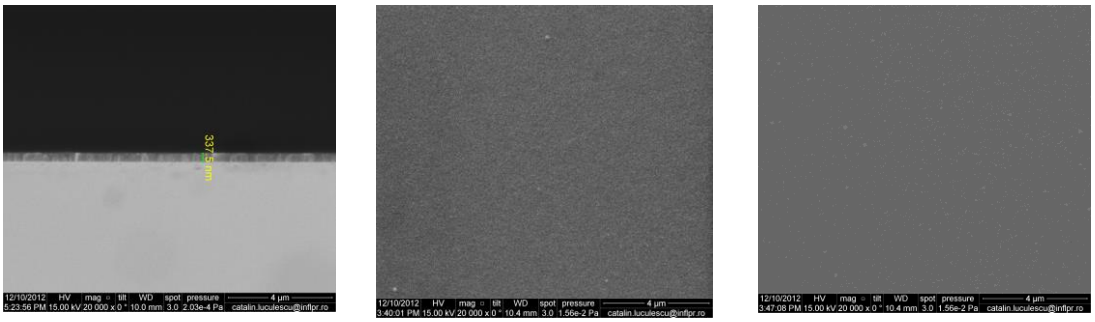

(a) *(b)* *(c)*

Figure 2 - a) cross section SEM image of the W layer deposited with 8.5% D_2 ; and surface SEM images of samples deposited using only Ar (b) and with 15.7% D2 (c)

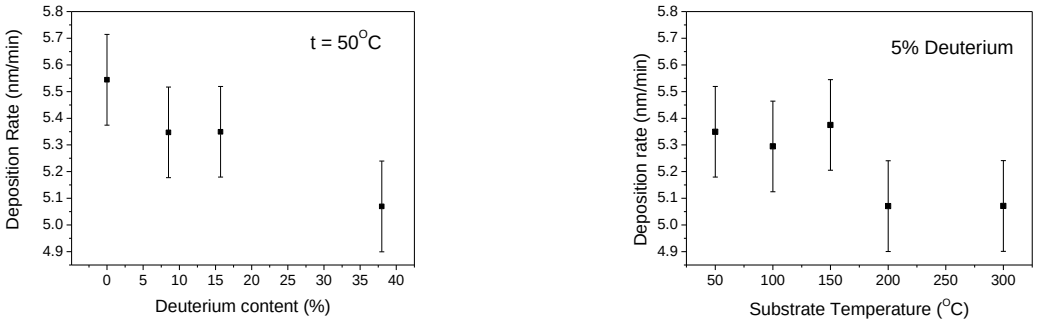

a) *b)*

Figure 3 - Variation of W deposition rate as a function of: a) content of D_2 in sputtering gaseous mixture; b) substrate temperature

As regarding W_{Ar} (deposited by MS on Si substrate) type samples exposed to D_2 plasma, the first effect observed (visually) was the modification of the W thin film aspect: while the deposited W layer is adherent to the substrate and presents a smooth surface, it becomes more rough and can be easily detached from the substrate after the plasma treatment. SEM investigations before and after plasma treatments do not reveal any change; such as, the exfoliation of the W layers was related to thermal stress induced by plasma treatment.

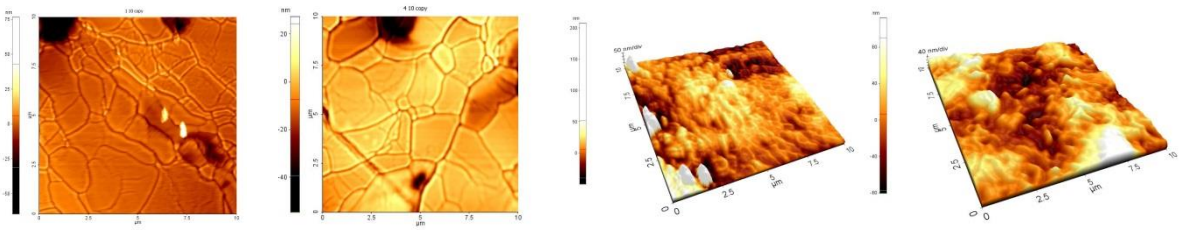

a) RMS 8.2nm *b) RMS 8.1nm* *c) RMS 23.4nm* *d) RMS 30.2nm*

Figure 4 - AFM images of ECH1 sample surface before (a, c) and after (b, d) exposure to D_2 plasma

AFM investigations performed on bulk W samples surface highlight between smoother and rougher regions (Figure 4), revealing the boundaries of the W grains from which the samples were produced.

Exposure to D_2 plasma of both ECH1 and ECH3 samples do not modify their surface topography (see Figure 4 for ECH1 sample).

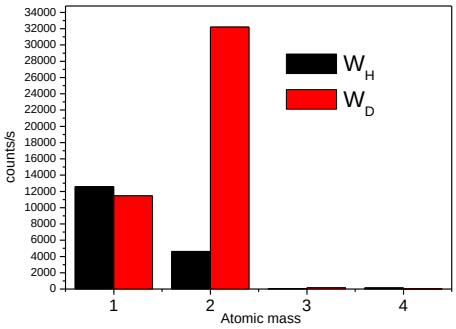

Figure 5 - Comparison between SNMS signals of W samples deposited in Ar/H_2 and Ar/D_2 gaseous mixtures

We note that the different values of the roughness observed before and after plasma exposure in Figure 4 are due to evaluation of RMS in different places of the sample rather to a plasma treatment effect.

Results of the SNMS (Secondary Neutral Mass Spectrometry) measurements performed over the preliminary deposited W_H and W_D are presented in Figure 5. The signal for 1 a.m.u. corresponds to H atoms while the signal of 2 a.m.u. can be associated, in addition to D atoms, with H_2 (present in the sample or in the SNMS chamber as residual, for example originating from the insufficiently pumped water). While the SNMS signal corresponding to 1 a.m.u. is near identical in both W_D and W_H samples, the signal for 2 a.m.u. is much higher in the W_D sample compared with the W_H one, proving the presence of D in W_D type sample.

Figure 6 presents the ERDA energetic spectra of the recoil D nuclei for two W samples, i.e. the sample deposited using only pure Ar (0% D_2, black curve) and the sample deposited using 38% D_2 (red curve). A higher content of D in the sample deposited with higher content of D_2 in sputtering Ar/D_2 mixture is noticed. The presence of deuterium in the sample deposited only with pure Ar can be explained as a contamination of the deposition chamber from the previous depositions.

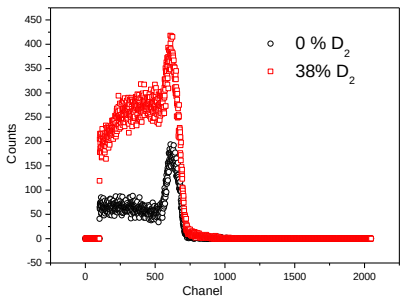

Figure 6 - ERDA spectra of recoil particles (D nuclei) for samples deposited in pure Ar (black) and in D_2/Ar mixture containing 38% D_2

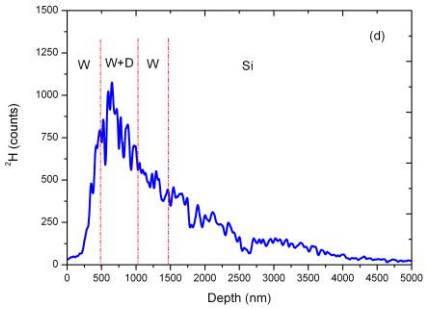

Figure 7 - Dependence of Deuterium counts as function of depth in "sandwich" sample (three tungsten thin layers on silicon substrate), measured by AMS

Figure 7 presents the deuterium depth profile of the "sandwich" sample, recorded by AMS; it can be observed a maximum of the deuterium signal in the middle of the sample. We mention that AMS measurements proved also incorporation of deuterium in W_{Ar} sample exposed to D_2 plasma. While the ECH1 and ECH3 samples were subjected in the same condition to D_2 plasma (but for a longer duration), we can suppose that ECH1 and ECH3 samples were successfully implanted with deuterium.

5. Conclusions

A new experimental setup was configured for preparing deuterated W samples, using plasma methods, i.e. using magnetron sputtering (MS) in Ar+D_2 gaseous mixture or exposure of W substrates to a deuterium plasma.

Preliminary samples of deuterated tungsten thin films (W_D) were prepared using MS. A parametric study of MS deposition of deuterated tungsten layers was performed. Two parameters of the deposition process were considered: the D_2 content in Ar/D_2 working gas mixture and the substrate temperature. Scanning Electron Microscopy (SEM) investigation show that samples surface morphology is slightly dependent on deposition conditions: the layers appear pretty smooth and no specific features (pores or blisters) similar to that reported in literature were observed. This result proves that our deposition setup and established working conditions allow deposition of deuterated W layers in different experimental conditions, while preserving similar morphological features. The presence of deuterium in W_D deposited layers was proved by qualitative SNMS measurements (for preliminary samples). ERDA (Elastic Recoil Data Analysis) technique investigations of two samples (included in the parametric study) shown a higher content of deuterium in the samples deposited by using an Ar/D_2 mixture richer in D_2.

In addition, a three-layer sample with variable deuterium profile (a W_D layer in between two non-deuterated W layers) was prepared. The deuterium depth profile of the "sandwich" sample was recorded by AMS (Accelerated Mass Spectrometry); the maximum content of D_2 was detected in the middle of the sample.

Other samples of W bulk material (delivered by CEA partner) and W thin films (deposited by MS in pure Ar on silicon) were deuterated by exposure to D_2 plasma. AFM investigations of bulk samples did not show changes in the samples topography due to plasma treatment. AMS investigation proved incorporation of deuterium in pure W thin films; exposure of MS-W thin films to D_2 plasma leads to loss of their adherence.

The W bulk samples (after treatment in D_2 plasma) and the sample with variable deuterium profile (three layers "sandwich") were delivered to project partners.

Acknowledgments

The reported results were obtained in the frame of Euratom Task **WP12-IPH-A03-2-03/BS-01/MEdC**

References

[1] Dieke G.H., Blue R.W. , Phys.Rev. 1935; 47:261;
[2] S. Menmuir et al , J. Quant. Spectr. Radiat. Transfer , 2007, vol. 105, n°3, pp. 425-437 ;
[3] G. De Temmerman, R.P. Doerner, J. Nucl. Mater., Vol. 389, Issue 3, 1 June 2009, pp. 479-483;
[4] T. Kawasaki, Y. Manabe, K. Katayama, T. Takeishi, M. Nishikawa, Fusion. Sci. Technol. Volume 48, Number 1, July 2005, Pages 581-584]

PREPARATION AND COMPLEX CHARACTERIZATION OF (BE, W, C) CONTAINING FILMS FOR FUEL RETENTION

V. Kuncser[1], G. Filoti[1], P. Palade[1], G. Schinteie[1], S.G. Sandu[1], A. Lungu[1] C.P.Lungu[2], I. Jepu[2], C.Porosnicu[2]

[1]*National Institute of Materials Physics, 077125 Bucharest-Magurele, Romania*

[2]*National Institute for Lasers, Plasma and Radiation Physics, 077125 Bucharest-Magurele, Romania*

[BS_M5/WP12-IPH-A01-2-01/PS; BS18_A/WP12-IPH-A01-2-18/BS; BS18_A/WP12-IPH-A01-2-18/PS]

Abstract

With the final aim of the complex characterization of atomic intermixing processes and related structural properties of thin films and multilayers involving typical elements used in plasma facing components, this project was focused on both the issue of the buffer layers for subsequent growing of Be and W films and on the Be/W and W/Be bilayers grown on the previously studied buffers. The first stage was focused on atomic inter-diffusion processes and structural aspects in Fe-Cr and Fe-Cr-Al buffer layers, with compositions approaching the one of the special steel supporting plasma facing components. The buffers, enriched in the ^{57}Fe Mössbauer isotope, were deposited on Si(1 0 0) substrates by RF sputtering and subsequently processed by hydrogenation, while the top structures of Be/W and W/Be were deposited on the buffer layers by the TVA method. The buffer layers and the complex structures were characterized with respect to morphologic, structural, geometric and atomic diffusional aspects via atomic force microscopy (AFM), magneto-optic Kerr effect (MOKE) magnetometry, grazing incidence X-ray diffractometry (GIXRD), X-ray reflectometry (XRR), X-ray photoemission spectroscopy (XPS) and conversion electron Mössbauer spectroscopy (CEMS). The preparation conditions have a significant impact on the crystallization degree and the oxidation of the buffer films. Both the film thickness and the presence of Cr and Al atoms influence also the local surrounding of Fe. The hydrogenation treatment induces a crystallized bcc metallic phase, removes at different extents the oxide phases and remove Si and partially the Cr atoms from the bcc structure of Fe. No Fe-Be and Fe-W compounds are observed after the bilayer deposition. The strong atomic interdiffusion at the W/Be interface (independently on the deposition order) is confirmed by both XPS and XRR data, whereas CEMS data evidence the typical phase composition on the buffer side interface.

Papers:

R. Mateus, P.A. Carvalho, N. Franco, L.C. Alves, M. Fonseca, C. Porosnicu, C.P. Lungu, E. Alves, *Formation and delamination of beryllium carbide films*, J. Nucl. Mater, In Press, 2013;
http://dx.doi.org/10.1016/j.jnucmat.2013.04.009

V.Kuncser, S.G.Sandu, P.Palade, G.Schinteie, G.A. Lungu, C.M.Teodorescu, C.Porosnicu, I.Jepu, C.P.Lungu, G.Filoti, *Effects of annealing in Be/W and Be/C bilayers deposited om Si(001) substrates with Fe buffer layers*, sent to J.Nucl.Mater

Detailed results

1. Introduction

In a fusion reactor, e.g. tokamak in the ITER project, the materials presenting the highest challenge are, from a technological point of view, the components which interact with plasma - the so-called plasma facing components (PFC) [1]. In spite of the complex plasma confinement, the extreme temperatures and higher discharge time may cause the apparition of a melt layer and the occurrence of sputtering from the PFCs, with negative impact on the operation, safety and performance of the device. The PFCs play a crucial role in the efficiency of the plasma discharge and the protection of the inner walls of the device. The plasma-wall interactions may be limited by

covering the walls with complex protective PFCs. Reduced interdiffusion and intermixing at high temperatures, low corrosion yields, as well as low impact on the plasma discharge become of great importance. Therefore, the PFCs have to fulfil complex and even opposed properties and more than one type of material is needed. Heavy materials – of which the best candidate is W [2] – can be interfaced with lighter materials (Be). In previous studies we showed that Be/W bilayers, deposited on Si substrates with Fe buffer layers, are strongly influenced by deposition method and especially by annealing treatments, with high atomic intermixing and diffusion all over the structure [3].

The purpose of this study is, on one hand, the modification of the buffer composition by replacing the simple Fe buffers with Fe-based alloys with Cr and Al, approaching the composition of the special steels envisaged to support the PCFs. On the other hand, we attempted to reduce intermixing and diffusion in the multilayers by introducing a thick W interlayer at the Fe/Be and Fe-Cr/Be interface. A complex characterization of the local phenomena and interfacial intermixing in the Be/W and W/Be/W layers deposited on Si substrates, is made by means of: grazing incidence X-ray diffraction (GIXRD), X-ray reflectometry (XRR), atomic force microscopy (AFM), magneto-optic Kerr effect (MOKE) magnetometry, conversion electron Mössbauer spectroscopy (CEMS) and X-ray photoemission spectroscopy (XPS).

2. Experimental details

The Fe, Fe-Cr and Fe-Cr-Al buffer films (4 nm thick), partially enriched in the ^{57}Fe Mössbauer isotope, were deposited on Si(0 0 1) substrates by RF sputtering with the substrate held at room temperature, at 100W and at a working pressure of 5×10^{-2} torr. The native Si oxide layer was not chemically removed from the substrate, but an etching process of 30 minutes was applied before deposition. The buffers were subsequently reduced in hydrogen atmosphere, before the bilayer deposition. The hydrogenation has been done at 300 C for 90 minutes under 20 bars H_2 pressure. The Be/W and W/Be structures were deposited on the Fe, Fe-Cr and Fe-Cr-Al by means of the thermionic vacuum arc (TVA) method [4] (Dr. Cristian Lungu's group), at roughly 150°C. The W/Be structure was capped with a thin W layer (3-5 nm). The geometrical structure, the composition, the deposition parameters and the codes of the considered layered samples are resumed in Table 1. The main results, derived from Mössbauer spectroscopy and X-ray photoemission spectroscopy (XPS), are corroborated with atomic force microscopy (AFM), Magneto-optic Kerr effect (MOKE), grazing incidence X-ray diffractometry (GIXRD) and X-ray reflectometry (XRR). The atomic force microscopy (AFM) images have been obtained using a MFP-3D SA (Asylum Research) instrument working in intermittent contact mode at 0.5 Hz and with Si cantilevers (AC240TS, Olympus). Both GIXRD and XRR measurements have been performed with a Bruker type (AD 8 ADVANCED) diffractometer working with Cu(K_α) radiation of 0.154 nm wavelength. The Bruker LAPTOS software package has been used for fitting the XRR spectra whereas the qualitative analysis of the diffraction pattern has been performed via the EVA program. The depth dependent XPS studies have been performed in a dedicated photo-emission vacuum room (SPECS GmbH) equipped with a Mg cathode emitting X-rays at 1253.6 eV and an electron analyzer of type Phoibos 150 mm with an energy window of 50 eV and spectral resolution of 0.2 eV. Superficial charge effects have been compensated through a flood gun operating at 1 eV acceleration voltage and 0.1 mA electron current. The depth profile has been realized with a high intensity Ar^+ gun (IQE 12/38) generating a current of 10 μA at the sample under an acceleration voltage of the ions of 5 kV. The investigated depth has been estimated via straightforward crystallographic considerations, under the assumption that each Ar^+ ion incident on

the sample sputters just one atom from it. Surface sensitive ^{57}Fe Conversion Electron Mössbauer Spectroscopy (CEMS) has been performed in order to study the phase composition and the local structure. The spectra have been acquired at room temperature, in perpendicular geometry (with the gamma radiation perpendicular to the sample plane) with the sample placed in a home-made gas flow proportional counter. The isomer shifts are reported relative to α-Fe at room temperature. Magneto-optic Kerr effect (MOKE) magnetometry measurements have been performed at room temperature using a miniMOKE (AMACC Anderberg & Modéer Accelerator AB).

Table 1 - Sample code, composition and deposition parameters for the Fe-Cr buffer layers and the Be/W and W/Be/W top structures. *The label of the hydrogenated samples carries a suffix _h.

Sample code	Composition	Fe-Cr and Fe-Cr-Al buffers	
		Deposition time (min)	Etching time (min)
S 1	Si/Fe+Cr(7%)+ Fe^{57}	40	30
S3/7 a, b	Si/Fe+Cr(7%)+ Fe^{57}	3	30
S4(9) a, b	Si/Fe+Cr(11%)+ Fe^{57}	3	30
S5 a, b	Si/Fe+Cr(15%)+ Fe^{57}	3	30
S6 a, b	Si/Fe+Fe^{57}	3	30
S8 a, b	Si/Fe+Cr(11%)+Al(5,5%)+Fe^{57}	3	30
S10 a, b	Si/Fe+Cr(11%)+ Fe^{57}	40	15
T6a	Si/Fe+Fe^{57}/Be/W	3	30
T6b	Si/Fe+Fe^{57}/W/Be	3	30
T4a	Si/Fe+Cr(11%)+ Fe^{57}/Be/W	3	30
T4a_h	Si/Fe+Cr(11%)+ Fe^{57}/Be/W	3	30
T4b_h	Si/Fe+Cr(11%)+ Fe^{57}/W/Be	3	30
T8a_h	Si/Fe+Cr(11%)+Al(5,5%)+Fe^{57}/Be/W	3	30

3. Results and discussions

In order to have an approximate calibration of the film thickness, the FeCr film with highest deposition time (sample S10, deposited for 40 minutes) has been measured by total interferometry contrast. In this respect, during the preparation by RF sputtering, a step was made by simply covering a part of the substrate with a suitable mask. The thickness of the FeCr film (sample S10) was estimated as 50 nm ± 5 nm, with a deposition rate of 1.25 nm/minute. AFM measurements on samples S3, S5 and S4a – the latter presented in Figure 1 left – structures, as well as MFM measurements on sample S4a (shown in Figure 1 right) have been performed. All samples evidence a tri-dimensional type of growth with formation of island-like morphologies. The island size seems to be higher in S4 sample. Structures S3a and S5a have relatively low root mean square (RMS) roughness of 0.3 and 0.4 nm, respectively, while S4a presents considerably higher RMS roughness of 1.8 nm. The GIXRD patterns of structures S10 before hydrogenation and S4a after hydrogenation are presented in Figure 2. The GIXRD pattern of S10 sample does not exhibit any peaks, due to amorphous like structure. The quality of the films can be much enhanced with respect to their crystalline structure, surface roughness and especially reducing oxidation, via a subsequent hydrogenation. After hydrogenation, the thin film corresponding to S 4a sample evidenced a slight (and relatively broad) peak characterizing both bcc Fe and bcc Cr. In the case of the GIXRD patterns

of the samples T4a, T4b, T8a and T6b, slight relatively broad peaks are observed for both bcc Fe and bcc Cr, as well as for W and Be, supporting for a partially amorphous like structure.

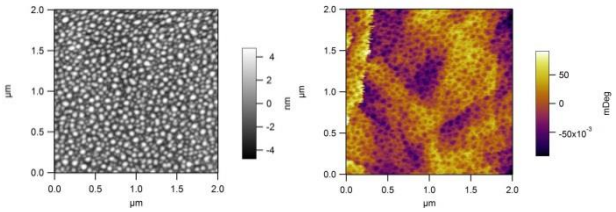

Figure 1 - AFM (left) and MFM (right) images of sample S4a

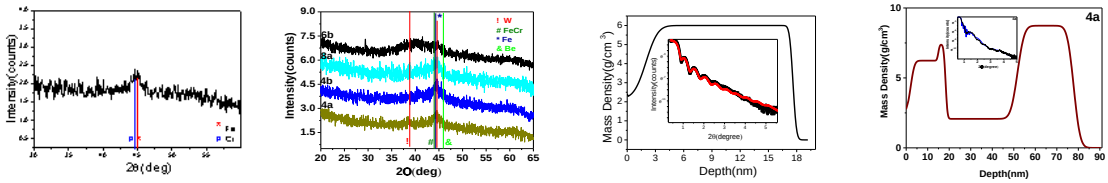

(a) *(b)* *(c)* *(d)*

Figure 2 - GIXRD patterns of samples S10 and S4aH (a), and T4a, T4b, T8a and T6b (b). The mass density profile of samples S5 (c) and T4a (d), as obtained from fitting the XRR data (inset).

The thickness, density and roughness of each Fe-Cr buffer layer have been checked via X-ray reflectometry technique based on reflection of X-rays from surfaces and interfaces. A model structure consisting of (a) the silicon substrate, (b) an interfacial SiO2 oxide, (c) the Iron/chromium buffer layer and (d) a top layer presumed to be Fe oxide, was used as an initially assumed structure for the calculation of a reflectometry curves by using the X-ray reflectometry theory. In the case of the density profile of sample S5a obtained via XRR patterns (Figure 2 c), the roughness of the top Fe layer is 0.31 nm, close to value obtained by AFM. The unexpected low value of the mass density for the main layer gives a first hint about its possible strong oxidation. Samples S4b and S8b exhibit quite similar mass density profiles, standing for mostly metallic Fe based films of about 10 nm, with a top Fe/Cr oxide layer and an SiO2 natural oxide layer at the interface with the Si substrate. Comparison of experimental and calculated XRR profiles is presented in the inset of each figure. The high density of SiO_2 observed for sample S8b proves that Fe is able to penetrate deep into SiO_2 layer at the interface with the Si substrate. Also it is to be mentioned the same trend showing an increase of roughness for sample S4a as compared with S5a, as evidenced by both AFM and XRR techniques, in spite of different values related to the specific method of estimation. In the case of samples T4a and T4b, a structure model consisting of (a) the Si substrate, (b) an interfacial SiO2 oxide, (c) the Fe and/or Fe-Cr buffer layer, (d) the Be layer, and (e) the W top layer, was used. The W and Be layers present unexpected densities, suggesting strong intermixing in the top structure.

The MOKE hysteresis loops of sample S 4a (Figure 3) evidence that the non-hydrogenated sample show a strong magnetic texture with the easy axis of magnetization oriented along the Si [110] direction. The low values of the coercive field indicate very soft magnetism related to an amorphous Fe-Cr-Si alloy (a possible reason for the magnetic texture being the induced stress during preparation). On the other hand, after the hydrogenation, the coercive field increases by one order of magnitude, whereas the texture is partially lost, suggesting both a possible phase transition and a relaxation of the internal stress. In case of sample S 8a, the MOKE measurements at different field orientations clearly evidence the strong texture in case of the as prepared sample, but with the easy

axis of magnetization oriented at 45 degree versus the Si [110] direction. The low coercive field indicates again a very soft magnetic character, in agreement with the presence of an amorphous Fe-Cr-Al-Si phase where the presence of the Al atoms modifies both the softness as well as the direction of the magnetic texture (internal stress). By hydrogenation, the initial texture is partially destroyed (at a lower extent as in the case of sample S 4a) and the coercive field increases just 3 times (at about 30 Oe). The presence of the Al atoms in the Fe-Cr thin films makes the structure more stable with respect to structural changes induced by the hydrogenation treatment.

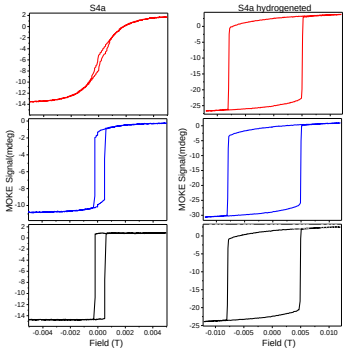

Figure 3 - MOKE loops collected on samples S 4a (left) and S4_h (right), at different azimuthal angles (between the field direction and Si[110] direction): 0°(black line), 45°(blue line) and 90°(red line)

Some examples of the Mossbauer spectra of Fe-Cr based buffers, directly as obtained by the RF sputtering preparation are shown in figure 4. All spectra of non-hydrogenated buffers, excepting the one with the highest Cr content, consist of a superposition of dominant magnetic pattern (large sextet, fitted via a probability distribution of hyperfine magnetic fields) and a less significant quadrupole paramagnetic contribution (doublet). Conversion electron Mössbauer (CEM) spectrum of sample S_6a shows a magnetic quasiamorphous pattern fitted with a distribution of magnetic hyperfine fields as the main phase, attributed to an Fe_3Si phase. A superparamagnetic phase is also present, as evidenced via the central doublet with a relative spectral contribution of ~11%, attributed to Fe^{3+} in defect maghemite. The results are similar with our previous work [3]. The CEM spectrum of sample 4a presents a magnetic quasiamorphous pattern and has been fitted with a distribution of hyperfine magnetic fields, attributed to an Fe3Si phase with Cr atoms inside, and a paramagnetic doublet, attributed to defect maghemite, with a contribution of ~22% from the total iron. It is worth to mention that the average hyperfine field of an Fe film with just 7at% Cr is of about 22.5 T, resulting so in this quasiamorphous structure an average decreasing of the hyperfine field of about 0.2 T per each Cr at. %. In addition, it seems that the Cr presence decreases slightly the IS. Unfortunately, the CEM spectrum of sample S 5a is completely paramagnetic, with Fe^{3+} ions in maghemite and Fe^{2+} ions in distorted wüstite (FeO) phases. It is worth to mention that this strong oxidation process is not related to an intrinsic behavior related to an increased amount of Cr, but has to be due juts to peculiar conditions (accidental enhanced oxidation) during sample preparation. Therefore, for further studies related to the Be/W multilayers, just as prepared samples without strong oxidation (to wustite) will be considered. The CEM spectrum of sample S 8a is similar to the case of S4 sample. The Al atoms decrease slightly the hyperfine field (of ~0.2 T per Al at. percent) and increase the IS values (by about 0.04 mm/s per Al at. percent). The central doublet component (relative spectral area of 22%) is assigned as usually to a superparamagnetic Fe^{3+} oxide. Finally, the CEM spectrum of sample S 10 is similar to the one of the thinner sample, with the only difference of a lower average hyperfine field and slightly higher IS of the sextet (indicating just a higher Si content

related to the longer rf sputtering process) and a lower relative content of the superparamagnetic Fe^{3+} oxide phase, due to the relatively lower superficial oxidation. In order to observe the influence of the hydrogenation process on the structural aspects of the buffer layers, just two types of samples were considered: the ones presenting main intermetallic phase and respectively the ones presenting just oxide phases, including wustite type. It might be observed that after the hydrogenation treatment, the initial metallic (amorphous structure) is transformed in a well crystallized bcc structure (one phase). If an initially oxidized film is considered (e.g. as in case of sample S 5a), secondary paramagnetic/superparamagnetic Fe oxide phases are formed. In this respect, just the well metallized initial films will be considered for the deposition of Be/W layer, where no secondary phase excepting the well crystallized bcc one is expected.

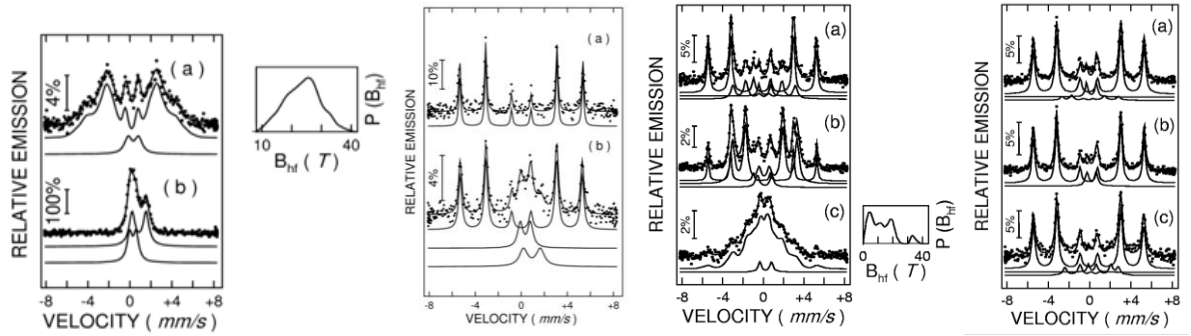

Figure 4 - CEM spectra collected at room temperature on the samples: A (a) S6a, (b) S 5; B S 4a_H (a), S 5a_H (b); C T6a (a), T6b (b), T4a (c); D: T4ah (a), T4bh (b) and T8ah (c)

The spectrum of sample T4a consists of a dominant wide magnetic pattern and has been handled with a probability distribution of hyperfine magnetic fields, shown on the right side of the corresponding spectrum. The CEM spectrum of T6a shows a main sextet attributed to a well formed metallic α-Fe phase. In addition, it is observed the formation of a secondary sextet that is attributed to a Fe-Si phase, Fe_3Si in a distorted configuration, most likely [6]. This is due to the fact that some of the buffers have not been treated in hydrogen atmosphere previously to the Be/W bilayer deposition and a diffusion process of Si atoms into the Fe layer caused the formation of a mixture phase. A less pronounced paramagnetic phase is also observed, assigned to Fe^{3+} ions in distorted maghemite. By taking into consideration the preferred type of growth of type Volmer-Weber (island-like) of the buffers studied with AFM, the oxide phase has a superparamagnetic behavior. The CEM spectrum of T6b, presents a similar pattern to the case of the sample 6a, showing two magnetic components (an α-Fe and a silicide phase), and a superparamagnetic doublet (Fe^{3+} ions in highly distorted maghemite). The presence of the W interlayer between Fe and W determines, for the sextet attributed to the silicide phase, increase of both isomer shift and hyperfine magnetic field. The sample T4a presents a very wide pattern fitted with a probability distribution of hyperfine magnetic fields with several maxima, assigned to the metallic Fe phase, Fe-Si mixtures and paramagnetic contributions. The second phase is found in a low amount and is assigned to defect maghemite. The CEM spectrum of T4ah (with buffers treated in hydrogen atmosphere) shows the presence of a main sextet attributed to a well formed metallic α-Fe phase, similar to the case of the previous sample. In the case of the second sextet, assigned to the Fe_3Si silicide phase, the hyperfine field is reduced relative to the case of the sample without Cr in the buffer layer. Therefore, it is observed, similar to the results from Phase I/2012, that Cr atoms reduce the hyperfine magnetic field. A paramagnetic phase is also present, assigned to a distorted Fe^{3+} oxide phase (maghemite),

similar to the sample T6a. The CEM spectrum of T4bh presents similar phases to the sample T4ah. However, the presence of the W interlayer determines a decrease of the hyperfine field and a considerably increase of the isomer shift. The sample with Fe-Cr-Al buffer layer, T8ah, presents a pattern of the CEM spectrum similar to the case of the sample T4ah. Though, the hyperfine magnetic field is reduced even more, while the isomer shift increases considerably. It is to be noticed that, as a general trend, the samples containing hydrogenated buffers have more magnetic α-Fe phase. It is important to have low amount of impurity (silicide) and oxide phases in order to have less diffusion and intermixing in the as-prepared state. Therefore, the treatment in hydrogen atmosphere is a viable approach in this concern. However, the Si atoms and partially the Cr(Al) atoms are also removed from the bcc structure of Fe. Although strong intermixing of W and Be layers occurs, Fe-Be and Fe-W phases are not formed. The intermixing is much stronger in systems with Cr containing buffers.

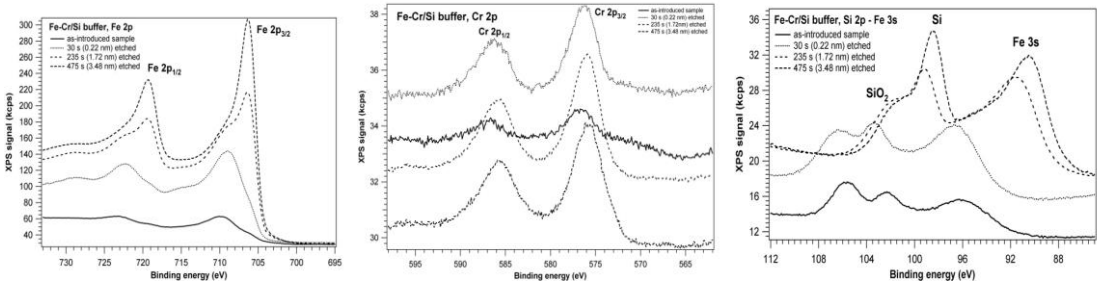

Figure 5 - XPS spectra of sample S 3a_h in the binding energy region of Fe 2p (left), Cr 2p (up-right) and Si 2p (right)

The XPS spectra on a sample similar to S 5a (completely oxidized after the RF sputtering and then processed via hydrogenation treatments), but with just 7at.% of Cr (sample S 3a_h), shown in figure 5, reveal the presence of mainly Fe oxide phases down to 1 nm, the apparition of a metallic Fe based compound at 1.7 nm and mainly metallic Fe at depths higher than 3 nm. Similarly, in case of Cr, mainly Cr oxide is formed at the surface and metallic Cr at deeper depths. It is worth the mention that at the very surface both Cr and Fe are in a very small amount, mainly due to the presence of a C based impurity layer. Atypical Si oxide and Fe oxide phases are also formed at the very surface. Finally, the amount of oxygen decreases continuously at increasing depths, where oxide phases involving mainly trivalent cations are to be reported.

It might be observed that the maximum relative content of 5at.% Cr is reached just at the surface, the relative content decreasing rapidly at just 2at.% of Cr at depths higher than 2 nm. In the case of sample T4a_H, it might be observed that Be is present in both neutral and oxidized states at all investigated etching depths. Mainly BeO phase is formed at lower etching depths (closer to the surface), and is reduced at higher etching depths (deeper into the structure). At the very surface, a Si peak corresponding to a SiO phase is also present. Neutral Si shows the presence of the substrate starting from 40 nm. An impurity phase of neutral C is also present, due to air exposure. The two W peaks, $4f_{7/2}$ and $4f_{5/2}$, are well resolved with a high spin-orbit splitting, showing neutral phases. The W concentration decreases drastically from 40 nm. The Fe peaks are in a reduced amount at etching depths between 1 and 27 nm. The Fe content increases considerably at 31 nm, and it increases even more starting from 34 nm, correlated with the drastic decrease of W content, indicating a W/Fe interface with atomic intermixing, although no thermal treatment has been applied on the sample. The relatively wide peaks are, most probably, superposition of the peaks corresponding to neutral and oxidized phases, both for Fe $2p_{1/2}$ and for $2p_{3/2}$. In the Cr 2p binding energy range W 4s is also found. The Cr peaks are seen starting from 29 nm and reveal the neutral phases in Cr $2p_{1/2}$ and $2p_{3/2}$

state. The Cr concentration decreases sharply at 47 nm, where Si signals are prevailing. As a consequence, it is observed that there is a relatively sharp Fe-Cr/Si interface, because both Fe and Cr signals decrease considerably at 47 nm, though Si atoms are present even at 40 nm. The sample T4b_H is less oxidized than the previous sample. Be signals are present down to a depth of 40 nm, while Fe in its neutral state is diffused into the Be and W layer, starting from 2 nm. Cr is less diffused in the top layers, starting to be observed at 33 nm, still in neutral state. A weak neutral Si peak is present at the very surface, appearing again with a considerable increased contribution at 40 nm. The two W peaks, $4f_{7/2}$ and $4f_{5/2}$, are a superposition of neutral and oxidized phases. An impurity phase of neutral C is also present only at the very surface. The atomic percent of W is about 3 times higher than of the Be, at any depth of the Be/W film, independently on the deposition order. Also, the oxygen is present in the whole structure (at a lower extent on the buffer/W/Be sample) increasing in content at the very surface but mainly toward the Si substrate (native SiO2 at the surface). However, the high relative oxygen content in the Fe films suggests the presence of WO2 phases in the buffer.

4. Conclusions

Bilayers of Be/W and W/Be were deposited on Si(1 0 0), with Fe, Fe-Cr and Fe-Cr-Al buffer layers. Some of the buffers were thermally processed in hydrogen atmosphere in order to reduce the oxidation and to improve the crystalinity of the films. The initially completely oxidized Fe-Cr buffer layer of about 9 nm, transforms by subsequent hydrogenation in a compositional gradient like layer, with an Fe/Cr oxide at the surface (about 35% of total Fe atoms are contained in the Fe oxide phases) and mostly bcc metallic Fe phase in the deeper (more than 1.7 nm) layers. The oxide phases involves unusual oxidation states just at the surface (layers of less than 0.2 nm in thickness), Fe oxide of low oxidation state (e.g. Fe2+) at about 0.2 nm depth and slightly increasing oxidation states (e.g. Fe3+) at deeper layers where also the oxide content becomes negligible. It is worth to mention that at depths higher than 2 nm, the predominant metallic phase contains just 2at.% Cr atoms, in contradiction with the expect value of 7%, designed by preparation conditions and evidenced in the as prepared sample by CEMS. Hence, according to the hyperfine field of about 33.2 T attributed to this phase, it results clearly the double action of the hydrogenation process, of building up a crystalline bcc Fe structure and removing O, Si and Cr atoms from it.

This double action has to be valid also in the case of mainly metallic phases in the as prepared sample, where just a metallic Fe phase is observed via hydrogenation. In this case, the relatively low fraction of oxide phase is completely removed by hydrogenation whereas the metallic crystalline structure has to contain an insignificant amount of Si impurities and about 3-4 times lower relative content of Cr, as designed by preparation. Such hydrogenated Fe-Cr based buffers will be further considered for the deposition of Be/W and W/Be layers. The Mössbauer spectra of samples Si/Fe-Cr/Be/W and Si/Fe-Cr/W/Be/cap layer, with hydrogenated buffers show clearly the presence of a narrow sextet (specific to bcc Fe) and an Fe-Si phase (just for sample 8ah) as well as a weak doublet assigned to a superparamagnetic Fe oxide. No Fe-Be and Fe-W compounds are observed in the spectra. However, a higher amount of W and oxygen atoms is provided by the XPS data also at the depth specific to the Fe layer.

Therefore, we may assume the formation of tungsten oxides in this layer (by Mössbauer we can observe just the Fe atoms and a few percent of Fe_2O_3 phase +90% of metallic Fe cannot explain a ratio of O/Fe about 3, as evidenced by XPS). The strong intermixing in the W and Be layers is clearly proven by the XPS data and supported also by the unexpected densities for W and Be, as obtained from XRR data.

References

[1] R.A. Pitts, S. Carpentier, F. Escourbiac, T. Hirai, V. Komarov, A.S. Kukushkin, S. Lisgo, A. Loarte, M. Merola, R. Mitteau, A.R. Raffray, M. Shimada, P.C. Stangeby, J Nucl Mater 415 (2011) S957–S964.
[2] V. Philipps, J Nucl Mater 415 (2011) S2–S9.
[3]V. Kuncser, P. Palade, G. Schinteie, S.G. Sandu, L. Trupina, C. Lungu, N. Gheorghe, C.V. Teodorescu, C. Porosnicu, I. Jepu, C.P. Lungu and G. Filoti, J. Alloys and Comp., 512 (2012) 199–206.
[4] C.P. Lungu, I. Mustata, G.Musa, V. Zaroschi, A.M. Lungu, K. Iwasaki, Vacuum 76 (2004) 127.
[5] R.A. Brand, Nucl.Instr. Meth. B 28 (1987) 398.
[6] K. Trunov, M. Walterfang, W. Keune, N.K. Utochkina, A. Trunova, Thin Solid Films 516 (2008) 6205–6209.
[7] http://srdata.nist.gov/xps/

PRODUCING AND CHARACTERIZATION OF THIN FILMS OF TERNARY AND QUATERNARY SYSTEMS: W/C/MG/O/N

Dan Colceag, Andreea Andrei, Rovena Pascu, Andreea Matei, Nicu Scarisoreanu,
Ruxandra Birjega, Maria Dinescu
National Institute for Laser, Plasma and Radiation Physics, Magurele, Bucharest, Romania

[BS_21/WP12-IPH-A01-2-02/BS]

Abstract

W/C/Mg/O thin films deposition and characterization are reposted. Two techniques were used for layers growth: pulsed laser deposition (PLD) and Radio-Frequency assisted PLD. Three types of targets, namely W, C and MgO were alternatively ablated in the presence of oxygen and of a discharge produced in oxygen to produce layers with different chemical composition. Studies on the physical and chemical properties of ternary compounds containing oxygen and on the influence of the ratios between elements on film properties were carried out using specific techniques as AES, XRD, SIMS, AFM, SEM, and Spectroellipsometry.

The deposited W/C/Mg/O layers are continuous, cracks free and exhibit smooth surfaces, as it results from AFM and SEM investigations. The substrate temperature, oxygen pressure and number of pulses were found to play an important role in the layers chemical and physical properties and compositions; the use of RF-PLD technique strongly influences the growth process.

Detailed results

1. The general goal of the project is to realize and characterize thin films of ternary and quaternary systems containing C, W and Mg in chemical compounds including oxygen. Considering the involved domain, that of Fusion reactors, which is very new on international stage, the proposed project will have a strong contribution to the objectives ITER Work program

2. Second stage objectives are: Studies regarding (W/C/Mg/O) thin films properties and influence of the ratios between different elements on layers characteristics.

3. Summary: Beryllium, carbon and tungsten materials/composites are considered candidate-materials for first wall/diverter in the Tokamak at the International Thermonuclear Experimental Reactor (ITER). Their behavior during plasma operation is important for their positive aspects, but also for the unavoidable formation of mixed layers on the surfaces of plasma facing components. Another important aspect is related to their behavior when include oxygen as unavoidably intrinsic impurity. For experimental purposes, Be (which is a very toxic material) was replace by Mg, which has similar properties.

The proposed methods to grow W/C/Mg/O containing compounds include Pulsed Laser Deposition (PLD) and Radiofrequency Assisted Pulsed Laser Deposition (RF-PLD). The addition of a Radio-Frequency (RF) discharge producing a beam of excited and ionized species to the PLD system leads to films surface structuring and controlled inclusion of oxygen in the layers. In this stage, three related activities were developed:

a. deposition of W/C/Mg/O thin films with smooth surfaces and different oxygen content;
b. studies on the physical and chemical properties of ternary compounds containing oxygen;
c. studies on the influence of the ratios between different elements on film properties.

Sequential PLD and RF PLD were used to produce thin films containing W/C/Mg/O, starting from W, C and MgO targets and working in oxygen reactive atmosphere at a pressure varying between 10^{-2} mbar and 10^{-1} mbar. Silicon and suprasil plates were used as substrates/collectors. The distance between the target and collector was set at 4.5 cm. The deposition temperature varied from room temperature (RT=24°C) up to 600°C; the substrate was heated with 40°C/min and cooled with 10°C/min.

To study the influence of the element ratios on the film properties, we used 2 sequences: the first one consists in 80, 40 and 80 pulses on W, C and MgO targets respectively; and the second, 40, 20 and 40 pulses.

The deposited layers have been characterized by XRD, AFM, SIMS, AES, SE for establishing the influence of the amount of a certain element on the films properties. The best sets of experimental conditions (substrate temperature, oxygen pressure) for growing continuous, smooth films were established.

4. Scientific and technical description

4.1 Introduction

As described in the first stage of this project, beryllium, carbon and tungsten materials/composites are considered candidate-materials for first wall/ diverter in the Tokamak at the International Thermonuclear Experimental Reactor (ITER). Their behavior during plasma operation is important for their positive aspects, but also because of the unavoidable formation of mixed layers on the surfaces of plasma facing components. [1, 2]

Beryllium is very attractive for engineering applications, as it exhibits high thermal conductivity, modest thermal expansion, combines a high elastic modulus with a low density. The use of Be for the wall, and of W and/or C for diverter are between the attractive solutions. However, the attributes of Be and its alloys are countered by two significant drawbacks: toxicity and high cost [3]. Beryllium properties are similar to those of aluminium and magnesium, so it can be replaced, for experimental trials, with these materials. It is then of big interest to deposit and characterize thin films containing C, W and Mg in chemical compounds including oxygen, as unavoidable impurity.

A simple method to grow W/C/Mg/O is Pulsed Laser Deposition (PLD) (or laser ablation). The PLD involves the interaction of a laser beam with a target material producing a plume that transports the particles onto a substrate, where a thin layer is formed. PLD is a clean, versatile and flexible method. The addition of a Radio-Frequency (RF) discharge beam to the PLD system leads to a structuring of films morphology.

In this stage, three interrelated activities were developed:

Activity 2.1: Deposition of W/C/Mg/O thin films with smooth surfaces and different oxygen content
Activity 2.2: Studies on the physical and chemical properties of ternary compounds containing oxygen
Activity 2.3: Studies on the influence of the element ratios on film properties
Details: The deposited layers were characterized by XRD, AFM, SIMS, AES, and SE, for establishing the influence of the amount of a certain element in the films properties.

Deliverables: Report on growth of ternary thin films with smooth surfaces and different content of oxygen; Data on the physical and chemical properties of ternary compounds containing oxygen; Data on influence the ratio between elements on film properties.

4.2 Experimental set-up; results and discussions

Activity 2.1 Deposition of W/C/Mg/O thin films with smooth surfaces and different oxygen content

In order to obtain ternary thin films with smooth surfaces of W/C/Mg/O, series of experiments were performed. The PLD and RF-PLD experimental set-ups have been described in detail in the project's first stage.

A beam with a wavelength of 193 nm generated by ArF laser irradiated the three targets: a single crystal plate of Magnesium Oxide, graphite and a metallic wolfram were used without any further treatments. Silicon (100) and suprasil plates, at room temperature (RT=21°C) or heated at 200°C, 400° C and 600°C during the depositions, were used as substrates. Distance between the targets and substrates, was set at 4.5 cm. Laser fluence was set to 3 J/cm^2, as a bigger fluence would destroy the graphite target, and a smaller one would not be able to ablate the tungsten target. The depositions were performed in oxygen atmosphere at 2 different pressures, 0.1mbar and 0.01mbar.

W/C/Mg/O deposited samples were first investigated using atomic force microscopy (AFM), using a PARK XE 100 instrument. It can be noted that the surface aspects of the samples obtained with the two pressures is similar: the layers have a continuous and relatively smooth aspect, without pores and cracks. The roughness, on the other hand, is different: for higher oxygen pressures, the roughness is 2.3nm, much bigger than those of the film deposited at 0.01mbar, which is only 0.8 nm.

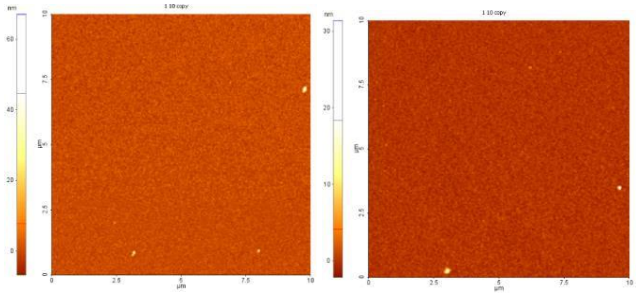

a. 0.1 mbar *b. 0.01mbar*

Figure 1 - AFM images of W/C/Mg/O thin film deposited at 3 J\cm^2, 200 C, RF=100W on Si

The behaviour is similar for the layers deposited on suprasil substrates: the roughness of the film deposited at 0.1mbar oxygen pressure is 8nm, while roughness for the layers grown at 0.01mbar is only 2.7nm.

From Scanning Electron Microscopy (SEM) investigations performed with an Inspect S50 FEI system, the role of substrate temperature in the development of structures based on W/C/Mg/O compounds was revealed; the temperature increases results in the appearance of nanosize grains.

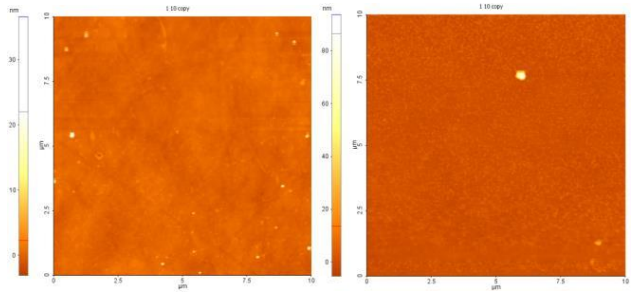

a. 0.1 mbar *b. 0.01mbar*

Figure 2 - AFM images of W/C/Mg/O thin film deposited at 3 J\cm^2, 200 C, RF=100W on suprasil

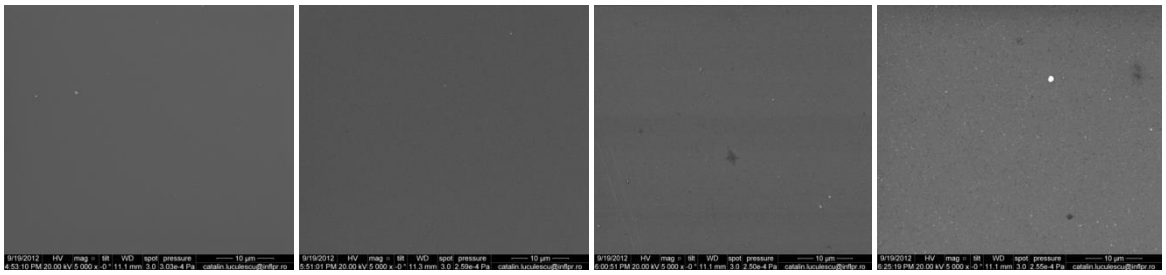

a. *b.* *c.* *d.*

Figure 3 - SEM images for W/C/Mg/O deposited on silicon substrates at a pressure of 0.01 mbar oxygen at: a. RT; b.200^{o}C; c. 400^{o}C; d. 600^{o}C

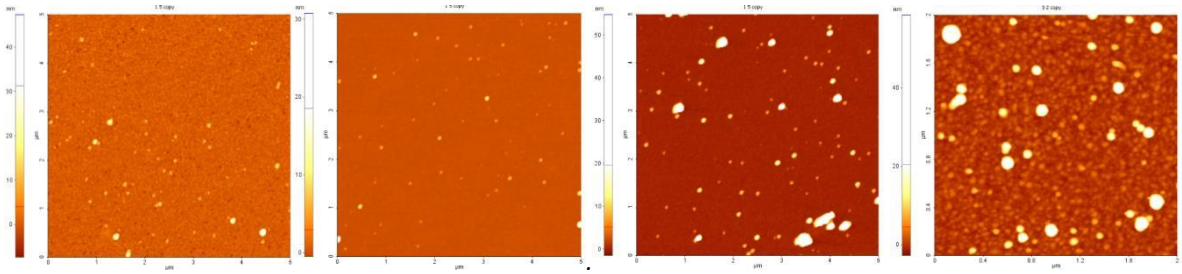

a. *b.* *c.* *d.*

Figure 4 - AFM images for W / C / MgO deposited on silicon substrates at a pressure of 0.01 mbar oxygen at: a. RT; b.200^{o}C; c. 400^{o}C; d. 600^{o}C

The results are confirmed by AFM investigations (Figure 4). Besides the grains growth, the roughness of the films increases from 2 nm for the sample deposited at RT and 200°C, to 4 nm at 600°C.

Activity 2.2 Studies on the physical and chemical properties of ternary compounds containing oxygen

Physical and chemical properties of W / C / Mg/O compounds were studied by Spectroellipsometry (SE), X-ray diffraction (XRD), Secondary Ion Mass Spectroscopy (SIMS) and Auger Electron Spectroscopy (AES).

Optical properties of W/C/Mg/O layers were investigated using a spectroscopic-ellipsometer Woollam V-VASE equipped with a monochromator HS-190 type. It is known that ellipsometry measures the two values Ψ and Δ. These represent the amplitude ratio Ψ and phase difference Δ between light waves known as p- and s-polarized. In spectroscopic ellipsometry, Ψ and Δ spectra are measured by changing the wavelength of light. The complex reflection coefficient ρ is defined as

$$\tilde{\rho} = \frac{\tilde{R}_p}{\tilde{R}_s} = \tan(\Psi)e^{i\Delta}$$

where *R*p and *R*s are the Fresnel reflection coefficients for the parallel and perpendicular polarizations, respectively. Experimental measurements were made on a spectral range between 300 and 1000 nm at an incidence angle of 70^0. Since ellipsometry method is a comparative method, is necessary to build a model which generate ψ and Δ curve parameters, which are compared with those obtained experimentally.

For W / C / Mg/O layer optical model consists in a set of 4 layers: silicon substrate, native silicon oxide layer, the thin film of W/C/Mg/O approximated as a material that shows Cauchy dispersion and a “roughness layer”, approximated as 50% air and 50% material.

In Cauchy-Urbach formalism the refractive indices and the extinction coefficients are given by:

$$n(\lambda) = A_n + \frac{B_n}{\lambda^2} + \frac{C_n}{\lambda^4}$$

$$k = A_k \cdot e^{B(E-E_b)}$$

$$\varepsilon_{Cauchy} = (n + jk)^2 \text{ or } \varepsilon = \varepsilon_1 + j\varepsilon_2 = (n + jk)^2$$

where: An, Bn, Cn are Cauchy parameters and Ak, Bk are Urbach parameters, Ak – amplitude, Bk is exponent. We have chosen two sets of samples: samples deposited at different temperatures (room temperature, 200°C and 400°C), at oxygen pressure of 0.1 mbar and another set of samples deposited at constant temperature (400°C) and pressure of 0.01 mbar and 0.1 mbar oxygen, with and without RF discharge.

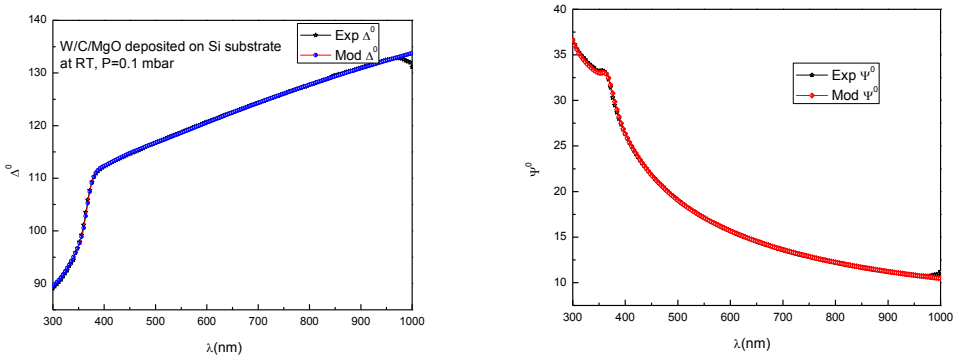

Figure 5 - Experimental and modelled curves using Cauchy model for thin film deposited at a pressure of 0.1 mbar at room temperature

Using the model described above, the experimental data were fitted on all measured spectral range, obtaining the refractive index, thickness values and the thin films roughness. From Figure 5, it can be observed that the simulated values of measured parameters are similar to those obtained experimentally, leading to the conclusion that the model is correct. As the difference between modelled and experimental curves is very

small, we can say that the material presents Cauchy dispersion without Urbach absorption, which means that it is virtually transparent.

Table 1: Parameters fitted using the Cauchy dispersion without Urbach absorption.
The errors are those given by the fitting routine.

Sample	Pressure O_2 (mbar)	T (^{0}C)	RF (W)	Thickness (nm)	Roughness (nm)	An	Bn	SE
1304	0.1	RT	-	22.604	2.1	1.416	0.0083	8.641
1305	0.1	200	-	16.129	0.187	1.5496	0.098	20.94
1306	0.1	400	-	5.557	0.518	1.6745	0.01	7.362
1314	0.01	400	-	9.535	0.513	1.6887	0.011	9.712
1322	0.1	400	100	13.890	7.404	1.5513	0.013	26.01
1330	0.01	400	100	15.391	9.966	1.7078	0.0135	5.794
1331	0.01	600	100	16.572	7.121	1.7559	0.0056	5.304

Using Cauchy parameter values presented in the table and resulted from the fitting process, the dependencies on refractive index of wavelength for both sets of samples was calculated (Figure 4). The main conclusion is that higher refractive index is obtained (about 1.73) when higher temperature of the substrate is used.

For layers deposited keeping constant the substrate temperature at 400^{0}C and varying the deposition pressure with or without radiofrequency discharge, it can be seen that both parameters, pressure and RF, influence the refractive index behavior. Indeed, the biggest value was reached for a pressure of 0.01 mbar and in the presence of RF discharge. We can suppose that at lower pressures films are denser, also due to the RF addition, which acts between the laser shots, delivering supplementary energy to the layers; this can result in an increase of refractive index [4, 5, 6, 7, 8]. Indeed, adding radiofrequency plasma, the refractive index values increase by about 0.1.

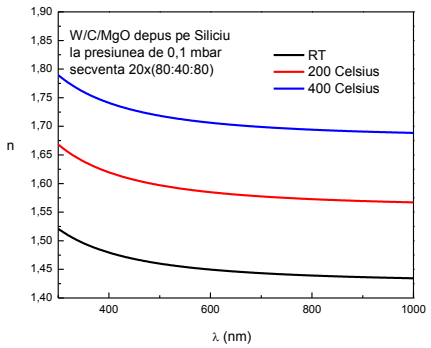

Figure 6 - Refractive index values for thin films of W/C/Mg/O deposited on silicon substrates at a pressure of 0.1 mbar oxygen

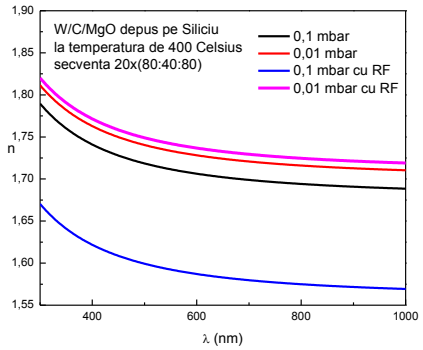

Figure 7 - Refractive index values for thin films of W / C / Mg/O deposited on silicon substrates at a temperature of 400^o C and different oxygen pressures with and without RF plasma

Increasing the substrate temperature to 600^o C and keeping the deposition pressure at 0.01 mbar oxygen, an increase of the refractive index of about 0.2 can be noticed (Figure 8).

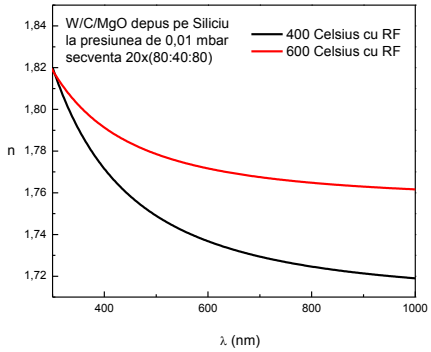

Figure 8 - Refractive index values for thin films of W / C / Mg/O deposited on silicon substrates at a temperature of 600^o C, 0.01 mbar O_2 and RF

X-ray diffraction studies were performed using a PANalytical X'Pert MRD diffractometer in Bragg-Brentano geometry. From the spectra (not presented here), the only identified peaks are very broad and weakly defined, coming from MgO.

The identification of chemical constituents in the sample was performed by Auger Electron Spectroscopy using an Auger spectrometer PHI AES-3017 model, Perkin-Elmer, Physical Electronics. Main features of the spectrometer: energy between 0 and 3200eV; energy resolution is about 0.6%.

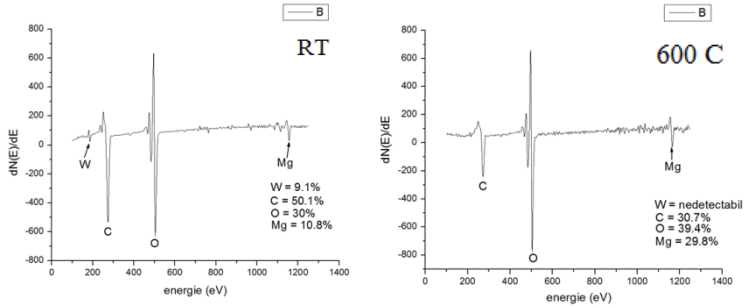

Figure 9 - AES spectrums of the W / C / Mg/O films deposited on silicon substrates at 0.01 mbar O_2 and RF plasma, 20 × (80:40:80) laser pulses

It can be noted that the substrate temperature influences the ratio between elements. The low amount of tungsten detected at the surface of thin films can be explained by the SIMS analysis shown previously: tungsten migrates towards the silicon substrate; therefore it is hard to detect it on the surface of the sample.

Activity 2.3 Studies on the influence of the ratios between elements on film properties

For the study on the influence of the ratios between elements on the films properties, we used Secondary Ions Mass Spectrometry - SIMS Workstation, Hiden Analytical (UK). It uses primary argon ions (but it can also work with a cesium gun) at a pressure of 3×10^{-5} mbar. It allows the realization of both SIMS investigation (Secondary Ions Mass Spectrometry) and SNMS analyses (Secondary Neutrals Mass Spectrometry). The spot dimension of the argon beam is around 100 microns, the in-depth resolution is 5 nm, and the pressure in the chamber where the sample is analyzed is around 1×10^{-8} mbar.

Two types of analyses have been carried out on the samples prepared by pulsed laser deposition. First type is called mass scan (ms) and involves the registration of the number of pulses corresponding to each atomic mass in a certain interval, in the case of thin films W/MgO/C, between 10amu (atomic mass units) and 200amu. The second type of analysis is the depth profiling one (dp), which involves the monitoring of the presence of certain elements of interest (W, Mg, O, C, Si) in the depth of the thin film, until the sputtering fascicle reaches the film-substrate interface.

For both analyses, a positively charged argon ion beam was used. Areas between 0.5mm^2 (ms) and 2mm^2(dp) have been investigated, several scans being registered for each sample in order to check its homogeneity on the entire surface.

A comparative study between deposition rates for the prepared samples has been carried out through SIMS analyses. As expected, two parameters have a strong influence on the deposition rates: the number of laser pulses on different targets and gas pressure in the ablation chamber.

A dependence of the ratio between the average thicknesses of different thin films on the two parameters can be seen in Table 2.

Table 2 - The ratio between the thickness of different thin films as a function of pressure during deposition and number of laser pulses on each target

Pressure (mbar) / Number of pulses	0.1	0.01
20 × (40:20:40)	1	2.5
20 × (80:40:80)	2.5	5.83

It has also been noted that the introduction of a radio-frequency oxygen plasma discharge during ablation process slightly diminishes the thickness of the prepared thin films, which is probably due to the presence of species from the rf plasma between the target and the substrate.

The composition and thickness of thin layers are not generally influenced by the modification of deposition temperature, as it can be observed in Figure 10. Slight oscillations in tungsten concentration are usually due to laser (slight) fluence variation and not to temperature variation. An increased level of oxidation can be seen in the case of sample deposited at 600 °C.

The most important conclusion of SIMS analyses is that there is a migration of tungsten inside the thin films towards different areas of the samples. Thus, in the case of thin films prepared in radiofrequency plasma discharge assisted PLD experiments, an increased level of tungsten is observed close to the silicon substrate interface; the tungsten signal increases with the increase of substrate deposition temperature. Figure 11 illustrates the effect described above. Again, a slightly bigger concentration of oxygen can be observed in the case of the sample deposited at 600°C.

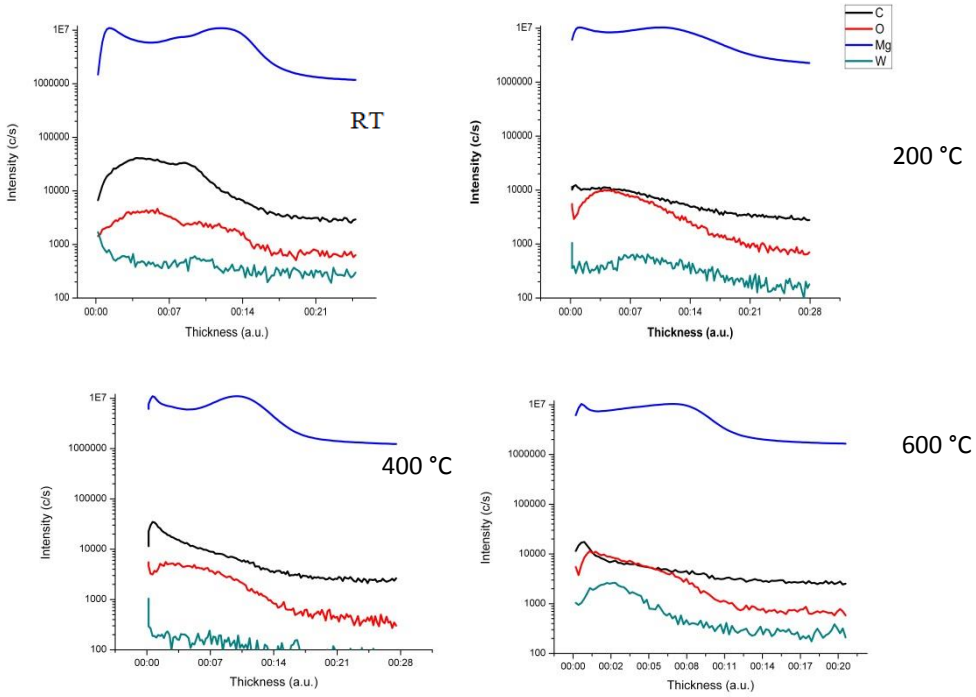

Figure 10 - Thin films composition and thickness for different deposition temperatures; the samples have been obtained in 0.1 mbar, 20 × (80:40:80) pulses, without RF plasma

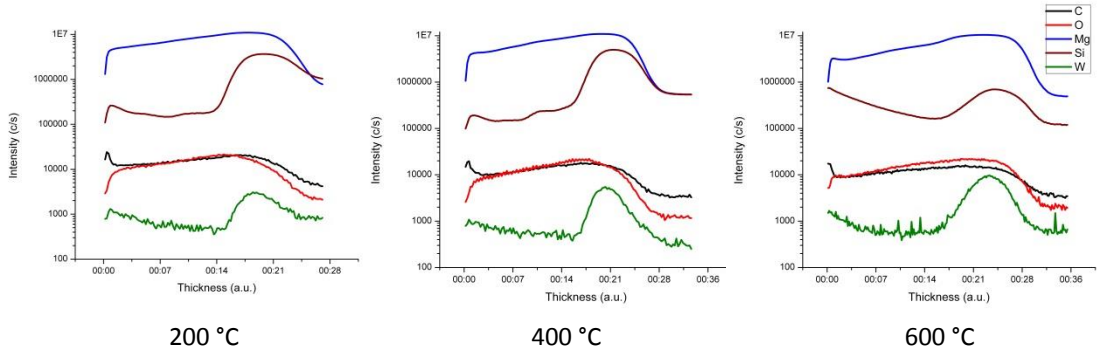

Figure 11 - The amount of tungsten that migrates towards the film-substrate interface increases with the deposition temperature; 20×(80:40:80) laser pulses, 0.01 mbar oxygen, 100W RF power

Comparing the level of oxygen recorded in the case of the two series of thin films presented in the Figures 10 and 11, the increased oxidation in the case of the films prepared with a plasma discharge becomes obvious: even when the pressure is 10 times lower, the oxygen level is higher.

A similar behavior of tungsten has been identified in the case of some samples deposited without RF plasma discharge; in this case, the amount of tungsten that gathers together in the layer is lower.

The mass scans have revealed the presence of all elements from the targets, C, O, Mg and W and no impurities have been detected in the thin films.

4.3 Conclusions

The results presented in this report prove that the objectives of the second stage of the project were achieved.

We deposited thin films of W/C/Mg/O by pulsed laser deposition (PLD) and Radio-Frequency assisted PLD. Three targets, namely W, C and MgO were alternatively ablated by an excimer (ArF) laser in the presence of oxygen and of a discharge produced in oxygen to grow thin films with different chemical composition.

The deposited W/C/Mg/O layers are continuous, cracks free and exhibit smooth surfaces, as it results from AFM and SEM investigations. Studies on their physical and chemical properties and on the influence of the ratios between elements on film properties were carried out by SIMS, Auger Electron Spectroscopy, XRD and spectroellipsometry. We observe that the substrate temperature, oxygen pressure and number of pulses play an important role in the layers chemical and physical properties and compositions and the use of RF-PLD technique strongly influences the growth process.

The objectives of this first stage were fulfilled.

4.4 References

[1] M.I. Guseva, A.L. Suvorov b, S.N. Korshunov, N.E. Lazarev, Journal of Nuclear Materials 266-269, 222-227 (1999)
[2] M. Rubel, Fusion Science and Technology, Volume 45, Number 2T, 467-474 (2004) http://www.sbir.gov/sbirsearch/detail/335706
[3] Handbook of Ellipsometry, Harland G. Tompkins, Eugene A. Irene, William Andrew, Inc., ISBN 0-8155-1499-9 (2005)
[4] Spectroscopic Ellipsometry Principles and Applications, Hiroyuki Fujiwara, Published by Maruzen Co. Ltd, Tokyo, Japan, ISBN-13:978-0-470-01608-4
[5] V. Ion, A. C. Galca, N. D. Scarisoreanu, M. Filipescu, M. Dinescu, Phys. Stat. Sol. (c) 5, No. 5, 1180–1183 (2008)
[6] S. Heiroth, R. Ghisleni, T. Lippert, J. Michler, A. Wokaun, Acta Materialia 59, 2330–2340 (2011)
[7] G. E. Stan, I. Pasuk, A. C. Galca, A. Dinescu, Digest Journal of Nanomaterials and Biostructures 5, No 4, 1041-1054 (2010)

GASEOUS INCLUSION TRAPPING MECHANISM STUDY OF ITER BERYLLIUM RELATED MIXED MATERIALS

C. Porosnicu

National Institute for Lasers, Plasma and Radiation Physics

[BS_18D/WP12-FRF-MEdC]

Abstract

Since the proposed plasma facing components (PFC) for ITER consists of three different materials: Be (for the first wall), C and W (in the divertor region), it is expected that material migration will occur due to extreme working conditions (high heat/power loads) followed by re-deposition / co-deposition.

It is well known that a secondary effect related to the plasma wall interaction consists of the fact that the sputtered atoms from the plasma facing components and also the plasma fuel can redeposit on critical points of various components, as improper mixed compounds, which might degrade their own initial performances.

As a result of the processes mentioned above, thin layers of so-called mixed materials of binary (Be_xC_y, Be_xW_y, W_xC_y) and ternary systems ($Be_xC_yW_z$) will be formed. These mixed materials will change the tritium retention/desorption behavior of the original materials as well as their physical and mechanical properties. Hence, the knowledge of the atomic intermixing process and related structural and thermal properties of thin films and multilayers involving typical elements used in plasma facing components becomes of high importance (Be/W/C/D).

The laboratory prepared co-deposited films will simulate the re-deposition of the ITER relevant mixed layers onto the first wall as well as the evolution of wall surface compositions. The deuterium will be co-deposited with beryllium based composite films using a controlled deuterium gas flux.

The structure and morphology of the films were characterized using atomic force microscopy (AFM), scanning electron microscopy (SEM), X-ray photoelectron spectroscopy (XPS) and Rutherford backscattering spectrometry (RBS). The D amount co-deposited into the prepared was determined by Nuclear Reaction Analysis (NRA) using 3He ion beam by means of ^4He (^3He, α)p reaction with the ^3He energy of 0.8 MeV. Thermal Desorption Spectroscopy (TDS) analyses were performed to correlate the influence of films thicknesses as well as gas flow on deuterium trapping mechanisms and release behavior with the films structure.

Papers

[1] K. Sugiyama, C. Porosnicu, W. Jacob, J. Roth, Th. Dürbeck, I. Jepu, C.P. Lungu; J. Nucl. Mater, In Press, 2013; http://dx.doi.org/10.1016/j.jnucmat.2013.01.245,

Conferences

[1] C. Porosnicu, K. Sugiyama, C.P. Lungu, C. Luculescu, W. Jacob, Th. Dürbeck, P. Osiceanu, "Influence of Thermal Treatment on Deuterium Retention and Release Behaviour for Ternary Be-C-W Thin Films", 20th International Conference on Plasma Surface Interactions 2012, May 21st – 25th, 2012, at Aachen, Germany

[2] C. Porosnicu, C.P. Lungu, I. Jepu, K. Sugiyama, W. Jacob, Th. Dürbeck, C. Luculescu, A. Marin, G. Iacobescu, "Characterization of Deuterium Doped Beryllium Containing Films Prepared by Thermionic Vacuum Arc Method", Symposium on Fusion Technology, 24-28 September 2012, Liege, BelgiumReports

Detailed results

In order to obtain depositions containing D gas, a setup as in the Figure 1 was developed. The anode was a crucible filled with beryllium. The sample holder-anode distances were around 28 cm. During

the deposition, deuterium was introduced using a special designed inlet that has many small holes (200-300µm in diameter) in order to achieve a uniform D flux.

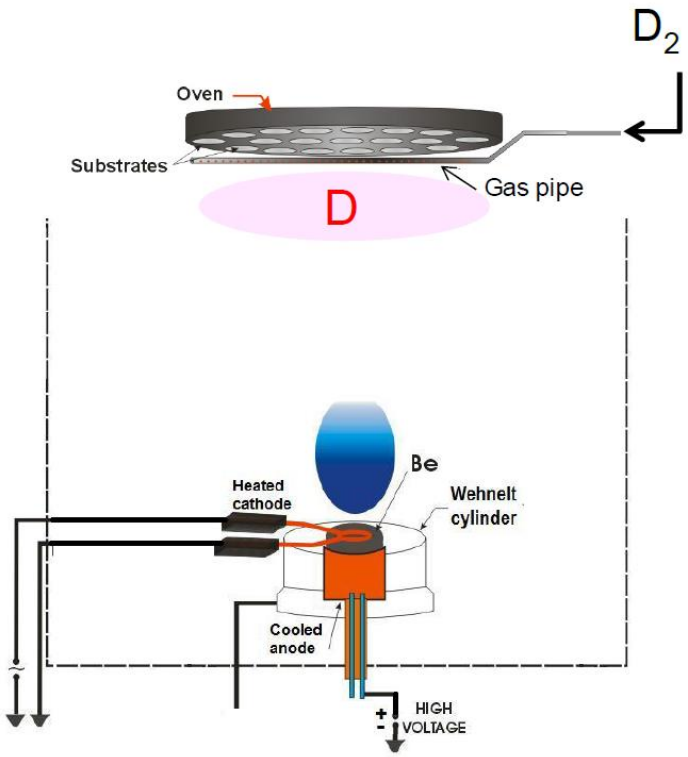

Figure 1 - Schematic representation of the deposition setup for deuterium co-depositions

The electron beams produced by circular heated filament to evaporate the beryllium used as anode, by applying a high voltage (1-2kV) between cathode and respectively anode. Bright plasma in beryllium vapors was ignited. In order to accelerate the ions to the substrates, fact that improves the layer's adherence and compactness proven in previous studies, a negative polarization voltage was applied on the substrates.

For each batch carbon and silicon substrates were used. Carbon substrates were mirror polished fine grain graphite. All the substrates were 12 by 14 mm rectangular shape. The films were deposited at room temperature.

Four sets of 500nm beryllium - deuterium were prepared: for the first three types' D pressure was kept constant at 4×10^{-5} torr but the Be deposition rate was varied (0.15, 0.31, and 0.50nm/s respectively). The last set of samples was deposited at a rate of 0.50nm/s but the pressure was increased to 6.5×10^{-5} torr.

Structural and morphological studies of the layers

Various analyses were performed on the samples to check the purity of the films and of the morphology as well.

XPS analysis was used to determine the chemical states of the elements present on the surface and, after quantitative analysis, to find the element and the chemical state relative concentrations, as well. After Survey XPS spectra, the high resolution photoelectron spectra of the most prominent XPS transitions (Be1s, O1s, C1s).

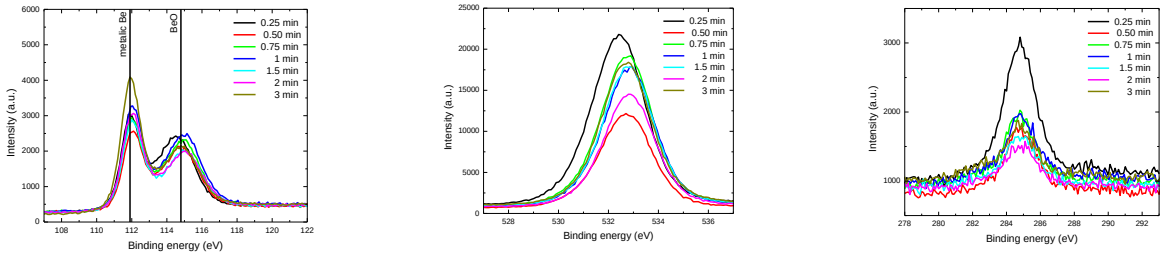

Figure 2 - High resolution photoelectron spectra of the most prominent XPS transitions (Be1s, O1s, C1s)

Be1s signal suggest two binding energies, for BeO (114.8eV) and pure Be (111.9eV). It can be observed the increase of 111.9 eV signal with the Ar sputtering time. The fact that C1 signal is not totally attenuated indicates that the surface contaminated layer and the Be1s signal should turn rise for the pure beryllium binding energy.

From the XPS spectra, after Ar cleaning (1keV) the incorporated C was found as carbides

SEM measurements

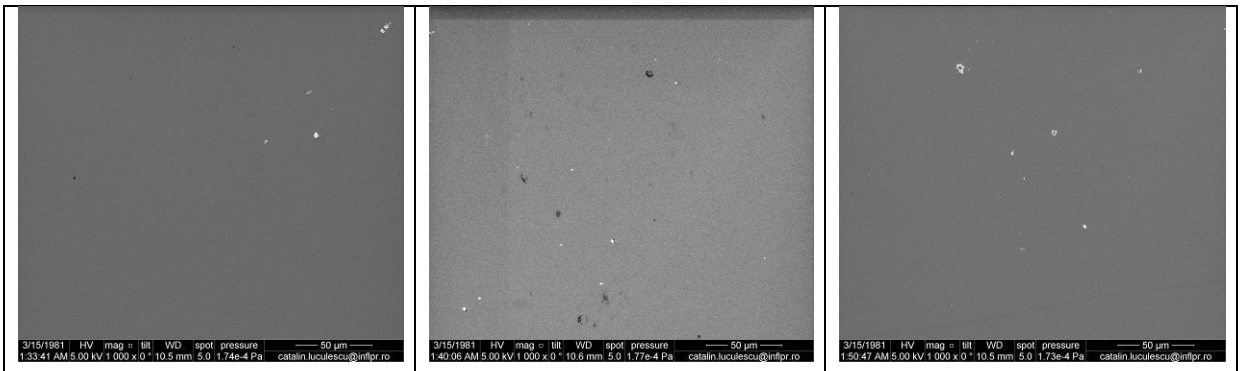

500nm Be+D sample on silicon substrate; Be deposition rate: 0.15 nm/s Pressure 5.3*10^{-3} Pa			500nm Be+D sample on silicon substrate; Be deposition rate: 0.31 nm/s Pressure 5.3*10^{-3} Pa			500nm Be+D sample on silicon substrate; Be deposition rate: 0.50 nm/s Pressure 8.5*10^{-3} Pa		
Elem	Wt %	At %	Elem	Wt %	At %	Elem	Wt %	At %
Be	52.09	65.62	Be	94.36	96.52	Be	92.15	95.20
C	2.04	1.93	C	1.44	1.10	C	1.41	1.09
O	45.55	32.32	O	4.02	2.32	O	6.29	3.66
Si	0.33	0.13	Si	0.18	0.06	Si	0.15	0.05
Total	100.00	100.00	Total	100.00	100.00	Total	100.00	100.00

Figure 3 - SEM images and EDS results concerning Be-D layer codeposited under deuterium atmosphere

The samples were analyzed by RBS and NRA at IPP Garching and were subject to TDS experiments.

RBS measurements were performed to investigate the films compositions, the position of the oxygen and to see if there is a mixture of the three elements. For this it had been used a ^{4}He energy beam of 2.4 MeV. The beam energy value was chosen taking into account the interaction cross section of ^{4}He and Be to avoid the non-Rutherford interaction that may cause errors in the data interpretation.

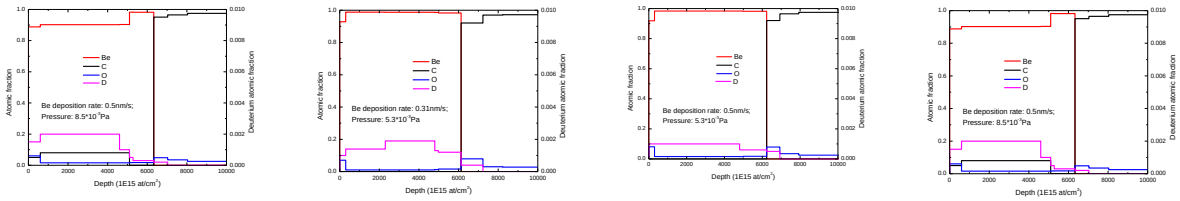

Figure 4 - The composition of the layers computed from RBS measurements, as well the deuterium depth profiles, from NRA measurements. The measurements were performed for samples deposited under different conditions, as shown on the graphs

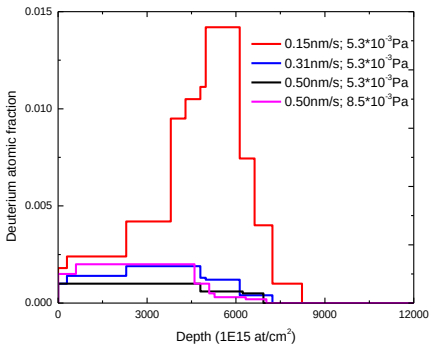

Figure 5 - Deuterium depth profiles as function of deposition conditions

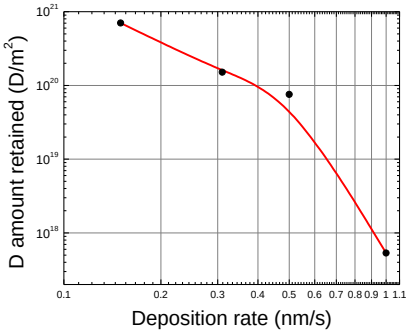

Figure 6 - The total amount of Deuterium retained as a function of the beryllium deposition rate

The amount of D retention was be determined by nuclear reaction analysis using ^{3}He (d, p) α reaction. The fitting of the experimental data form RBS and NRA measurements was performed using SIMNRA code, developed at IPP Garching.

The main aspect underlined by RBS measurements is high purity of the films, the oxygen content except the surface and the graphite interface being around 1at%.

Also, NRA measurements showed a different behavior of the D retention. As the deposition rate, the deuterium is retained in a smaller amount, but for the sample with the highest deuterium content, it is trapped deeper inside the film.

In TESS facility at IPP Garching, thermal desorption spectroscopy (TDS) experiment was performed for the implanted samples.

TDS profiles for the Be-D samples showed clear that the deuterium release temperatures are the same for all samples deposited at the same deuterium pressure but at different beryllium deposition rate, which implies that the same deuterium trapping mechanism occurs. High release temperature suggests high trapping energies. However, for samples deposited using the same beryllium deposition rate, there is a clear change of the trapping mechanism. As the deuterium flux is increased, the energy of the trapping state decreased. There is no obvious shift of the same

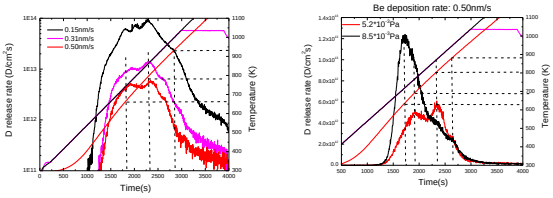

Figure 7 - Comparison of TDS spectra for Be-D samples regarding beryllium deposition rate (left) and deuterium pressure during the deposition (right)

trapping state but the appearance of totally new ones. If for low deuterium flux the energies correspond according to [1] with deuterium trapped in beryllium defects (800-900 K) and Be-O (700K) trapping mechanisms, for the samples subjected to lower fluxes, there is a high contribution of the trapping states corresponding to BeD_2 (550-600 K).

Composite films preparation

A new setup was developed that has the deposition chamber volume increased from 0.3 to 1 cubic meter. This allows the anodes to be placed at a distance from the chambers walls increased by 50%. Also, the distance between the anodes was increased from 15 to 30 cm, fact that minimized the risk of the Be, C and W plasma to interact. Also the new setup was equipped with a liquid nitrogen water vapors trap for the deuterium gas pipe.

Be-C and Be-W composite samples were prepared using thermionic vacuum arc method, under deuterium atmosphere. In order to investigate also the thickness influence on deuterium retention and release, two types of samples were prepared for each mixture. Ones having 300nm and the others having the thickness doubled. Each sample on each batch was subject to a specific deuterium flux. This way, identical samples, with different deuterium content were prepared. The samples were analyzed by RBS and NRA.

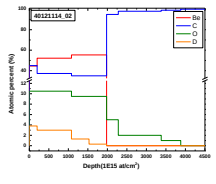

D ~3at%; O ~10at%
Be – 50at%; C – 35-40at%

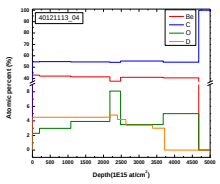

D ~4.5at%; O ~3at%
Be – 40at%; C – 55at%

*Figure 8 - Elemental composition and depth profiles for the **beryllium-carbon** composite films deposited under deuterium atmosphere*

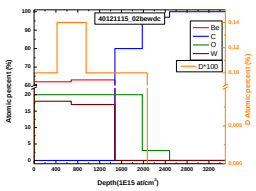

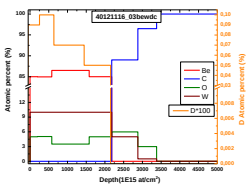

*Figure 9 - Elemental composition and depth profiles for the **beryllium-tungsten** composite films deposited under deuterium atmosphere*

As you can see in Figures 8 and 9, the obtained films had oxygen impurities below 5% due to the new set-up and also deuterium inclusions. The deuterium was present inside the whole deposited layer. The total amount of deuterium was determined from NRA proton count measurement (Figure 11). For the Be-C layers the D inclusions are up to 4 percent, according to the deuterium flux, while for Be-W layers the maximum deuterium content is around 0.1%. As expected, the thick beryllium-carbon films the total amount of deuterium double in comparison with the thin ones.

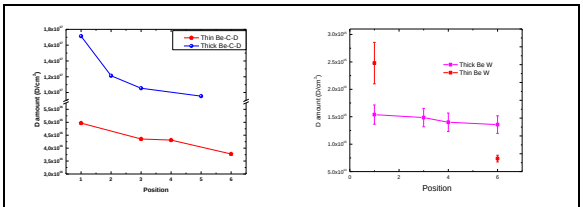

Figure 10 - Total amount of deuterium trapped inside the Be-C D (left) Be-W D (right) samples determined form NRA

Although the Be-W layers were subject to the same deuterium flux such small amount of D found inside the samples can be explained by the heat radiation coming from the tungsten target was much higher than the one from the carbon target, the temperature of the samples during the Be-W D deposition rising up to 500K. The deuterium remaining in the samples is the one that corresponds to higher energy trapping states, thing that was proved by TDS measurements.

In TESS facility at IPP Garching, thermal desorption spectroscopy (TDS) experiment was performed for all the samples. The ramp was set to 15K/min, with a 20 minute hold at 1000K. Then the sample was left to be cooled.

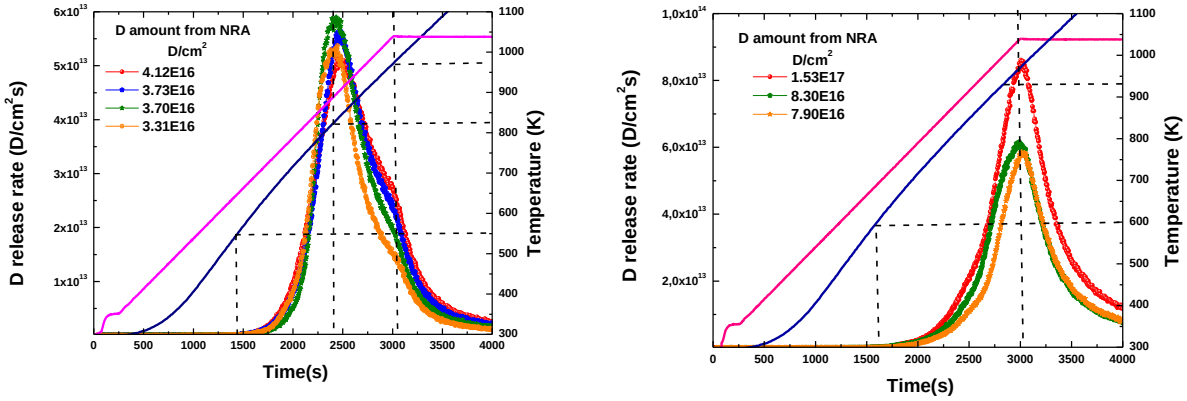

Figure 11 - TDS measurements for Be-C D films deposited in deuterium atmosphere. Results for the thin layers (300nm) are presented on the left, while for thick layers (600nm) are presented on the right

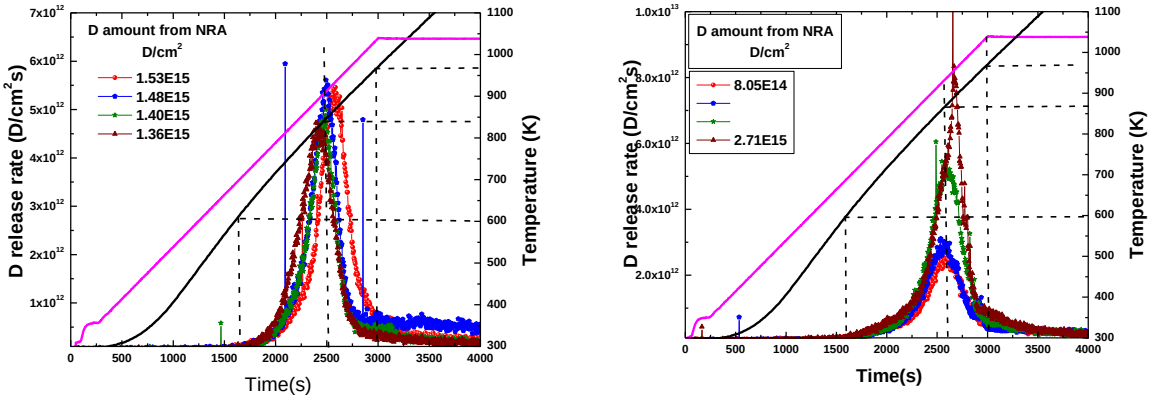

Figure 12 - TDS measurements for Be-W D films deposited in deuterium atmosphere. Results for the thin layers (300nm) are presented on the left, while for thick layers (600nm) are presented on the right

The TDS measurements are showed in Figures 11 and 12. The trapping mechanism for the Be-W thin films doped with deuterium seems to be the same. Deuterium releasing starts at around 600K with a maximum releasing peak at around 875K. The high energy trapping states of tungsten is characterized by this temperature mentioned above, as well as energies attributed to beryllium defects trapping states. By increasing the deuterium flux and quantity inside the samples, the peak is observed to become wider, due to the increase of contribution of the same trapping state. For higher temperatures, the right side of the peak is significantly wider, which could be a sign of even higher trapping energies. This type of samples became unstable after TDS.

The same behavior as for **Be-W** films was found also for the Be-C deuterium doped films. No clear peak was observed for thick films until the 1000K temperature was reached, the trapping energy corresponding to a greater value of the temperature than the maximum allowed in TESS facility for

beryllium containing thin films. The rate of the desorbed deuterium continuously decreased during the 20 minutes hold at 1000K.

NRA measurement was performed on the Be-C D samples in order to determine the remaining amount of deuterium present inside the thin films, after the TDS experiment. It was still observed a deuterium presence of more than 55% inside the samples. It was made a correlation between the deuterium amount remained inside the samples and the desorbed deuterium measured by TDS. After the TDS experiment, the Be-W D samples became unstable so it was impossible to perform NRA. The inventory of the released deuterium from TDS showed that more than 95% of the nuclear fuel was released when the experiment was performed.

Conclusion

Pure Be films, Be-C and Be-W thin films with deuterium inclusion were prepared using Thermionic Vacuum Arc method at the NILPRP-Magurele facility. For this type of thin films, in order to have a controlled impurities seeding of the plasma, a gas feed through was used.

Using SEM, EDS and XPS methods, morphological, structural and diffusion aspects were characterized on all of the structures in different stages.

In order to investigate the films compositions, the position and quantity of the deuterium in the prepared thin films, RBS measurements were performed. Nuclear reaction analysis (NRA) measurement was made to determine the total amount of retained and released deuterium as a function of deposition parameters and deuterium gas pressure. SIMNRA code, developed at IPP Garching was used for the fitting of the RBS and NRA experimental data.

Analysis on the beryllium-deuterium co-deposited samples showed no dependence of the deuterium trapping mechanism on the beryllium deposition rate, but clear dependence on the deuterium flux.

For the Be-C thin films it was found an atomic concentration of 50% beryllium, 45% carbon and 5% oxygen and 85% beryllium, 10% W and 5% oxygen for Be-W respectively.

Using NRA method it was determined a D concentration of about 4% in samples with a total amount around 1E21 D atoms/m^2 for Be-C thin films and 1E19 D atoms/ m^2 for Be-W ones. This difference is explained by the substrate temperature during the deposition process which was high, with an around value of 500 K, reason for Be-W samples to release the corresponding D to low energy trapping sites for this composite film. For Be-C films, D trapping energies have a greater value (corresponding to bigger release energies ~ 600K, and so the D remained inside the samples), results previously showed.

Acknowledgement

The reported work includes contributions from the following people outside the EUATOM-MEdC Association: K. Sugiyama, W. Jacob, Th. Dürbeck (IPP Garching, *Max-Planck-Institut für Plasmaphysik, EURATOM Association, D-85748 Garching, Germany)*

FUSION MATERIAL DEVELOPMENT

W-FGM-STEEL COMPONENTS BY POWDER METALLURGY ROUTES

A. Galatanu[1], I. Enculescu[1], M. Galatanu[1], B. Popescu[1], M. Valeanu[1], M. Walter[2]
[1]*NIMP, Atomistilor 105bis, 077125 Magurele, Romania*
[2]*KIT, 76344 Eggenstein-Leopoldshafen, Germany*
[BS-M3/WP-12-MAT-01-HHFM-01]

Abstract

The method to realize complex materials and pieces starting with W (plates, foils, pieces), W-steel FGMs and steel pieces was further developed for specific shapes. The composition and microstructure of the resulting structured materials was evaluated by electron microscopy (SEM, EDX, backscattering) and mechanical tests. Thin W-steel FGMs (<1 mm) can be used in single or multistep processes to create joints between plates of steel and W (like in the case of the reactor armor). Basic parts, as complex as possible, have been directly created by SPS and then test joined using the direct joining route by SPS.

Reports

[1] A. Galatanu, "W-FGM-steel components by powder metallurgy routes", Ljublijana, July 2012.
[2] A. Galatanu, "**Multi-component W materials and joining procedures**", Garching, February 2013.
[3] M. Walter, "Mechanical characterization of novel W-alloys at high temperatures", Garching, February 2013.

Detailed results

Summary of the work performed In the first stage we have focused the work on three main directions: a) optimization of the W-based components sintering; b) optimization of the mold design for large components sintering and c) optimization of W-steel FGM for W-steel joining. These steps are important for assessing different routes to create more complex components containing W, steel and W-steel FGMs. The main technical requirements can be summarized as: i) having a dense (lowest possible porosity) and solid bonded W part; ii) having a solid, well bonded FGM between W and steel parts; iii) preserving the mechanical properties in of the steel part and iv) defining and adapting the preparation route for different shapes of the components. In the second stage we have focused the work on multi-component materials and pieces from W and W-steel. That means creating basic parts as complex possible as our SPS equipment parameters and molds allowed and then join them using either the direct joining route by SPS (i.e. piece to piece) or via a FGM, the second procedure being mostly used to dual materials W-steel pieces.

Optimization of the W-based components sintering

Large W components, taking into account the current DEMO design, might be defined as parts with at least 2 dimensions larger than 1 cm. Sintering of such W materials adds some new problems as compared with the typical work on smaller samples. The main issue is related to possible inhomogeneous regions in the sample due, on one side to the larger amount of powder and the uniaxial applied pressure, and, on the other side, to possible inhomogeneous temperatures (hot or cold spots) created by the heat/current flow in the sample during sintering. Molds with complex shapes enhance the problem. To reduce at an acceptable level the presence of inhomogeneous regions in larger pieces we have set up an iterative procedure and performed two types of investigations: 1) create larger samples at different temperatures with a given mold design and analyze by microscopy the resulting sample and 2) use a special custom made thermocouple (Omega

Eng. Inc, USA - working up to 2300 C)) for our SPS equipment on mock-up molds/samples configurations. This method was applied for both simple W and W-steel FGMs, for different parallelepiped like samples and samples with curved surfaces, taking into account the present design for pieces in the DEMO divertor. For pure W samples, using micrometric, nanometric and mixture powders we succeeded in obtaining homogenous samples with only slightly modified molds for dimensions as large as 3 cm transversal to the heating/pressure axis (z-axis) and also for curved surfaces perpendicular to z-axis with a radius down to 3 cm. We note, however, that this good result is due mostly to the relatively high temperature (1550 C or above) and the good electrical conducting behavior of W.

Optimization of the mold design for large components sintering

One of the main advantages of SPS sintering arises from the double heating, by convection from the mold (which creates temperature gradients from outside to inside) and the electrical driven heating which in turn has two components: Joule effect heating in grains and electrical discharges (sparks) between not well connected grains. The former term strongly depends on the material specific electrical resistivity, while the latter is mostly influenced by the number of bad contacts between grains (big grains and/or irregular shapes meaning more sparks). In the case of multi material samples (like FGMs or joining/brazing pieces) the main problem arises from different electrical resistivities and therefore different Joule heating. This means that the mold should compensate with additional heating in the parts corresponding to low resistivity material. In a simplified picture the mold should have a higher resistivity in the region needing more heat, i.e. the section of the mold at that level should be reduced. Of course, this depends also on the material shape and implies a precise and adequate mold design for the specific requirements of the component design. Although a crude model was already developed, some factors as spark heating are not included in the calculations and the model should be tested using temperature measurements along the sample z-axis for every test mold design.

Optimization of W-steel FGM for W-steel joining

As previous stages results have already shown, it is possible to join W with steel using a spark plasma device and an intermediary W-steel FGM. Different routes, with one or several steps have been tested in previous work for small samples with thin plates of W and Eurofer as mock up for the main materials to be joined. To obtain FGMs, the layers have been realized by nano- and or micro-powders of W and steel or Fe in different proportions. The mixtures were prepared in glove box in Ar atmosphere with less than 5 ppm water and less than 20 ppm oxygen. Layers of 0.1-0.5 mm thickness have been realized and it was possible to join the steel and W thin plates obtaining consolidated components. However, the overall z-axis dimension of the resulting component was relatively small, with less than 3 mm total thickness and less than 1 mm the FGM thickness. Also larger samples (thickness between 1 and 10 mm) have been obtained but either with low quality sintering in the W rich part or with partial melting in the steel/Fe part. Figure 1 summarizes the results of various experiments.

W FGM composition		FGM thin (*l* < 1mm)			FGM large 1mm < *l* < 10 mm		
		good T (°C)	melting T (°C)	joining to W	low sintering at W part T (°C)	partial melting T (°C)	joining to W
ss	nano	1200-1250	> 1300	ok	< 1300	> 1300	bad
Fe	micro	1250-1350	> 1400	ok	< 1350	> 1400	ok
	nano	1050-1100	> 1150	bad	< 1150	> 1150	no way
Eurofer	micro	1200-1250	> 1250	ok	to be tested		

Figure 1 - Work status on W based gradient materials

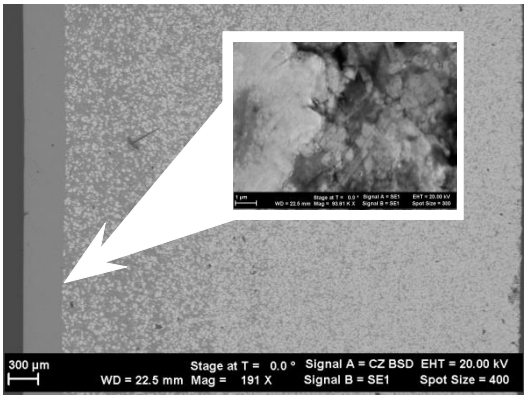

Figure 2 - 5 mm thick W-steel FGM joined on Eurofer 97 plate (main picture) and the very good quality joint with the steel plate (inset)

An assessment of these results shows that the main problem arises from the very different sintering temperatures in W and steel (T optimal for W at about 1750 and T optimal for steel at 1200-1250 C) and suggests, as possible route to create larger FGMs, to create a temperature gradient during sintering along the z-axis using a mold design as described in the previous section. Such a design was tested for a sample with about 5 mm thickness and the result is presented in Figure 2 (main), while the inset shows the very good quality of the joint between the FGM and the Eurofer plate.

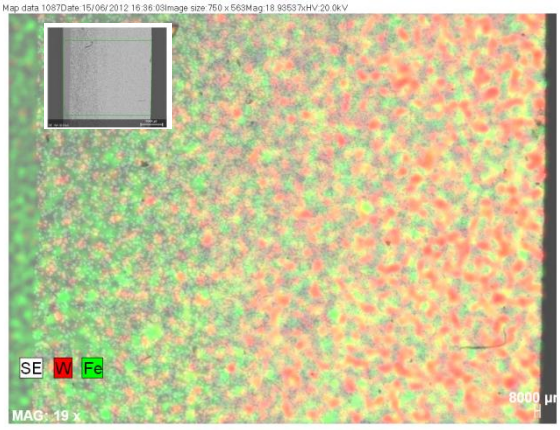

Figure 3 - Elements map of the W-steel FGM

In Figure 3 an element concentration map is shown for the same sample indicating a very good concentration gradient across the material. This was in fact confirmed by point EDX analysis in different regions of the sample. Since such a material is designed as an intermediate piece for components, it is important to check also if a conventional further joining to structural components (steel) is possible. In this view we connected the FGM to other Eurofer pieces by conventional arc welding. In Figure 4 one can see a SEM picture of the resulting material. The sample was etched in order to identify the original contact region between the FGM and the other Eurofer piece and also to assess the possible material damage during welding. No change in the morphology was detected in the whole original FGM, including the W rich side which remained without cracks, Also the original joint between the Eurofer thin plate and FGM was not affected by welding.

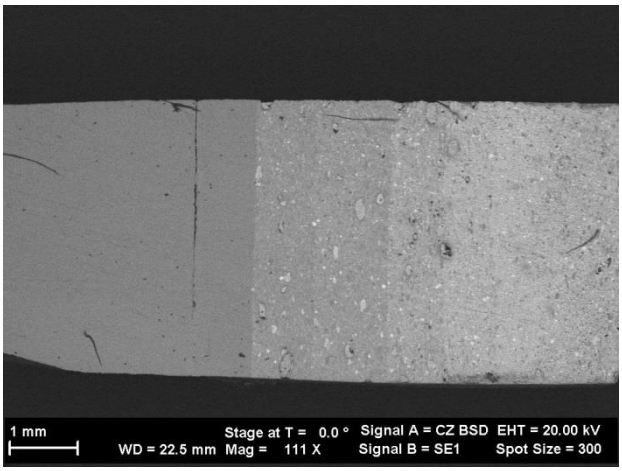

Figure 4 - SEM image of a conventional arc welding between Eurofer and W-steel FGM

Thus, the last point to be solved remains the joining of the W rich side of a large FGM to a large piece of W. To solve it, we propose several routes. One is be to directly sinter a W piece with an included thin W- low Fe (or V or Ti) concentration FGM and then to join it to the main W-steel FGM. A second route is to improve the mold design to create a much larger temperature gradient along the axis and directly sinter the whole piece in one step.

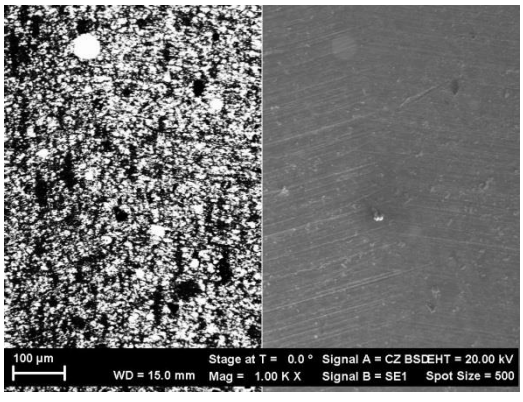

Figure 5 - W-stainless steel joining component 1:1 masic as EBS image (left) and SEM (right) of a polished and then etched sample. Note the smooth surface on the SEM image due to the corrosion resistance of the steel

To join the W piece to other W or to steel we have prepared and tested W-Fe and W-stainless steel mixtures in the masic proportions 1:1. The mixtures of nano-powders of W and steel (or Fe) were prepared in glove box in Ar atmosphere with less than 5 ppm water and less than 20 ppm oxygen

and then further mixed and partial alloyed by PMB. Then the resulting powders have been sintered as separated pieces using SPS. All procedures were performed in Ar atmosphere. The other test materials (Ti and V) could be used in a single step process to create a "self-brazing" layer.

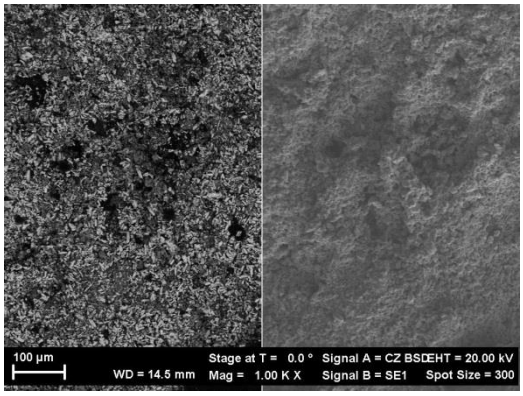

Figure 6 - W-Fe joining component 1:1 masic as EBS image (left) and SEM (right) of a polished and then etched sample. Note the porous surface on the SEM image due to the strong Fe corrosion.

In figure 5 the resulting W-SS piece was investigated by SEM and EBS. The sample shows a dense material with a uniform dispersion of W and preserves the nm W grains, although the particles form conglomerates. A similar result was obtained for W-Fe (see Figure 6), but in this case the porosity is much higher when using similar sintering parameters. This is due to the partial passivation of the initial Fe nm powders (as receives from the supplier). That is also the reason for a very low thermal transport as it can be seen from Figure 7. The low thermal conductivity is a setback for this joining procedure and should be improved by using micron sized particles instead of nanometric ones and/or by increasing the W content.

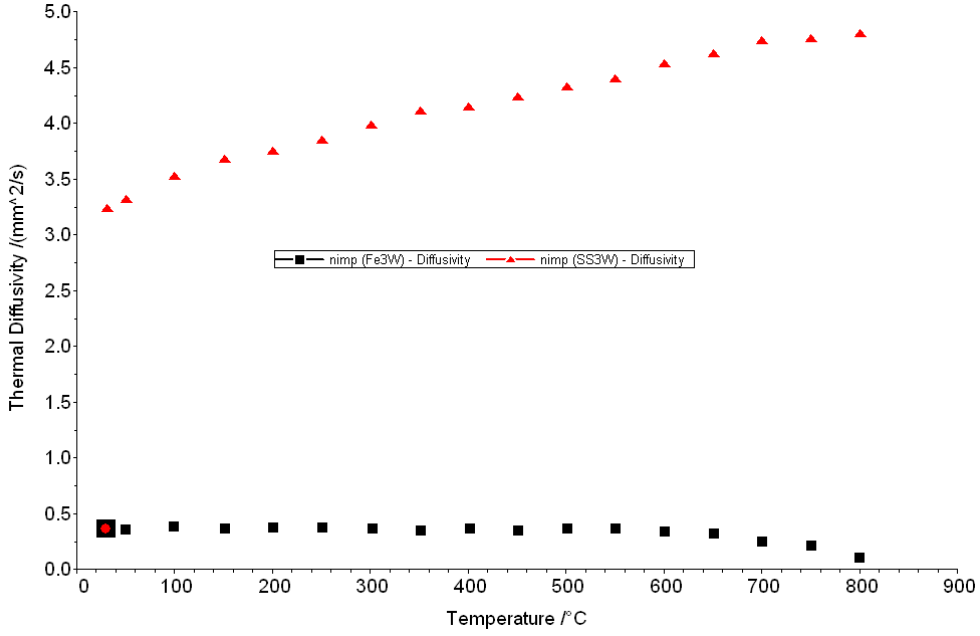

Figure 7 - Thermal transport properties of W-Fe and W-SS joining components measured on disc shaped samples of about 1 mm thickness

Mechanical tests (3 point bending, see Figure 8) have been performed in cooperation by the KIT association. The tests at 550 C were carried out compressing both W (test 1) and steel (test 2) rich

site on 3 mm x 4 mm x 27 mm specimens of W-Eurofer FGMs. The specimens with W-rich side under compression exhibited a good strength and ductility, with some local damage. On the other hand, the specimens with W-rich side under tension exhibited bad strength and continuous crack growth with increasing load.

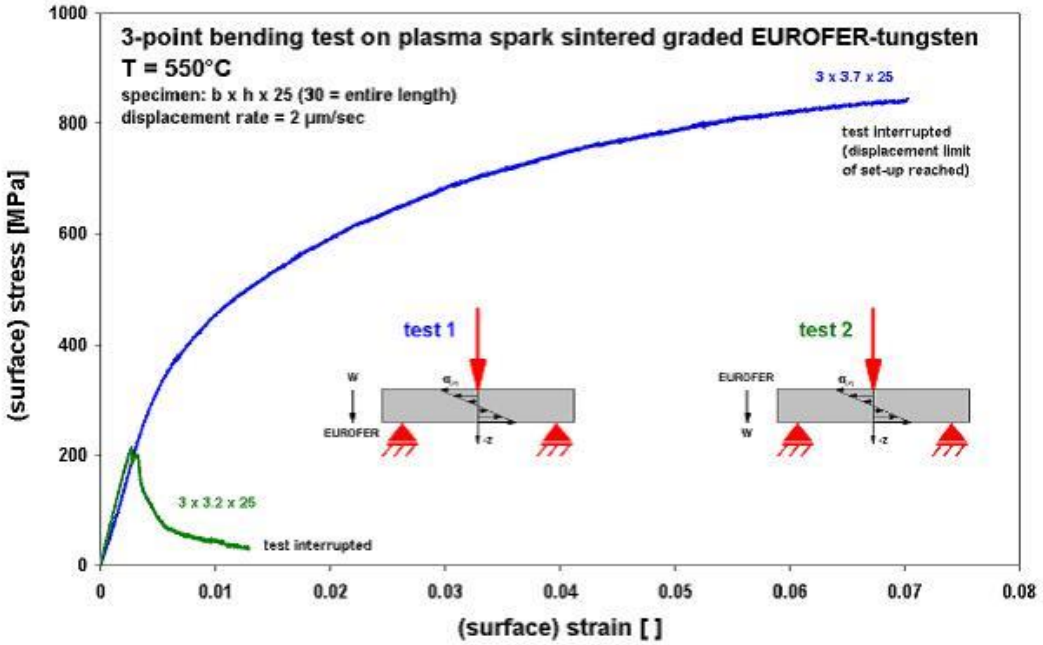

Figure 8 - 3 point bending test results on W-Eurofer FGMs (measurements performed by KIT association)

Obtaining W components

The current DEMO divertor model includes "finger"-type components consisting of an armor part (tile) made from W with a hexagonal plate shape, a bell shaped "cap" made from W or W-Re alloy and a Eurofer steel pipe, which is further connected to the complex He cooling system. The tiles can be realized by a PIM + HIP process or as we propose by SP sintering. The former method is more complex using several steps but can be better scaled up to industrial production, while the latter one is a one step process but more difficult to scale toward industrial production. Some other obvious advantages of SPS are the better grain size control and the easy application to multi-material components. For the W components a mixture of nm and µm powders was used. Tests on standard cylindrical samples have shown that the SP sintering parameters can be preserved for the samples with different grain sizes without affecting the final sample density.

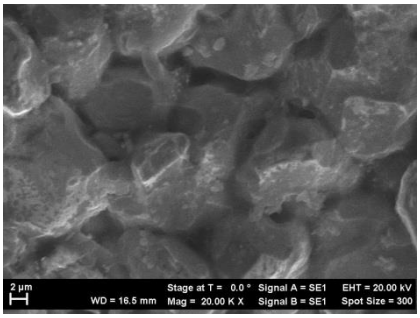

Figure 9 - High magnification SEM image pointing to the high quality sintering in the SPS process

Thus, slightly larger concentrations of nm powder have been disposed at the angular regions of the molds. In Figure 9 a SEM image for a 98% theoretical density sample is presented. The analyzed surfaces were polished and then etched. A picture of a mock-up piece for the divertor tile is shown in Figure 10.

Figure 10 - Divertor tile mock-up SP sintered in NIMP

Conclusions

W shaped pieces can be successful realized by SPS sintering and we were able to modify the molds design to create different possible components. Thin W-steel FGMs (< 1 mm) can be used in single or multistep processes to create joints between plates of steel and W (like in the case of the reactor armor). For larger pieces, needing thicker FGMs it is also possible to use a similar technique, but in this case several steps might be necessary. Also the corresponding processes need to be optimized, together with the molds design. Multi-component materials and pieces from W and W-steel can also be successful realized by SPS sintering and joining. In the next stages (2013-) we aim to create real mock-ups of the DEMO divertor components to be tested in working conditions.

Acknowledgement

The reported work includes contributions from the following people outside the EUATOM-MEdC Association: Mario Walter (EURATOM - KIT Association, Germany)

SPS JOINING&BRAZING W-W AND W-STEEL

M. Galatanu, B. Popescu, M. Enculescu, P. Palade, A. Galatanu
NIMP, Atomistilor 105 bis, 077125 Magurele, Romania
[BS-M3A/WP-12-MAT-01-HHFM-04-01]

Abstract

FAST (Field Assisted Sintering Technique) was applied to join W to W and W to steel (Eurofer 97) by brazing with an intermediate powder layer. A new procedure was defined for powder brazing, using a mixture of micron and nanometric sized metal powders. The results have been compared with the previously tested direct W-steel joining results and with classical foil brazing. Extension possibilities for using this method for different shaped samples have been evaluated. FAST technique was successfully applied to join W with W and W with Cu.

Conferences

[1] "Unconventional Routes for Joining W and Steel Using FAST", A. Galatanu, A.D. Jianu, M. Galatanu, I. Enculescu, in International Conference of Balkan Physical Union, July 2012, Constanta

Reports

[1] A. Galatanu, "Optimization of different routes for joining W and W-steel", Ljublijana, July 2012.
[2] A. Galatanu, "SPS joining method development", Garching, February 2013.

Detailed results

In the current DEMO design, plasma facing components are made of W, which is a very difficult material, due to its low mechanical quality and very high melting temperature. Joining such a material with similar W-based components or structural parts (usually made of steel) rises several technological problems. Since classical welding is excluded, a possible alternative is given by brazing. However, there are several restrictions. One problem is that in some cases, the joint must withstand temperatures around 1000 C and high irradiation levels, which excludes typical brazing materials. Another problem is related to the complex shapes of the pieces, which means larger surfaces requiring homogeneous thermal and mechanical properties. A schematic representation of the targeted work and proposed solutions for this topic is depicted in Figure 1, taking the design of the divertor tiles as reference.

FAST is a versatile technique and as heating arises for metallic samples both from Joule effect and electrical discharges between grains it looks promising for brazing. In the case of direct joining or foil brazing, one would expect discharges to take place in the microscopic narrow empty spaces between the materials. Thus, if the rugosity of the surface is not reduced, there are increased probabilities for incomplete joints. These defects will in turn decrease the thermal conductivity across the joint and also reduce the mechanical quality. Very well polished surfaces are needed in this case. Also, it might be beneficial for the process to have a high plasticity material (foil) as brazing material. An additional difficulty might also arise if the shape of the samples to be joined is slightly different. This situation is almost unavoidable if the original pieces are sintered (see e.g. the tile design in Figure 1 for the high temperature joint). On the other hand, in the cases of direct joining and foil brazing, the main heat will be generated by Joule effect, both in the sample and mold (if used). Thus, the joining process will on one hand take more time and, on the other hand, will depend on the conducting properties of the pieces. W and Cu have both low electrical resistivity, but

steels are notoriously poor electricity conductors. Hence, a higher heating will occur in the steel part, with possible melting and/or higher migration rates of the oxide dispersions in the ODSFS case.

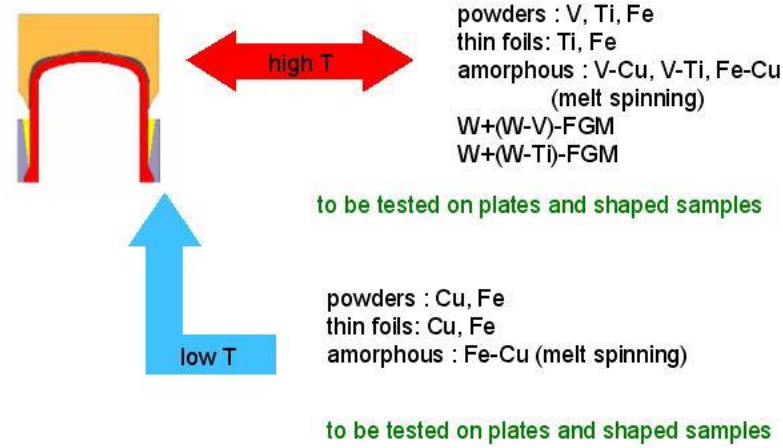

Figure 1 - Schematic description of our work plan and suggested solutions in the joining topic

There are basically two possibilities for improvement. One of them concerns the increase of the plasticity of the brazing material by alloying (this will be investigated in the next stages) or by heating first the sample to the DTBT of the brazing material and then applying a pressure to fit the brazing layers to the main pieces. It is more convenient to use powder as brazing material. An adequate mixture of nanometric and micrometric powders will perfectly fit all the space between the main pieces. Moreover, our SPS equipment can also apply pressure and this might help as already mentioned above. Note also that FAST allows for quick brazing times, and therefore the nm structured brazing material will keep its morphology. The second option will be to heat the brazing material to its melting temperature in order to use its viscous flow for fitting the joint.

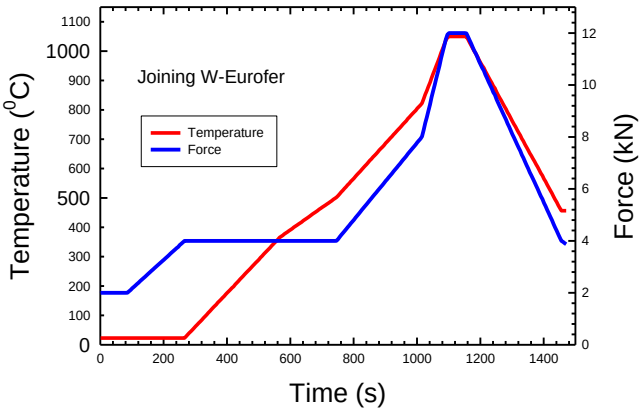

Figure 2 - SPS main process parameters for joining W and steel pieces

Figure 2 shows a typical joining process. The first step involves a cool pressing to mechanically adjust the W-brazing layer-steel ensemble. It follows a heating to DTBT of the brazing material, and thereafter a hot pressing step. Finally, the temperature is increased to the brazing value (with or without an additional hot pressing) for a short time, followed by a controlled cooling and pressure reducing to allow a better accommodation of materials with different expansions coefficients. By such a procedure, we have tested and compared a direct joining W-steel, Cu-foil brazing, with or without mold configurations and Cu powder brazing only in mold. Note that using nanometric sized

powders implies that all the preparation steps are also performed in Ar atmosphere and therefore one needs shaped samples to work without molds.

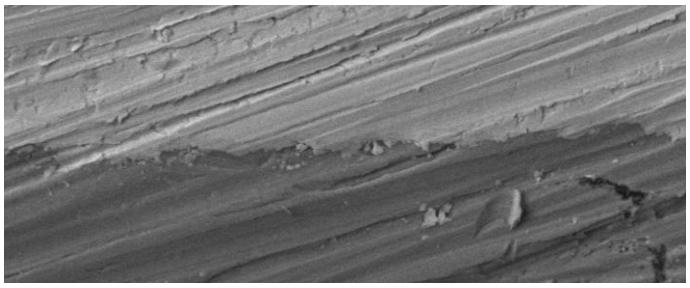

Figure 3 - Direct SPS joint between W and Eurofer 97

Figure 3 shows a SEM image of a direct joint between W (top part) and steel (bottom part). It is possible to observe that a good diffusion process occurred. Since the sample was firstly analyzed for its thermal properties up to 700 C, it is also possible to consider that the joint quality was preserved after at least thermal cycling. Nevertheless, such a good joint could only be obtained after the W and steel pieces have been polished to under micrometer size (using diamond powders).

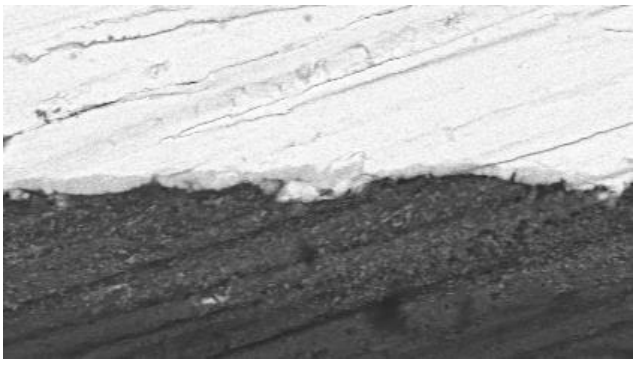

Figure 4 - SPS Cu-foil brazed joint between W and Eurofer 97

Figure 4 shows a SEM image of a brazed W-steel joint using an 8 um Cu thin foil. A careful inspection along the joint revealed that in spite of the finely tuned process parameters, some areas show Cu-foil damage. This can be due either to differences between the expansion coefficients of the materials, or to electrical discharges in the process at points were the mechanical contact was poorer.

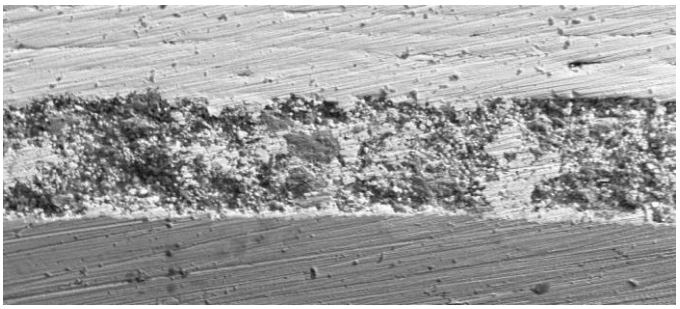

Figure 5 - SPS Cu powder brazed joint between W and Eurofer 97

In Figure 5, a Cu-powder brazed joint is presented. It is easy to observe that even for different distances between the main pieces the continuity of the joint is preserved. The SEM images show

also that partial melting of the Cu has occurred, although the brazing temperature was bellow Cu melting point. This might be explained by small inhomogeneities in the sample temperature (due to spark heating). A better tuning of the process parameters can correct this.

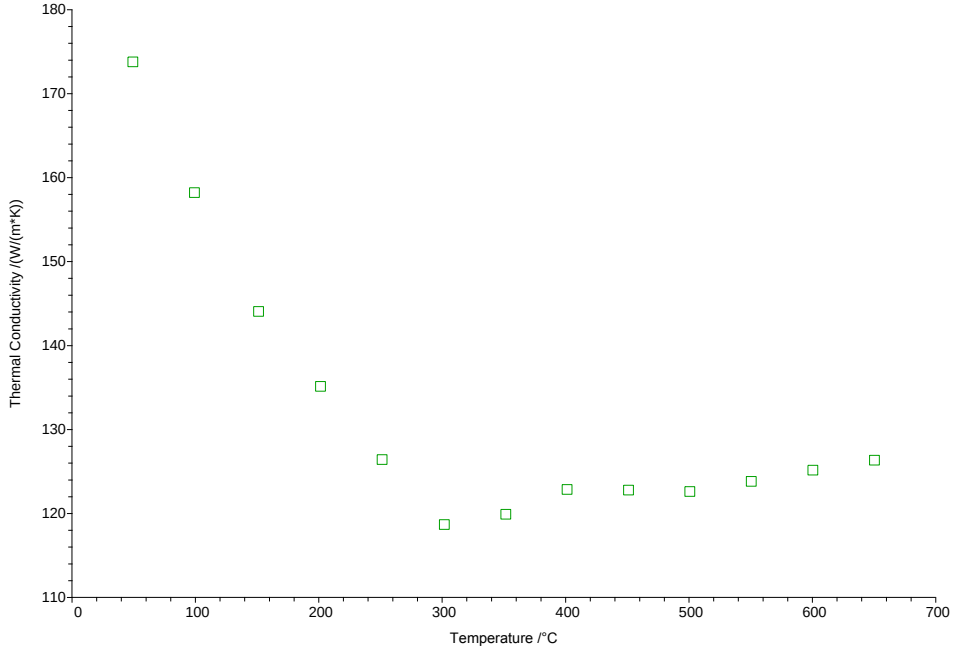

Figure 6 - Thermal conductivity of a W-Cu SPS direct joined piece

Since Cu and W have more than 2000^{o}C difference between melting points, and also a big difference between the thermal expansion coefficients we wanted to assess the W-Cu joint behavior. In this view, we have prepared a W-Cu direct joint and analyzed its thermal properties at high temperatures. The result for thermal conductivity is shown in Figure 6 for this composite. Since one can assume a hardening process during the composite cooling under pressure the kink around 300-400^{o}C can be related to an annealing process. This behavior should be taken into account for fine-tuning the SPS process parameters in the future steps

The second part of the work was devoted to W-W joining. The previously defined procedure was applied directly to W materials, with process parameters optimized for various configurations. We have tested the FAST joining technique for W following two main directions: 1) joining W-Cu at the Cu melting temperature limit, and 2) joining W-W using nm W powders.

The first direction, as proposed previously, is to perform the joining procedure at the limit of Cu melting temperature. Due to statistical distributions of temperatures in the FST process, one should expect that at least in bad contact zones, the temperature will be higher thus melting the Cu and improving the contact.

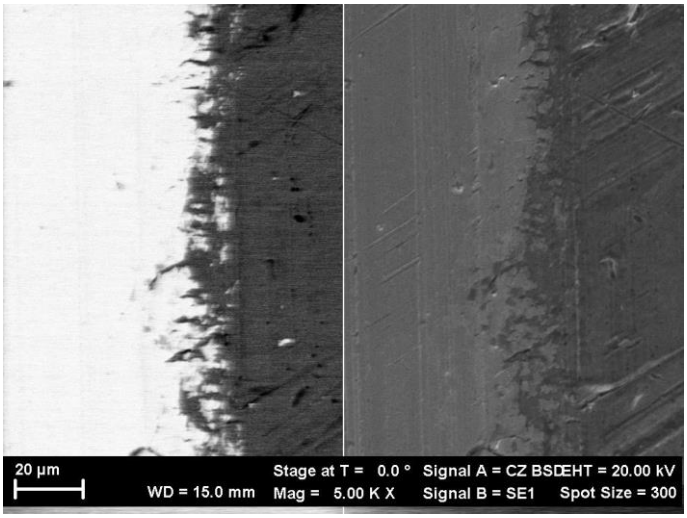

Figure 7 - EBS (left) and SEM (right) images of W-Cu joint realized by FAST at the Cu melting limit

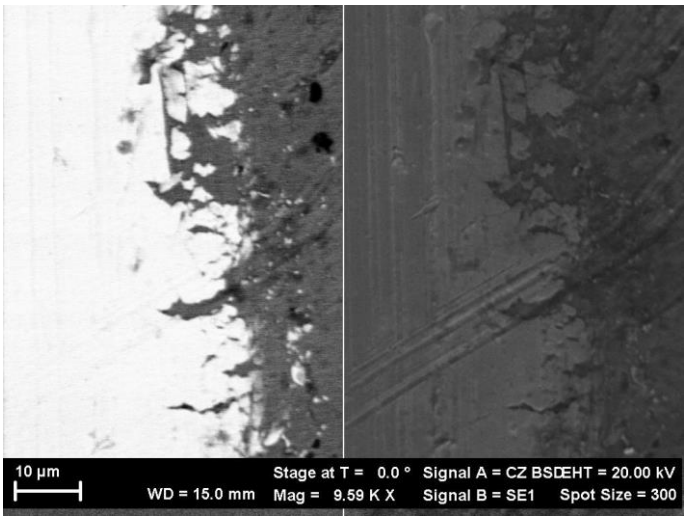

Figure 8 - Detailed EBS/SEM images of the W-Cu joint. Note the W zone fragmentation due to Cu partial melting and diffusion in W

In Figure 7, an EBS/SEM image of a W-Cu joint is presented. One can directly observe an unusual wide contact region at the W-Cu interface, of about 20 um. This value can be compared with the previous results, where a Cu foil was used for brazing. In this case the final contact region was around 1 um. A magnified image of the present joint (see Figure 8) reveals some W islands inside the Cu area and possible cracks developed in the W region. Indeed, as a higher resolution SEM image shows in Figure 9, micrometer sized cracks are present in W. The most likely explanation is related to the Cu-W thermal expansion mismatch. The effect takes place both during the joining process and also further during thermal cycling. To avoid such behavior some improvements could be considered such as a better surface preparation, using a buffer nm Cu powder or better temperature adjustment.

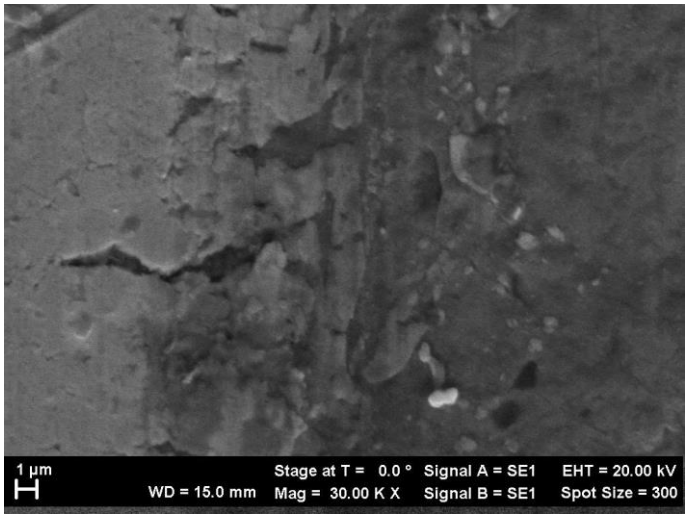

Figure 9 - Cracks development in W at W-Cu contact region

The second approach was suggested by the shortcomings observed during W-W direct joining by FAST, i.e. the presence of a discontinued interface between the W pieces. The solution implies the addition of a nm W powder as a thin buffer layer.

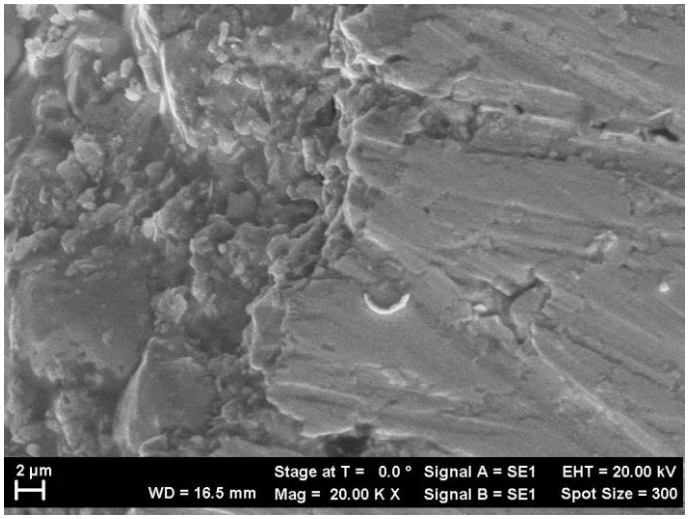

Figure 10 - Direct joining of a standard (commercial, um size grains, left part) W with a SPS sintered W piece (NIMP) using nm sized powders (right part)

Figure 10 shows the joint area between a commercial W piece (HIP, nm sized grains) and one of our SPS W made from nm powders. One can observe that an improved continuous interface appears at the joining place while the nm grains are preserved (see right part of Figure 10). To better understand the FAST process in this case we have also joined 2 of our nm grains W pieces, as depicted in Figure 11. One can observe that the grain size increase occurs mostly in the buffer layer, pointing to much higher local temperatures as the main SPS process temperature. Thus, this method seems to be a very promising solution for joining large surface W pieces and should be further developed and tested.

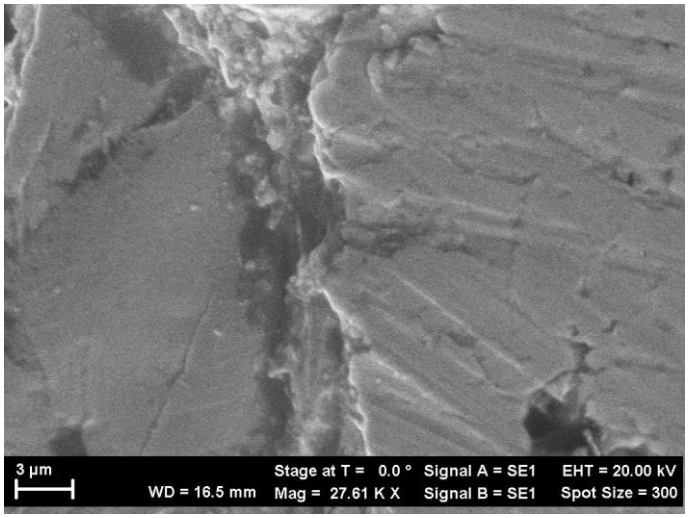

Figure 11 - FAST powder brazing of two W pieces using nm W powder as brazing material (The W main pieces have been produced by SPS on nm powders.)

Conclusions and future steps

FAST was applied to join W and steel (Eurofer 97) by brazing with an intermediate Cu layer. A new procedure was defined for powder brazing, using a mixture of micron and nanometric sized Cu powders. The results have been compared with the previously tested direct W-steel joining results and with classical foil brazing. Extension possibilities for using this method for different shaped samples have been evaluated. FAST was also successfully applied to join W with W. A promising procedure was defined using nm W powder as buffer layer between large W pieces while W-Cu joining at the Cu melting temperature limit induces cracks in the W part, a phenomena detrimental to the material. The FAST process parameters have been adjusted for work with and without molds. In future stages, we plan to develop the method for other (low activation) materials, such as V and Ti, and to investigate in detail the shape restrictions and SPS equipment potential for joining armor and structural pieces from the current DEMO design. Extensive work will also be devoted to further development of the procedure to assess the joint quality using thermal diffusion

ODSFS BY SPARK PLASMA SINTERING OF PLANETARY MILLED AND MELT SPINNING PRECURSORS

P. Badica, P. Palade, M. Burdusel, C. Bartha, V. Kuncser
National Institute of Materials Physics, Atomistilor 105 bis, 077125, Magurele, Romania
[BS-M8/WP-12-MAT-01-ODSFS-01-01]

Abstract

Spark Plasma Sintering (SPS) was used for fabrication of ODSFS from precursors obtained by two routes: planetary ball milling and melt spinning.

Mixtures of powders with model-like compositions (Fe9Cr-0.3Y_2O_3 and Fe14Cr-0.3Y_2O_3) were mechanically alloyed for 20h in Ar and under ethanol by planetary ball milling. Raw powders, non-alloyed (manually mixed in an agate mortar) and alloyed powder mixtures were characterized by thermal analysis (DSC), X-ray diffraction (XRD), scanning electron microscopy (SEM) and Mossbauer spectroscopy. Differences between powders were revealed. Non-alloyed mixtures of Fe, Cr and Y_2O_3 raw powders and mechanically alloyed powders (containing FeCr α-bcc phase) were SPSed at two temperatures of 850 and 1050°C selected based on thermal analysis data. SPSed samples were characterized by XRD, SEM/EDS and Vickers hardness (HV). The main results are:

1. SPS on non-alloyed mixtures leads to formation of a composite composed of a Fe matrix, Cr island grains and an intermediate region of Fe around the Cr islands. For SPS at 850°, Fe-matrix is composed of equiaxial grains, while at 1050°C it is of lamellar morphology. SPS is not effective for alloying.

2. SPS at 1050 °C applied on the mechanically alloyed powders leads to ODSFS samples (containing FeCr α-bcc phase) with density above 95% showing a HV of about 450 HV units and an average crystallite size of about 80 nm. SPS at 850°C results in densities below 90%, a lower HV of about 250 HV units, and a smaller crystallite size as determined from XRD of about 2 times lower than in the previous case.

Precursor ribbons were obtained by melt spinning using SPSed ODSFS with composition (Fe14Cr-0.3Y2O3) and produced as addressed above. X-ray diffraction (XRD) and Mossbauer spectroscopy indicate that ribbons are composed mainly from γ-fcc phase FeCr alloy instead of FeCr α-bcc phase from the SPSed ODSFS used for melting. However, SPS at 1050°C on precursor ribbons produced α-bcc (ferritic) ODS. Sample has a density of 99% (Archimedes method) and is composed according to XRD analysis from crystallites with a small size of 28±5nm. SPSed sample has Vickers Hardness of 474 HV units.

Reports

[1] P. Badica et al, Production and characterization of laboratory-scale batches of nano-structured ODSFS fabricated by Spark Plasma Sintering (ODSFS by Spark Plasma Sintering: preliminary experiments, part 1, 2012), Ljubljana, Slovenja, June 2012.
[2] P. Badica et al, Production and characterization of laboratory-scale batches of nano-structured ODSFS fabricated by Spark Plasma Sintering (ODSFS by Spark Plasma Sintering: preliminary experiments, part 2, 2012), Garching, Germany, February 2013.

Detailed Results

The development of the DEMO fusion reactor is established as a priority in EU. The reactor's structure is complex, fast evolving and needs for its construction the support of different materials with certain specifications. With the stop of the production of Eurofer steels - a former candidate to be used as a structural material on which the armour material is placed -, a replacement is looked for among ODS steels. At this stage of research, laboratory scale fabrication and characterization of ODS are one of the key aspects.

To respond to presented problem we proposed to look on new laboratory scale routes based on powder metallurgy and spark plasma sintering (SPS). The main objective of 2012 is to evaluate the potential of powders processing involving SPS for fabrication of ODSFS. We target good mechanical properties of the as-fabricated ODS materials so that they can be useful and compatible with the requirements of the DEMO design.

Samples as powders and SPSed bulks are gathered in Table 1.

Table 1 - Powders and SPSed bulks. Average Vickers hardness (obtained on one sample for 10 indentations), Archimedes density, relative density, lattice parameters and crystallite size (from XRD and Rietveld refinement using MAUD software). Theoretical density of the alloys was calculated: Fe9Cr-0.3Y_2O_3 = 7.5971 g/cm^3, Fe14Cr-0.3Y_2O_3=7.5644 g/cm^3.

No	Sample	Vickers Hardness $HV_{0.5Kg}$ load average	ρ [g/cm^3]	Relative density [%]	Lattice parameter a [Å] bcc	Crystal size [Å]
Precursors (P)						
P1	Fe raw powder (ICSD 76747)	-	-	-	2.866	-
P2	Cr raw powder (ICSD 64711)	-	-	-	2.88575	814±15
P3	Fe9Cr-Y_2O_3-0h, Mixture of Fe + Cr powders by hand milling	-	-	-	-	-
P4	Fe14Cr-Y_2O_3-0h, Mixture of Fe + Cr powders by hand milling	-	-	-	-	-
P5	Fe9Cr-Y_2O_3-20h powder (ball milling)	-	-	-	2.8701	108±4
P6	Fe14Cr-Y_2O_3-20h powder (ball milling)	-	-	-	2.869	98±4
P7	MS ribbons (melt spinning using S10), initial batch amount 3.8g	-	-	-	-	-
P8	MS ribbons (melt spinning using S10), initial batch amount 5.8g	-	-	-	fcc 3.6191(3)	980±30
Bulk SPSed samples						
S1	Fe 850°C (SPS on P1)	134	7.53	97.6	-	-
S2	Fe 1050°C (SPS on P2)	259	7.67	95.8	-	-
S3	ODS 9 -0h- 850°C (SPS on P3)	123	7.52	98.9	Fe 2.8667(1)	1750±60
		198			Cr 2.8841	750±100
S4	ODS 9 -0h- 1050°C (SPS on P3)	-	7.39	97.2	Fe 2.8665(3)	1010±40
					Cr 2.8861	620±50
S5	ODS 14 -0h- 850°C (SPS on P4)	138	7.46	98.6	Fe 2.8674	1710±50
		211			Cr 2.8868	712±35
S6	ODS 14 -0h- 1050°C (SPS on P4)	-	7.36	97.2	Fe 2.8663(5)	1010±20
					Cr 2.8861	513±25
S7	ODS 9 -20h- 850°C (SPS on P5)	275	6.57	87.1	Fe-Cr 2.8709	407±9
					Fe3C 5.093	900±350
S8	ODS 9 -20h- 1050°C (SPS on P5)	449	7.26	95.6	Fe-Cr 2.8699(2)	910±7
					Fe3C 5.083	1320 ±200
S9	ODS 14 -20h- 850°C (SPS on P6)	245	6.14	82.1	2.8683(8)	475±10
S10	ODS 14 -20h- 1050°C (SPS on P6)	469	7.34	97.1	2.8704(5)	809±20
S11	ODS on MS-P5 (SPS at 1050°C on P8)	474	7.48	99	2.8742	280±5

1 Raw powders, mechanical milling and characterization

Mixtures of powders with model-like compositions (ODS9Cr-0.3Y2O3, P5 and ODS14Cr-0.3Y2O3, P6) were mechanically alloyed for 20h in Ar by planetary ball milling (250ml jars, 10:1 balls/powder ratio, 300rpm, milling media was ethanol, Retsch PM400). Raw powders (P1, 2), non-alloyed (P3, 4) and alloyed (P5, 6, Table 1) powder mixtures were characterized by thermal analysis (DSC), X-ray diffraction (XRD, Bruker, $Cu_{K\alpha}$-radiation), scanning electron microscopy (SEM/EDS, EVO Zeiss 50/Bruker) and Mossbauer spectroscopy (Figs. 1, 2, Table 1). Differences between powders are as follows:

1. On DSC curves [1] two peaks for Fe can be observed and were ascribed to $\alpha_{ferromagnetic} \rightarrow \alpha_{paramagnetic}$ (Curie temperature) at 795°C and to $\alpha \rightarrow \gamma$ at 973°C (on the heating curves). Cr shows no transformations. Non-alloyed mixtures (P3, 4) have the two DSC peaks specific to Fe (Figure 1, top). However, peaks are located at lower temperatures than for pure Fe, and the respective temperatures are decreasing with a higher Cr content. Use of vacuum (4Pa) or of Ar atmosphere during DSC experiments does not change significantly the two peaks temperatures. An explanation for these results can be the difference in thermal conductivities of Fe and Cr.
2. For the mechanically alloyed powders (P5, 6) also two peaks can be observed in DSC. However, the peaks location shifts to higher temperatures when compared to Fe (Figure 1 bottom). The shift for each of the two peaks and samples is also very different. This suggests that FeCr alloy formed. XRD confirms this result (Figure 1 inset): only one phase, i.e., FeCr is observed and this is a bcc α-type phase with lattice parameter *a* taking values between those for Fe and Cr and closer to Fe (Table 1). DSC differences also indicate that there are also differences in the alloys details. To reveal them Mossbauer spectroscopy was performed (see Report. [1]). Non-alloyed powders have the typical spectra for Fe. For the alloyed powders lines of the bcc Fe is broadening. It indicates that Cr is entering the lattice of Fe. The extra peak that occurs in the spectra of the milled samples suggests the presence of defected paramagnetic Fe or of Fe entering the crystal structure of Cr. Well known is that solubility of Fe in Cr is very low. This extra line has a position different than for oxide-Fe phases. Analysis of Mossbauer data (see Report [1]) lead to conclusion that alloys are different and a higher amount of Cr is dissolved in Fe in the sample with a higher concentration of Cr, i.e. Fe14Cr-0.3Y2O3 (P6). The result is somehow expectable since a higher amount of Cr in the starting composition increases the probability that more Cr will enter the lattice of Fe.

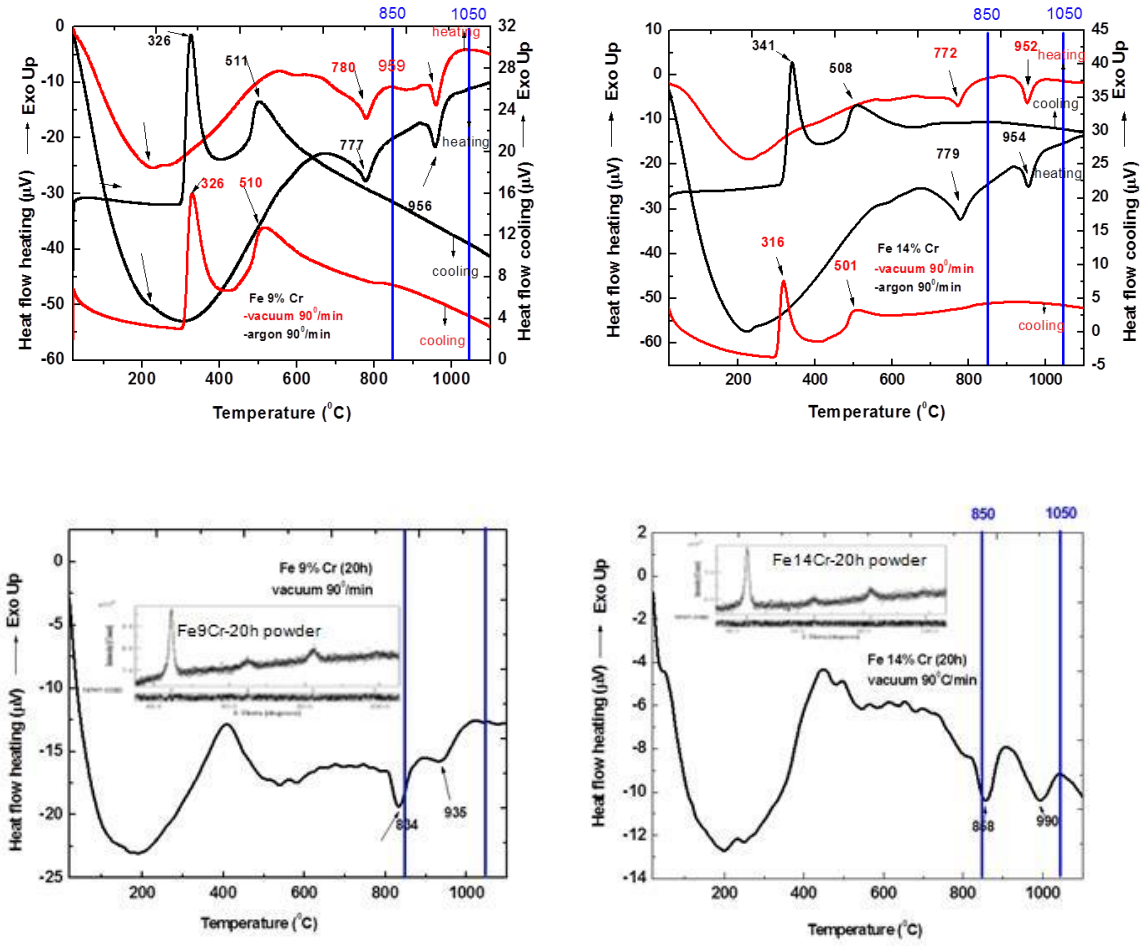

Figure 1 - DSC (90°/min) in vacuum (4 Pa) and in Ar for un-milled powders (top graphs) and for milled powders (20 h, bottom graphs) measured in Ar. Insets show XRD patterns for the milled powders.

After mechanical alloying (P5,6), the crystallite size from XRD (Table 1) is smaller and around 10nm than for the raw materials (P1,2). However, alloyed powders are composed of particles with size of 0.5-2µm and welded blocks with a size up 20µm that sometimes contain closed pores. Blocks size is larger than the average size of raw Fe and Cr powders.

2. SPS of Fe powder, non-alloyed mixtures and mechanically milled powders

We used a SPS machine FCT, Germany. We selected a heating rate of 150°/min. A uniaxial loading force of 20KN during SPS experiments was applied on samples of 2cm diameter. DSC on powders was measured at 90°C/min (see section 1), the highest heating rate for our apparatus, and this information was used to select SPS temperatures of 850°C and 1050°C (i.e. approximately below and above the peak located at the highest temperature on the DSC heating curves, Figure 1). Dwell time was 3min. Samples were polished and characterized by Archimedes method, XRD, SEM/EDS and Vickers hardness.

1. In the non-alloyed powders after SPS (S3-6), Fe and Cr peaks in XRD spectra are observed (not shown). SEM shows a microstructure composed of a Fe matrix, Cr large grains and a transition region. The Fe matrix is made of equiaxial grains for SPS at 850°C and has a lamellar structure in

the bulks SPSed at 1050°C. To check that this behavior is intrinsic to Fe we prepared 2 samples from Fe powder (S1, 2) by SPS at 850 and 1050°C. Equiaxial and lamellar grains were confirmed. Result indicates that Fe-Cr alloying under our SPS conditions is not effective and that is necessary to work with alloyed powders.

2. FeCr bcc α-phase observed after alloying is preserved also after SPS (e.g. Figure 2). Lattice parameters are gathered in Table 1 (S7-10).

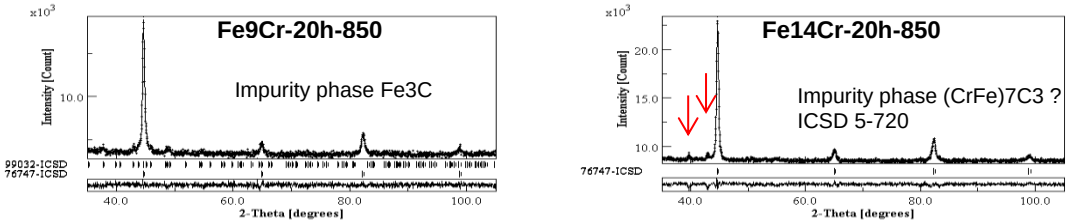

Figure 2 - XRD patterns for SPSed samples S7,9 obtained from milled powders (20h).

Some carbide impurities such as Fe3C or likely (Fe, Cr)7C3 are present in the samples (see peaks indicated with red arrows in Figure 2). Their origin requires further research. SPS samples obtained from the alloyed powders have a uniform morphology and composition (see Report [1]). Crystallite size as determined from the XRD data (Table 1) is higher (approximately double) for samples SPSed at higher temperature (1050°C). These samples have also a higher density, above 95% and a higher Vickers hardness (around 460 vs. 250 HV units for the samples SPSed at 850°C).

3. Preparation and characterization of precursor ribbons obtained by melt spinning

Pieces from SPSed sample S10 with a total weight of 3.8 (P7) or 5.8g (P8) were loaded into quartz tubes with a certain geometry and inductively heated in a melt spinning commercial furnace produced by Buehler, Germany. Initial vacuum in the chamber was 0.4 atm and Ar was used to spray the melt (~1540°C) on a cold and rotating (2000 rot/min) Cu-roll. Ribbons have a length of 1-20mm, width of 0.3-1.5mm and thickness of 0.07-0.12mm. According to XRD (Bruker, $Cu_{K\alpha}$-radiation) ribbons are mainly composed of fcc FeCr (Figure 3b). Rietveld analysis (see Report [2]) show lattice parameter *a*=3.6191(3) A and crystallite size = 98±3 nm (sample P8). Parameter *a* is between the values for fcc Cr (*a*=3.6 A) and fcc Fe (*a*= 3.6544 A). This suggests that fcc FeCr alloy formed. Lines of unidentified phase are also present. Considering that Mossbauer spectroscopy (Figure 4) shows only the typical pattern for fcc alloy and these patterns are insensitive to ratio between the fcc FeCr alloy and the unidentified phase, we believe that unidentified phase is perhaps also a FeCr alloy with identical local structure around Fe. However, it has a different crystal quality/structure and crystal size than the main fcc FeCr phase. Curves of thermal analysis for a heating and cooling rate of 10°C/min and under vacuum (30Pa) taken on ribbons P7 (see Figure 3b-1) are shown in Figure 5. Peak at 835°C is ascribed to $\gamma \rightarrow \alpha$ transformation taking into account that literature indicates for Fe that phase γ (ICSD 53449) is stable up to around 850-900°C. Peak at lower temperature (646°C) is probably related to the unknown phase from XRD. Statements for the un-known phase require further investigations.

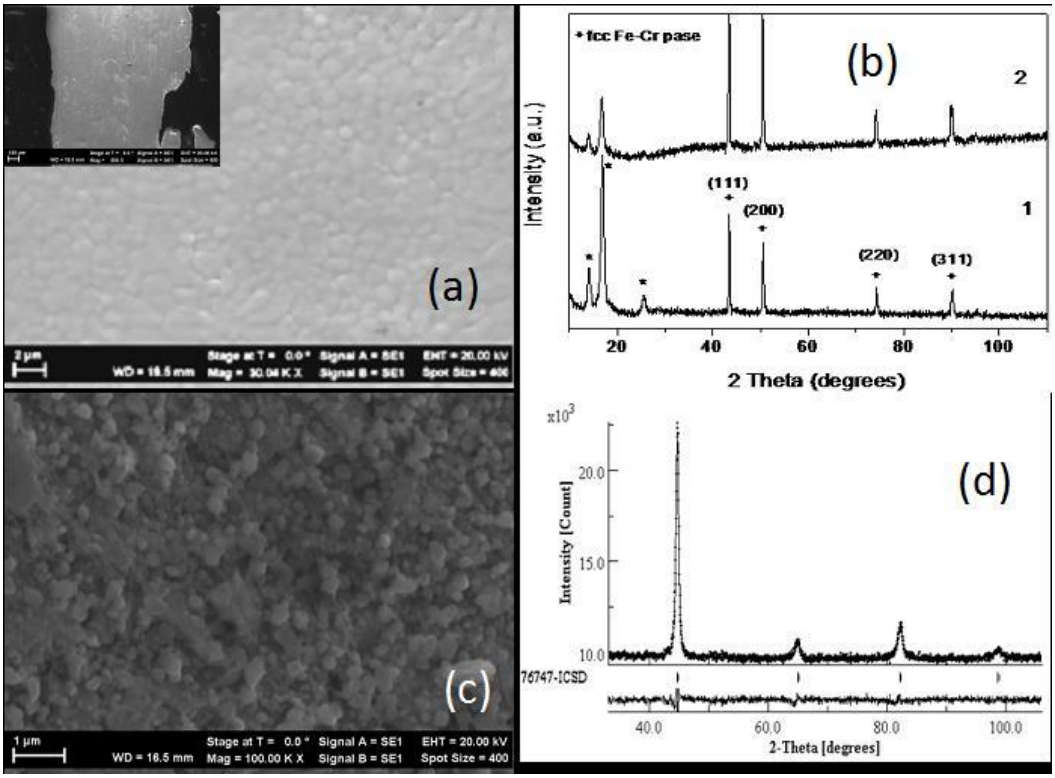

Figure 3 - SEM images of ribbon P8 - (a) and SPSed sample S11- (c) and XRD patterns for ribbons P7 – (b)-1, P8-(b)-2 and for SPSed sample S11 – (d).

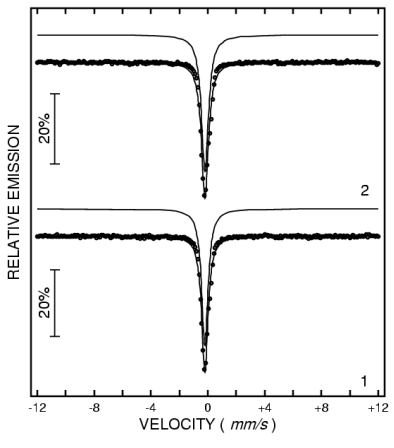

Figure 4 - Room temperature Mossbauer spectra for ribbon samples P7 (1) and P8 (2).

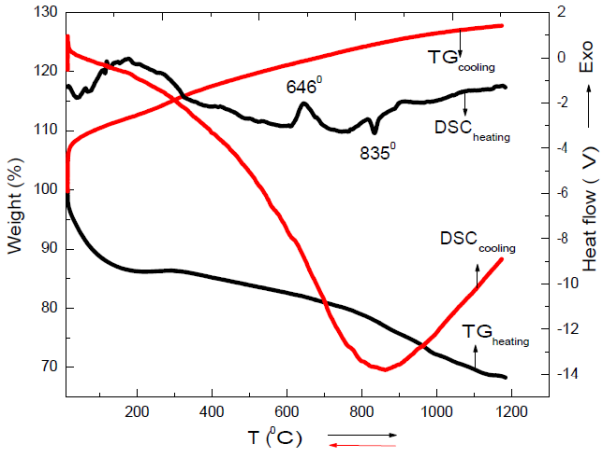

Figure 5 - Differential scanning calorimetry and thermogravimetry curves for ribbons P7 (see Figure 3b-1).

4 Spark Plasma Sintering of ribbons obtained by melt spinning

As prepared precursor P8 was pressed under a load of 250KN into a disc with a diameter of 20mm and height of about 3mm. Disc was processed by Spark Plasma Sintering at 1050°C. The other conditions were the same as presented in section 2. Relative density (S11) was 99%. XRD indicates the presence of ferritic bcc FeCr phase (Figure 3d) instead of fcc FeCr from the precursor (Figure 3b).

Lattice parameter *a*=2.8742 A and crystallite size is 28±0.5nm. Crystallite size is surprisingly low and it is lower than in the ribbon-like precursor 98±3 nm. This observation requires further studies and confirmation. However, the fact that material (Figure 3c) is composed of small grains can be observed from SEM images after chemical etching with 2% HNO3 water solution. Particle size (<1μm) for the SPS sample S11 is apparently lower than for the ribbon precursor (~1μm in P8) (compare Figure 3 a and c) supporting observation on crystallite size. Average Vickers hardness on SPSed sample S11 was 474 HV units.

Conclusion

ODSFS samples were successfully prepared by SPS from precursors obtained by 20h planetary milling and by melt spinning as ribbons. X-ray diffraction (XRD) and Mossbauer spectroscopy indicate that mechanically milled powders are composed of an α-bcc type FeCr alloy phase, while ribbons are composed (mainly) from a γ-fcc phase FeCr alloy. However, Spark Plasma sintering at 1050°C on both precursors produced α-bcc (ferritic) ODS.

The highest density of 99% (Archimedes method), the smallest crystallites with size of 28±5nm estimated from XRD and the highest Vickers Hardness of 474units were found for the SPSed sample using ribbon-like precursor.

We conclude that further characterization and complex optimization of ODSFS prepared by indicated routes is of much interest for a full understanding of the potential of these materials for DEMO construction and other related applications.

THE INFLUENCE OF THE CHEMICAL COMPOSITION AND RESIDUAL PROCESS CONTROL AGENT ON THE MICROSTRUCTURE AND MICROHARDNESS OF ODSFS'S

V. Mihalache, I. Mercioniu, A. Velea, G. Aldica, P. Palade
National Institute of Materials Physics, 77125, Magurele
[BS-M7/WP-12-MAT-01-ODSFS-01-02]

Abstract

The work for 2012 was related to the production of the ODSFS-s (as potential structural material for DEMO fusion reactor) and improvement of their mechanical properties. With this aim in view: (a) the chemical solution techniques (sol-gel) was used for production of (dispersion hardening) Y_2O_3; the grain size was varied from 5 up to 350 nanometers by controlling processing parameters such as: solution concentration, sintering temperature and dwell time; (b) Ti was introduced into steel matrix as precipitation hardening element; (c) W was introduced into steel matrix, in order to increase the solid solution strengthening; (d) three types of powders with the chemical compositions Fe-14Cr-0.4Ti-3W-0.25Y_2O_3, Fe-14Cr-0.4Ti-0.25Y_2O_3 and Fe-14Cr-0.4Ti were prepared; (e) two processes of milling were used: wet milling with ethanol as process control agent, PCA, and dry milling without PCA; (f) mechanically alloyed, MA, powder was consolidated by SPS method at four different temperatures: 900 °C, 1000 °C, 1065 °C and 1100 °C. A special emphasis was put on the study of the influence of residual PCA in MA powders on the mechanical properties of consolidated ODSFS-s. Structure, composition, density and microhardness strongly depend on the specific milling conditions / on the quality of MA powders.

Papers

V. Mihalache, I. Mercioniu, A. Velea, G. Aldica, P. Palade, Effect of residual process control agent on the microstructure and mechanical properties of Fe-14Cr-0.4Ti ODSFS-s prepared by mechanical alloying (submitted)

Reports

[1] V. Mihalache, Optimization of the chemical composition and production route of ODSFS-s with a precipitation hardening element. Ljubljana
[2] V. Mihalache, Effect of composition and some process variables on the microstructure and mechanical properties of ODSFS-s, Garching

Detailed results

1. Steels derived from powders mechanically allowed by dry milling

- Some improvement of microhardness was obtained for steels containing 0.25wt.Y2O3 and especially for those containing 3%wt. W (Table 1, Figure 1).

- FeCrTiW-Y_2O_3 shows the highest microhardness among the studied steels. It reaches *a maximum of 1147.34 VH at 1065* C (Table1). γ - phase (austenite) and a trace of $(Cr, Fe)_7C_3$ carbide appeared in the consolidated steels, especially for higher sintering temperatures, influence the microhardness (Figure 1, Table 1). The Archimedes density increases with increasing temperature. A *maximum of 7.63 g/cm3 is reached for 1100C* (Table 1).

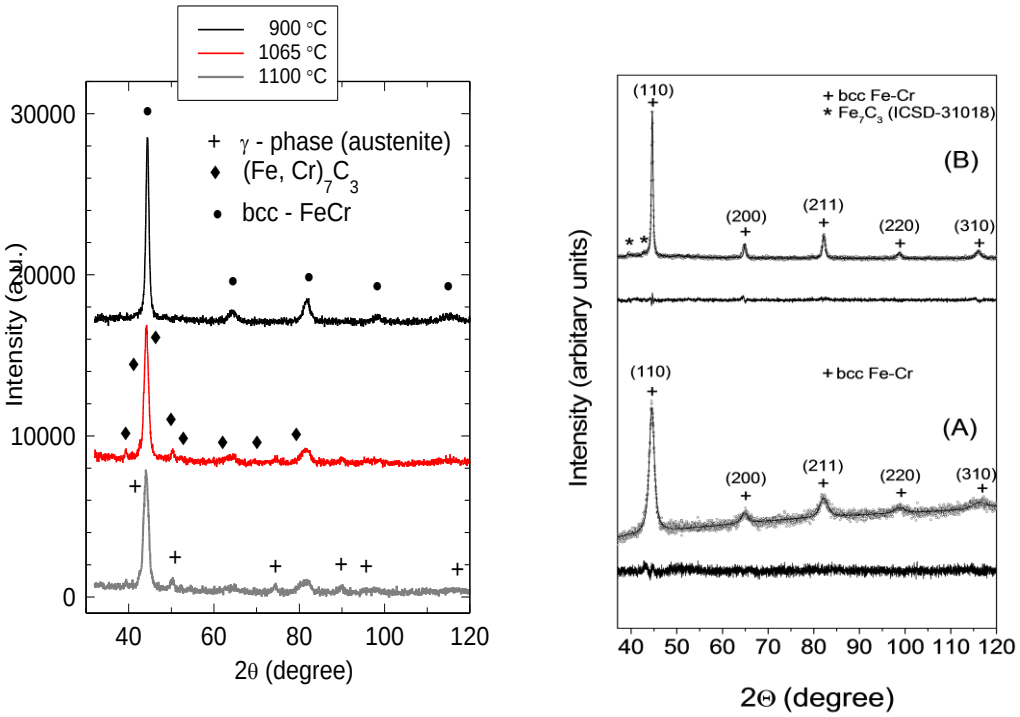

Figure 1 - XRD patterns of: (left) FeCrWTi-Y_2O_3 steels derived from powders mechanically allowed by dry milling and consolidated at 900C, 1065C and 1100C); (right) (a) FeCrTi-Y_2O_3 MA powder prepared by wet milling; (b) FeCrTi-Y_2O_3 steel consolidated from powders mechanically allowed by wet milling

- In the ODSFS of the composition FeCrTi-Y_2O_3 a trace of $(Cr, Fe)_7C_3$ at temperatures above 1000 °C, was observed. Microhardness vs. temperature of consolidation shows *a maximum of 940.47 VH at 1065* °C, lower than for steels containing W. The density reaches a maximum *of 7.67 g/cm3 at 1100* °C (Table 1).
- In the ODSFS of the composition FeCrTi (used as a reference composition) a trace of $(Cr, Fe)_7C_3$ was observed at highest sintering temperatures. FeCrTi steel consolidated at 1065 °C has the lower values of microhardness as compared to FeCrTi - Y_2O_3 and FeCrTiW-Y_2O_3 consolidated at the same temperature (Table 1).
- No improvements of microhardness in the reproducible way were observed by variation of grain size of Y_2O_3 introduced into initial powders.

Table 1 - The density and microhardness measured on ODSFS derived from powders mechanically alloyed by dry milling

Consolidation temperature	Fe14Cr0.4Ti	$Fe14Cr0.4Ti0.25Y_2O_3$	$Fe14Cr3W0.4Ti0.25Y_2O_3$			
	Density (g/cm^3)	Microhardness (VH)	Density (g/cm^3)	Microhardness (VH)	Density (g/cm^3)	Microhardness (VH)
900			5.54	477.9	6.31	655.33
1000			6.03	551.93		
1065	7.7	837.9	7.23	940.74	7.61	1147.33
1100			7.67	832.19	7.63	1008.29

2. Steels derived from powders mechanically allowed by wet milling

- ODSFS properties strongly depend on the amount of PCA used in the milling process as well as on the amount of residual PCA in the presintering powder. So it was hard to distinguish some important influence of Y2O3 and W addition.

- Densities as high as 6.7 g/cm3 and microhardness up to 968 VH were obtained (Table 2).

Table 2 - The density and microhardness measured on ODSFS derived from powders mechanically alloyed by wet milling

Milling conditions	Composition	Consolidation temperature	5 nm Y_2O_3	350 nm Y_2O_3		
			Density (g/cm^3)	Microhardness (VH)	Density (g/cm^3)	Microhardness (VH)
1	$Fe14Cr3W0.4Ti0.25Y_2O_3$	1000	7.66	717.71	7.4	782.3
2	$Fe14Cr3W0.4Ti0.25Y_2O_3$	1000	7.4	968.82	7.4	956.7
	$Fe14Cr3W0.4Ti0.25Y_2O_3$	900	6.88	750.86	6.8	821.8
3	$Fe14Cr0.4Ti0.25Y_2O_3$	900	6.691	603.9745	6.6	514.3
			5.886	362.54	5.6	458.7
			6.569	329.33	7.6	508.9
			6.478	542.2151	5.8	592.2
			6.51	504.7637	6.8	534.5
			6.34	347.6523	6.6	514.3
4	$Fe14Cr3W0.4Ti0.25Y_2O_3$	900		6.3	533.9	
		1000		7.0	631.2	
		1065		7.4	853.6	

- ODSFS-s SPS-sintered from MA powders obtained by higher energy of milling exhibit higher microhardness.

- The steels are characterized by pronounced tendency of carbides formation/precipitation. Three type of carbides were observed depending on the used milling conditions: $(Cr, Fe)_{23}C_3$, $(Cr, Fe)_7C_3$ and especially $(Cr, Fe)_3C$ (Figure 2).

- Figure 1a (right) and the data given in Table 2 demonstrate that SPS-consolidated ODSFS-s characterized by pure α-phase and high microhardness contain carbides and oxides.

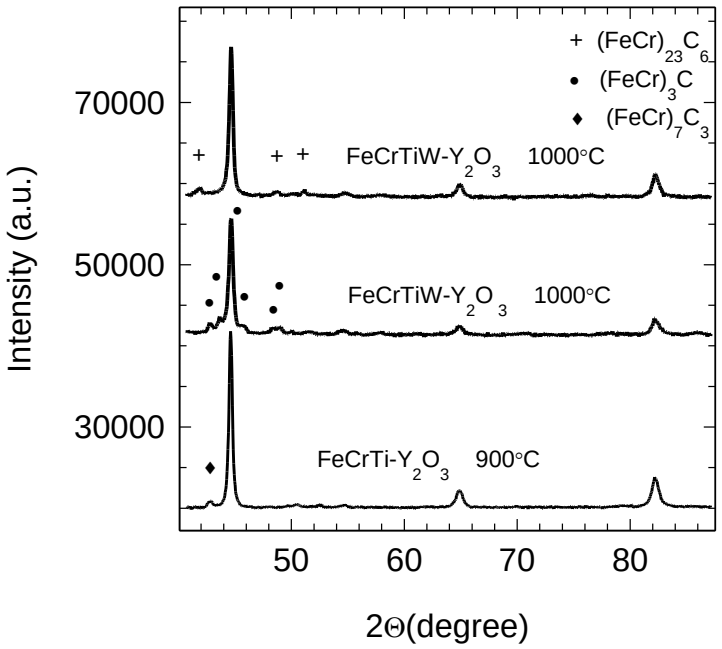

Figure 2 - XRD patterns of steels consolidated from powders mechanically allowed by wet milling at different milling conditions

- The microhardness values are correlated with the amount of gases evacuated during SPS-sintering, consequent on the amount of residual PCA in the products: microhardness decreases with the increasing of the residual quantity of PCA (Figure 3). Residual PCA influence the mechanism of densification which, particularly, arises in inefficient pressuring: the preserved interparticle spaces in the final consolidated steel affect both density and microhardness (Figure 4).

- One of the possible reasons of carbide formation/precipitation is the reaction of the decomposed residual PCA with the heated product. The MA powder characteristics and the residual PCA determine the capacity of heated product to dissolve carbon and to change particle composition during sintering and thus, to influence the material hardness.

- Unexpected improved microhardness was obtained for larger crystallite size of Y_2O_3 (added to and mechanically alloyed together with elemental powders). As the quantity of residual PCA decrease the situation seem to revert in favour of smaller crystallite size of Y_2O_3, More thoroughly investigations are required.

- EDS investigations show the regions reach in Y (up to 3% wt.) near the surface of steels (Table 3).

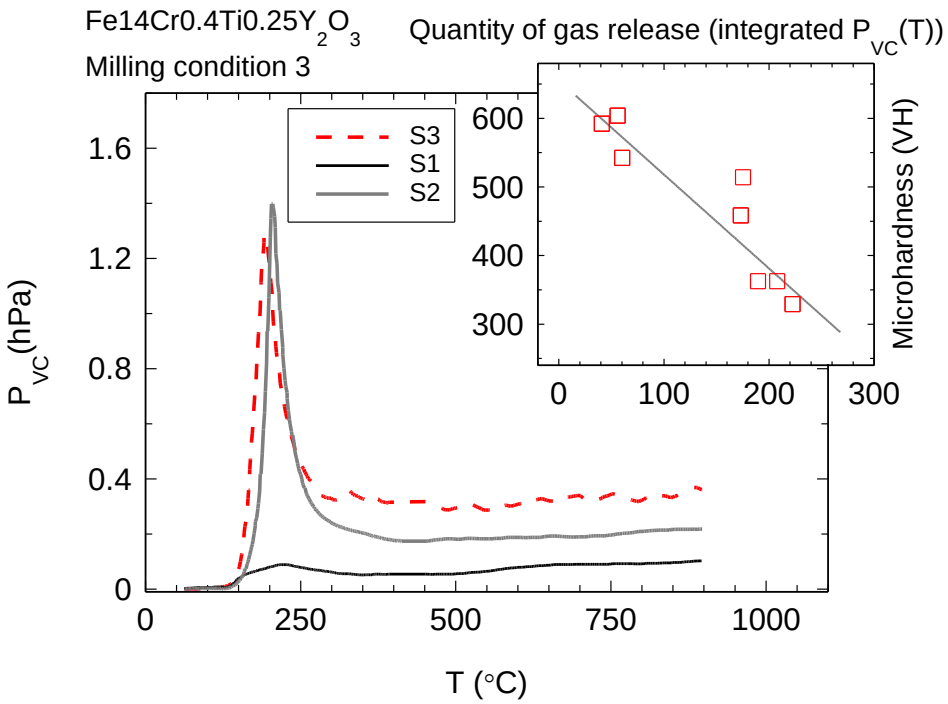

Figure 3 - The dependence of pressure in SPS vacuum chamber, P_{VC}, (proportional to residual PCA in the presintering powders) on the temperature for three representative products with different amount of residual PCA. Inset: The dependence of microhardness on the integrated aria of Pvc (T) curves

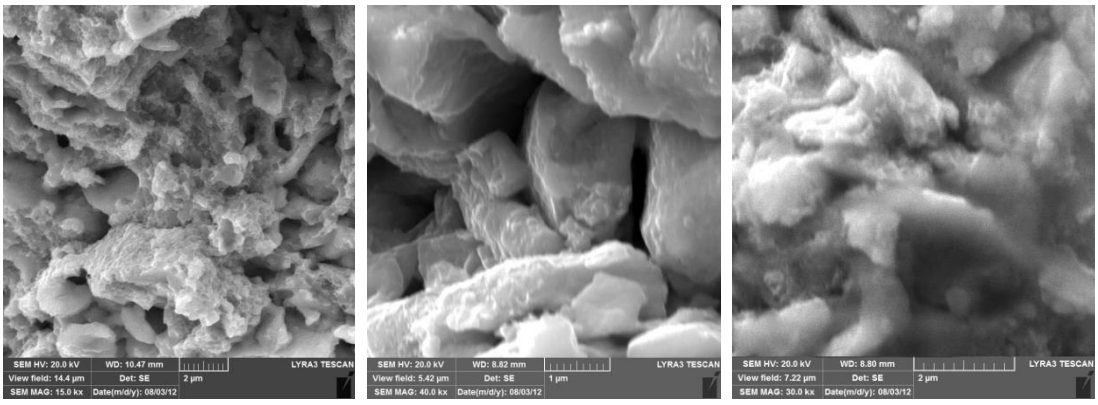

Figure 4 – Cross-sectional SEM images of the fractured Fe14Cr0.4Ti0.25Y_2O_3 ferritic steels S1 (left), S2 (center) and S3 (right) same as in those described in the main panel of Figure 5

Table 3 - The chemical composition investigated by EDS on the surface of FeCrTi-Y_2O_3 steel derived from powders mechanically allowed by wet milling

Element	series	[wt.%]	[norm. wt.%]	[norm. at.%]	Error in wt.%
Carbon	K-series	2.549073	2.141572	9.004079	0.616245
Oxygen	K-series	0.881798	0.740831	2.338307	0.23714
Chromium	K-series	13.34366	11.21051	10.88783	0.403444
Iron	K-series	101.5515	85.31717	77.1476	2.748338
Titanium	K-series	0.702168	0.589918	0.62219	0.058259
Yttrium	L-series	0	0	0	0
	Sum:	119.0282	100	100	

Element	series	[wt.%]	[norm. wt.%]	[norm. at.%]	Error in wt.%
Carbon	K-series	1.245245	0.96487	4.335185	0.641548
Titanium	K-series	0.608298	0.471336	0.531244	0.059488
Chromium	K-series	16.02045	12.41335	12.88359	0.472134
Iron	K-series	107.5983	83.37189	80.5634	2.784878
Yttrium	K-series	3.585959	2.778557	1.686579	0.357399
	Sum:	129.0583	100	100	

Conclusion

This report demonstrates the great importance of the quality of MA powders on the properties of final consolidated ODSFS-s. Most important results are:

- Improved microhardness after introduction of Y_2O_3 and 3%W into steel matrix.

- ODSFS-s with microhardness as high as 1161 VH were obtained.

- high density of ODSFS-s (up to 6.7 g/cm3).

- dense ODSFS-s with highest microhardness contain some γ - phase.

- SPS-consolidated ODSFS-s characterized by pure α-phase and high microhardness contain carbides and oxides.

PARTICIPATION AT JET ENHANCEMENT AND EXPERIMENTAL PROGRAM

THE LIMITS OF THE W COATINGS DEPOSITED ON CFC TILES FOR THE ITER-LIKE WALL AT JET

C. Ruset, E. Grigore, I. Munteanu, M. Gherendi
National Institute for Laser, Plasma and Radiation Physics, Bucharest, Romania,
Euratom-MEdC Association

[BS_12B/FT-12-4.22 MEdC_IPP]

Abstract

Using the electron beam high temperature test facility an attempt to improve the CMSII W coating technology was made. No significant influence of the magnetron current intensity and high voltage pulse frequency on the thermo-mechanical properties of the W coatings was found, but it was demonstrated that the load configuration and the plasma exposure of the surfaces to be coated to the magnetrons are important.

Preliminary investigations carried out on the W coatings subjected to the high heat fluxes (HHF) by SEM/FIB (focused ion beam) techniques revealed a network of nano-pores at the CFC/Mo and Mo/W interfaces. This aspect might be important for the W coating properties and it should be studied in more details.

W coatings with a thickness of 35 μm and 75 μm were produced and tested. It appears that 30-35 μm is the thickness limit for the actual CMSII technology.

Papers:

- C. Thomser, V. Bailescu, S. Brezinsek, L.W. Coenen, H. Greuner, T. Hirai, J. Linke, C.P. Lungu, H. Maier, G. Matthews, Ph. Mertens, R. Neu, V. Philipps, V. Riccardo, M. Rubel, **C. Ruset**, A. Schmidt, I. Uytdenhouwen, Plasma Facing Materials for the JET ITER-like Wall, *Fusion Science and Technology*, Vol. 62, Issue: 1 Pages: 1-8, Published: Jul-Aug 2012

Conferences:

- **C. Ruset**, E. Grigore, D. Falie, M. Gherendi, H. Maier, M. Rasinski, G. Matthews, V. Zoita, The impact of thermal fatigue and carbidisation on the W coatings deposited on CFC tiles for the ITER-like Wall project at JET, Symposium on Fusion Technology (SOFT), Liege, Belgium, 24-28 Sept. 2012

Reports:

- The limits of the W coatings deposited on CFC tiles for the ITER-like wall at JET, Final report, 01.04.2013.

Presentations:

- C. Ruset, H. Maier, The limits of the W coatings deposited on CFC tiles for the ILW at JET (JW12-FT-4.22), 1st Semi-annual Monitoring Meeting, 13-14 June, 2012, JET, Culham
- C. Ruset, E. Grigore, M. Gherendi. H. Maier, M. Rasinski, The limits of the W coatings deposited on CFC tiles for the ITER-like wall at JET, JET Task: Fusion Technology JW12-FT-4.22, 2nd Semi-annual Monitoring Meeting, 11-14 December, 2012, JET, Culham

Detailed results

1. Background

The experiments carried out in 2011 with the electron beam High Temperature Test Facility (HTTF) in MEdC Association revealed the following aspects:

- The damage of the W coatings deposited on CFC substrate occurs gradually, with the increasing number of the heating pulses.
- It is clear that the thinner coatings have a better behaviour from the thermo-mechanical point of view than thicker coatings.

- The damage of the W coatings occurs by buckling with the size of delaminated zones in the range of 50-400 μm.
- No delaminations were detected for a W coating of 20 μm subjected to 5100 pulses when the peak temperature was 1000±50°C.

2. Project objectives

The first objective of the project was to investigate the influence of the CMSII coating parameters on the thermo-mechanical properties of the coatings with the aim to improve these properties.

The second objective was to investigate the capability of the CMSII technology to increase the W coating thickness towards 100 μm.

On the other hand the general objective of the project was to find out the limits of the W coatings deposited by CMSII technology with the aim to assess the status of the W coatings in the ITER-like wall at JET.

3. Results and discussions

3.1. Testing samples

Dunlop DMS 780 CFC samples of 30×30×6 mm were W-coated perpendicular to fiber planes, using different processing parameters. Then the quality of the W coatings was evaluated in terms of thickness, impurities and thermo-mechanical properties.

3.2. Evaluation of the thermo-mechanical properties of the W coatings

The thermo-mechanical properties of the W coatings were quantitatively assessed using the degradation curves obtained with the HTTF. The maximum power of the electron beam was 1.5 kW for an accelerating voltage of 15 kV. The cross section of the electron beam on the surface of the testing sample was an ellipse with axes 18/12 mm and an area of ~170 mm^2. The electron gun, the diagnostics and the support for the sample to be tested are installed on the top lid of the vacuum chamber (Φ540 × 640 mm). A number of pulses between 500 and 3,000 produce a degradation of the W coating which can be quantified by measuring the damaged area. The High Heat Flux (HHF) tests are periodically stopped and the damaged area of the W coating is measured with a stereomicroscope at a 40× magnification. The results are usually obtained in 5-10 days and they were used as a feedback in the investigation of the influence of the coating processing parameters (magnetron current, high voltage frequency, etc.) on the thermo-mechanical properties of the coating.

3.3. A new experimental device for W coating of small samples for high temperature tests.

The W coating technology is not a cheap one. A full set of Mo/W target costs more than € 2000. Due to limited resources of the present project, a special three axes rotation device was designed and manufactured with the aim of coating the necessary samples with minimum consumption of Mo and W (Figure 1).

Figure 1 - Three axes rotation device for W coating of small samples

The system is very flexible, allowing both radial and axial change of position of the samples in front of the magnetrons. A typical coating load for these experiments contains the following samples: (i) two CFC samples (30×30×6 mm) which are coated perpendicular to fiber planes, (ii) three fine grain graphite lamellas (40×5×0.8 mm) positioned in a special steel protection box. These lamellas are used to measure the internal stress induced into the Mo/W coating during the deposition process, (iii) one Ti witness sample (30×25×2.5 mm) which was used for the measurement of thickness and chemical composition of the coating with the Glow Discharge Optical Spectrometry (GDOS) equipment.

3.4. The influence of the magnetron current intensity on the thermo-mechanical properties of the W coatings

Using the three axes rotation device, 10 μm W coated CFC samples were produced at $I_{mag}=I_{standard}$, $I_{mag}=1.3\cdot I_{standard}$ and $I_{mag}=0.75\cdot I_{standard}$. These coatings were tested in the HTTF at 1500°C for 1400-1600 pulses. The results are shown in Figure 2. Taking into account the experimental errors, one can say that there is no significant influence of the magnetron current intensity on the thermo-mechanical properties of the W coatings. In Figure 2 it is also shown the curve corresponding to a 10 μm W coating deposited with the two axes rotation device and tested at 1450°C. The difference in their thermo-mechanical properties is significant and cannot be attributed to the difference of 50°C between the testing temperatures. It is clear that coatings produced with the two axes rotating device are better. From the technological point of view, this is an important result. It demonstrates that the exposure of the W coating to the magnetron plasma must be taken into consideration seriously.

3.5. The influence of the high voltage frequency and of the magnetron target-surface to be coated distance on the thermo-mechanical properties of the W coatings

The next experiments were carried out with the two axes rotating device modifying the high voltage frequency from 25 Hz to 50 Hz and the distance between the magnetron target and the surface to be coated in the range of 70-135 mm. No significant influence of these parameters on the thermo-mechanical properties has been found. The results are shown in Figure 3.

It appears that the coating parameters do not have a significant influence on the thermo-mechanical properties of the W coatings and they cannot be used for the optimization of the coating technology. Of course, the variation of those parameters was in reasonable limits.

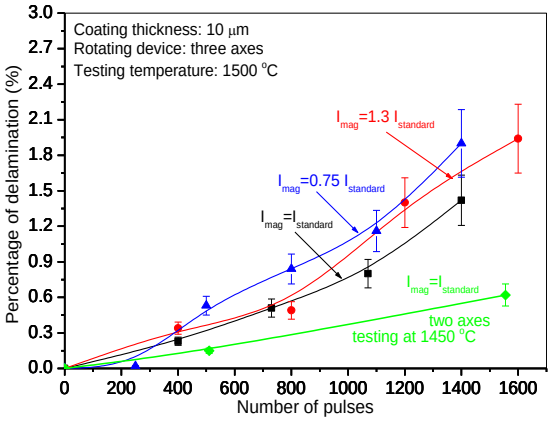

Figure 2 - Influence of the magnetron current intensity on the thermo-mechanical properties of the W coatings

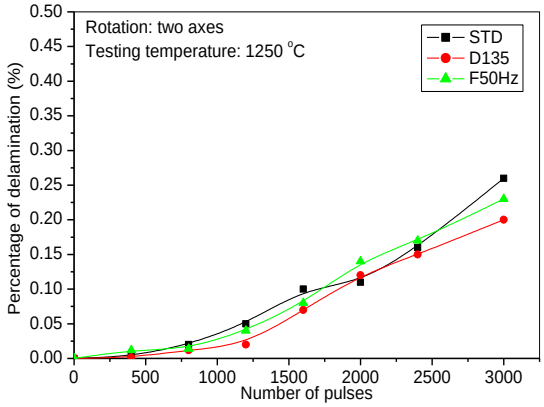

Figure 3 - Influence of the high voltage frequency (F= 50 Hz) and magnetron target-surface to be coated distance (D=135 mm) on the thermo-mechanical properties of the W coatings

3.6. Investigation of the W/Mo/CFC interfaces after HHF tests

In addition to the microscopic examination of the W coating surface during the HHF tests, an investigation of the W/Mo/CFC interfaces was performed using SEM with FIB (Focused Ion Beam) cut facility. This research was carried out together with IPP Garching and Faculty of Materials Science and Engineering, Warsaw University of Technology, Poland, on a 20 μm W coating tested at 1450°C, 3015 pulses of 24s. A typical delamination of the W coating, as a result of cyclic thermal loading, taking with SEM, is shown in Figure 4. A clear buckling of the coating can be seen. Using FIB cut technique, the W/Mo/CFC interfaces were investigated in non-delaminated areas at different distances away from the delaminated zone. The dimensions of a FIB cut, shown in Figure 5, are about 25×35 μm. A cross section of the W coating in region A, at about 10 mm away of the delaminated zone, is shown in Figure 6. Although the coating is not delaminated in this zone, a network of nano-pores can be seen at CFC-Mo and Mo-W interfaces. TEM analysis indicated a carbidization process, since the Mo interlayer was transformed in MoC and a thin WC layer appeared at the bottom of W coating. The delaminated chips remained on the coating during the high heat flux (HHF) test. Without contact to the substrate, these chips were heated over the melting temperature. This induced a temperature non-uniformity of the coating surface. The regions near to the chips were hotter than those at a larger distance of chips. In Figure 7 it is shown the same W coating in a non-delaminated zone, but at about 0.2 mm from the chips (region B).

It can be seen that the damage of the CFC/Mo/W interfaces and of the Mo interlayer is much more severe. Since the temperature in region B was higher than that in region A, a thicker WC layer was expected. Interestingly, no WC layer was detected by TEM analysis in area B. It seems that the pore structure acts like a diffusion barrier for the carbon from the substrate. The degradation of the Mo interlayer and of CFC/Mo/W interfaces impeded the C diffusion from the substrate and the formation of carbides. On the other hand, at the beginning of the testing process, it is possible that W carbide layer to be formed at the bottom of W coating, and to be dissociated later, due to the thermal instability of the W carbides. These are only hypotheses, and further investigation is necessary in order to clarify the origin of pores and their role in the degradation of the W coating.

The pores can be seen not only at the CFC/Mo/W interfaces, but in the W coatings as well (Figure 7). With increasing the temperature, the number and dimensions of pores increase. This is clearly shown in Figure 8, where W coating chips and a cross section through a chip are shown. It is obviously that these chips were melted and re-solidified many times during testing.

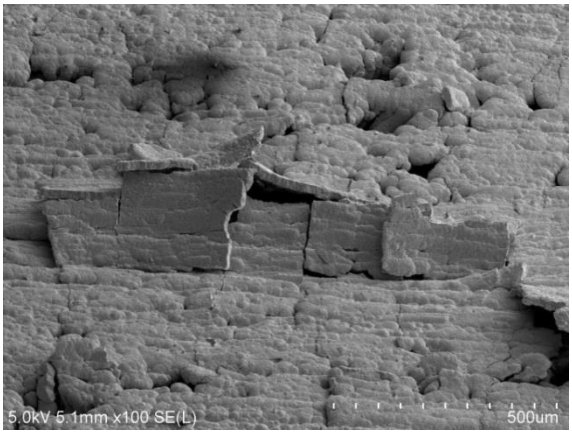

Figure 4 - Typical delaminations of W coatings

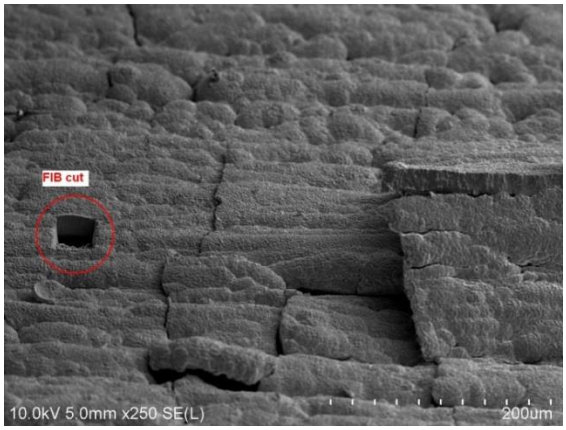

Figure 5 - FIB cut of the W coating

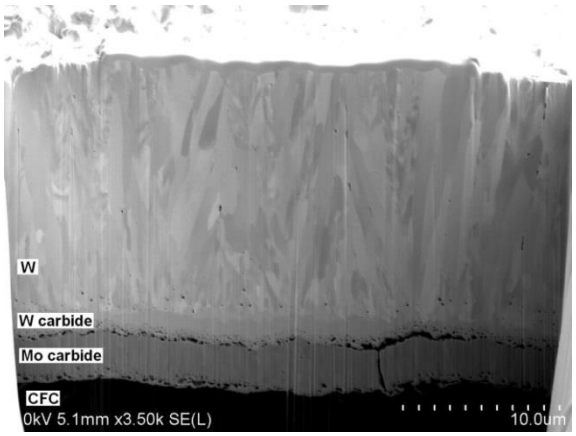

Figure 6 - SEM cross section image through a W coating at 10 mm away of the delamination

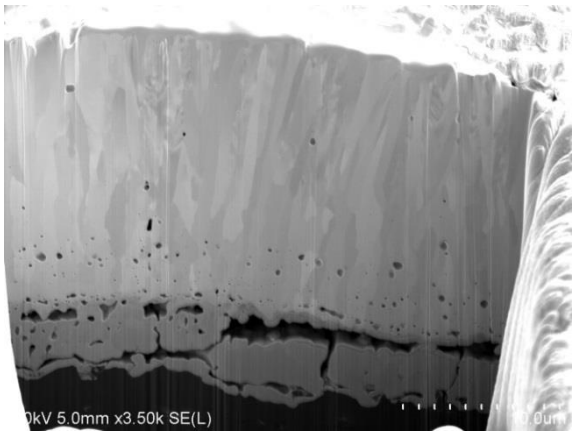

Figure 7 - SEM cross section image through a W coating at 0.2 mm away of the delamination

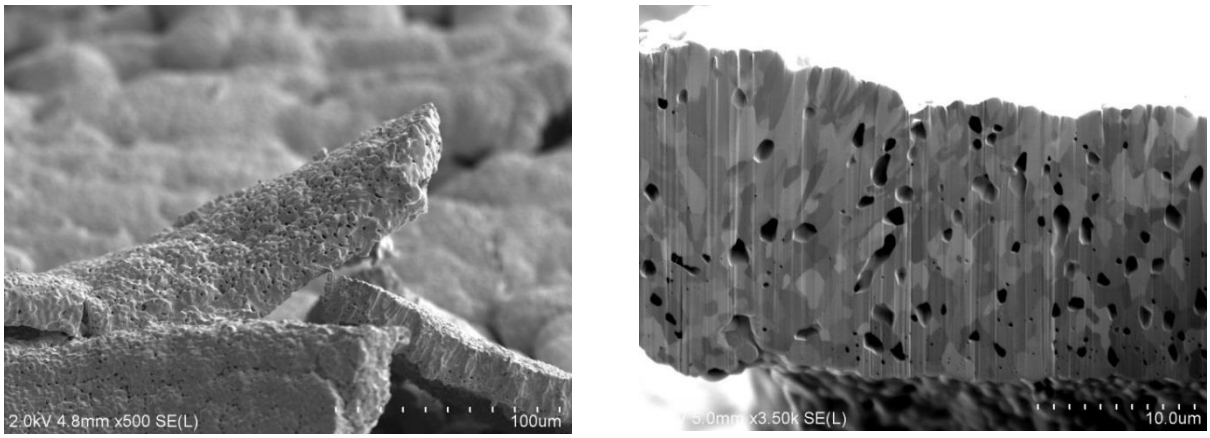

(a) *(b)*

Figure 8 - SEM images of the melted and re-solidified W coating chips (a) and cross section through a chip (b)

3.7 Extension of the CMSII W coating technology towards 100 μm.

The HHF tests indicated a better behavior of the thinner coatings in comparison with thicker coatings, but in some cases, the erosion of the W coating during the operation of the fusion device is important. For the areas where the erosion of the wall is dominant, such as outer divertor in tokamaks, a thicker W coating would be desirable. In order to find out what the limits of the CMSII technology are, in terms of W coating thickness, a special experiment was planned and carried out.

The load included 2 Layout CFC samples (~80×70×40 mm), 8 CFC 30×30×6 mm samples and 10 Ti samples. After 15 h of coating, the run was stopped in order to change the W magnetron targets. On this occasion, a lot of samples were taken out and analyzed. The coating thickness was 35-37 μm, as it can be seen in the GDOS (Glow Discharge Optical Spectrometry) depth profiles (Figure 9). The coatings were fine on all samples, without any delamination. The W targets were changed, and the coating process was resumed. The second run lasted 19 hours. The total thickness of the W coating was about 75 μm as shown in the GDOS profiles (Figure 10). The small peak of C from the middle of the coating is associated with the change of magnetron W targets, when the load was exposed to the atmosphere.

3.7.1 Testing of W coatings of 35 μm

One small sample of 30×30×6 mm coated with 35 μm (IU-363-5) was tested in HTTF as WCL-18 at the following parameters: (i) peak temperature: 1250±6°C, (ii) pulse duration: 22±1 s, (iii) inter-pulse duration: 35±1 s, (iv) total number pulses: 3000, (v) inspections of the W coatings were carried out with the stereomicroscope at a magnification 40× after each 500 pulses. Craters and build-ups with conical and spherical shape of 30-70 μm have been detected. The melting phenomenon seems to be present at thick coatings. As far as the thermo-mechanical properties of the 35 μm W coating are concerned, they are quite good. They are comparable with those of 10 μm W coating, as it can be seen in Figure 11.

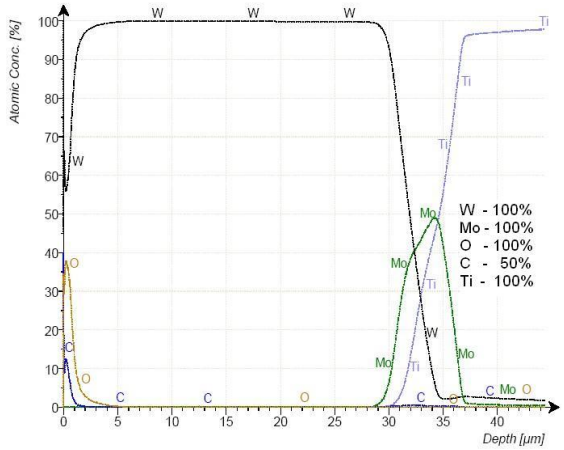

Figure 9 - GDOS depth profiles for 37 μm W coating

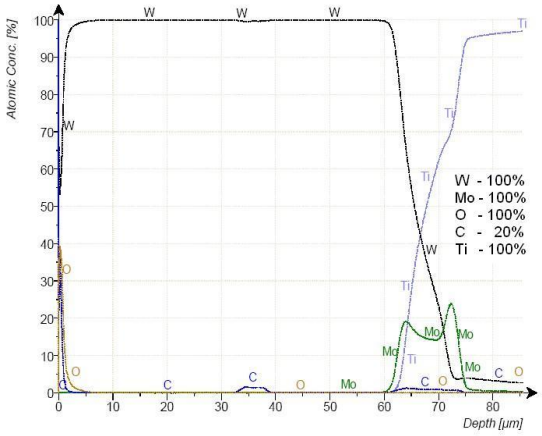

Figure 10 - GDOS depth profiles for 75 μm W coating

3.7.2 Testing the W coatings of 75 μm

Another small sample (30×30×6 mm) coated with 75 μm of W (IU-364-11) was tested in HTTF as WCL-19 at the same parameters as the coating of 35μm. Inspections were carried out after 500 pulses, 858 pulses and 919 pulses. The coating survived very well 500 pulses. The inspection carried out after 500 pulses revealed about 20 craters with diameters of 50-400 μm and small balls (Φ50-

1000 µm), but no delaminations were observed. After about 800 pulses, a relatively large hot spot appeared on the surface. It was clear that it was a delamination. The chip, after loosing the contact with the substrate, became very hot. The test was stopped and the coating was examined. A massive delamination (~ 1.0×2.25 mm) was detected (Figure 12). The test was repeated with another sample, coated with 75 µm, but the results were similar. The thick coatings can only survive about 500 pulses, as it can be shown in Figure 11.

4. Conclusions

- The thermo-mechanical properties of the W coatings are not significantly influenced by the coating parameters (under the reasonable limits), but they could be influenced by the structure of the CFC-W interface including Mo interlayer. A nano-pores structure was detected at the interfaces even in zones where the microscopic examination does not indicate any defects.
- The jigging device and consequently the exposure of the surface to be coated to the magnetron plasma is an important aspect of the coating technology, and it must be taken into account for each coating load.
- Thick coatings of 37 µm and 75 µm have been produced and tested at high heat fluxes. It appears that 30-35 µm is the thickness limit of the W coatings with good thermo-mechanical properties, when they are deposited by the present CMSII technology on Dunlop DMS 780 CFC material.
- The thermo-mechanical properties, and consequently the lifetime of a coating seem to be determined by the thermal fatigue and carbidization process. The carbon from the substrate diffuses into the Mo and W layers and forms carbides. These carbides are brittle and in this way the integrity of the coating is affected.

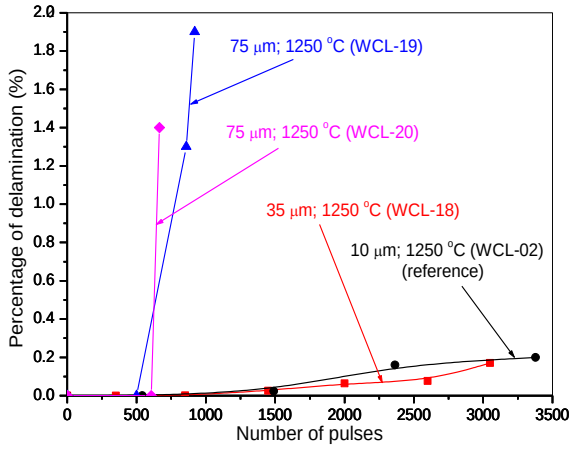

Figure 11 - Degradation curves for thick W coatings (35 µm and 75 µm)

Figure 12 - Delamination of the 75 µm W coating after 858 pulses

Acknowledgement

The reported work includes contributions from the following people outside the EUATOM-MEdC Association: Hans Maier (Max-Plank Institut für Plasma Physik, Euratom Association, Garching, Germany), Marcin Rasinski, Euratom Association IPPLM, Poland and G. Matthews (CCFE, Euratom Association, Abingdon, UK)

¤ADVANCED CALIBRATION OF THE PIW IR CAMERAS

C. Ruset[1], D. Falie[1], E. Grigore[1], I. Munteanu[1], M. Gherendi[1], V.L. Zoita[1,2]
[1] *National Institute for Laser, Plasma and Radiation Physics, Bucharest, Romania, Euratom-MEdC Association*
[2] *EFDA Close Support Unit, Culham, Abingdon, UK*
[BS-12C/JW-10-NEP-MEC-21]

Abstract

The protection of the ITER-like Wall (ILW) at JET is achieved by a special real-time system (PIW) including twelve Hitachi type KP-M1AP IR cameras, pyrometers and thermocouples. From the IR images provided by the cameras it is possible to calculate the temperature, but the correct value of the surface emissivity must be known. The W coating of the CFC tiles was carried out by Combined Magnetron Sputtering and Ion Implantation (CMSII) technology at MEdC and the emissivity of this coating was not known. In the first phase of the project, a value of 0.63±0.03 was found for the emissivity of 10 μm W coating deposited on CFC Dunlop DMS 780 material, using a pulse heating regime with an electron beam.

In order to investigate the influence of the substrate structure, viewing angle and W coating temperature on the emissivity in more detail, a new experimental setup, operating in steady state regime, was used. The same value of 0.63±0.07 was found for 10 μm thickness, while for 20 μm, the emissivity was 0.59±0.06. The large spread of values is due to the structure of the CFC substrate. In the temperature range of 700 – 1,200 °C, there is no significant influence of the temperature on the emissivity of W coatings. There is also no significant influence of the viewing angle on the emissivity in the range of 0° – 55°. For further increase of the viewing angle, the emissivity decreases gradually to 0.43 for 85°. The measurements were carried out at λ=1064 nm and λ=940 nm.

Papers:

- G. Arnoux, S. Devaux, D. Alves, I. Balboa, C. Balorin, N. Balshaw, M. Beldishevski, P. Carvalho, M. Clever, S. Cramp, J.L. de Pablos, E. de la Cal, D. Falie, P. Garcia-Sanchez, R. Felton, V. Gervaise, A. Goodyear, A. Horton, S. Jachmich, A. Huber, M. Jouve, D. Kinna, U. Kruezi, A. Manzanares, V. Martin, P. McCullen, V. Moncada, K. Obrejan, K. Patel, PJ Lomas, A. Neto, F. Rimini, C. Ruset, B. Schweer, G. Sergienko, B. Sieglin, A. Soleto, M. Stamp, A. Stephen, PD Thomas, DF Valcarcel, J. Williams, J. Wilson, KD Zastrow, A protection system for the JET ITER-like wall based on imaging diagnostics Review of Scientific Instruments, Volume: 83, Issue: 10, Article Number: 10D727, Published: Oct. 2012, Part 2

Reports:

- Advanced Calibration of the PIW IR cameras, Task Agreement code JW10-TA-PIW-ACIR-03, Progress Report, 03.04.2012

Detailed results

1. Background

Since August 2011, JET operates with the ITER-like Wall (ILW) containing Be in the main chamber, bulk W (divertor-tile 5) and tungsten coated CFC tiles for the main chamber and divertor (tiles G1, G3, G4, G6, G7 and G8). In contrast with the carbon wall, the new metallic wall is more sensitive to the temperature. In order to protect the investment, a real-time protection system of the ILW (PIW) was developed and implemented at JET. Protection is based on temperature limits (1200°C for bulk W and W coatings and 900°C for Be tiles) and involves twelve IR cameras (Hitachi KP-M1), pyrometers and thermocouples. From the IR images provided by the cameras, it is possible to deduce the temperature, but the correct value of the surface emissivity must be known.

In the first phase of the project, a value of 0.63±0.03 was found for the emissivity of 10 μm W coating deposited on the CFC Dunlop DMS 780 material, using a pulse heating regime with an electron beam.

In order to investigate the influence of the substrate structure, viewing angle and W coating temperature on the emissivity in more details, a new experimental setup operating in steady state regime was used.

2. Project objectives

Using the good thermal stability of the new experimental arrangement, the research was focused on the following objectives:

- Investigation of the influence of the CFC structure on the W coating emissivity
- Measurement of the bulk W emissivity in comparison with that of the W coating
- Investigation on the influence of the temperature and viewing angle on the W coatings emissivity
- Issue of the calibration files for the Hitachi KP-M1AP IR camera
- Measurement of Be emissivity and its dependence on the temperature.

3. Results and discussion

3.1 Experimental setup

In order to confirm the value of emissivity of 0.63±0.03 found in pulse regime, a new experiment was carried out. The sample was a W coated CFC tube Φ16 × 0.75 × 85 mm. The thickness of the W coating was 10 μm. A hole of Φ2.0 mm was drilled in the middle, to play the role of a black body. A type K thermocouple was introduced into the tube through an end and the welding was in contact with the wall. The temperature was also measured by an IMPAC IGA-5 pyrometer with a rage of 250 °C-2,000 °C. The sample was heated by electric conduction, using a high current power supply (I_{max}=300 A, U_{max}=6 V). In this way, the surface temperature is uniform and it can be kept constant for a long time. The experimental setup is shown in Figure 1.

The axis of the optical system including the Hitachi camera is perpendicular to the CFC tub axis and passes through the black body hole. At the same time it makes an angle of 45° with the vacuum chamber axis.

3.2 The influence of the substrate structure on the emissivity of W coatings

The tube was visualized by an IR Hitachi KP-M1AP video camera at different temperatures.

A filter with a bandwidth of 10 nm centred on 1064 nm was used. A typical IR image of the heated sample is shown in Figure 2. It is an average of 256 pictures taken during 12 s at a constant temperature of 1172 °C.

It is important to notice that the surface temperature is equal with the black body temperature. As it can be seen the light intensity significantly depends on the CFC structure, particularly on the nature and orientation of fibers. Since the temperature is constant, this means that the emissivity is different for different areas of the W coated fibers. A number of 8 regions of interest were selected and they are shown in Figure 2.

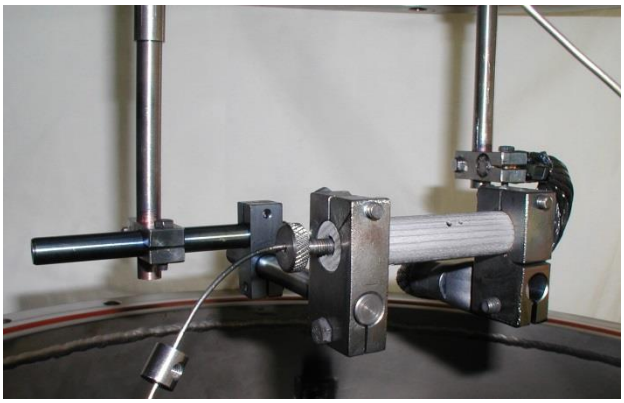

Figure 1 - Experimental arrangement for measurement of surface emissivity

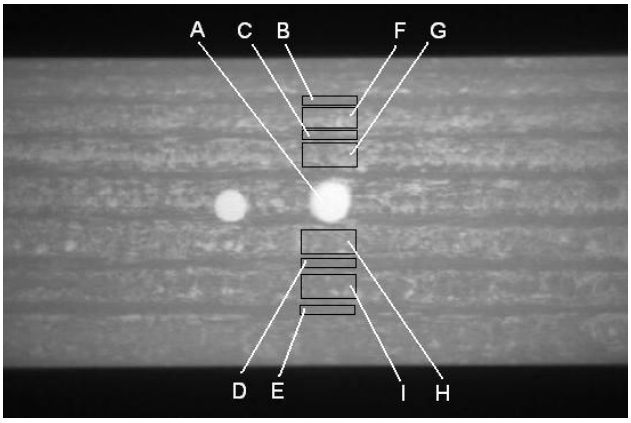

Figure 2 - IR image of the W coated CFC tube at 1172 ℃ and the regions of interest

The temperature dependence of the emissivity for these regions at 1064 nm is shown in Figure 3. The emissivity is higher for lighter zones and lower for darker zones, varying between 0.56 and 0.7. The average for all those areas is 0.63, which is the value found in the first experiments. Due to this large spread of the values, it is difficult to analyze the influence of the viewing angle on the emissivity. In Figure 4a, an IR image of the CFC tube at 1,172 °C with two regions of interest perpendicular to tube axis, one crossing the black body and the other one near the black body is shown. The corresponding emissivity for these two regions is shown in Figure 4b. As can be seen, the variation of the emissivity is within the above mentioned limits and it appears to be mainly influenced by the structure of the CFC substrate and less by the viewing angle. In order to investigate the influence of the viewing angle on the emissivity values, the CFC tub was replaced with a fine grain graphite (FGG) W coated tube with the same dimensions and the same thickness of the coating. Due to the uniform structure of the FGG, the emissivity of the W coating is, in this case, more uniform. An IR picture of the W coated FGG tube heated at 1,172°C with the regions of interest and the corresponding emissivity for these regions are shown in Figure 5.

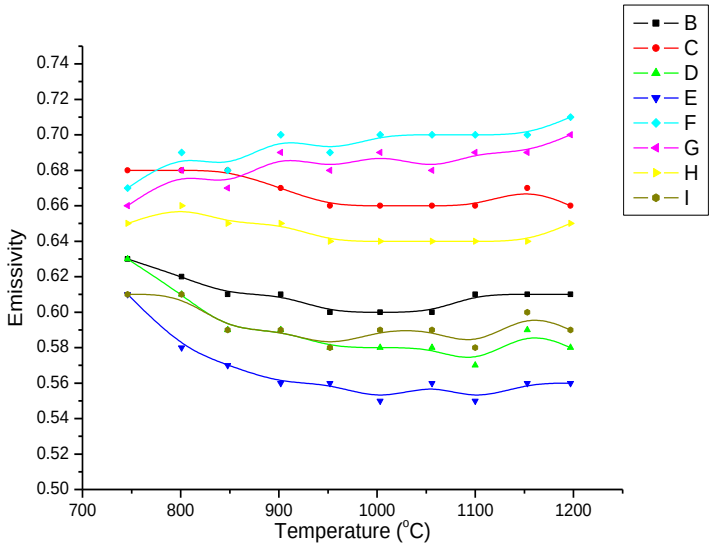

Figure 3 - Temperature influence on the emissivity of a W coating with a thickness of 10 μm deposited on CFC for λ=1064 nm

One can say that the W coating emissivity has in this case a value of 0.55±0.02 and it is more uniform in comparison with that of the W coating deposited on CFC substrate. It is clear that the structure of the substrate influences the W coating emissivity.

3.2. The influence of the viewing angle on the emissivity values

Since the heated object is a cylinder, the IR images shown in Figures 5a and 6a are produced by different areas of the cylinder seen at different angles relative to the perpendicular to the surface in those areas. As it was discussed above, the substrate structure has a significant influence on the emissivity of the W coatings deposited on carbon based materials (CFC or FGG).

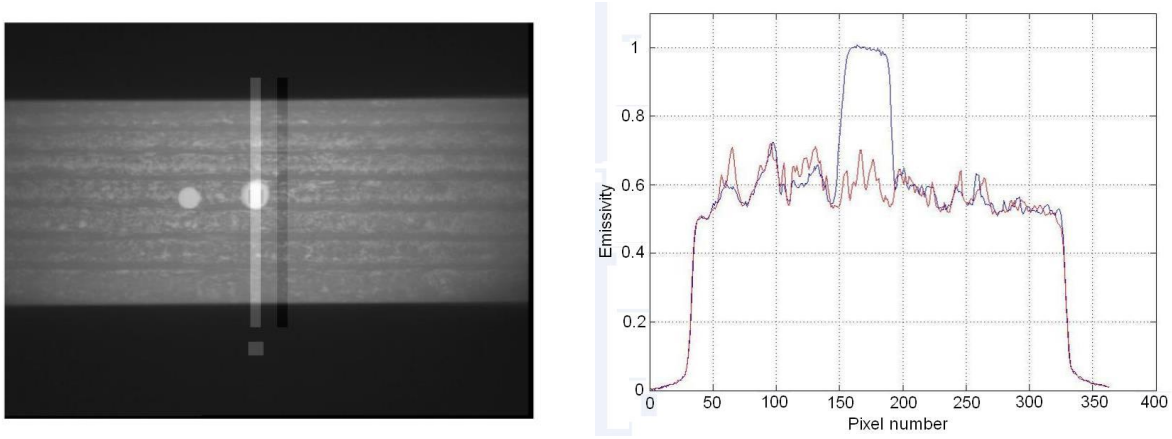

(a) *(b)*

Figure 4 - IR image and two regions of interest of the CFC tube coated with 10 μm W (a) and the corresponding emissivity for those regions (b)

In the case of CFC, the emissivity varies between 0.56 and 0.7. Under these conditions, it is difficult to estimate the influence of the viewing angle, but with FGG this can be done. In Figure 6, the variation of the emissivity with the viewing angle can be seen in the range of 0°-85°. There is no significant influence up to 55° and then the emissivity drops from 0.54 to 0.43 at 85°.

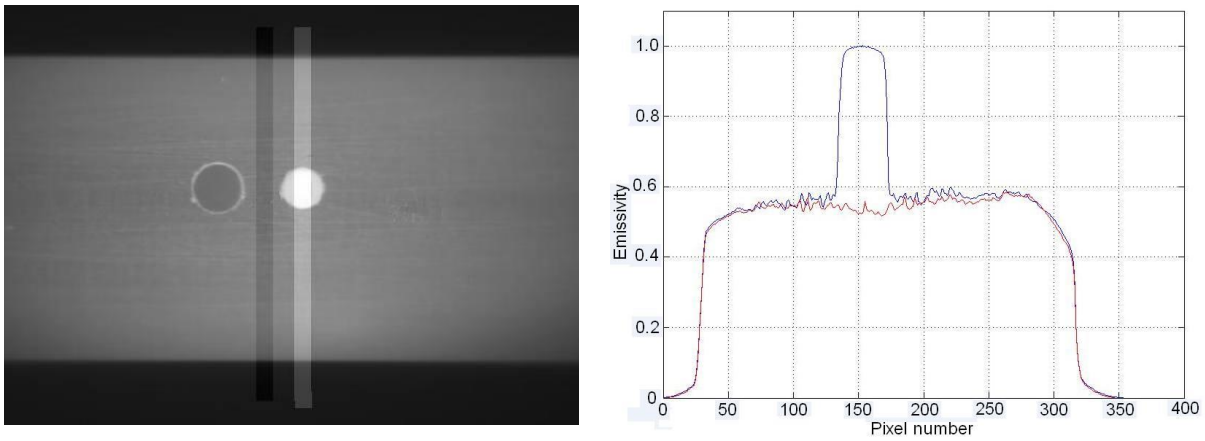

(a) *(b)*

Figure 5 - IR image and two regions of interest of the FGG tube coated with 10 μm W (a) and the corresponding emissivity for those regions (b)

This means a decrease to 87% of the maximum. A similar variation can be assumed for the W coatings deposited on CFC tiles.

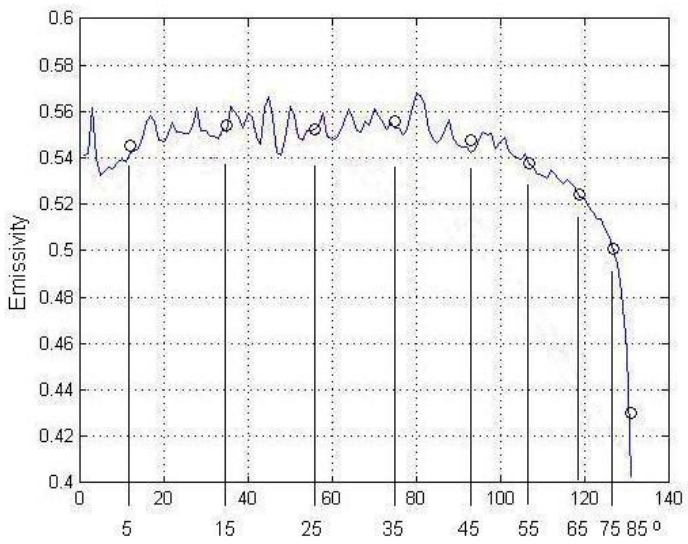

Figure 6 - The influence of the viewing angle on the emissivity of the 10 μm W coating deposited on FGG substrate

3.3. The influence of temperature on the W coating emissivity

By analyzing the curves shown in Figure 3, one can say that there is no significant influence of the temperature on the W coating emissivity. Even if it would be a small influence, this cannot be detected, due to the large influence of the CFC structure. However, this influence was investigated in the case of W coating deposited on FGG substrate.

The results are shown in Figure 7 for the three regions of interest marked in Figure 8. The emissivity was measured for each region, at similar temperature, two or three times, both during the heating up and cooling down. Before recording the IR images, the temperature was kept constant for 6-7 min, to ensure that the surface and the interior of the tub are at the same temperature. No significant influence of the temperature on the W coating emissivity in the range of 700°C-1,200°C can be seen. Even if there is a small decrease of 1-2%, this is within the error limits.

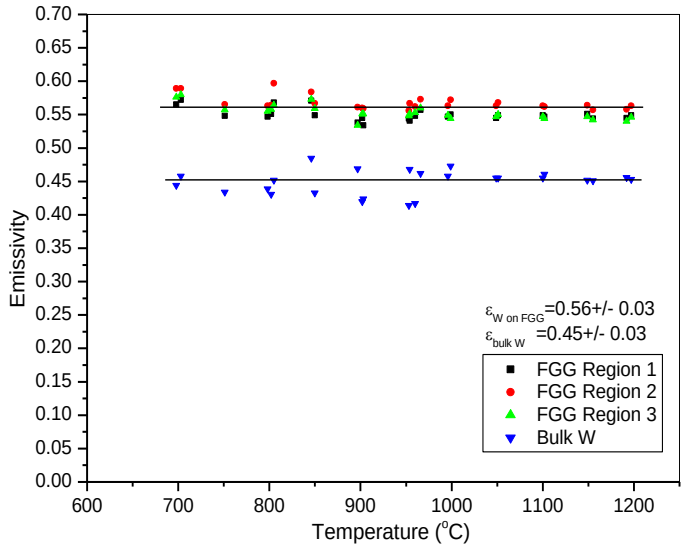

Figure 7 - Temperature influence on the emissivity of W coating deposited on FGG and bulk W for λ=1064 nm

Close to the black body hole, at about 5 mm, a W pin with a diameter of 2.5 mm and a length of 14.8 mm was introduced through a hole in the FGG tube (Figure 8). In this way, the bulk W emissivity was measured simultaneously with that of the W coating deposited on FGG and the temperature influence is shown in Figure 8. The average value is 0.45±0.03 and it is lower than that of W coating.

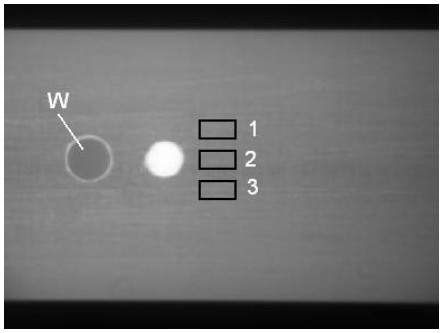

Figure 8 - W coated FGG tube with a bulk W pin

3.4. The influence of the W coating thickness on its emissivity

In the ITER-like wall, the CFC tiles are coated with two different thicknesses (10-15 μm and 20-25 μm). The results shown so far in this report were obtained on 10 μm W coating. In order to find out the influence of the structure on the emissivity for thicker coatings, the CFC tube was further coated with W up to a thickness of 21 μm, and the measurements were repeated using again Hitachi KP-M1AP IR camera.

A typical IR image of the heated 21 μm W coated CFC tube with the regions where the emissivity was calculated is shown in Figure 9. The influence of the substrate structure is still visible but the difference between the light intensities produced by W coating deposited on different types of fibers seems to be lower than that observed for a thickness of 10 μm. This could be explained by the fact that the small pores were partially covered with the thicker W coating and they do not act as "black bodies" any more. This effect is still produced by larger pores. This explanation is confirmed by the emissivity values at different temperatures calculated for the regions of interest indicated in Figure 10. It can be seen that in this case the emissivity is in the range of 0.53 – 0.65 with an average value of 0.59±0.06 if individual fibers are taken into account. There is no significant influence of the temperature on these values in the temperature range 750-1,200 °C.

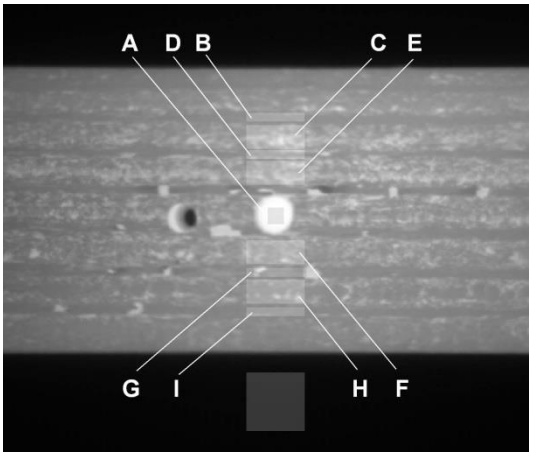

Figure 9 - CFC tube coated with 21 μm W and the regions of interest

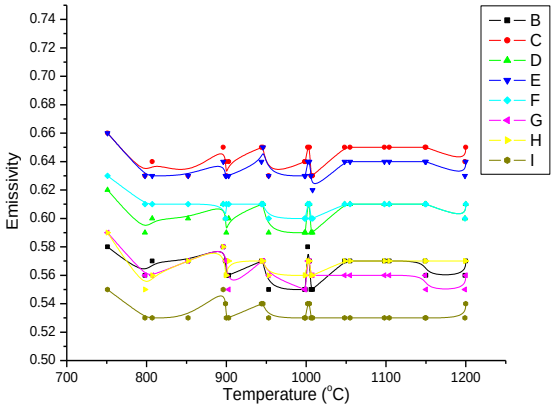

Figure 10 - Temperature influence on the emissivity of a W coating with a thickness of 21 μm deposited on CFC for λ=1064 nm

3.5. The emissivity of bulk Be

Using the same experimental device and a pin of Be with approx. dimensions 3 × 3.5 × 15 mm the emissivity of Be was measured in the temperature range 600 – 1,150 °C. A value of 0.49±0.05 was found. The spread of values is quite large and this might be associated with some modifications of the surface including oxidation. Preparation of the Be pin and experiments were carried out in the "Beryllium coating laboratory" from MEdC.

4. Calibration files

The emissivity of the W coatings was measured on λ=940 nm as well. A synthesis of all results described in this report is given in Table 1. This table can be used for calibration of the Hitachi KP-M1AP IR camera under various experimental conditions.

5. Conclusions

1. The emissivity of the W coatings deposited on Dunlop DMS 780, 2D CFC material was investigated in the range of 700-1,200 °C using a steady state heating regime. A value of 0.63±0.07 was found for 10 μm thickness, while for 20 μm the emissivity was 0.59±0.06. This large spread of values is due to the structure of the CFC substrate. If the emissivity is averaged for an area of at least 4 mm the average values become 0.63±0.01 and 0.59±0.01 for 10 μm and 20 μm coating thickness respectively.
2. In comparison with CFC, the emissivity of 10 μm W coatings deposited on FGG was found to be 0.56±0.03.

Table 1 Calibration files for emissivity of W coatings deposited on CFC and FGG substrates

No.	Material	Emissivity for the temperature range 750-1200 °C; λ=1,064 nm			
		θ = 0° - 55°	θ = 65°	θ = 75°	θ = 85°
1	10 μm W coated CFC (individual fibers) (average for at least 4 mm)	 0.63±0.07 0.63±0.01	 0.59*	 0.54*	 0.49*
2	20 μm W coated CFC (individual fibers) (average for at least 4 mm)	 0.59±0.06 0.59±0.01	 0.55*	 0.53*	 0.46*
3	10 μm W coated FGG	0.56±0.03	0.52	0.50	0.43
4	Bulk W	0.45±0.03			
		Emissivity for the temperature range 750-1200 °C; λ=940 nm			
1	10 μm W coated CFC (average for at least 4 mm)	 0.62±0.01			
3	10 μm W coated FGG	0.54±0.03			
4	Bulk W	0.45±0.03			
		Emissivity for the temperature range 700-1150 °C; λ=1,064 nm			
5	Bulk Be	0.49±0.05			

* The values were estimated in accordance with the characteristics of 10 μm W coatings deposited on FGG

3. In the same experiments the emissivity of bulk W was measured. It was found to be 0.45±0.03.
4. In the temperature range of 700 – 1,200 °C there is no significant influence of the temperature on the emissivity of W coatings or bulk W.
5. There is no significant influence of the viewing angle on the emissivity in the range of 0° – 55°. For further increase of the viewing angle the emissivity decreases gradually to 0.43 for 85°. These measurements were carried out with 10 μm W coatings deposited on FGG substrate.
6. The experiments were performed using bandwidth filters of 10 nm centred on 1,064 nm and 940 nm wavelengths. No significant difference of the emissivity values was observed.
7. The emissivity of Be was measured in the temperature range of 700°C – 1,150°C. A value of 0.49±0.05 was found. No temperature influence was detected.

Acknowledgement

The reported work includes contributions from the following people outside the EUATOM-MEdC Association: Gilles Arnoux (CCFE, Euratom Association, Abingdon, UK)

W-COATING ELM-LIKE TESTS IN MAGNUM-PSI

C. Ruset, E. Grigore, I. Munteanu, M. Gherendi, D. Nendrean
National Institute for Laser, Plasma and Radiation Physics, Bucharest, Romania,
Euratom-MEdC Association
[BS-12E/FT-12-4.23 MEdC IPP FOM]

Abstract

The W coatings deposited on CFC tiles from the ITER-like Wall at JET were tested at high thermal loading of long duration (1.5-24 s) and short duration (~ 1 ms), but in JET they are subjected to quasi-stationary thermal loading (10-20 s) and transients due to ELMs (τ ~ 1-2 ms, f ~ 10-20 Hz). In order to get more information about the W coating limits under more realistic loading conditions (including steady-state plasma and ELM-like transients), additional tests were carried out in Magnum-PSI, DIFFER, Netherlands.

A CFC sample with approx. dimensions 80×70×40 mm coated with 20 μm of W was tested in Magnum-PSI was tested at the following parameters: (i) Plasma source power: about 40 kW; (ii) Shot duration: 12s; (iii) Pulse duration: about 1 ms; (iv) Pulse frequency: 5-20 Hz; (v) Estimated power density of short pulses: 80 - 120 MW/m^2; (vi) Total number of pulses: ~ 2875.

The coating survived the tests without any delamination, but the peak temperature on the surface was in the range of 320 - 540°C only.

Conferences

- C. Ruset, H. Maier, E. Grigore, G. Matthews, G. De Temmerman, A. Widdowson and JET-EFDA Contributors, W coatings under high thermal loads in JET and Magnum-PSI, 14th Int. Conf. on Plasma-Facing Materials and Components for Fusion Applications, 13 –17 May 2013, Jülich, Germany

Presentations

- G. De Timmerman, C. Ruset, H. Maier,, E. Grigore, W-coating ELM-like tests in Magnum-PSI, 2nd Semi-annual Monitoring Meeting, 11-14 December, 2012, JET, Culham, UK

Detailed results

1. Background

Combined Magnetron Sputtering and Ion Implantation (CMSII) technology was applied for W coating of about 1,800 CFC tiles for the ITER-like Wall project at JET. Since August 2011 JET operates with the new wall comprising beryllium, W coated CFC and bulk W tiles. During JET operation, W coatings are subjected to quasi-stationary thermal loading (10-20 s) and transients due to ELMs (τ~1ms, f~10-20 Hz).

As far as long pulse thermal loading is concerned, tests have been carried out on W coatings in the GLADIS ion beam test facility (IPP Garching) and with the high temperature test facility (HTTF) at MEdC (electron beam heating). Three phenomena which can limit the W coatings lifetime have been identified so far. These are: thermal fatigue, carbidization due to the carbon diffusion from the substrate and formation of brittle carbides and melting. Recent results indicated that a fraction of ~ 0.2% of a 10 μm W coating subjected to a cyclic thermal loading (3,400 pulses) with a peak temperature of 1,300°C is damaged by small delaminations with a size of 50-400 μm. For coatings with a thickness of 20 μm, this percentage increases to ~1%. These results have been reported and some of them are already published [1, 2].

ELMs-like simulations carried out in JUDITH 1 and JUDITH 2 (electron beam heating) at FZ Jülich indicated as a limit for 20 μm W coatings 150 MW/m^2, pulse duration – 1 ms, 1000 pulses.

ELMs-like simulations carried out in GLADIS have shown that the 20 μm W coating can survive without delamination at 1000 pulses of 30 MW/m^2, pulse duration – 70 ms. This is equivalent, from the surface temperature point of view, with 250 MW/m^2, pulse duration – 1 ms. Unfortunately, at the moment, 30 MW/m^2 is the upper limit of the power density for GLADIS.

In order to get more information about the W coating limits under more realistic loading conditions (including steady-state and ELM-like transient heat loads), additional tests were carried out in the framework of this project in Magnum-PSI, DIFFER (Dutch Institute for Fundamental Energy Research), Holland.

Magnum-PSI can provide transient heat loads of up to 1GW/m^2 for durations of 0.5-1ms superimposed on quasi steady-state heat loads of 10MW/m^2 for durations of up to 12s. This makes the device ideally suited to study the behaviour of tungsten coatings used in the JET divertor. The results of these tests together with those obtained on GLADIS and HTTF will provide a good characterization of the W coatings deposited on JET tiles from the thermo-mechanical point of view. In this way, the limits of these coatings for various thermal loading conditions (power density, surface temperature and time) could be predicted. This is extremely important for the exploitation of the new JET wall.

2. Project objectives

Specific objectives of this project include:

- To investigate the behaviour of the W coatings (10 μm and 20 μm) under simultaneous steady-state and transient heat loads, characteristic for a JET ELM-ing discharge.

- To establish a correlation between the percentages of W coating damaged area, the power density (surface temperature) and number of pulses.

- To identify the mechanism for W coating failure for this type of thermal loading. In particular, a comparison of the results from Magnum and from GLADIS may allow us to decide whether the damage is solely due to thermal effects or whether the influence of power density and pulse duration can be separated.

3. Results and discussion

3.1. Preparation of W-coated samples

A set of four Layout #1 samples have been coated with 10-15 μm of W and another set with 20-25 μm of W.

The samples are shown in Figure 1. The samples have been characterized from the point of view of coating thickness and impurities using the Ti witness samples. The GDOS depth profiles for the two coating runs can be seen in Figure 2. The real coating thickness is 12.4 μm for the first set of samples and 21 μm for the second set of samples.

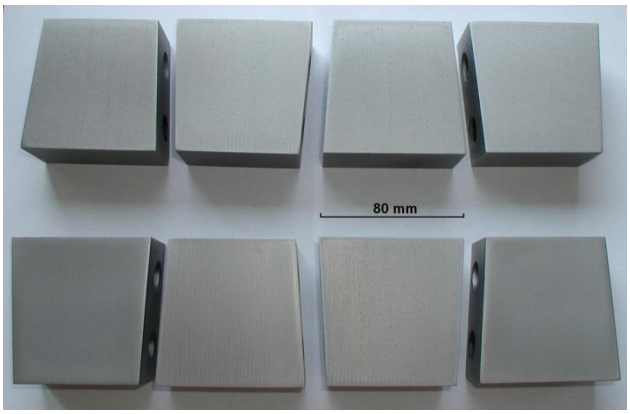

Figure 1 - Layout #1 samples coated with 10-15 μm and 20-25 μm of W

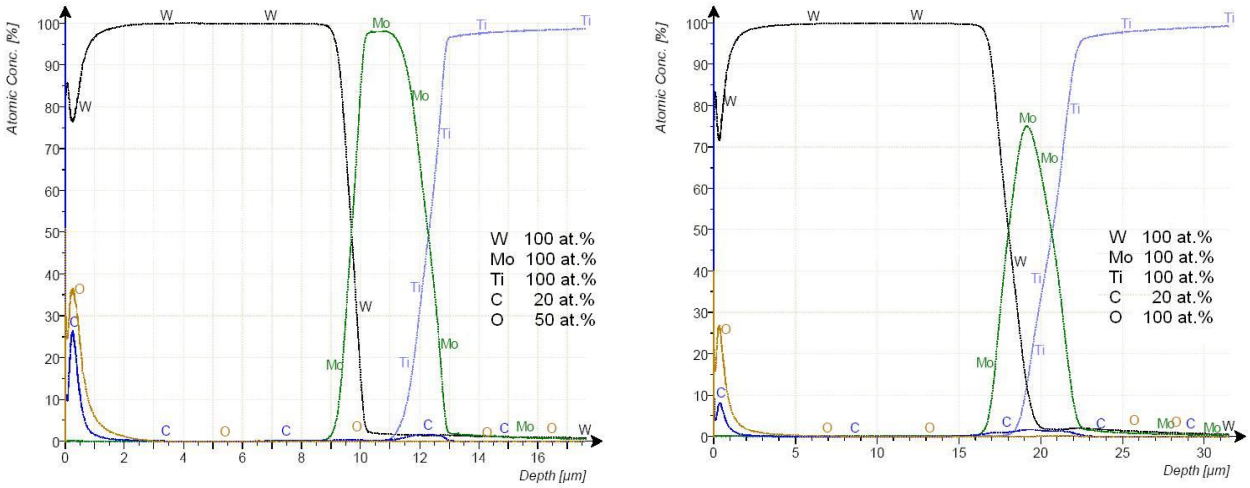

(a) (b)

Figure 2 - GDOS depth profiles for W coatings deposited on CFC Layout #1 samples to be used for ELM-like tests in MAGNUM-PSI; (a) 12.4 μm and (b) 21 μm

3.2. Magnum-PSI, brief description

Magnum-PSI (MAGnetized plasma and NUMerical simulations of Plasma-Surface Interactions) (Figure 3) is a large machine, generating high intensity plasma fluxes. The plasma source is a cascaded arc working at a power of about 40 kW (U_{plasma}~ 200 V, I_{plasma}~ 200 A). It is located at the right end in Figure 3b and it is pushed inside the vacuum chamber near to the magnetic coils (left side-Figure 3b). The samples to be tested are installed in the samples chamber (Figure 3a) on a special arm (Figure 4). This arm is pushed in the target chamber near to the magnetic coils. The samples chamber shown in Figure 1a has a 1.6 m diameter. The plasma generated by the plasma source is confined by the magnetic field with intensity up to 1.8 T, and it strikes the target (the sample to be tested). Magnum plasma has a high density and low temperature, similar to the divertor plasma in tokamaks.

(a) *(b)*

Figure 3 - Magnum-PSI samples chamber (a) and the magnetic coils (b)

The tests started with 20 μm W coating because this coating is more sensitive to the high thermal loading in comparison with 10 μm. The results are presented below.

3.3. Testing parameters

- Plasma source power: about 40 kW
- Diameter of the plasma beam at the target surface: ~ 30 mm
- Gas: hydrogen
- Magnetic field: ~ 1.3 T
- Shot duration: 12s
- Pulse duration: about 1 ms
- Pulse frequency: 5-20 Hz
- Total number of shots: 30
- Energy stored in the capacitor bank for short pulses: 30 J, 108 J, 217 J, 260 J and 324 J
- Estimated power density of short pulses: 80 - 120 MW/m^2
- Total number of pulses: ~ 2875
- Cooling time between two successive shots: about 20 min.
- Temperature due to the steady state plasma was in the range of 200 - 400°C.
- Peak temperature due to short pulses was in the range of 320 - 540°C.
- The increase of surface temperature due to short pulses was about 100-120 °C.
- The temperature was measured with an IR camera at a frequency of 4 kHz on the wavelength of 4 μm.

The temperatures were obtained by taking the peak value of a Gaussian fit through the maximum of the 2D IR-profile. This was done to diminish the effect of hot spots on the target and bad pixels in the camera. The emissivity was set to 0.25. The typical temperature trace is shown in Figure 5.

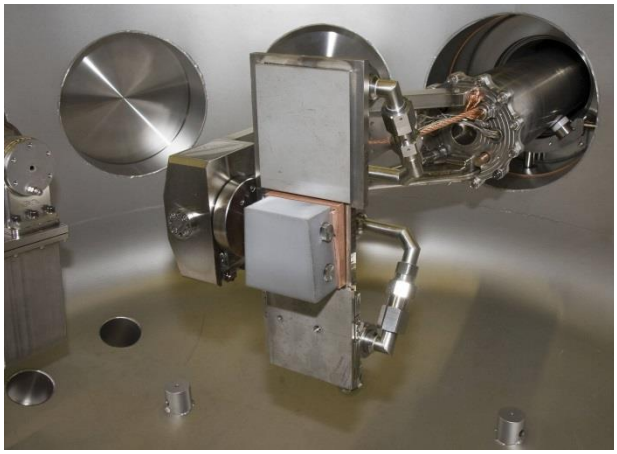

Figure 4 - Layout 1 sample installed in Magnum

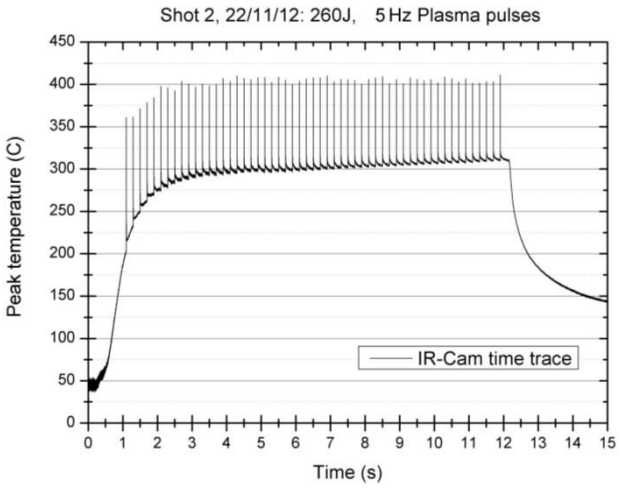

Figure 5 - Typical temperature -time trace for tests in Magnum-PSI

3.4. Inspection of the W coating

The W coating was inspected with a stereomicroscope at a magnification 40×. No delaminations or other damages have been detected, except two small spots with the dimensions of 100-200 µm where the coating was melted, but without detachment from the substrate. A picture of the sample at the end of experiment is shown in Figure 6. It is clear that the plasma source was damaged and the nozzle, made of Cu, was melted. A thin Cu layer was deposited on the sample surface. The pressure in the target area during testing was about 0.2 Pa.

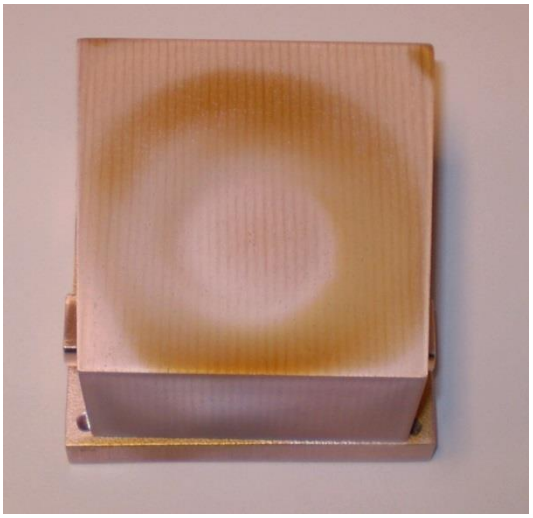

Figure 6 - 20 µm W coated sample at the end of test in Magnum-PSI

Conclusion

The 20 µm W coating survived without delamination to 2875 pulses of about 1 ms with a power density of 80-120 MW/m^2. The peak surface temperature during tests was in the range of 320-540 °C. Due to the high conductivity of the CFC and to the limited power of the plasma beam, the surface

temperature could not be increased over 1000 °C to produce delaminations. The ELM-like pulses do not induce damage of the coating if they are not associated with a high temperature (T>1000°C).

Acknowledgement

The reported work includes contributions from the following people outside the EUATOM-MEdC Association: Gregory de Timmerman and Thomas Morgan (EURATOM - DIFFER Association, Netherlands.

References

[1] C. Ruset, E. Grigore, H. Maier, R. Neu, H. Greuner, M. Mayer, G. Matthews, Development of W coatings for fusion applications, Fusion Engineering and Design, 86 (2011), 1677-1680

[2] H. Maier, M. Rasinski, E. Grigore, C. Ruset, H. Greuner, B. Böswirth, G.F. Matthews, M. Balden, S. Lindig, and JET-EFDA contributors, Performance of W Coatings on CFC with respect to Carbide Formation, Journal of Nuclear Materials, 415 (2011), S310-S312.

EROSION/DEPOSITION STUDIES OF SELECTED PFC SAMPLES FROM JET BY X RAYS

I. Tiseanu[1], T. Craciunescu[1], C. Dobrea[1], A. Sima[1], M. Lungu[1],
C. P. Lungu[1], I. Jepu[1], A. M. Lungu[1], P. Chiru[1], J. Likonen[2], A Hakola[2]
[1]*National Institute for Laser, Plasma and Radiation Physics, Bucharest-Magurele*
[2]*VTT Helsinki, Finland*
[BS_20B/WP12-IPH-A01-1-05/BS; BS_20C/FT-12-3.72 MEdC_TEKES]

Abstract

Erosion/deposition studies of selected PFC samples from JET were performed using X-ray absorption/fluorescence method. Using surface analytical method as SEM, XPS and grazing XRD, the selected samples were characterized and correlated with SIMS results. Optimization studies of tungsten coating characterization by X-ray fluorescence have been carried out concerning: (i) W thickness calibration using specially prepared samples with following characteristics: 5, 10 and 15 µm W coated on Ti substrate with 2.5 or 5 µm Mo interlayer; the layer thicknesses of the calibration samples were measured by SEM and GDOS; (ii) W thickness measurements of CFC and FGG samples coated with ≈10 and 13.5 µm W and 3.5 µm Mo interlayer; (iii) Mo thickness measurements of the tile 5 lamellas coated in INFLPR by CMSII method.

X-ray micro-radio and tomography measurements with the nanoCT submicron resolution tomograph of INFLPR were performed on the DMS780 CFC samples in order to assess the CFC morphology. Obtained values of W/Re thicknesses follows the trend indicated by the X-ray micro-radio/tomography and are in good agreement with previous SEM images and recent RBS data. Line profiles of W/Re thicknesses pattern show strong correlation of W erosion and CFC morphology.

The samples exposed in 2007-2009 and the samples cut from 2 tiles exposed in 2004-2009 were analyzed using XRD and Grazing XRD, ESCA and SEM. Were identified C, Be, BeO, Be_2C, BeNi, and Cr, Fe, Ni, Cu impurities depending on the samples positions of the divertor tiles.

In order to reproduce in laboratory the identified BeNi intermetallic phase using TVA method, mixed Be-Ni films with variable relative concentration were prepared. The same phase of cubic BeNi material was identified on films deposited on Si and fine grain graphite substrates. A map of concentration distribution was presented including comparison with the SIMS results.

Papers

[1] Thomser, C., Bailescu, V., Brezinsek, S., Coenen, J. W., Greuner, H., Hirai, T., Linke, J., Lungu, C. P., Maier, H., Matthews, G., Mertens, Ph., Neu, R., Philipps, V., Riccardo, V., Rubel, M., Ruset, C.; Schmidt, A., Uytdenhouwen, I."PLASMA FACING MATERIALS FOR THE JET ITER-LIKE WALL"; FUSION SCIENCE AND TECHNOLOGY Volume: 62 Issue: 1 Pages: 1-8 Published: JUL-AUG 2012

Conferences

[1] I.Tiseanu, M. Mayer, T. Craciunescu, A. Hakola, S. Koivuranta, J. Likonen, C. Dobrea, A. Sima, Two-dimensional erosion mapping of metal layers coated on carbon based plasma facing materials, 20th International Conference on Plasma Surface Interactions 2012, Eurogress, Aachen, Germany, 21. – 25.05.2012
[2] C. P. Lungu, J. Likonen, A. Hakola, C. Porosnicu, I. Jepu, A. M. Lungu, P. Chiru, Gh. Oncioiu, A. Victor, P. Osiceanu and JET-EFDA Contributors**, Characterization of Mixed Materials in Support of the ITER Like Wall, 20th International Conference on Plasma Surface Interactions 2012, Eurogress, Aachen, Germany, 21. – 25.05.2012

Reports

[1] I. Tiseanu, C. P. Lungu, Erosion/deposition studies of selected PFC samples from JET by X-rays JW12-FT-3.72, JET Fusion Technology monitoring meetings the 11th - 14th December 2012 (remote presentation)

Detailed results

1. Introduction

There is an increased activity for the experimentation of mixed material combinations that will be used in the ITER tokamak. Tungsten is one of the most interesting materials to be used in bulk or carbon coated plasma facing components (PFC).

The problem of erosion and redeposition of tungsten is central to the modelling of the behaviour of an all metal first wall tokamak. Currently, the ASDEX Upgrade (AUG) tokamak use FGG coated with thin layer of tungsten (~3 μm) while in JET one uses CFC coated with thicker tungsten layer (~10 μm) and a molybdenum (2~3 μm) interlayer.

A combination of X-ray non-destructive techniques have been developed in INFLPR in order to perform the coating tungsten coating thickness analysis. These methods are based on: i) high resolution X-ray absorption, ii) X-ray fluorescence mapping, and iii) X-ray backscattering [1]. This allows the measurement of the thickness of layers and, therefore, the determination of the 2-dimensional erosion pattern on a whole PFC, for example a divertor tile.

Using Thermionic Vacuum Arc (TVA) technology, mixed films were produced, with concentrations similar to those found after the operation of the tokamak device. The TVA deposition method offers a high degree of flexibility, due to its unique combination of properties [7, 8]. The experimental set-up is presented elsewhere [2]; briefly, it consists of a tungsten filament cathode externally heated by a low voltage supply. The emitted thermal electrons are focused on the top of the anode surface by a Wehnelt cylinder. The anode is a Be rod on which positive high voltage is applied. Due to electron bombardment, the anode material evaporates and, at a certain vapor pressure, the electron-atom ionizing collisions generate plasma in pure anode material. The substrates to be deposited were placed 150-200 mm away from the plasma. Silicon wafers and fine grain graphite plates were used as substrates.

2. Methods and materials

The method for tungsten coating analysis was implemented using the Tomo-Analytic system, which was developed especially for the fusion materials analysis [9-10].

Tomo-Analytic is a configurable and versatile tool in which different measuring methods can be accommodated for the characterization of the thickness uniformity of FGG/CFC with metallic coatings:

- X-ray fluorescence (μXRF) - the coating X-ray fluorescence peak intensities are converted to elemental concentrations and/or film thicknesses. The key element of the μXRF component is a policapillary lens which provides a focal spot size in a range from few tens to a few hundreds of micrometers. A significant increase of the X-ray intensity (up to three orders of magnitudes) is obtained [11] which allow improved detection sensitivity.
- μXRFS) the X-ray fluorescence radiation emitted by the substrate is attenuated by the coating material; a correlation can be derived between the secondary emissions and the coating thickness.
- X-ray backscattering (μXRFB) - the coating thickness is determined from the correlation with the attenuation of the X-ray back-scattered radiation by a substrate with low effective atomic

number. This procedure has the advantage to be more suitable to carry out reference free thickness measurements.

- X-ray transmission (μXRT) - the X-rays are detected by an energy selective detector after passing through the investigated sample where they are attenuated accordingly with the composition and thickness of the materials.

Figure 1 depicts the above-mentioned principles and the experimental μXRT / μXRBS setup.

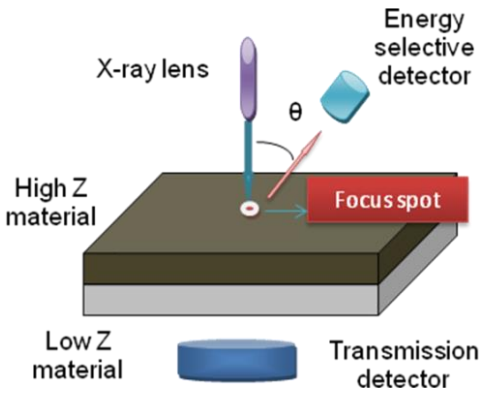

Figure 1 – Principle of the X-ray transmission / fluorescence / backscattering

The method for tungsten coating analysis was implemented using the Tomo-Analytic system, which was developed especially for the fusion materials analysis (https://tomography.inflpr.ro). For the analysis of CFC samples coated with relatively thick layers of tungsten and rhenium we have developed a new version of the X-ray absorption technique in which the thickness of multilayer coatings is determined by transmission measurements of multiple mono-energetic X-rays. The measurement of thickness of micron-sized coatings consisting of several known elements can be made by measuring the attenuation by the sample of mono-energetic X-rays at a number of energies, equal or greater than the number of layers. The choice of particular energies must be appropriate, to ensure the well-behaved character of the linear system resulting from the maximization condition imposed on the agreement between attenuations measured and those calculated with the mass attenuation coefficients at X-ray energies used for measurements. Validation of the method on test samples (Au and Sn foils on graphite substrates): This approach was validated by measuring a test sample made from a blade of fine-grained graphite, covered on one side with a 5μm gold foil and a 3 μm foil of tin. As sources of mono-energetic X-rays, available sheets of various elements were used, irradiated with an X-ray tube working at 45 KeV to excite emission of characteristic Kα lines. The choice of the secondary sources was made by considering the energy dependence of mass attenuation coefficients for gold, tin and carbon. If the energy dependence of mass attenuation coefficients is represented in a log-log graph, the curves are practically linear between the shell threshold jumps and have nearly equal slopes. In this case, if energies of Ka fluorescence lines used for measurements fall on an interval where neither Au nor Sn have threshold jumps for attenuation coefficients (the group of secondary sources Ag, In, Nb, Sn, Zr), the linear system for thicknesses of Au and Sn is ill-behaved and cannot be solved reliably. This was the reason to add Ni and Cu as secondary sources of fluorescence X-rays and it leads to stable solutions of the system of equations for the thickness of gold and tin foils.

As in the case of the probes cut from CFC slabs, considering the high transparency of graphite layer to X-rays and its thickness much larger than that of foils, the attenuation of graphite was deduced from its thickness measured directly with a caliper.

The XRD, GXRD and XPS spectra were acquired using the following equipments: for standard XRD: X-ray Difractometer (Rigaku MiniFelx II unit); -X-ray tube: Cu target, 1.0 kW, Normal Focus, 1.0 mm x 10.0 mm focus size; for GXRD: X-ray diffractometer, D8 ADVANCE type (BRUKER-AXS Germany, 2007),Vertical theta-theta goniometer in powder XRD setting; lowest step size (2θ)= 0.0002°; for XPS measurements: X-ray Photoelectron Spectrometer (XPS), ESCALAB 250 produced by Thermo Scientific Co. USA, The energy domain of the electron analyzer: 0-5000 eV, energetic resolution ≤ 0.45eV, XPS imaging: spatial resolution ≤ 3μm; XPS spot diameter: ≤120 μm.

3. Experiments and results

Following optimization, studies of tungsten coating characterization by X-ray fluorescence have been carried out:

- W thickness calibration by X-ray fluorescence measurements of specially prepared samples with following characteristics: 5, 10 and 15 μm W coated on Ti substrate with 2.5 or 5 μm Mo interlayer. The layer thicknesses of the calibration samples were measured by SEM and GDOS.
- W thickness measurements of CFC and FGG samples coated with ≈10 and 13.5 μm W and 3.5 μm Mo interlayer.
- W and Mo thickness measurements of the tile 5 lamelas coated in INFLPR by CMSII method.

3.1 Tungsten and Rhenium coated Tiles 7 & 8 of 2007-2009 JET irradiation campaigns

The two tiles were coated by a multilayer structure of W and Re. Our task is to determine the total thickness of the metallic coating in order to evaluate its net erosion. Since we did not encounter such structures in the previous works, we have implemented an ad-hoc technique.

In this technique one uses a secondary monochromatic X-rays source in order to obtain a set of transmission coefficients which are the known terms in a system of equations with unknown variables the layer thicknesses.

We also performed a composition mapping by microbeam X-ray fluorescence on W & Re coatings from the JET campaign 2007-2009 (Figure 4). The X-ray spectra of W / Mo coated DMS870 CFC CMSII (sample IU-318-5) and of the multilayered W & Re coated DMS870 CFC (sample G8A-7b, JET 2007-2009 campaign) is shown in Figure 2.

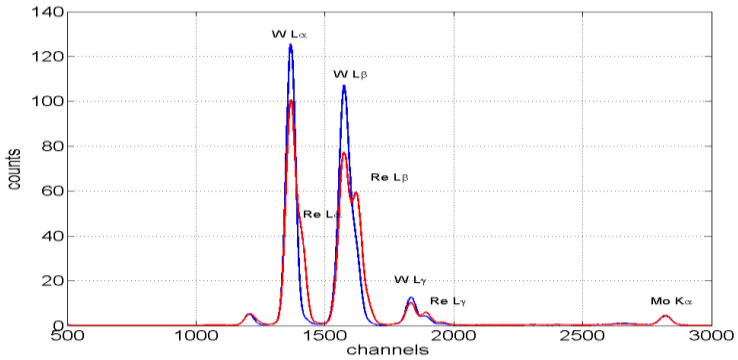

Figure 2 - μXRF spectra of W / Mo coated DMS870 CFC CMSII (sample IU-318-5) ***(blue)*** *and W & Re coated DMS870 CFC (sample G8A-7b, JET 2007-2009 campaign)* ***(red)***

During the current reporting period, we focus our work on the determination of the W/Re coating thickness of the JET samples cut out of the of outer divertor tiles G7B and G8A.

The morphology of the CFC substrate is relevant for the X-ray backscattering investigations.

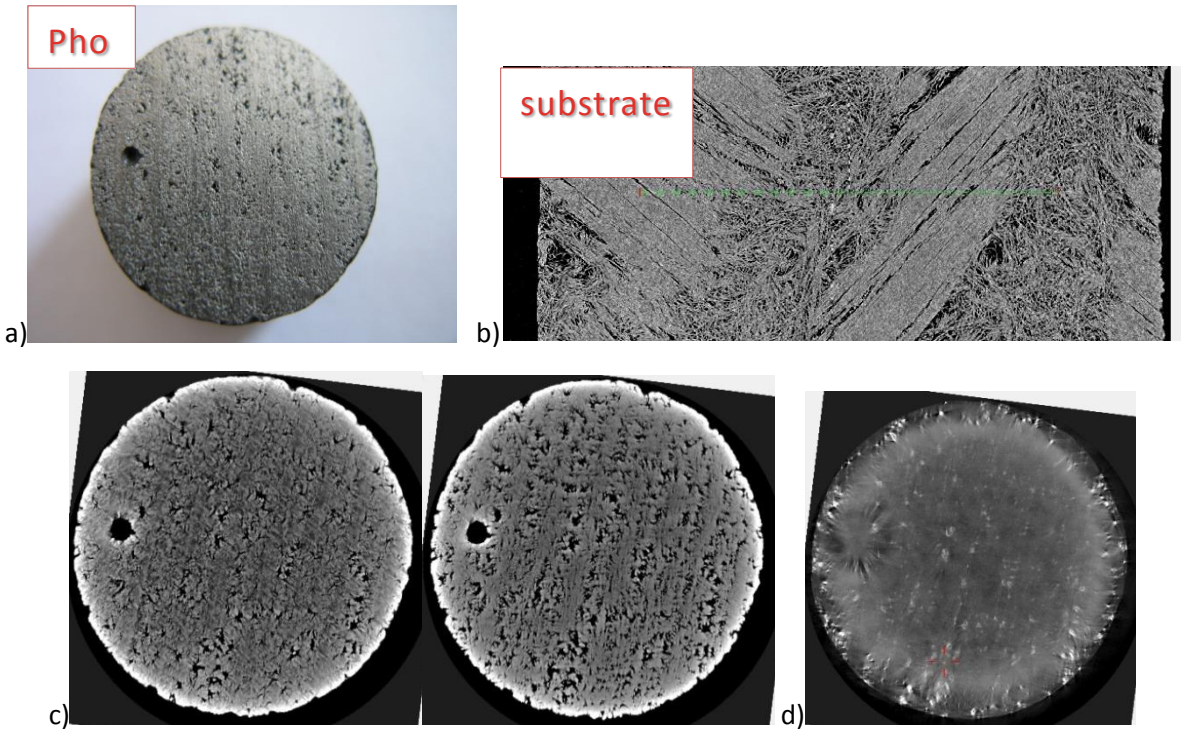

Figure 3 – G8A_7b sample. a) photo; b) CFC substrate; c) W & Re coating; d) W & Re infiltrated

For the determination of the thickness of Tungsten layer deposited on CFC slab samples, it was preferred to measure the attenuation of fluorescence X-rays produced at 45° by secondary targets placed in the beam emitted by the X-ray tube. The use of mono-energetic fluorescence X-rays allows a simpler calculation of thickness from attenuation factors, avoiding the need to know the energy spectrum of the X-ray tube, or to perform the corresponding calibration. In this case the measurements have also the advantage of small dead-time and pile-up corrections and can be used for Tungsten layers up to tens of microns. For the actual measurements, secondary targets made of Sn, In, Ag, Nb and Zr were used and the attenuation caused by the samples for their Kα lines [3] was measured.

X-ray micro-radio and tomography measurements with the nanoCT submicron resolution tomograph of INFLPR [4] were performed on the DMS780 CFC samples in order to assess the CFC morphology. The CFC thickness and density variation are necessary ingredients to determine the metallic layer thickness. Obtained values of W/Re thicknesses follows the trend indicated by the X-ray micro-radio/tomography and are in good agreement with previous SEM images. Line profiles of W/Re thicknesses pattern show strong correlation of W erosion and CFC morphology. Figure 4 presents micro-radiographies of the samples placed side by side or stacked together. From Figure 4 one can have a good visualization of the erosion pattern. Thus the G7B tile suffers much more erosion as the G8A one.

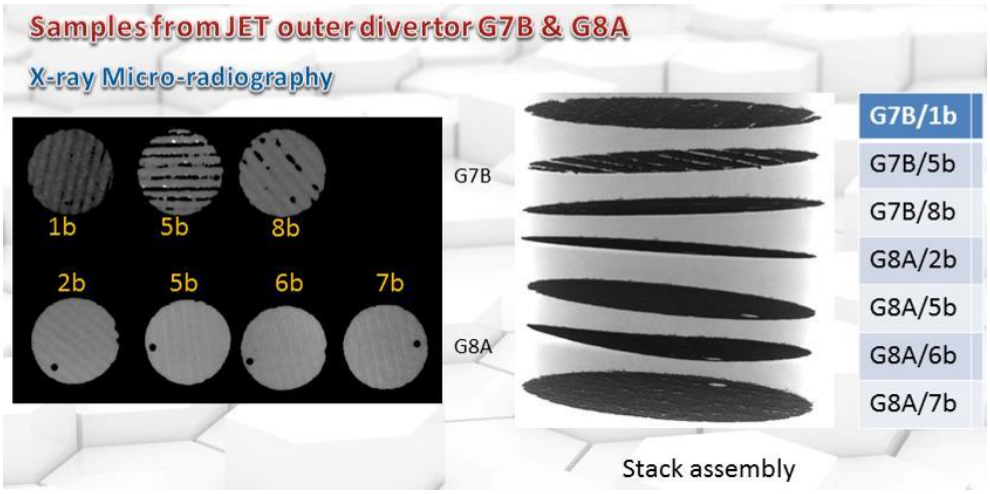

Figure 4 – Microradiography of the W/Re coated CFC samples

X-ray microtomography analysis of CFC samples has two purposes: i) to determine the morphology and the porosity factor of the CFC substrate and ii) to evaluate the integrity of the W/Re coating. The porosity factor is relevant for the evaluation of the CFC substrate transmission of mono-energetic X-rays. The porosity factor is determined from the histogram of a statistically relevant reconstructed volume (Figure 5) [4]. The value of 14.3 % for DMS780 CFC is in good agreement with the manufacturer specifications.

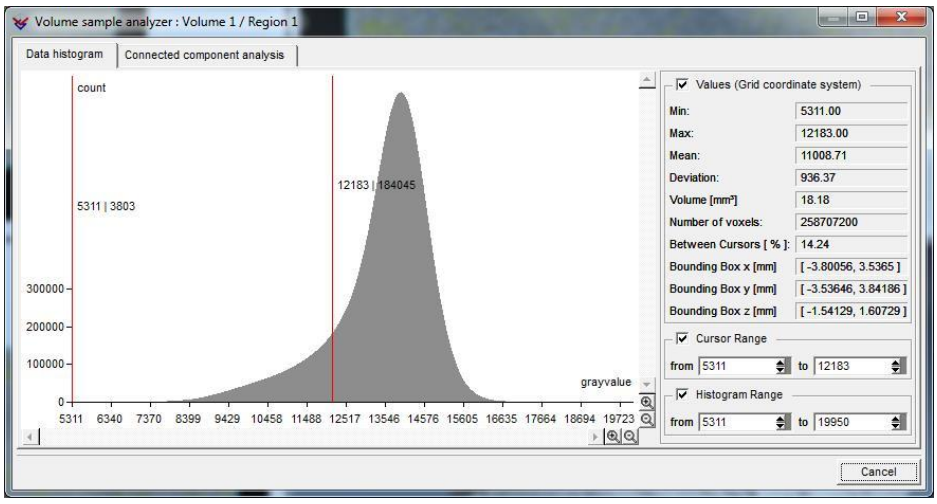

Figure 5 – Porosity measurement (porosity factor ≈ 14.3%)

The integrity of the eroded layer of W/Re is checked by an overview microtomography measurement presented in Figure 6.

With the information about the substrate morphology from microtomography and the erosion pattern from microradiography we could proceed to thickness measurements with the multi-energy transmission method.

Main steps of data processing i) recording of X-ray fluorescence spectra and ii) evaluation of transmission factors are illustrated in Figure 7 a, b. Only two spectra are plotted (Figure 7 a) for the Nb and Ag secondary sources. Secondary X-ray sources using Zr, In an Sn have been also used (Figure 7 b).

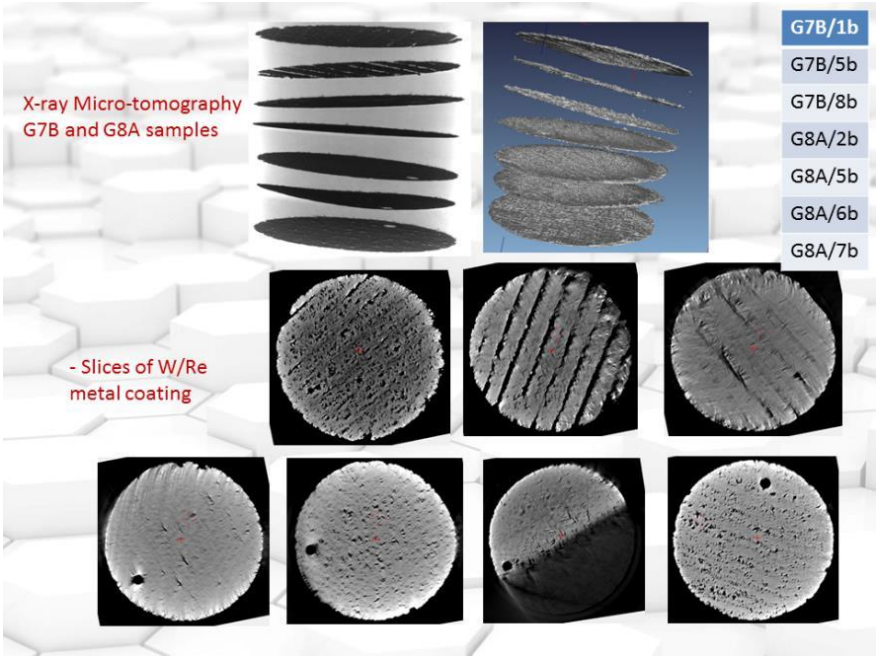

Figure 6 - X-ray microtomography of the stacked G7B & G8A W/Re coated CFC samples

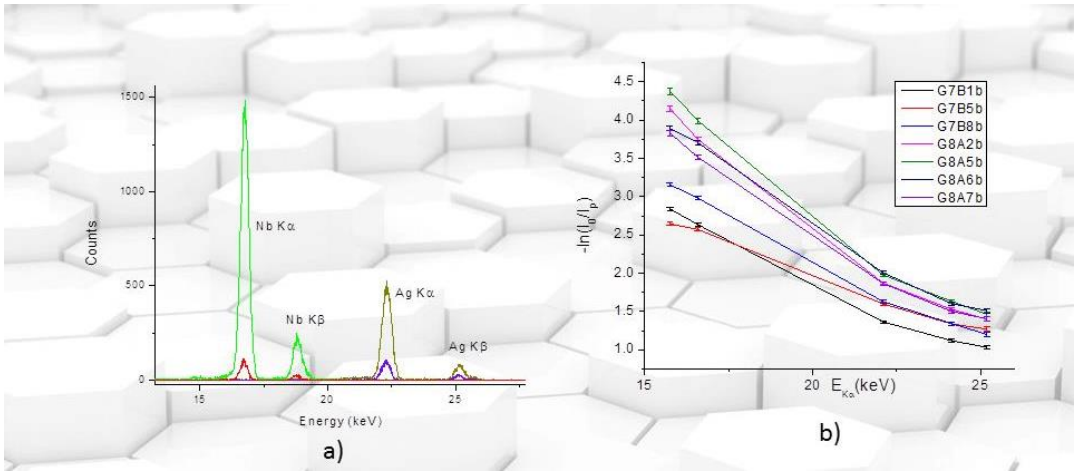

Figure 7 - Data processing steps: a) recording of X-ray spectra, b) ii) evaluation of transmission factors

From previous SEM analysis of samples and from X-ray fluorescence composition mapping it is known that the deposit is formed by alternate layers of Tungsten and Rhenium. As the attenuation of Rhenium to X-rays in keV range is nearly indiscernible of that of Tungsten (Figure 8), the measured attenuation of X-rays was assumed to be caused by an equivalent layer of pure Tungsten and the thickness values of Tungsten presented in this work were derived under this assumption.

Having the attenuation data [5] for X-ray energies corresponding to the Kα lines of the five elements listed earlier and the attenuation coefficients of Tungsten and Carbon at these energies, the thickness of Tungsten layer for each sample was computed in an Excel file, by minimizing a weighted

sum of squared differences between observed and calculated transparency of sample. The sum included a term for each of five Kα lines used, and the corresponding weight was the squared statistical error of the logarithmic transparency. The minimization was made using the Excel Solver add-in.

The uncertainties of Tungsten thickness data are affected by the statistical errors of the selected Kα peak areas and by the imprecision of mass attenuation coefficients taken from literature. In our case the contribution of statistical errors is at the level of 0.5% while the typical uncertainty for mass attenuation coefficients for heavy elements in the energy range of a few tens of KeV is thought to lie between 1% and 3% [6].

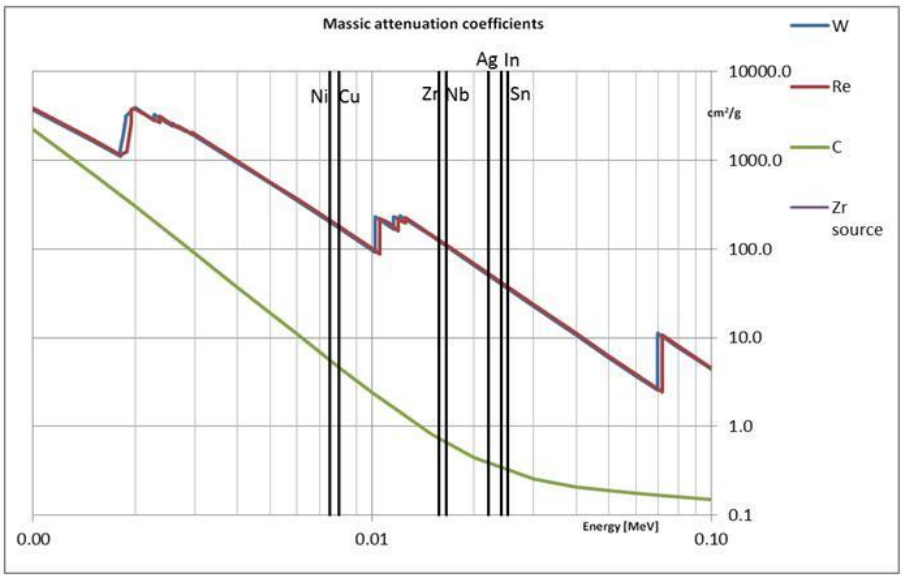

Figure 8 - Mass attenuation coefficients for W, Re and C in the energy range of used XRF secondary sources

Samples	Thickness(µm) W equivalent	1e+18 Atoms/cm^2
G7B/1b	13.0±0.3	81.97
G7B/5b	12.8±0.3	80.71
G7B/8b	14.9±0.4	93.95
G8A/2b	18.9±0.4	119.11
G8A/5b	20.2±0.4	127.37
G8A/6b	18.7±0.3	117.91
G8A/7b	17.9±0.3	112.87

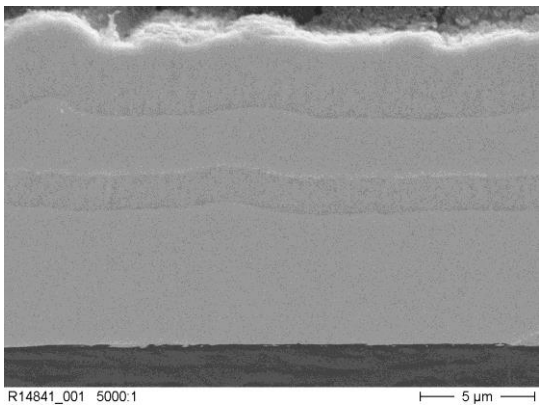

Figure 9 - Average thickness of the W/Re coatings expressed in W equivalent and atoms/cm^2. The measuring errors cumulate the statistical and the mass attenuation uncertainties effects. On the left panel one shows a correlation with SEM image taken before irradiation.

The results of the application of the new developed multi-energy transmission method are presented in the table below. Figure 9 (right panel) shows a good agreement with total thickness measured on a SEM image taken before the exposure. One remark: in Figure 6, with

microradiography of samples placed side by side, one capture very well the trend in the erosion pattern.

Finally, in Figure 10, the XRT and RBS thickness measurements are compared. The RBS measurements are provided by Dr. Matej Mayer of IPP Garching.

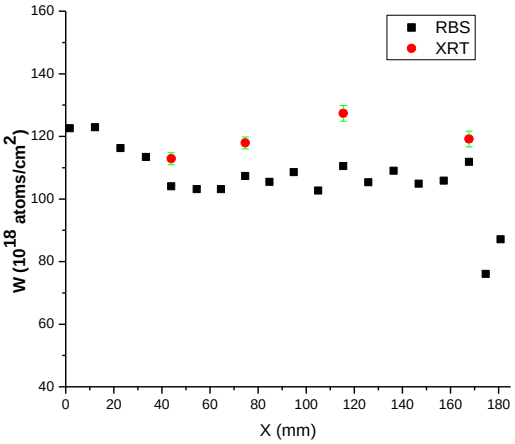

Figure 10 - Comparison between XRT and RBS methods

3.2 W and Mo thickness measurements on 12 Tile 5 tungsten lamelas

Supplementary to the contract we had performed W and Mo thickness measurements on all 12 Tile 5 lamelas coated in INFLPR by CMSII method (Figure 11). The tungsten lamelas are to be installed into the JET tokamak. These measurements would allow us to determine the absolute tungsten erosion during the JET 2012-2013 campaign.

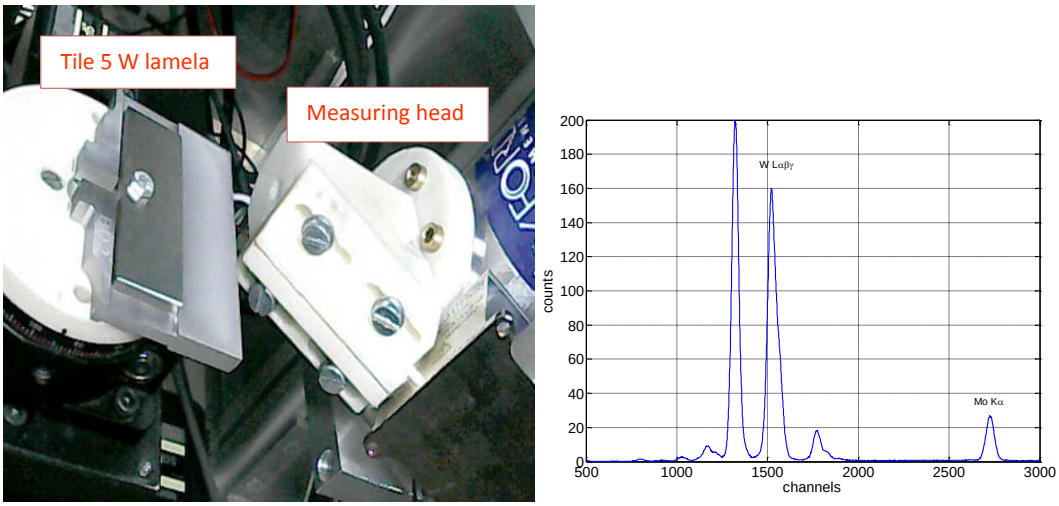

Figure 11 –Tungsten measurement - lamelas - experimental setup (left), utilization of Mo markers for in situ W erosion measurement by X-ray backscattering fluorescence (right)

The measuring technique takes advantage of the existence of a Mo interlayer (≈ 4-5 µm) under the tungsten layer of similar thickness. Figure 11 shows the experimental setup and a typical X-ray spectrum with the W $L_{\alpha\beta\gamma}$ characteristic lines and Mo K_α. The W thickness is related to the ratio of the Mo K_α peak area with and without tungsten coating.

For the preparation of the task included in the 2013 JET Technology working program we have optimized the mono-energetic X-rays used in the multi-energy transmission method. Existing samples of FGG and DMS780 CFC coated by W/Mo whiting the CMSII technique have been measured and the W and Mo thickness values were found to be in good agreement with the GDOS determinations.

In this case the calculations are even facilitated, for the same choice of secondary sources as before, because for Nb or Zr fluorescence X-ray energies the mass attenuation coefficient of Mo is notably different now of that of W (Figure above), and thus the computational difficulties met in the case of tungsten and Rhenium disappear.

The preliminary results of thickness measurement of W coating with Mo interlayer are presented in the table below. One notices a good agreement with the GDOS measurements.

Table 1 - W and Mo thickness measurements on FGG and DMS780 CFC samples.
The X-ray multi-energy transmission and the GDOS techniques give comparable results.

Sample	Substrate (mm)	W (µm)		W+Mo (µm)	
		GDOS	X-ray	GDOS	X-ray
IU 313 25 CFC	2.95	8.7	10.2	11.1	11.3
IU 313 27 CFC	2.90	9.0	9.6	11.5	12.1
IU 318 29 FGG	4.72	8.7	9.2	11.1	11.3

The very good agreement with the GDOS method gives us the confidence that we will be able to fulfil the 2013 task of post-mortem analysis of more than 20 samples of W/Mo coated CFC (ILW) type) which have been exposed in JET during 2011-2012 campaigns.

3.3 Morphological, compositional and structural characterization of the JET tiles

Methods addressing the properties of deposited mixed layers, such as morphology, composition, structure and chemical states, were used to study selected samples from the JET divertor tiles exposed to the plasma experiments. The results obtained using scanning electron microscopy (SEM), energy dispersive spectroscopy (EDS), X-ray diffractometry (XRD and GXRD), electron scattering for chemical analysis (ESCA) (X-ray photoelectron spectroscopy – XPS) and X-ray fluorescence (XRF) techniques were compared with those obtained by secondary ion mass spectrometry (SIMS).

Altogether 19 samples originating from the inboard divertor tiles (1, 4, 5, 6) exposed in 2007-2009 and 2004-2009 were analyzed. Particular attention was paid to C, Be, BeO, Be_2C, BeNi Cr, Fe, Ni, Cu phases on the samples. Due to the specific history of the experiments the layered structure of the deposited films was highlighted. Because the intermetallic compound, BeNi, was identified in the analyzed samples, was prepared an experiment using TVA technique in order to highlight the experimental conditions for the formation of this compound. A separate experiment was performed using simultaneous deposition of Be and Ni on silicon and fine grain graphite substrate by thermionic vacuum arc (TVA) method. As conclusion of this experiment was found that when Be is in excess in the film, the beta phase (BeNi) is dominant together with Ni phase (at Ni concentration larger than 50at%), or a solid solution BeNi-Ni.

The XRD and XPS analysis of the samples showed that the plasma significantly changes the phase structure of the wall material, producing new compounds which affect, e.g., the sputtering rates and fuel retention. The Cr, Fe, Ni, Cu impurities were identified and quantified using XRF technique up to a space resolution of ~20 µm. The analyzed mixed materials had a high Be/C ratio near the bottom of the tiles while they were also enriched in Cr, Fe and Ni from the Inconel present in the JET vessel wall and from internal metal fittings, bolts etc.

Correlation of the ESCA, XRD, XRF and SIMS analyses are presented in Figure 12. ESCA method provide the chemical bonding shift of the elements and compounds revealing the formation of Be near the top surface of the layers and metallic Be deep inside the film, XRD shows the cristallografic structure of the pure elements and compounds, highlighting the formation of Be2C and BeNi compound during device operation as well as the graphitic phase of the redeposited carbon layers. XRF provided a quantitative analysis of the heavy elements permitting to obtain a poloidal distribution of the impurities. SIMS is a very sensitive (non-calibrated) method that reveals the presence of light and heavy elements.

The poloidal distribution of the Cr, Fe, Ni, and Cu impurities was plotted in Figure 13. One can observe the high concentration of Ni in the sample G1A-11, where BeNi formation was identified.

	ESCA	XRD	XRF	SIMS
G1 A-2	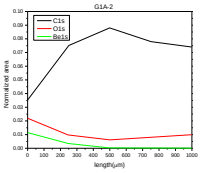	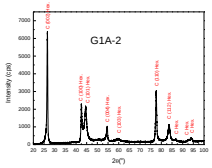	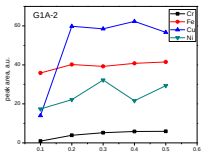	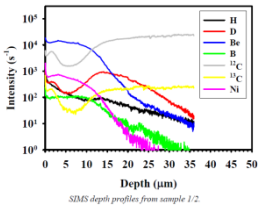
	Elements: Be, C, O	Elements: C	Elements: Cr, Fe, Ni, Cu	Elements: H, D, Be, B, C, Ni
G1 A-5	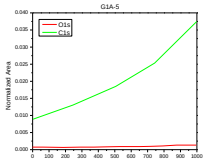	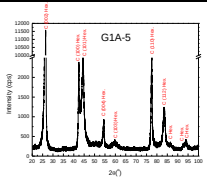	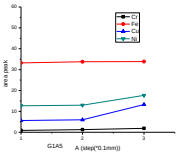	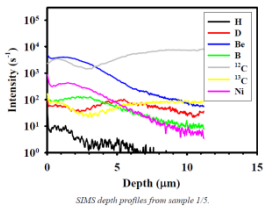
	Elements: O, C	Elements: C	Elements: Cr, Fe, Ni, Cu	Elements: H, D, Be, B, C, Ni
G1 A-11	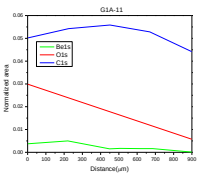	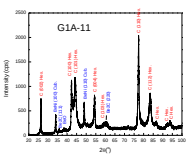	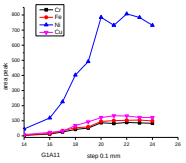	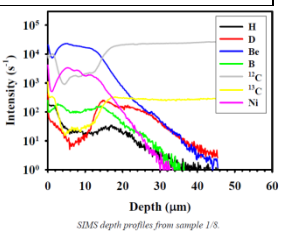
	Elements: Be, O, C	Elements, compounds: C, BeNi, BeO, Be_2C	Elements: Cr, Fe, Ni, Cu	Elements: H, D, Be, B, C, Ni

Figure 12 - Correlation between ESCA, XRD, XRF and SIMS analyses on the 2IG1A (2, 5 and 11) samples.

Elements and compounds identified by ESCA, XRD, XRF and Ion beam analysis (RBS): Be, C, Ni, Cr, Cu, O, BeO, BeNi, Be_2C

Elements identified by SIMS: H, D, Be, ^{12}C, ^{13}C, Ni

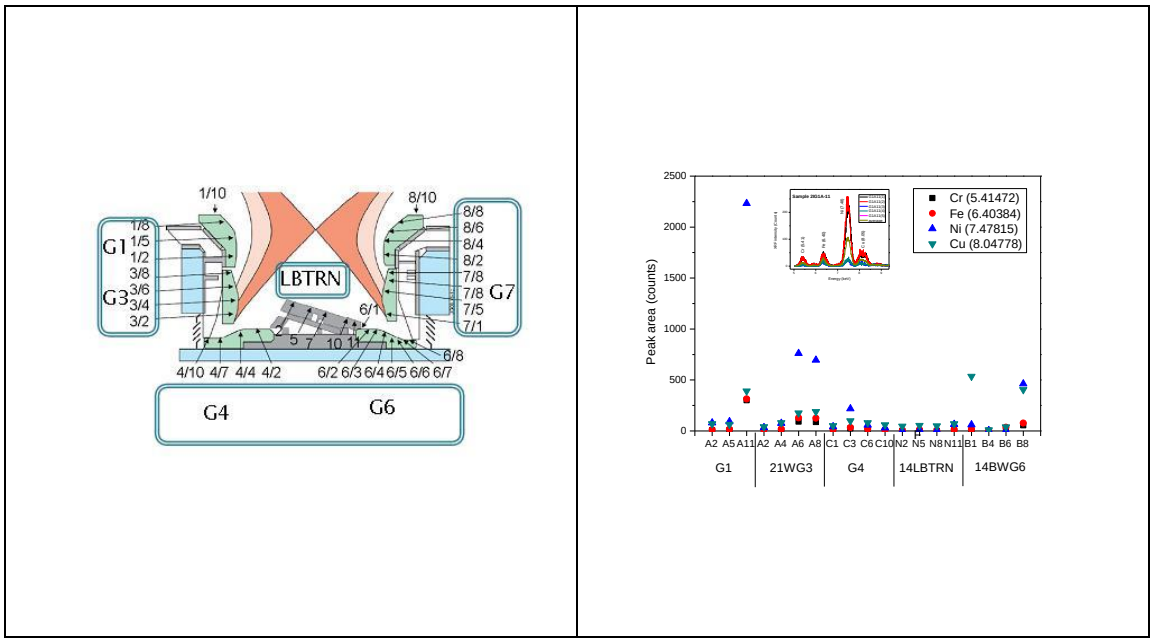

Figure 13 Poloidal distribution of Cr, Fe, Ni, Cu impurities

4. Conclusions

Following the extensive optimization works performed in the first reporting period of the contract a number of investigations have been carried out:

- Post-mortem coating thickness measurements of samples from the W-coated JET outer divertor tiles 7 and 8 (exposed in 2007-2009).
- Comparison of the W thickness values obtained by SEM imaging and RBS.
- Elaboration of calibration samples and calibration methods for the ILW CFC tiles. Samples with different W thicknesses that have been produced in MEdC in the same conditions as the ILW tiles. The X-ray fluorescence thickness results will be correlated with the thickness measurement by other methods (GDOES and SEM).
- Using SEM, EDS, XRF, XRD, GXRD and ESCA investigation methods, the samples cut form the 1, 4 and 5 CFC divertor tiles were characterized. Were found the elements deposited on the tiles due to the erosion produced during tokamak device operation.
- The XRD and XPS analysis of the samples showed that the plasma significantly changes the phase structure of the wall material, producing new compounds which affect, e.g., the sputtering rates and fuel retention. The Cr, Fe, Ni, Cu impurities were identified and quantified using XRF technique up to a space resolution of ~20 µm. The analyzed mixed materials had a high Be/C ratio near the bottom of the tiles while they were also enriched in Cr, Fe and Ni from the Inconel present in the JET vessel wall and from internal metal fittings, bolts etc. The poloidal variation of

the Cr, Fe, Ni, Cu impurities was obtained. The formation of compounds were also pointed out: BeO, Be_2C, BeNi.

Acknowledgement

The reported work includes contributions from the following people outside the EUATOM-MEdC Association: J. Likonen, A Hakola (*VTT Helsinki, Finland*).

References

[1] Ion Tiseanu, et al. *Surface & Coatings Technology* ***205*** *(2011) S192–S197,* doi:10.1016/j.surfcoat.2011.03.049

[2] G. Musa, H. Ehrich, M. Mausbach, J. Vac. Sci. Technol. A 12(5), 2887-2895, 1994.

[3] http://www.kayelaby.npl.co.uk/

[4] Tiseanu I. et al. Fusion Engineering and Design, Vol. 86, Issue 9-11, October 2011, Pages 1646-1651

[5] http://physics.nist.gov/PhysRefData/XrayMassCoef/tab3.html

[6] E. B. Saloman, J. H. Hubbell and J. H. Scofield Atomic Data and Nuclear Data Tables **38**, 1-197 (1988)

[7] C. P. Lungu, I. Mustata, G. Musa, V. Zaroschi, A. M. Lungu and K. Iwasaki: Vacuum, 76 (2004), 127.

[8] C. P. Lungu, I. Mustata, G. Musa, A. M. Lungu, V. Zaroschi, K. Iwasaki, R. Tanaka, Y. Matsumura, I. Iwanaga, H. Tanaka, T. Oi, K. Fujita, Surf. and Coat. Techn., 200, (2005) 399.

[9] I. Tiseanu, et al., *Proc. of Fachtagung Prozessnahe Röntgenanalytik*, PRORA 2009, Berlin, Germany, 2009.

[10] I. Tiseanu, et al. *Surface & Coatings Technology* ***205*** *(2011) S192–S197,* doi:10.1016/j.surfcoat.2011.03.049

[11] A. Bjeoumikhov et al. 2005 *Rev. 292 Sci. Instrum.* ***76*** *063115-1.*

A STRIKING EFFECT OF FUEL RETENTION IN PROTECTION TILES OF TOKAMAK VESSELS

C. Stan-Sion [1], G. Kizane [2], M. Enachescu [1], J. Likonen [3], N. Bekris [3], P. Batistoni [3]

[1] *Horia Hulubei National Institute for Physics and Nuclear Engineering, 077125 Bucharest, Romania, Association Euratom - MEdC*

[2] *Institute of Chemical Physics, University of Latvia, Association Euratom - AEUL*

[3] *VTT Technical Research Centre of Finland, Association Euratom-Tekes, Finland*

[BS_17/FT-12-1.20 MEdC_AEUL_TEKES]

Abstract

The work presents complete depth profiling distributions of tritium retention in the divertor carbon tiles from JET, revealing an unexpected accumulation at the back side of the protection tiles. Experimental data were measured independently and confirmed by two different experimental techniques: Accelerator Mass Spectrometry and Full Combustion followed by scintillation detection of tritium. The enhanced accumulation of tritium on the back side of the tile in comparison to the bulk was measured to by more than 3 orders of magnitude.

1. Introduction

So far, the best achieved magnetic configuration to perform a controlled fusion reaction is the tokamak. Today, in order to finalize the construction of the first International Thermonuclear Reactor (ITER) in Cadarache-France, there is a high and special interest for the research performed at the Joint European Torus (JET) that is the biggest testing fusion device.

As the heavier isotopes of hydrogen are supposed to be fuels of the process, namely deuterium and tritium, this retention must be avoided by all means. The Fusion Technology team at JET has investigated various methods to prevent, recover and analyze tritium in a variety of plasma facing materials. In order to withstand the huge temperature during the fusion reactions, the JET vessel was lined up with carbon tiles. However, they are retaining all particles participating in the reaction. Tritium retention and removal in JET [1-6] has been extensively reported.

During 2009-2011, JET has been completely equipped with beryllium and tungsten materials that cover the plasma facing side of the carbon tiles and to reduce the retention of hydrogen isotopes. The use of tungsten PFC's would avoid this issue and tungsten is planned as an alternative for ITER.

This paper describes a striking effect of the fuel retention in the protection tiles of the JET divertor system, where the thermal and dynamic encumbrances are, by far, smaller than in the mid plane of tokamak vessel.

2. Experimental

In the past 10 or more years, the measurements of tritium retention in plasma facing components (PFC) have been performed by two different experimental methods: the full combustion (FC) [7-9] method followed by scintillation spectrometry and the Accelerator Mass Spectrometry (AMS) [10-13]. Both methods are highly effective and sensitive in measuring the tritium content in carbon samples and have been used in many applications for fusion experiments.

Investigations of the tritium retention in protection tiles extending over the entire or almost the entire thickness are rare since it was believed that the tritium concentration has its peak on the surface and drops rapidly towards inside of a tile [14].

The present research, when started, didn't have the primordial goal of determining the tritium retention in the tiles. It was meant to determine the detritiation of divertor tiles by laser ablation and also to establish a comparison between the two experimental methods in performing depth profiling of the tritium concentrations.

Since AMS and FC require for their analyzes samples of reduced size these were cut from the divertor protection tile 14ING3B as cylinders with diameters of 16 mm and then, the hollow cut samples were cut into 1 mm thick slices (see Figure 1). To emphasize that AMS is measuring continuously the concentration of the element into the depth and its resolution can be varied from few nanometers to several micrometers. This is due to the fact that the samples to be analyzed are loaded into the ion source of the AMS machine and are collided by a ^{133}Cs accelerated ion beam to produce by sputtering negative ions from the sample material. Depending on the elapsed time, the sputtered particles are extracted from a progressively larger depth of the produced crater in the sample. The detector, placed at the end of the AMS analyzing system, will register the concentration depth profile by counting the atoms one by one.

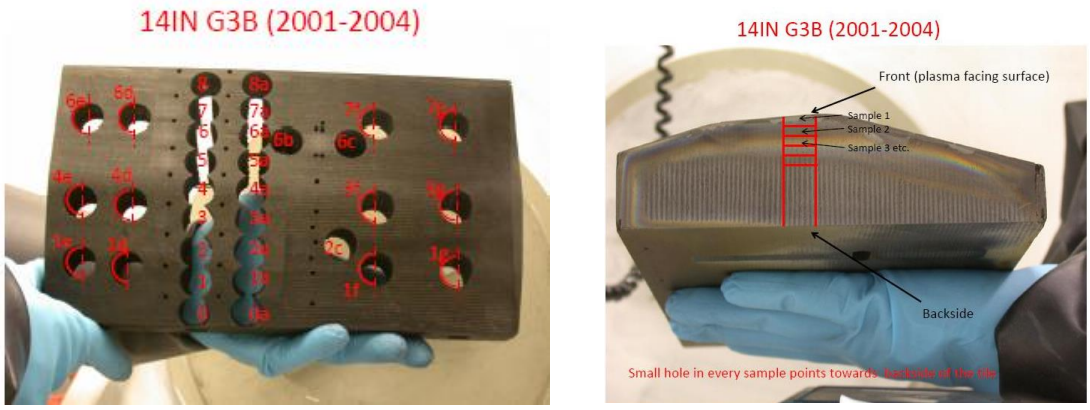

Figure 1 - The 14 IN G3B 2001-2004 divertor tile and the various locations of the cuts. The right half part is the laser treated (detritiated) surface. The corresponding drilled cylinders for the AMS and FCM measurements are 7f, 3f and 1f. While the non-detritiated cylinders 4e and 6e were extracted from the left side of the tile.

After the experiment the time scale is converted to depth by using optic profilometry that measures the depth and form of the produced crater. These data will also be used to calculate the correction of rim effects contained in the depth profile.

On the other hand, the FC measures the beta decay of tritium for the event detection. However, in order to avoid absorption of the low beta energy (average energy 5.9 keV) in the carbon or beryllium hosts, FC will first combust the entire sample material and then capture the tritium in water. This liquid solution will be introduced into a scintillation detector. In this way, the measured tritium concentration will reveal an average value over the entire mass of the sample and will be expressed in Bq/g. The thickness of the slices determines the depth resolution of FC measurement.

In order to compare the results of the two methods, one the AMS measured values have to be convert from atoms/cm3 to atoms/cm^2 (by integrating the depth profile concentration over the thickness value of the slice (1mm) and then to Bq/g.

Finally, since both experimental analyzing methods are relative methods they use for calibration standard samples [15].

Figure 2 (a, b, c, d, e) presents the averaged results of AMS and FC of the integrated depth distribution of tritium retention in five cylinders (1f, 3f, 7f, 4e, 6e) drilled from tile *14ING3B of the JET* divertor*. The integration interval of the experimental data was 1 mm.* The distributions show pronounced increased tritium retention at the end (bottom) of the tile.

Cylinders 1f, 3f and 7f were drilled form the same half-side of the tile shown in Figure 1 and that part was exposed to tritium removal procedure by laser ablation. Regardless the amount of the removed tritium from the tile surface (92%) all five cylinders have the same trend of the T- depth profile: 1) a maximum of the tritium concentration is at the surface of the tile ; 2) then follows an exponential decrease towards the bulk ; 3) the T-concentration remains at a low value for more than 30-40 mm inside of the tile; 4) finally, a peaking of the tritium retention occurs in the last 1mm of the tile. The enhanced accumulation of tritium on the backside of the PFC was clearly determined by the two analyzing methods in all performed measurements.

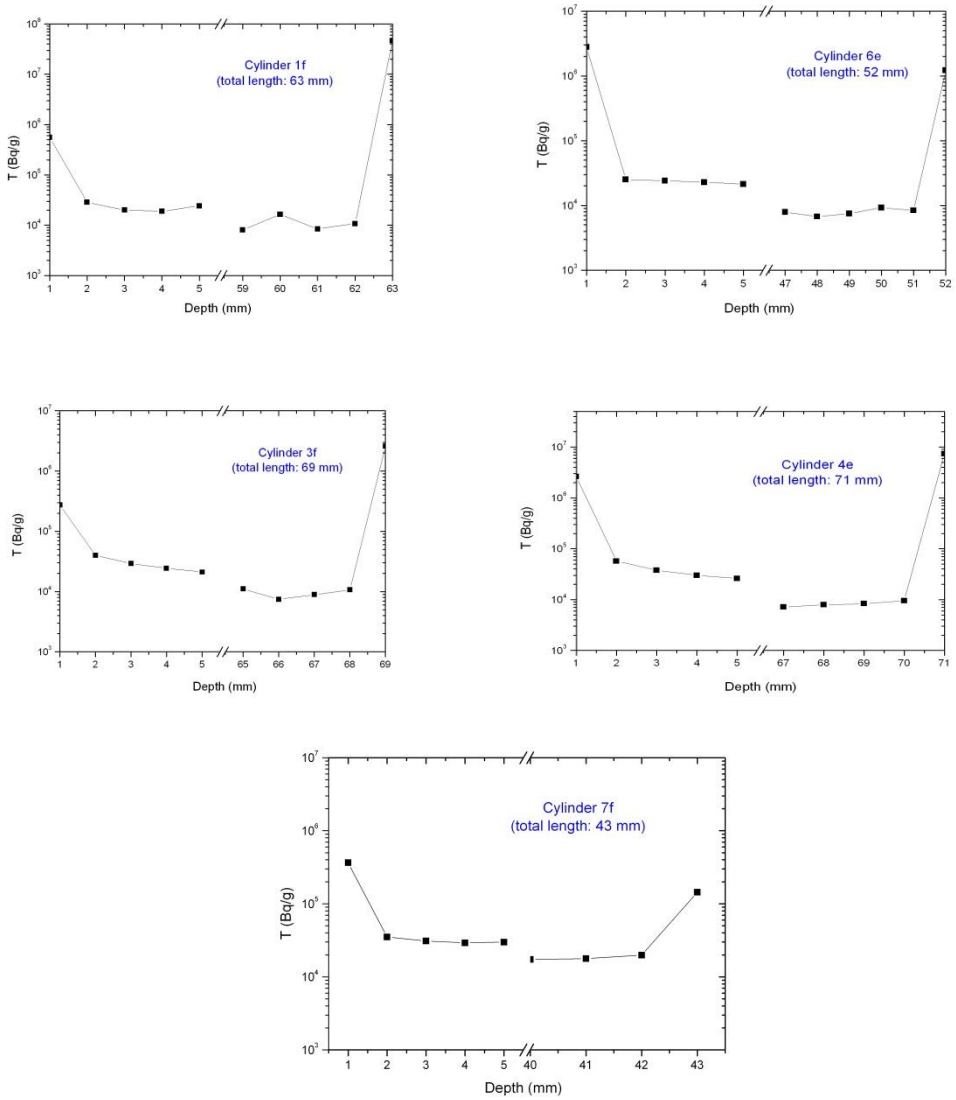

Figure 2 - The depth profiles of tritium accumulation in divertor tile 14ING3B (2001-2004) as measured in five drilled different cylinders (1f, 3f, 7f, 4e, 6e). Since the tile has a saddle-*like shape. The heights of the drilled cylinders are different, extending between 43 to 71 mm. In each of the spectra the first point was measured from the surface slice and the last point from the back side last 1 mm slice.*

As can be seen from Figure 1 the divertor tile has a saddle type shape of the plasma facing surface and therefore some of the drilled cylinders are longer than the others. The tritium accumulation measured in the backside of long cylinders (h = 60-75 mm, 1f, 3f, 4e) is about 3 orders of magnitude higher than the average concentration in the bulk. However, shorter cylinders (h = 40-55 mm, 7f, 6e) have a lower the tritium accumulation. For example, the thickness of cylinder 7f is only 43 mm and was drilled from the curved region of the tile that is also shadowed in respect to the plasma flux. It has a low input of tritium but also the relative accumulation in back is smaller.

In order to compare the retention effect in the different drilled cylinders (different locations) from the *14ING3B* tile, in Figure 3 we present a plot were all tritium retention values were represented on an arbitrary depth scale.

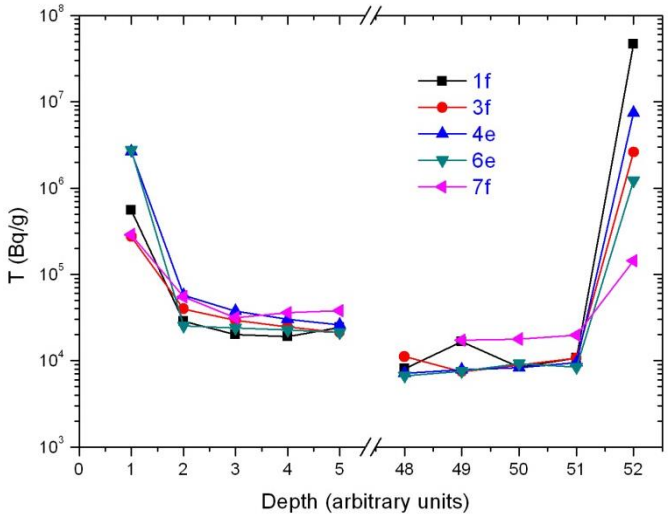

Figure 3 - Comparison of tritium retention distributions in the 14ING3B tile

The tritium removal by laser ablation of the tile has no consequences on the tritium retention or on the amount of the retained tritium quantity in the back side of the tiles. This is obviously due to the detritiation that is performed after the tiles are exposed to the tritium fluxes. For the same reason the bulk values are also similar. The only persuading dependence remains that on the width of the tile.

Similar behaviour of enhanced tritium accumulation was measured also for tile G1 and G8 of the same MkII-HD divertor of JET and looks to be e general trend.

It is known that gaseous hydrogen can penetrate deeply or permeate through a graphite tile. The retention of tritium is strongly dependent on temperature [16]. Diffusion of gas tritium becomes dominant above 800 K. Therefore, migration of the molecular tritium steaming from the gas fuel might be main responsible for the observed accumulation. A contribution could also come from the edge plasma producing a high localized co-deposition of the hydrogen isotope on shadowed areas with low surface temperatures as the inner divertor itself. The supplementary heating from the laser ablation was not producing a noticeable effect.

The backsides of the divertor graphite tiles are fixed on water cooled base plates and in JET were very likely at a temperature below 500 K. The hydrogen isotopes coming to this region of the tile will be trapped and the back side region will be saturated by tritium. The effect could be very much like that in the surface region were at a temperature below 550 K the saturation H/C is about 0.4 and the

hydrogen diffusion stops. If this saturation effect on the backside of the tiles is responsible of the severe increase of tritium accumulation, a simple way would be to warm up the base plate and to perform an aspiration of the tritium in excess.

Tungsten coating for the divertor porous graphite tiles (carbon fiber composite structure) of fusion devices are meant to contribute to the reduction of the hydrogen retention. However, the tungsten coating will only reduce the tritium accumulation and retention in a tile but will not be able to eliminate it.

3. Conclusions

The tritium retention in the MkII-HD divertor protection tiles of JET tokamak was experimentally investigated by the FC and by the AMS analyzing methods. All measured data from tile *14ING3B* obtained in this work have clearly shown an enhanced accumulation of tritium on the back side of the tile in comparison to the bulk by more than 3 orders of magnitude.

Since these tiles are made by a porous carbon material (CFC structure) tritium molecules and in general the molecular hydrogen can penetrate along open pores reaching the end of the tile width. At temperatures below 500K the tritium becomes trapped in the carbon structure and accumulation runs to saturation in those regions. The water cooled base plate and the shaft supporting the protection tiles could be the reason of the observed effect.

The tritium inventory may be reduced significantly if the temperature of the back side area of the tile would be kept or be changed temporary only at a temperature above 1000 K together with a powerful action of evacuation pumps contributing to the degassing of the tritium vapors.

References

[1] L. C. Alves, E. Halves, N. P.Barradas, R. Mateus, P.Carvalho, J. P.Coad, A.M. Widdowson, J.Likonen, S. Koivuranta, Nucl. Instrum. Methods Phys. Res., Sect. B 268 (2010) 1991 – 1996.
[2] M. Rubel, J. P. Coad, J. Likonen, V. Philipps and JET EFDA contributors, Nucl. Instrum. Methods Phys. Res., Sect. B 267 (2009) 711 – 717.
[3] P. Paris, M. Aints, M. Laan, M. Kiisk, J. Likonen, J. Kolehmainen, S. Tervakangas, Fusion Eng. Des. 84 (2009)1465 – 1467.
[4] J. Likonen, J.P.Coad, D.E. Hole, S. Koivuranta, T. Renvall, M. Rubel, E. Vainonen-Ahlgren, A. Widdowson and JET EFDA contributors, J. Nucl. Mater. 390 - 391 (2009) 631 – 634.
[5] A. Widdowson, J.P. Coad, D. Farcage, D. Hole, J. Likonen, T. Renvall, A. Semerok, P.-Y. Thro and JET EFDA contributors, Fusion Sci. Technol. 54 (2008) 51 – 54.
[6] J. Likonen, E. Vainonen-Ahlgren, L. Khriachtchev, J.P. Coad, M. Rubel, T. Renvall, K. Arstila, D.E. Hole, Contributors to the EFDA-JET, J. Nucl. Mater. 377 (2008) 486-491.
[7] R.-D. Penzhorn, N. Bekris; U. Berndt, J.P.Coad, H. Ziegler, W. Nägele, J. Nucl. Mater. 288 (2001) 170-178.
[8] M. Friedrich, W. Pilz, G. Sun, R. Behrisch, C. Garcia-Rosales, N. Bekris, R.-D.Penzhorn, Nucl. Instrum. Methods Phys. Res., Sect. B 161-163 (2000) 216-220.
[9] M. Friedrich, W. Pilz, G. Sun, R. Behrisch, C. Garcia-Rosales, N. Bekris, R.-D. Penzhorn, Nucl. Instrum. Methods Phys. Res., Sect. B 172 (2000) 655-658
[10] C. Stan Sion, R. Behrisch, J. P. Coad, U. Kreissig, F. Kubo, V. Lazarev, S. Lindig, M. Mayer, E. Nolte, A. Peacock, R. Rohrer, J. Roth, J. Nucl. Mater. 290-293 (2001) 491-495.
[11] C. Stan-Sion, L. Rohrer, P. Hartung , V. Lazarev, R.Luther, E. Nolte, R. Behrisch, J. Roth, Nucl. Instrum. Methods Phys. Res., Sect. B 192 (2002) 331-338.
[12] C. Stan-Sion, J. Roth, K. Krieger, M. Enachescu, K. Ertl, V. Lazarev, H. Reithmeier and E. Nolte, Nucl. Instrum. Methods Phys. Res., Sect. B 259 (2007) 694-701.
[13] M. Dogaru, M.A.Calin, C.Stan-Sion, J. Radioanal. Nucl. Chem. (2011) DOI 10.1007/s10967-011-0981-6.
[14] C. H. Skinner, N. Bekris, J.P. Coad, C.A. Gentile, M. Glugla, J. Nucl. Mat. 313-316 (2003) 496-500.
[15] C. Stan-Sion, Mihaela Enachescu, I. Dorobantu, R. Behrisch and C. Postolache University Politehnica of Bucharest Scientific Bulletin, Series A: Applied Mathematics and Physics, Volume 66, Number 2-4, (2004) Pages 95-102.
[16] T. Tanabe, N. Bekris , P. Coad , C.H. Skinner , M. Glugla, N. Miya, J. Nucl. Mater. 313–316 (2003) 478–490.

UPGRADE OF THE JET TANGENTIAL GAMMA-RAY SPECTOMETER (KM6T)

Sorin Soare, Marian Curuia
EURATOM-MEdC Association, National Institute for Cryogenic Technologies and Isotopes Separation, Rm. Valcea
[BS_15.1/JW09-TA-EP2-TCS-02]

Abstract

The main objectives of the project "Tandem Collimators for the Gamma-Ray Spectrometer" (JET code TCS), were the design, construction and testing of a gamma-ray diagnostics configuration consisting of two neutron and gamma-ray collimators. The project started due to the necessity to regain the full operation capability and to extend the diagnostics capability of the gamma-ray spectrometer (affected by the removal of nearby equipment that coincidentally/also acted as a shield for gamma-ray and neutrons) for high power DD and DT discharges. The collimators were designed to work in tandem, defining the field-of-view at the source end (plasma) of the diagnostics line-of-sight. The collimators have been built, delivered and installed at JET. The collimators have been surveyed (individually and as a system) and the alignment was considered acceptable.

In preparation for the validation experiments, some work was needed to be done regarding the geometry of the actual configuration. Two sets of recorded data had to be compared:

- an old set, obtained with the KJ5 pre-collimator (removed) without the TCS system
- a new set of results, obtained with the TCS system.

Moreover, the old results were obtained with the Carbon wall in place as opposed to the new results obtained with the new Be wall.

Papers

[1] Vasile Zoita, Sorin Soare, Teddy Craciunescu, Marian Curuia, Vasily Kiptily, Nick Balshaw, Patrick Blanchard, David Croft, Andrea Murari, Brian Syme, JET-EFDA contributors, Definition of the radiation fields for the JET gamma-ray spectrometer diagnostics, Fusion Engineering and Design, In press, corrected proof, 2013

Conferences

[1] Vasile Zoita, Sorin Soare, Teddy Craciunescu, Marian Curuia, Vasily Kiptily, Nick Balshaw, Patrick Blanchard, David Croft, Andrea Murari, Brian Syme, JET-EFDA contributors, Definition of the radiation fields for the JET gamma-ray spectrometer diagnostics, 27th Symposium on Fusion Technology (SOFT) September 24-28, 2012, Liege, Belgium

Reports

[1] S. Soare, N. Balshaw , P. Blanchard, D. Croft, M. Curuia, G. Kaveney, V. Zoita, Tandem Collimator System (KM6T-TC), Installation Report, FEB. 2012
[2] T. Craciunescu, V. Kiptily, S. Soare, V. Zoita, Tandem Collimators for gamma-ray Spectrometer (TCS), Commissioning of the tandem collimators for the KM6T tangential gamma-ray spectrometer, 2012
[3] S. Soare, N. Balshaw , P. Blanchard, T. Craciunescu, V. Kiptily, V. Zoita, Tandem Collimators for the gamma-ray Spectrometer (TCS), Final Project Report, June 2012

Detailed results

KM6T TC installation

The collimators axis is coincident with the KX1 beam line, the front collimator being placed at 1.3 m from the Octant 8 vacuum port and the rear collimator 4.5m behind the front collimator, Figure 1.

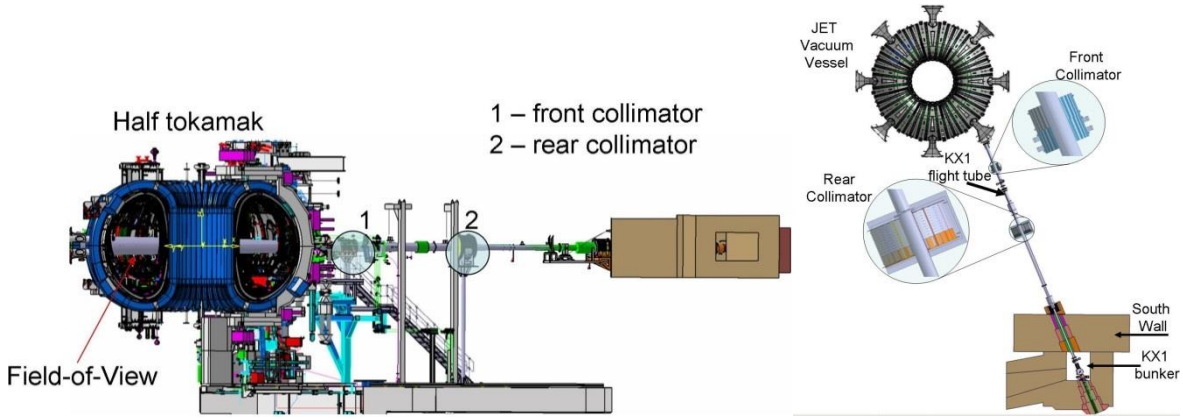

Figure 1 - Locations of KM6T Tandem Collimators - side view and mid-plane section

Front collimator

The front collimator defines the spectrometer field of view at the plasma end of the line-of-sight. Its dimensions (outer diameter and length) have been determined in terms of the available space in front of the Octant 8 vacuum port. The front collimator acts as a shield for both the neutron and gamma radiation. It uses polyethylene plates for the neutron shielding and lead plates for the gamma-ray shielding.

Rear collimator

The rear collimator defines (by its external diameter) the horizontal (toroidal) and vertical (poloidal) extent of the shielded neutron and gamma-ray filed-of-view seen by the BGO gamma-ray detector. The thickness of the rear collimator is determined by the necessary amount of material needed to shield the BGO detector from the neutron (2.45 MeV) and gamma radiation (9 MeV). The rear collimator is made up of polyethylene plates for the neutron shielding and lead plates for the gamma-ray shielding.

The two components of the KM6T-TC (Front & Rear Collimators) have been installed during Dec. 2011 (Front Collimator) and January 2012 (Rear Collimator) by JOC, Figure 2.

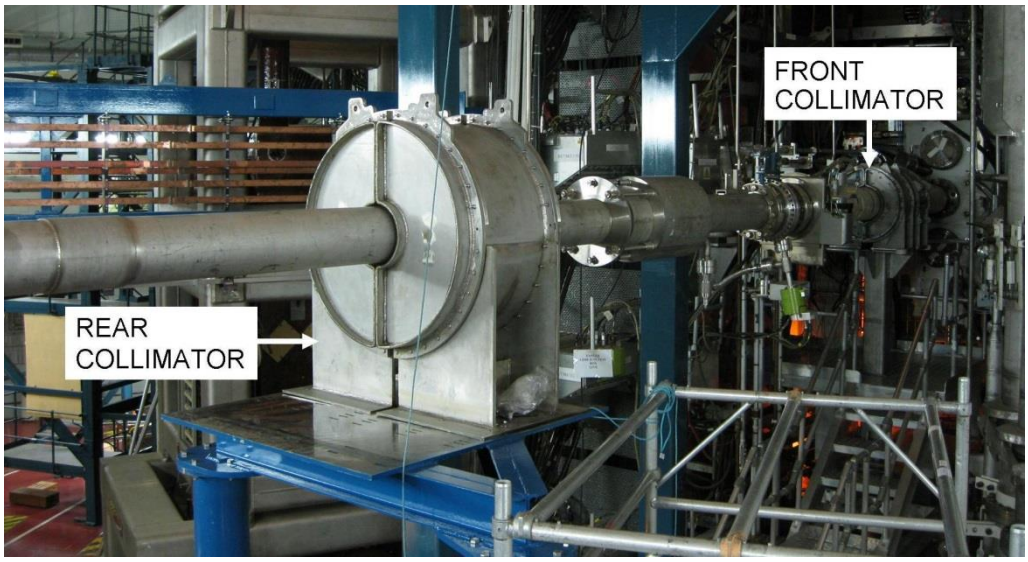

Figure 2 - Tandem Collimators system installed

Each installed collimator was surveyed independently; sections of KX1 beam line adjacent to the collimators were targeted as well:

- survey SX 1978036_FC_on_KX1BeamLine for the Front Collimator (Annex 1); KX1 beam line section surveyed starts at the MHVP flange and ends at the nest flanged connection (cca. 3m section); FC is positioned half-way from these reference points, Figure 3.

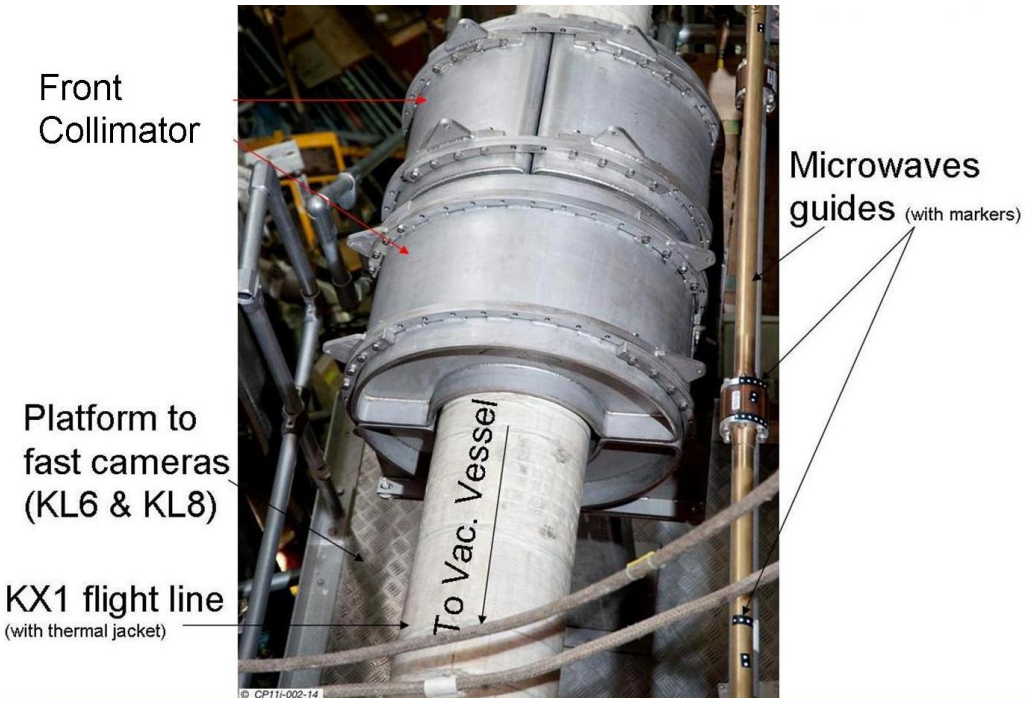

Figure 3 - Front Collimator installed

- survey SX 1978054_A_KM6T_RearCollimator for the Rear Collimator (Annex 2); KX1 beam line section surveyed extends less than one meter from the back face of RC; RC is positioned just behind the flanged connection with the KX1 first beam line section with bellow, Figure 4.

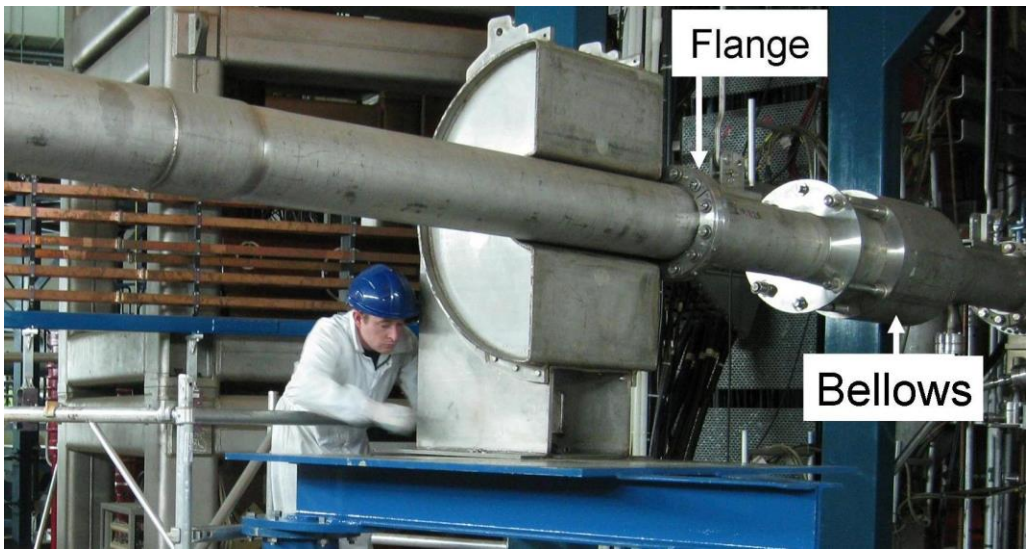

Figure 4 - Elements along KX1 pipe next to the Rear Collimator

Data produced during these surveys were converted into .igs file for a later use.

These surveys were then compared with data from survey SX_1977225_KX1_TORUS carried out with targets placed on vacuum port flange and on wall penetration flange along KX1 beam line (machine temperature 200deg.C) during 2007. The axis produced by the survey data was used as design axis for the Tandem Collimator system (Line-of-Sight axis). Later it was confirmed by a similar survey (SX_1978040) carried out during 2011.

2. Alignment check of installed Front Collimator

The Front Collimator CATIA model was loaded and superimposed with the .igs file produced by the survey. The survey-determined axis was extended to the BGO detector and then compared with the design LoS axis. At the Front Collimator position the superposition of CATIA model and .igs file shows the following, Figure 5:

- FC survey (SX1978036) with respect to KX1 at 200degC axis (SX1978040):

  - at MHVC end: 3.7mm;
  - at the opposite end: 22.08mm
  - deviation from the design axis at FC 0.381deg (divergent)

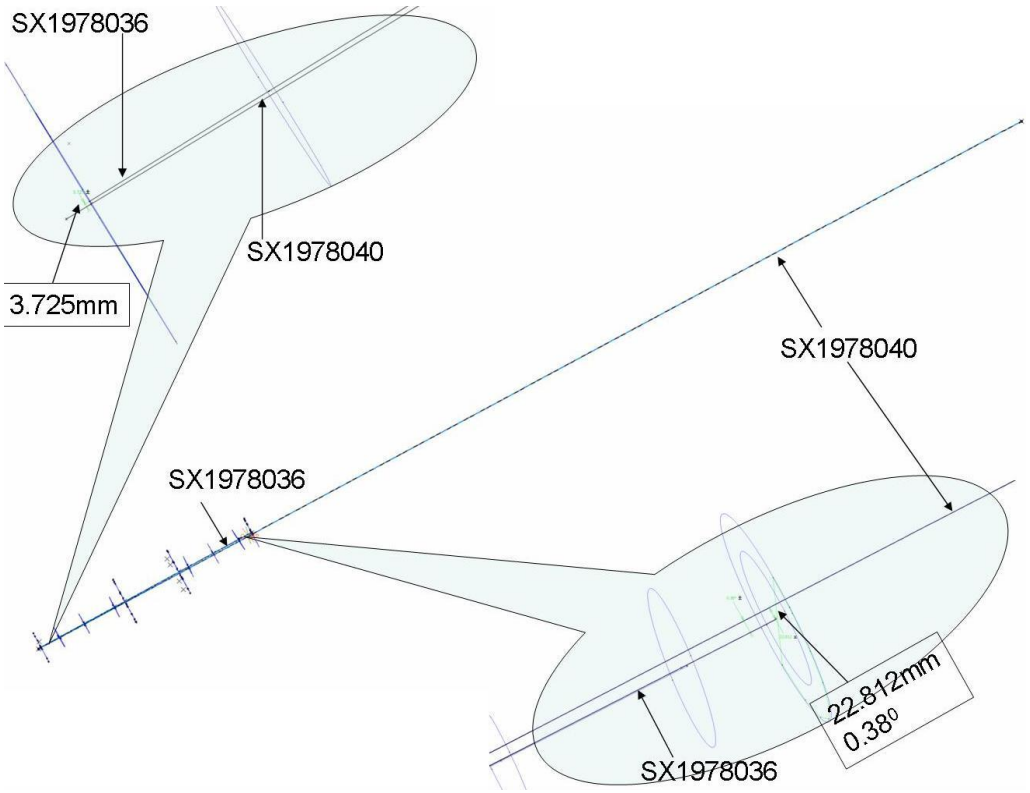

Figure 5 - Axis determined by FC survey and by KX1 Beam Line survey

Alignment check of installed Rear Collimator

The same procedure as that applied to the Front Collimator was applied to the Rear Collimator. At the Rear Collimator position the superposition of CATIA model and .igs file shows the following, Figure 6:

- RC survey (SX1978054_A_KM6TRearCollimator) with respect to KX1 at 200degC axis (SX1978040):

- at RC back face	6.9mm
- at RC front face	no data available
- deviation from design axis	0.49deg (convergent).

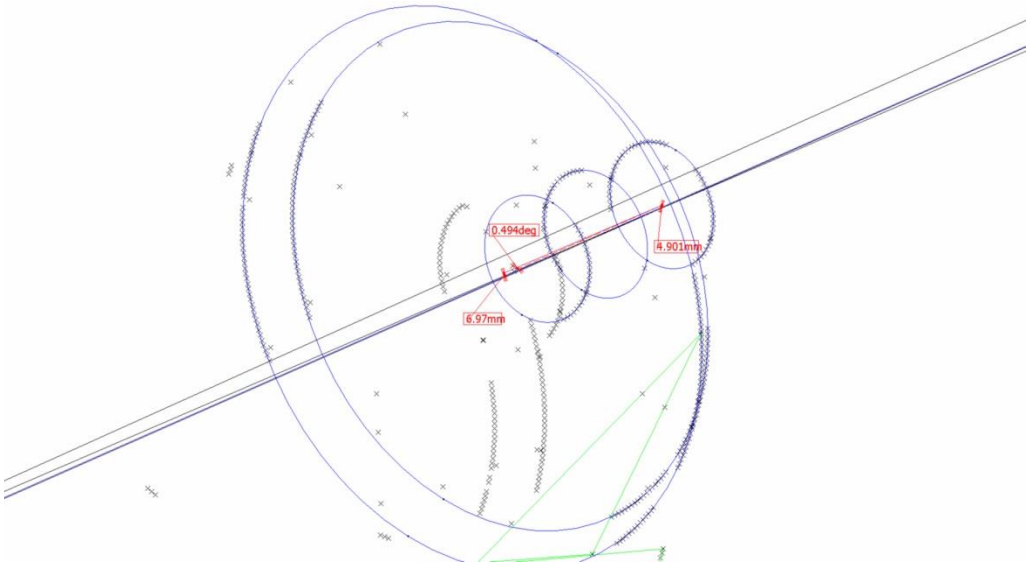

Figure 6 - Axis determined by RC survey and by KX1 Beam Line survey

At the BGO detector the extended axis of surveys SX1978036 (FC) and SX1978054(RC) show a maximum deviation of about 135mm for the FC axis, Figure 7:

The estimated deviations from the axis are acceptable compared with the cross-section of the collimator bore (diameter 244 mm).

Schematically, the system should define the two Fields of View shown in Figure 8 which is cross-section in the area were the first inner tokamak component falls into the tandem collimators fields of view, OCT 1 inner guard wall limiter. A plan-view section shows the Be components falling within the fields of view determined by the collimators.

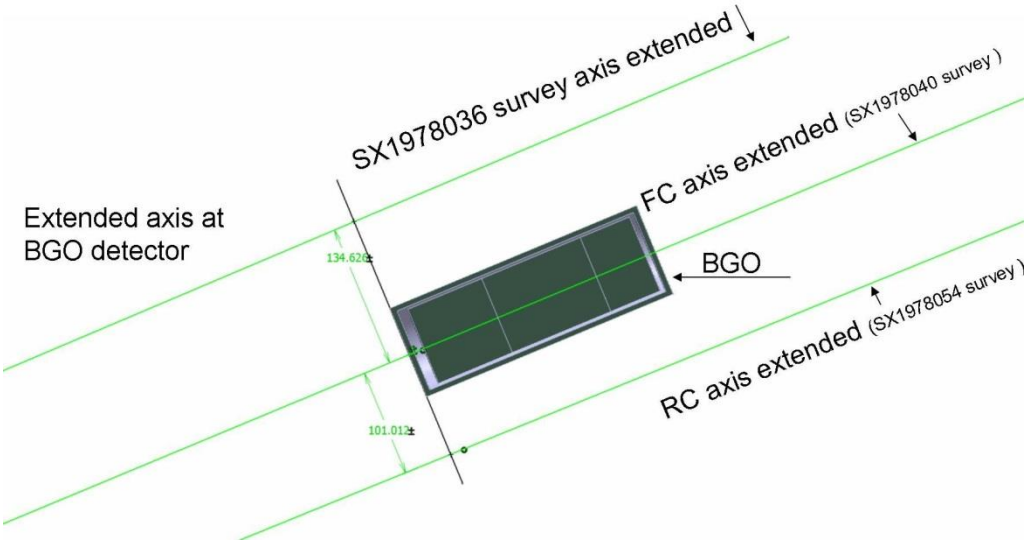

Figure 7 - Extension of axis (RC & FC surveys vs. design axis)

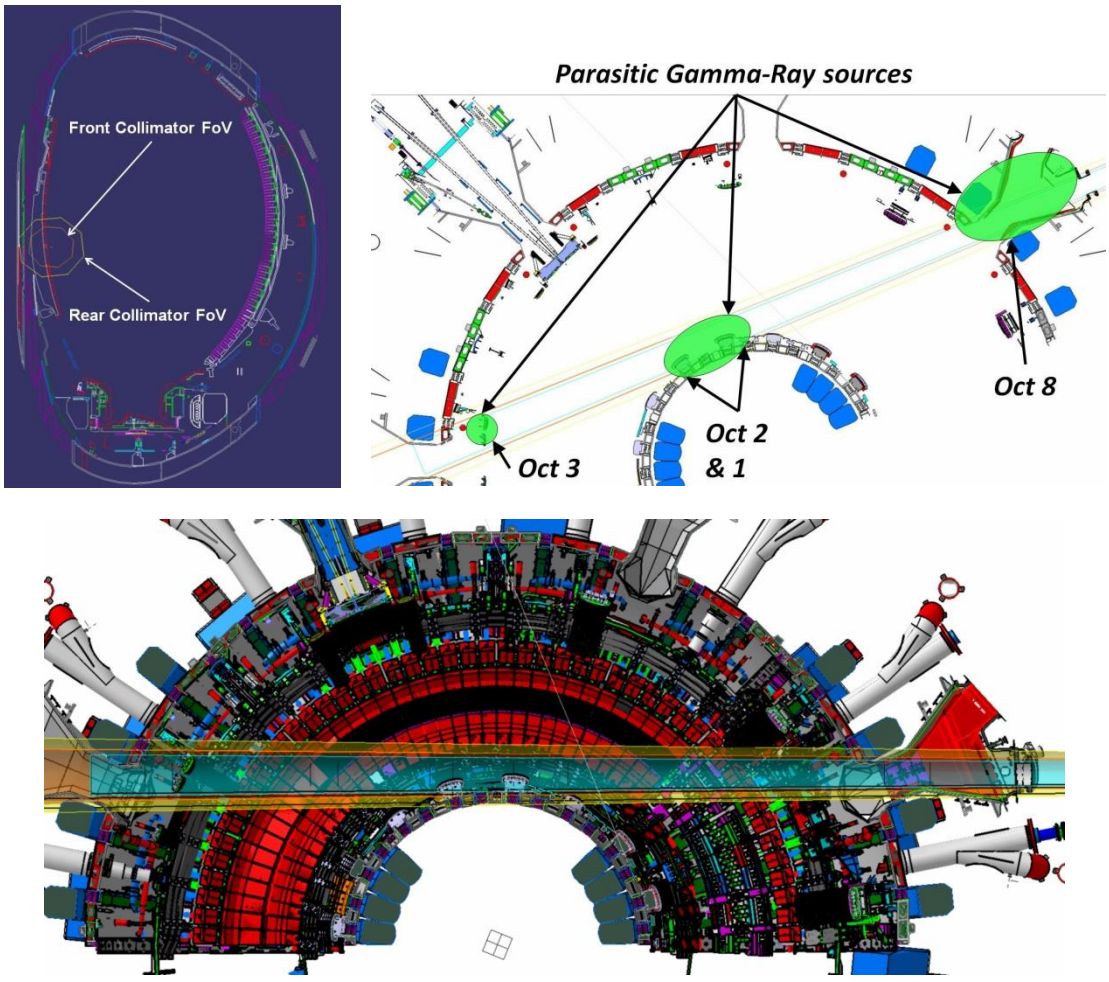

Figure 8 - Fields Of View determined & new components (Be) within the Fields Of View

Conclusions

The alignment of the KM6T Tandem Collimators is as good as we can get due to:

-component deformation during manufacturing

-limited access to place survey targets

-precision of the survey theodolite (mm)

The KM6T-TC models were transferred into CATIA SmarTeam. The only update will be in the axial position of the RC.

Extensive experiments were performed for the validation of the KM6T system. The experiments proved the improvement in the signal-to-background ratio. The results were included in the Commissioning Report which was approved at the Final Project Board

Acknowledgement

The reported work includes contributions from the following people outside the EUATOM-MEdC Association:

[1] Nick Balshaw, David Croft, Brian Syme, Vasily Kiptily (Association EURATOM-CCFE, Culham Science Centre, Abingdon, UK),

[2] Patrick Blanchard (EFDA-JET CSU Culham, Culham Science Centre, Abingdon, UK & Association EURATOM-CRPP-EPFL, Lausanne, Switzerland)

[3] Andrea Murari (EFDA-JET CSU Culham, Culham Science Centre, Abingdon, UK & Association EURATOM-ENEA, RFX, Padova, Italy)

UPGRADE OF GAMMA RAY-CAMERAS: NEUTRON ATTENUATORS

Marian Curuia[1], Mihai Anghel[1], Teddy Craciunescu[2], Mihaela Gherendi[2], Sorin Soare[1], Vasile Zoita[2]
[1] *National Institute for Cryogenics and Isotopic Technologies, Rm. Valcea, Romania*
[2] *National Institute for Laser, Plasma and Radiation Physics, Magurele, Bucharest, Romania*
[BS_7/JW06-TA-EP2-GRC-06]

Abstract

The JET gamma-ray cameras provide information on the spatial distribution of the interacting fast particles within the tokamak plasma.

The main objective of the Upgrade of gamma ray cameras neutron attenuators (GRC JET EP2) project is the design, construction and testing of neutrons attenuators for the two sub-systems of the KN3 gamma-ray imaging diagnostics: KN3 gamma-ray horizontal camera (KN3-HC-NA) and KN3 gamma-ray vertical camera (KN3-VC-NA). This diagnostics upgrade should make possible gamma-ray imaging measurements in high power deuterium JET pulses, and eventually in deuterium-tritium discharges.

The commissioning of KN3-NA system has been done in two steps: the first – engineering commissioning; and the second – complex experiments and analysis for KN3-NA system validation.

The reason for taking the first step was to ensure without a doubt that the entirely system works properly, both for the vertical attenuator and for the horizontal attenuator. A lot of tests, starting with mechanical tests and finishing with electrical tests, were performed for each attenuator. Also, the PLC-CODAS interface has been checked.

The second step of the commissioning of KN3-NA system has also been successfully performed. Complex and extensive experiments were performed for the validation of the neutron attenuator KN3-NA system. The neutron attenuation factors retrieved in the experiments are in agreement with values initially proposed, taking into account the additional technical constraints (port insulation thickness, thermal expansion, disruption displacements) which were imposed. It was clearly demonstrated that KN3-NA provides adequate n/γ filtering for deuterium experiments.

Papers

- Vasile Zoita, Sorin Soare, Teddy Craciunescu, Marian Curuia, Vasily Kiptily, Nick Balshaw, Patrick Blanchard, David Croft, Andrea Murari, Brian Syme, JET-EFDA contributors, Definition of the radiation fields for the JET gamma-ray spectrometer diagnostics Fusion Engineering and Design, http://dx.doi.org/10.1016/j.fusengdes.2013.01.083

Reports

- V. Zoita, T. Craciunescu, M. Curuia, M. Anghel, V. Kiptily, S. Soare, A. Fernandez, L. Giacommeli, I. Lengar, D. Kina, D. Falie, M. Gherendi, M. Riva, B. Syme, KN3-NA commissioning report, JET, 27 November 2012, .

Detailed results

1. Commissioning of the KN3-NA system

The commissioning of KN3-NA system has been done in two steps: firstly engineering commissioning and secondly complex experiments and analysis for KN3-NA system validation.

The reason for what the first step has been performed was to have doubtlessness that the entirely system both for vertical attenuator and for horizontal attenuator work properly. Complex tests starting with mechanical tests and finishing with electrical tests were performed for each attenuator. Also the PLC-CODAS interface has been checked.

Figure 1 shows a picture taken from a CODAS diagnostic computer where is presented the status of KN3-NA system, “YES” meaning system OK and “NO” meaning system is out of work. In this frame by clicking on KN3-NA symbol we can see the status of the system, Figure 2: if the system is or not pressurized and where the attenuators are (parking or working position).

Figure 1 –Diagnostics subsystem status

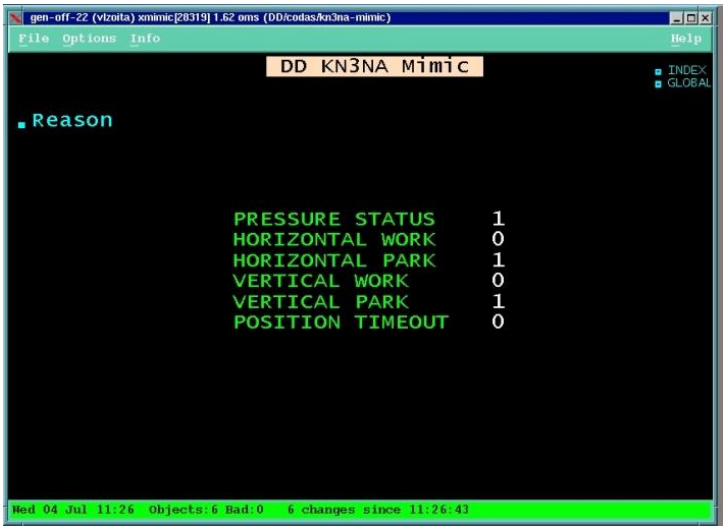

Figure 2 – KN3-NA mimic

2. Complex experiments and analysis for KN3-NA system validation

A detailed analysis of the available experiments was performed in order to select that one’s which are most appropriate the commissioning requirements. The following experiments were selected for our experiments:

Ex-2.3.1 Low delta Hybrid development: JET pulses #83408, #83409, #83410, #83412, #83420, #83517, #83518, #83521, #83523, #83525
Ex-2.3.2 Baseline scenario to high Ip: #83477
Ex-1.1.4 Fuel retention studies - Vertical target: #83507, #83509
Ex-2.3.1 Hybrid scenario development: #83520, #83521, #83523, #83525
Ex-1.2.5 Pulses prior to LTS retrieval: #83670, #83672, #83673
They ensure the availability of a high power experiments (NBI power > 20 MW).

The Neutron Attenuation Factor was calculated as the ration between the integrated counts in channel N for the reference pulse and integrated counts in channel N for the pulse when the Neutron Attenuator was in working position. We considered:

- N = 15 for the VC-NA (Vertical Camera Neutron Attenuator)
- N = 4 for the HC-NA (Horizontal Camera Neutron Attenuator)

The experimental data on attenuated values were normalised with respect to the following data obtained on the same JPN:

For VC-NA measurements

- KN3 horizontal camera (KN3-HC), same channel
- KN1 Time resolved total neutron yield monitor

For HC-NA measurements

- KN3 vertical camera (KN3-VC), same channel
- KN1 Time resolved total neutron yield monitor

The KN1 data integrated over the duration of the JET pulse to get the neutron yield (Yn). Obviously, for simultaneous VC-NA and HC-NA measurements only the KN1 time resolved total neutron yield monitor was used for normalization. In order to ensure a proper and accurate normalization, the reference pulses were chosen so that they have similar characteristics with the pulse used for the attenuation factor evaluation – see Figure 3 for a representative example.

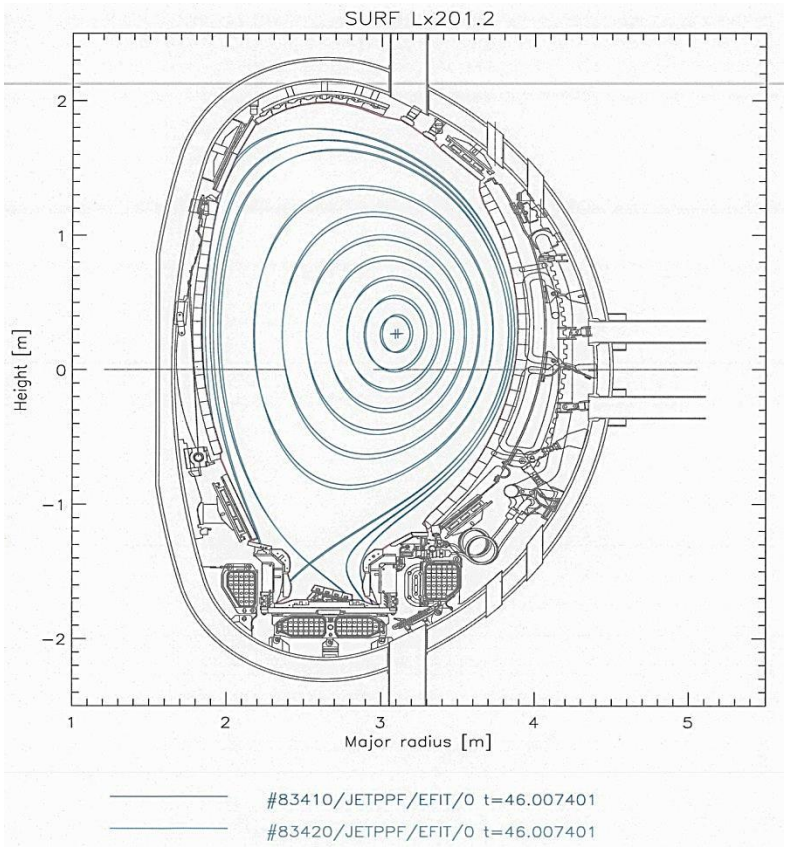

Figure 3 – The flux surface configurations for the JET pulse #83420 and the reference pulse #83410, VC-NA. Experiment 2.3.1, Hybrid scenario development. The flux surface configurations is shown at t=46 s.

The complete lists of the JET pulses used for the determination of the neutron attenuation factor (NAF) are given in Table 1 for the vertical attenuator (VC-NA) and in Table 2 for the horizontal attenuator (HC-NA).

The NAF values are evaluated for channel 4 in case of the horizontal camera and for channel 15 in case of the vertical camera. These channels correspond, in most cases, to a maximum of the neutron emission and therefore ensure a good statistic for the determination of NAF (Figure 4).

The effect of NAF on the neutron profiles is presented in Figures 5-6. The NAF profiles are presented in Figure 7.

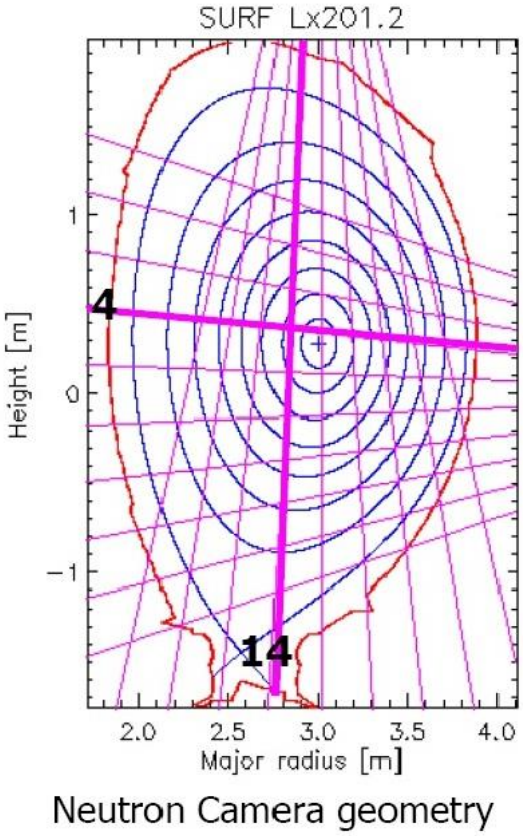

Figure 4 – The peak emission channels were used for the determination of NAF

Table 1 - VC-NA NAF results

No	JPN Attenuated pulse	JPN Reference number	Neutron attenuation factor		Experiment
			Normalized to KN3-HC(4)	Normalized to KN-1	
1	83408	83412	90	91	03/07/12 Ex-2.3.1 Hybrid scenario development
2	83409	83412	109	111	
3	83410	83420	114	117	
4	83517	83420	96	93	10/07/12 Ex-2.3.1 Hybrid scenario development
5	83518	83420	116	112	
6	83521	83420	-	92	
7	83523	83420	-	92	
8	83525	83420	-	91	
Average			**105**	**100**	

Table 2 - HC-NA NAF results

No	JPN Attenuated pulse	JPN Reference number	Neutron attenuation factor		Experiment
			Normalized to KN3-VC(15)	Normalized to KN-1	
1	83477	83476	61	61	06/07/12 Ex-2.3.2 Baseline scenario to high Ip
2	83507	83504	80	76	09/07/12 Ex-1.1.4 Fuel retention studies-vertical target
3	83509	83504	73	70	
4	83520	83420(*)	65	70	10/07/12 Ex-2.3.1 Hybrid scenario development
5	83521	83420	-	61	
6	83523	83420	-	64	
7	83525	83420	-	60	
8	83670	83679	62	63	18/07/12 Ex-1.2.5 pulsed prior to LTS retrieval
9	83672	83679	61	62	
10	83673	83679	64	65	
Average			**67**	**65**	

(*) 83420 from Ex-2.3.1 Hybrid scenario development (03/07/12)

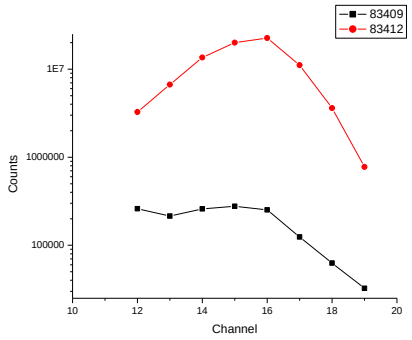

Typical KN3 profiles obtained for the vertical camera with the VC-NA attenuator in working position (black) and without the attenuator (red).

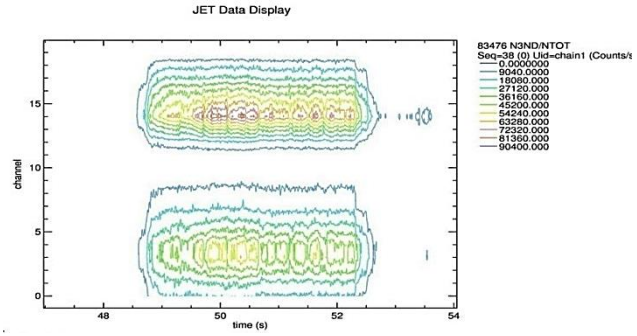

Typical KN3 profiles without attenuators.

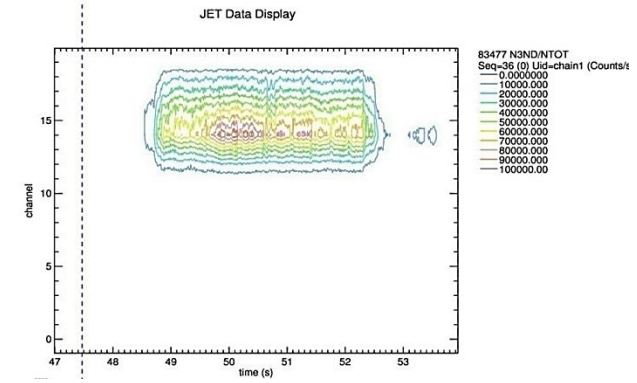

Typical KN3 profiles with the vertical attenuator (VC-NA) in working position.

Figure 5 – The effect of the VC-NA attenuator on the neutron profiles in case of the vertical camera. The effect is illustrated for the JET pulse 83412, using the reference pulse 83409.

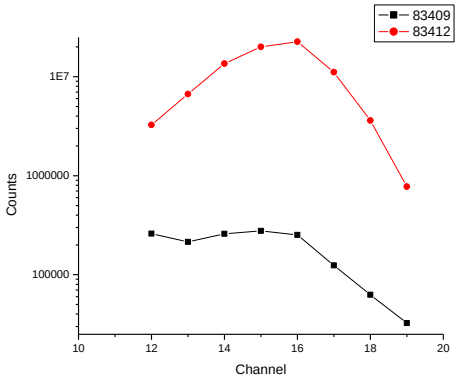

Typical KN3 profiles obtained for the horizontal camera with the HC-NA attenuator in working position (black) and without the attenuator (red).

Figure 6 – The effect of the HC-NA attenuator on the neutron profiles in case of the horizontal camera. The effect is illustrated for the JET pulse 83412, using the reference pulse 83409.

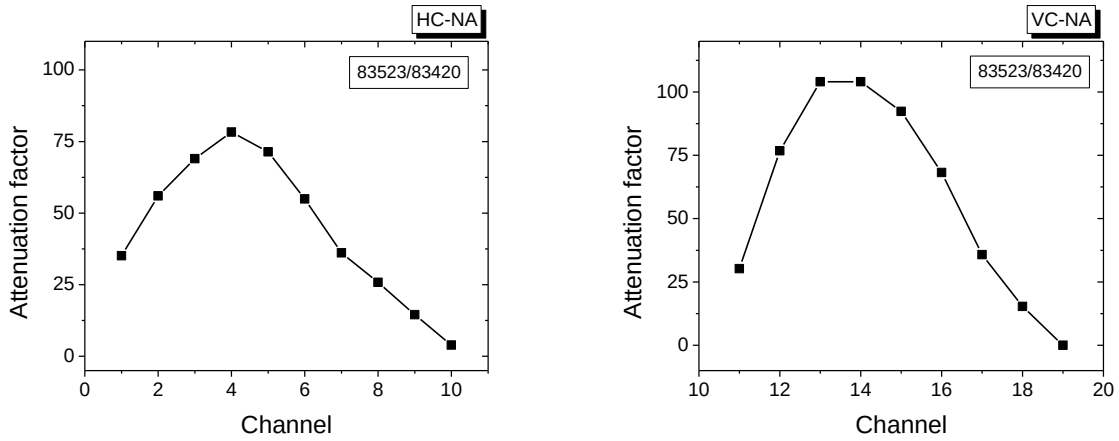

Figure 7 – Neutron attenuation factor (NAF) profiles.

The averaged values for NAF obtained in these experiments are: 105 for VC-NA and 70 for HC-NA. For VC-NA the experimental value is in good agreement with that one provided by the MCNP calculations. The difference obtained for the HC-NA attenuator arises from the hypothesis used in the MCNP calculation. The MCNP calculations were performed in 2007- 2008, considering a H2O attenuation thickness, for both attenuators, of 240 mm. Therefore for both VC-NA-S and HC-NA, the attenuation factor was estimated to be ~100. However, due to several technical constraints which became obvious in the later phases of the project (port insulation thickness, thermal expansion, disruption displacements), the attenuators were constructed with different lengths: VC-NA: 250 mm (with 240 the shortest attenuation paths) and HC-NA: 220 mm. The non-uniform shape of the NAF profiles can be explained by the neutron in-scattering process which arises in case of the lateral channels.

The main objective of the neutron attenuators is to reduce the neutron field and to determine an increased signal-to-noise ratio for the gamma spectroscopy measurements. Therefore it was necessary to estimate this effect in order to have a full qualification of the neutron attenuators system. The experiment consists in performing measurements with the CsI gamma detectors i) in line of sight (LOS) and in parking position (in shadow) without attenuator and ii) in line of sight (LOS) and in parking position with attenuator. The results are presented in Figure 8.

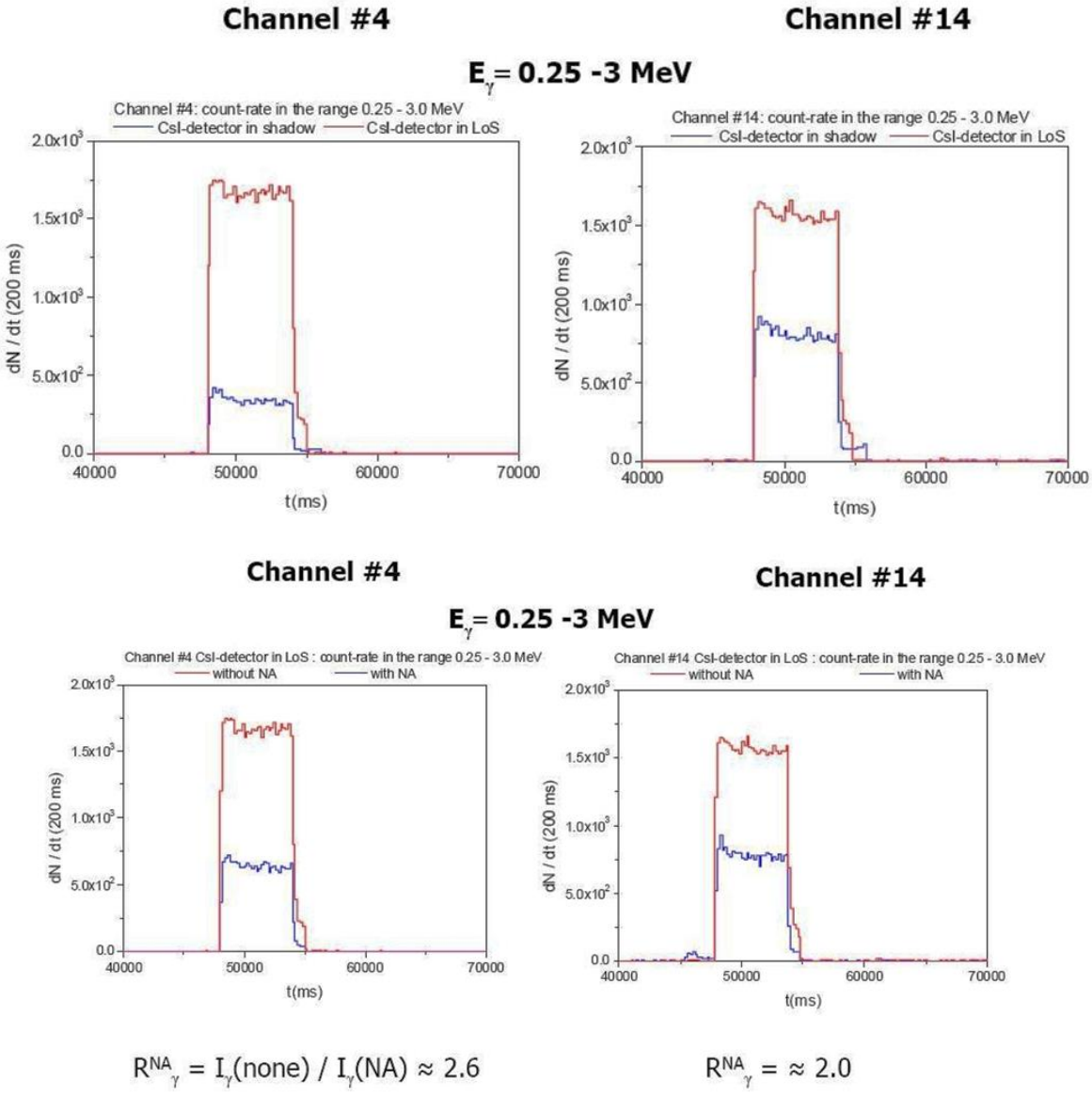

Figure 8 – The effect of neutron attenuators (VC-VA and HC-NA) on the gamma measurements

Conclusion

The commissioning of KN3-NA system has been successfully done. Complex and extensive experiments were performed for the validation of the neutron attenuators KN3-NA system. The neutron attenuation factor retrieved in the experiments are in agreement with values initially proposed, taking into account the additional technical constraints (port insulation thickness, thermal

expansion, disruption displacements) which were imposed. It was clearly demonstrated that KN3-NA provides adequate n/γ filtering for deuterium experiments.

Acknowledgement

The reported work includes contributions from the following people outside the EURATOM-MEdC Association: P. Blanchard (EFDA/CSU, Culham Science Centre, Abingdon, UK), N. Balshaw, V. Kiptily, D. Croft, G. Kaveney, D. Paton and David Kina (Association EURATOM-CCFE/JOC, Culham Science Centre, Abingdon, UK), A. Murari (Association EURATOM-ENEA, RFX, Padova, Italy), I. Lengar, Association EURATOM-MHST (Slovenia).

The authors would like to gratefully acknowledge the continuous support received from their institutes and laboratories.

References

[1] V. Zoita, T. Craciunescu, M. Curuia, M. Anghel, V. Kiptily, S. Soare, A. Fernandez, L. Giacommeli, I. Lengar, D. Kina, D. Falie, M. Gherendi, M. Riva, B. Syme, KN3-NA commissioning report, JET, 27 November 2012 .

AUTOMATIC REAL-TIME DISRUPTION PREDICTION BY FAST VISIBLE CAMERA VIDEO IMAGE PROCESSING

Teddy Craciunescu[1], Andrea Murari[2], Ion Tiseanu[1], Jesus Vega[1]

[1]*A EURATOM-MEdC Association, National Institute for Lasers Plasma and Radiation Physics, Bucharest*

[2] *Consorzio RFX, Associazione EURATOM-ENEA per la Fusione, Padova, Italy*

[2] *Asociación EURATOM0CIEMAT para Fusión, Madrid, Spain*

[BS_9/WP12-IPH-A07-2-03/PS; BS_15B/JET]

Abstract

MARFE instabilities may reduce confinement leading to harmful disruptions. They cause a significant increase in impurity radiation and therefore they leave a clear signature in the video data. This information can be exploited for automatic identification and tracking. MARFE classifiers, based on the phase congruency (PhC) theory and also on sparse image representation (SIR) in an overcomplete dictionary have been developed and adjusted to extract the structural information in the images of JET cameras. The methods were tested on JET experimental data and have proved to provide a good prediction rate.

Papers

[1] T. Craciunescu, A. Murari, I. Tiseanu, J. Vega, Phase Congruency Image Classification for MARFE Detection on JET with a Carbon Wall, Fusion Science and Technology 62-2(2012)339-346.

[2] Murari, A.; Vega, J.; Mazon, D.; Arena, T.; Craciunescu, T.; Gabellieri, L.; Gelfusa, M.; Pacella, D.; Palazzo, S.; Romano, A., Latest developments in image processing for the next generation of devices with a view on DEMO, Fusion Engineering and Design, Volume 87-12(2012)2116-2119.

Conferences

[1] T. Craciunescu, A. Murari, I. Tiseanu, J. Vega, Advanced Image Processing Techniques for Physics Studies, 7th Workshop on Fusion data Processing Validation and Analysis, 28-30 March 2012, Frascati, Italy.

[2] A. Murari, J.Vega, T.Craciunescu, P.Arena, D.Mazon, L.Gabellieri, M.Gelfusa, D.Pacella, S.Palazzo, A.Romano, J.F.Delmond, A. De Maack, The challenges of image processing: an introduction, 7th Workshop on Fusion data Processing Validation and Analysis, 28-30 March 2012, Frascati, Italy.

[3] A. Murari, J.Vega, T.Craciunescu, P.Arena, D.Mazon, L.Gabellieri, M.Gelfusa, D.Pacella, S.Palazzo, A.Romano, J.F.Delmond, A. De Maack , T.Lesage, Latest Developments in Image Processing on JET, 7th Workshop on Fusion data Processing Validation and Analysis, 28-30 March 2012, Frascati, Italy.

Reports

[1] T. Craciunescu, A. Murari, I. Tiseanu, J. Vega, Automatic Real-Time Disruption Prediction by Fast Visible Camera Video Image Processing (1), I Meeting EFDA WP12-IPH-A07-2: Development of Real-Time Disruption Prediction, Remote Meeting, 06 July 2012.

[2] T. Craciunescu, A. Murari, I. Tiseanu, J. Vega, Automatic Real-Time Disruption Prediction by Fast Visible Camera Video Image Processing (2), II Meeting EFDA WP12-IPH-A07-2: Development of Real-Time Disruption Prediction, Remote Meeting, 28 November 2012.

Detailed results

1. Introduction

Video cameras have recently become diagnostic tools widely used on the Joint European Torus (JET) for fusion plasma diagnostic and control. Camera based instruments provide essential information for both the control of the experiments and the physical interpretation of the results. These cameras

can produce up to hundreds of kframes per second and their information content can be very different, depending on the experimental conditions. However, the relevant information about the underlying processes is generally of much reduced dimensionality compared to the recorded data. The extraction of the relevant information, which allows the full exploitation of these diagnostics, is a challenging task.

Recently, several methods were developed for the automatic identification and tracking of objects in videos. A complete MARFE identifier, based on morphological operators and Hu moments [1], and a MARFE tracking method, based on the motion estimation within the MPEG video compressed domain [2], were reported. These methods can be applied to explore JET database for retrieving specific events needed for physical studies.

The real-time detection is extremely important as these instabilities may trigger harmful disruptions. Currently, at JET, the fast imaging systems are not yet used for their real time control. Two main aspects will have to be solved to use fast cameras for protection and control: the streaming of the data in real time and the developments of image processing algorithms fast and accurate enough to extract the relevant information. This work deals only with the second class of issues.

Several approaches, which aim to use the video data for the real time identification of MARFEs, have been reported in the literature. A hardware solution is based on the real-time image processing capability of cellular nonlinear/neural network-based chips [3]. A highly parallelized software implementation of the method introduced in Ref. 1 was recently reported [4].

Although a good rate of correct classifications and high speed implementations were achieved by the above mentioned methods, the problem remains open for approaches based on different paradigms which may lead to further improvements. Here we report first results obtained by using the phase congruency (PhC) theory.

2. Methods

2.1 Phase congruency

PhC theory is based on physiological and psychophysical evidences which show that visually discernible feature coincides with those points where the Fourier waves, at different frequencies, have congruent phases. PhC was introduced by Morrone et al. [5] and it provides a simple but biologically plausible model of how mammalian visual systems detect and identify features in an image. The extraction of features at points of high PhC is supported by some recent studies in neurobiology using functional magnetic resonance imaging [6]. PhC has the advantage to be a dimensionless quantity and to provide information that is invariant to image illumination, contrast and magnification.

PhC was used in the past as a tool for several image features significance estimation [7-10]. Recently, it was brought back into attention together with the development of Image Quality Assessment (IQA) methods. IQA methods attempt to quantify the differences between a distorted image and a reference image using a variety of known properties of the human visual system. The interest for accurate and easy to use IQA methods increased dramatically in a wide range of applications like image acquisition, transmission, compression, restoration and display. Several IQA methods make use of the assumption that the human visual system is adapted to the structural information in images. The visual information in an image is often very redundant, but the human visual system understands the image mainly based on its low-level features, such as edges and zero-crossing. A

measurement of structural similarity should provide a good approximation of perceived image quality. PhC, as a dimensionless measure of the significance of a local structure was used as a component in defining the FSIM (Feature Similarity Index) index [11]. A similarity score was developed based on the cross correlation between partitioned PhC maps [12]. PhC was extended to phase coherence in order to characterize the image blur [13] and sharpness [14].

The ability of PhC to extract highly informative features is used in our approach for MARFE automatic identification by full reference similarity. Reference 'pristine' MARFE frames are used in order to identify distorted or displaced similar patterns in input video data. The PhC concept and its implementation for MARFE automatic identification is presented in Section 2. Experimental results and the method assessment are presented in section 3.

Morrone and Owens [15] define the PhC function in terms of the Fourier series expansion of a signal at some location *x* as:

$$PC(x) = max_{\bar{\phi}(x)\in[0,2\pi]} \frac{\sum_n A_n cos\left(\phi_n(x) - \bar{\phi}(x)\right)}{\sum_n A_n} \quad (1)$$

where: A_n represents the amplitude of the *n*-th Fourier component, $\phi_n(x)$ represents the local phase of the Fourier component at position *x* and $\bar{\phi}(x)$ is the mean local phase angle of all the Fourier terms at the position x. The construction of PhC from the Fourier components is illustrated in Figure 1.

An alternative approach is to calculate points of maximum PhC by searching for peaks in the local energy function, which is defined by the following relation:

$$E(x) = \sqrt{F(x)^2 + H(x)^2} \quad (2)$$

where $F(x)$ is the signal with its DC component removed, and $H(x)$ is the 90 deg. phase shift of F(x) (the Hilbert transform). The energy is equal to phase congruency scaled by the sum of the Fourier amplitudes [16]:

$$\mathrm{PhC(x)} = \frac{\mathrm{E(x)}}{\sum_n \mathrm{A_n}} \quad (3)$$

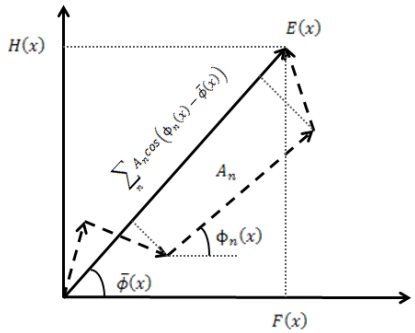

Figure 1 - Illustration of the construction of PhC. The local Fourier components, at a specific location x, are plotted as complex vectors adding head to tail. The energy of the signal $E(x)$ and its components ($F(x)$ - the signal with its DC component removed and $H(x)$ - the Hilbert transform of $F(x)$) are shown.

Approximations of $F(x)$ and $H(x)$can be obtained by convolving the signal with a quadrature pair of filters. Linear-phase filters must be used in order to preserve phase information. A widely used approach is represented by nonorthogonal wavelets that are in symmetric/antisymmetric quadrature pairs [17]. Let $\mathrm{Q^n_{even}}$ and $\mathrm{Q^n_{odd}}$ be the the even-symmetric and odd-symmetric filters on

scale n and let be $[e_n(x), o_n(x)]$ the responses of the quadrature pairs to a 1-D signal $I(x)$. The local amplitude on scale n is given by the relation:

$$A_n = \sqrt{e_n(x)^2 + o_n(x)^2} \tag{4}$$

and the energy components are:

$$F(x) = \sum_n e_n(x), \qquad H(x) = \sum_n o_n(x) \tag{5}$$

Therefore the 1-D PhC can be calculated as:

$$PhC(x) = \frac{E(x) - T}{\sum_n A_n(x) + \varepsilon} \tag{6}$$

where:

- ε is a small positive constant introduced in order to address the case when all the Fourier amplitudes are very small, and therefore the PhC calculation become ill conditioned.
- T is a multiple of the mean noise response; T is introduced in order to eliminate spurious responses to noise. It ensures that PhC of a legitimate feature is significant relative to the level of noise.

PhC is significant only if it occurs over a wide range of frequencies, for a specific location. Therefore a multiplicative weighting factor $w(x)$ must be introduced in (6), in order to penalize PhC at locations where the spread $s(x)$ of the filter responses is narrow. Kovesi [18] suggested that a measure of filter response spread can be achieved by the following relation:

$$s(x) = \frac{1}{N} \frac{\sum_n A_{n(x)}}{A_{max(x)}} \tag{7}$$

where N is the total number of scales being considered and Amax(x) is highest individual response at x. The weighting function is constructed by applying a sigmoid function to the filter response spread value:

$$w(x) = \frac{1}{1 + e^{\gamma(c - s(x))}} \tag{8}$$

where *c* is the cut-off value of the filter response spread below which phase congruency values become penalized, and γ is a gain factor that controls the sharpness of the cutoff.

The PhC calculation for 2-D images is obtained by applying the 1-D calculation over several orientations and combining the results in some appropriate way. A lateral extension of the filters is introduced by mean of a spreading function applied across the filter, perpendicular to its orientation. An appropriate choice is the Gaussian function which may induce amplitude modulation in the image, but leaves the phase unaffected. Therefore it ensures PhC preservation of any features in the image.

An adequate solution for constructing the symmetric/antisymmetric quadrature pairs of filters are the Gabor filters:

$$G(\omega) = e^{-\frac{\left(\log\frac{\omega}{\omega_0}\right)^2}{2\left(\log\frac{k}{\omega_0}\right)^2}} \tag{9}$$

where ω_0 is the filter's centre frequency. To obtain constant shape ratio filters the term $\frac{k}{\omega_0}$ must also be held constant for varying ω_0. By using Gaussians as spreading functions, the 2D log-Gabor function is defined by the following relation:

$$G_{2D} = e^{-\frac{\left(\log\frac{\omega}{\omega_0}\right)^2}{2\sigma_r^2}} \times e^{-\frac{\left(\theta-\theta_j\right)^2}{2\sigma_\theta^2}} \quad (10)$$

Where $\sigma_R = \log\frac{k}{\omega_0}$, θ_j is the j-orientation angle of the filter and σ_θ determines the filter's angular bandwidth.

The PhC values obtained for different orientations have to be combined ensuring that features or conjunction of features, at all orientations, are treated equally. This can be achieved by summing and normalization over all orientations and scales:

$$PhC(x) = \frac{\sum_o \sum_n w_{no}(x) E_{no}(x) - T}{\sum_o \sum_n A_{on}(x) + \varepsilon} \quad (11)$$

PhC can be used to identify significant features in the image as it values varies between 0 (a feature with no significance) and 1 (a very significant feature).

2.2 MARFE automatic identification

The MARFE instability is a tokamak edge phenomenon characterized by greatly increased radiation, density and density fluctuations, and decreased temperature in a relatively small volume. MARFE usually occur on the high field side of the torus [19] and are the manifestation of a thermal instability, with impurity radiation being the main energy loss mechanism from its volume. MARFEs can reduce confinement and, more importantly, they can cause disruptions which lead to the sudden losses of plasma confinement determining the abrupt end of the discharge. They may represent a risk for the integrity of the devices. As MARFEs cause a significant increase in impurity radiation, they leave a clear signature in the videos recorded by visible cameras in JET with the carbon wall, they appear as ribbons of radiations moving up and down the vacuum vessel on the high field side. A typical MARFE sequence of images recorded at JET is presented in Figure 2. For the JET database, the video signature is visible for a number of frames between 3 and 65 [10].

Some specific MARFEs characteristics can be exploited for automatic identification. MARFEs are characterized by their top-to-bottom movement, and they have a clearly defined ribbon-like shape, at least for the first part of the movement (Figure 2). However, the identification method must be able to avoid the confusion with other video objects, like e.g. flashes, probably caused by ELMs (Edge Localized Modes) or high radiation from the poloidal limiters.

A region of interest can be defined to encompass the area corresponding to the first part of the evolution of a MARFE (Figure 3). PhC is calculated over several orientations θ_k(Figure 4). PhC is evaluated for the current frame in the input video data and also for one or more reference frames, over several orientations θ_k, determined by the MARFE ribbon-like shapes (Figure 4).

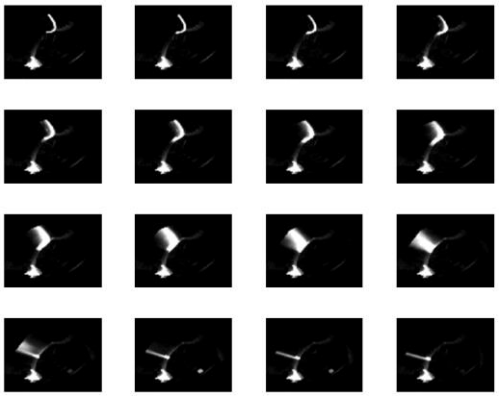

Figure 2 - MARFE image sequence recorded during JET pulse #70050 during the time interval 53.869477-53.869953 s (frames 1621-1636).The MARFE evolution can be retrieved following the images along the rows in the figure.

Figure 3 - Video frame showing a video shape similar to a MARFE one (JET pulse #70050, frame recorded at t = 53.718185 s).

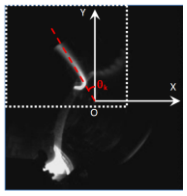

Figure 4 - A region of interest (dotted square) and a particular orientations θ_k used for the calculation of PhC.

A similarity map between these frames can be constructed using the following relation [20]:

$$\mathrm{SIM(x)} = \frac{2\cdot \mathrm{PhC_i^{cur}}\cdot \mathrm{PhC_i^{ref}} + \mathrm{T'}}{\left(\mathrm{PhC_i^{cur}}\right)^2 + \left(\mathrm{PhC_i^{ref}}\right)^2 + \mathrm{T'}} \tag{12}$$

where Im_{cur} is the current image, Im_{ref} is the reference image and T′ is a positive constant introduced in order to ensure the stability of the calculation of SIM. The SIM map contains similarity values for each location x, ranging within (0, 1]. For multiple reference images PC^{ref_j} $(j = 1,..,N)$ the corresponding similarity indexes SIM_j are multiplied in order to obtain a global structural similarity map:

$$SIM(x) = \prod_j^N SIM_j\,(x) \tag{13}$$

where N is the total number of reference images.

The SIM map, which contains similarity values calculated at each location x, can be pooled into a single similarity score using the relation:

$$SIM_{score} = \frac{1}{\mathcal{D}} \int_{x\epsilon\Omega} SIM(x)dx \tag{14}$$

where Ω is the map domain and $\mathcal{D}$ is its area.

3. Results

The PhC image classification method has been implemented following the steps described previously.

For each analyzed image, the PhC evaluation implies the calculation of its Fourier transform, and the convolution with the pre-calculated odd and even filter components, at each scale. The amplitudes of odd and even responses are used for the calculation of energy (Eq. 2) and PhC (Eq. 6) values.

We used a total number of 4 wavelet scales and a scaling factor of 2 between successive filters. The ratio of the standard deviation of the Gaussian describing the log Gabor filter's transfer function in the frequency domain to the filter center frequency is $\frac{k}{\omega_0} = 0.5\ (\mathrm{Eq.}\ 9)$. The standard deviation for the angular filter component is $\sigma_\theta = 1.3$.

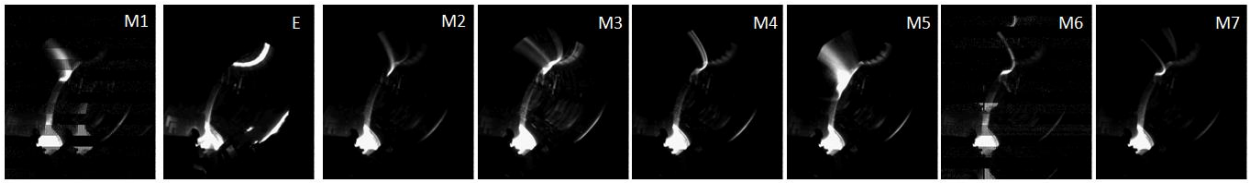

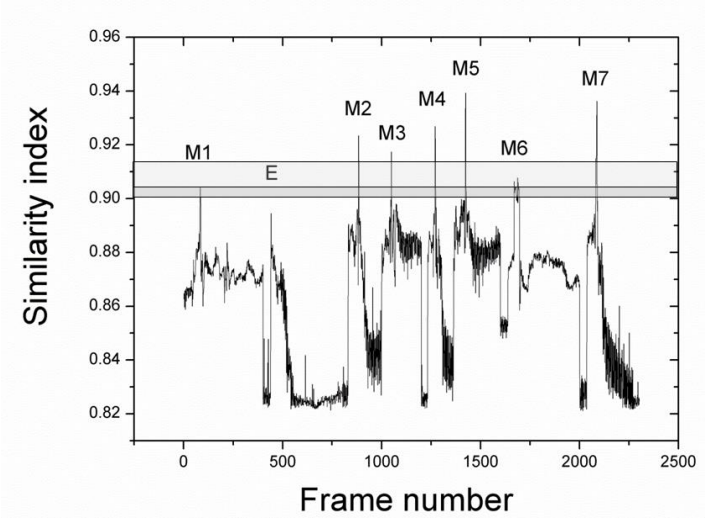

Figure 5 - The evolution of the similarity score SIM_{score} for JET pulse #50053. The range in the SIM_{score} where a threshold level can be introduced to separate peaks corresponding to MARFE events (peaks M_1,…M_7) from non-MARFE ones (peak E) is represented: i) dark grey band for the all videos, no matter of the image quality and ii) light grey band for the case when frames affected by camera artifacts are removed.

The parameters of the frequency spread weighting function (8) have been set to $c = 0.5$ and $\gamma = 10$. The value of the constant introduced in order to address the case when the all the Fourier amplitudes are very small (Eq. 6), has been set to ε =0.001.

The method has been tested on videos extracted from the JET database. All the videos were recorded using the wide angle view fast visible camera (Photron APX) installed in the Joint European Torus JET [21].

A representative result is illustrated in Figure 5 for JET pulse #50053. The evolution of the similarity score SIM_{score} is characterized by clearly revealed peaks corresponding to MARFE events (peaks *M1÷M7*). A threshold level, can be introduced to separate peaks corresponding to MARFE events from non-MARFE ones (peak *E*). Taking into account all the videos analyzed, it results that the threshold value can be set anywhere in the range $SIM_{score} \in (0.900 \div 0.904)$. If the severe degradation of the image quality of several frames (like e.g. M_1 and M_6), due to camera artifacts, can be avoided, the range can be significantly increased $SIM_{score} \in (0.900 \div 0.965)$. This will allow a more reliable discrimination of MARFE events.

The phase congruency analysis was applied for a number of ten JET pulses. The method ensures a success rate of 96.2% with 0.03 false positive events and 3.5% false negative events.

4. Conclusion

A method based on PhC principle has been developed for MARFE automatic identification. The method combines PhC information over multiple orientations creating a highly localized operator, with higher values at locations with increased structural significance. PhC has the advantage to be invariant to contrast and luminosity and therefore can work well with JET videos, which can be affected by a variable background. PhC proved to be robust with respect to the distortion and magnification of MARFE's shapes. A good prediction rate is achieved. The method depends on several adjustable parameters. However, once tuned, they remain valid for all JET videos.

References

[1] A. Murari et al., IEEE Trans. On Plasma Science, 38-12(2010)3409.
[2] T. Craciunescu et al., Nucl. Instr. Meth. A, 659-1(2011)46.
[3] G. Vagliasindi et al., IEEE Transaction on Instrumentation and Measurement, 58-8(2009)2417.
[4] M. Portes de Albuquerque et al., IEEE Transactions on Plasma Science, 40-12(2013)3485.
[5] M. C. Morrone et al., Pattern Recognition Letters, 16(1995)667.
[6] R. A. Owens et al., Pattern Recognition Letters, 9(1989)223.
[7] S. Venkatesh et al., Pattern Recognition Letters, 11(1990)339.
[8] B. Robbins, Image and Vision Computing, 15-5(1997)353.
[9] P. Kovesi, Proc. VIIth Digital Image Computing: Techniques and Applications, Sun C., Talbot H., Ourselin S. and Adriaansen T. (Eds.), 10-12 Dec. 2003, Sydney, pp. 309-318.
[10] M.C. Morrone et al., Proc. R. Soc. Lond. B, 235-1280(1988) 221.
[11] L. Zhang et al., IEEE Transactions on Image Processing, 20-8(2011)2378-2386.
[12] Z. Liu et al., Pattern Recognit. Letters, 28-1(2007)166-172.
[13] Z. Wang et al., Adv. Neural Information Processing Systems, 2004, pp. 786-792.
[14] R. Haseen, et al., Proc. IEEE Int. Conf. Acoust., Speech, and Signal Processing, 2010, pp. 2434-2437.
[15] M.C. Morrone et al., Pattern Recognit. Letters, 6-5(1987)303.
[16] S. Venkatesh et al., Proc of International Conference on Image Processing, Singapore, 1989, pages 553–557,.
[17] J. Morlet et al., Wave propagation and sampling theory - Part II: Sampling theory and complex waves. Geophysics, 47(2):222–236, February 1982.
[18] P. Kovesi, VIDERE: J. Comp. Vis. Res., vol. 1, no. 3, pp. 1-26, 1999.
[19] B. Lipschultz et al., Nuclear Fusion, vol. 24-8(1984) 977-988.
[20] Z. Wang, IEEE Trans. Image Process, 13-4(2004)600.
[21] J.A. Alonso, International Conference on Burning Plasma Diagnostics, Varenna, Italy, 24–28 Sept. 2007, AIP Conf. Proc. 988, pp. 185-188.